INFORMATION TO USERS

Folding of Stratigraphic Layers in Ice Domes

Herbert Paul Jacobson III

A dissertation submitted in partial fulfillment
of the requirements for the degree of

Doctor of Philosophy

University of Washington

2001

Program Authorized to Offer Degree: Earth and Space Sciences

UMI Number: 3013974

UMI®

In presenting this dissertation in partial fulfillment of the requirements for the Doctoral degree at the University of Washington, I agree that the Library shall make its copies freely available for inspection. I further agree that extensive copying of this dissertation is allowable only for scholarly purposes, consistent with "fair use" as prescribed in the U.S. Copyright Law. Requests for copying or reproduction of this dissertation may be referred to Bell and Howell Information and Learning, 300 North Zeeb Road, Ann Arbor, MI 48106-1346, to whom the author has granted "the right to reproduce and sell (a) copies of the manuscript in microform and/or (b) printed copies of the manuscript made from microform."

Signature

Date
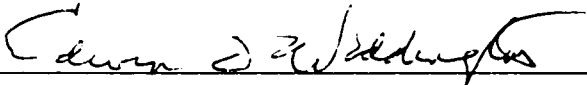
University of Washington

Graduate School

This is to certify that I have examined this copy of a doctoral dissertation by

Herbert Paul Jacobson III

and have found that it is complete and satisfactory in all respects,

and that any and all revisions required by the final

examining committee have been made.

Chair of Supervisory Committee:

_____

Edwin D. Waddington

Reading Committee:

_____

Charles F. Raymond

_____

Bernard Hallet

Date: _____ June 7 2001 _____

University of Washington

Abstract

Folding of Stratigraphic Layers in Ice Domes

by Herbert Paul Jacobson III

Chair of Supervisory Committee:

Professor Edwin D. Waddington
Dept. of Earth and Space Sciences

This dissertation presents a two part model of the formation of recumbent folds in stratigraphic layers of ice sheets such as those in Greenland and Antarctica. The initial disturbances in the stratigraphy have their roots in transient dynamic processes and local rheological inhomogeneities, but the kinematics of even a simple ice flow model can deform these disturbances enough to alter paleoclimatic interpretation of an ice core. This study focuses on this deformation, treating the disturbed stratigraphic layers as passive markers in the large–scale flow.

The two major tools that I use to study overturning are core–relative isochrones (precores) and the deformation gradient tensor along a particle path. This tensor is used to calculate the rotation of stratigraphic segments of various orientations.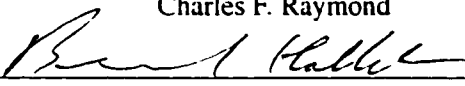 It is also used in a stochastic model to derive the probability distribution of observing overturned segments given a probability distribution of the initial disturbances.

Overturn probabilities increase downstream along a path. They also increase with depth, unless the initial disturbance processes are concentrated at a particular depth. Because of rapid rate of rotation of near–vertical segments, the probability of seeing obvious overturning in a small ice–core cross–section is low even if recumbent folds are present. Gentle disturbances are more likely to be overturned if they occur deep in the ice where the shear is strongest.

Overlaying precores on divide arch isochrones shows that ice divide movement can produce recumbent folds. This movement must have a stop–start quality, with enough stability to produce ma-

ture arching. but also enough movement to leave an orphaned disturbance on the flank where it can be overturned. Such folding may be most likely downstream from ice ridges bounded by variable ice streams.

The variation in the vertical thickness of a disturbed layer is also examined. Even if a disturbance is not overturned. some portions will be thinned more than undisturbed layers while other portions will be thickened. Passive deformation may reduce or exaggerate certain aspects of dynamically produced stratigraphic disturbances. but it does not obliterate them.

TABLE OF CONTENTS

LIST OF FIGURES

v

LIST OF TABLES

ACKNOWLEDGMENTS

I wish to express sincere appreciation to the members of my committee for their advise and encouragement. Possibly even greater thanks is due to my wife and son for their support and encouragement.

INTRODUCTION

This dissertation examines the possibility that recumbent folding could disturb the stratigraphic layering in cores taken from ice sheets in Greenland and Antarctica. I use a two–stage model of folding in which the large–scale flow of the ice sheet shears and overturns disturbances in the steady state stratigraphy (Figure 0.1). The initial disturbances must be produced by transient dynamic processes and local rheological inhomogeneities. The core of this work is a finite strain analysis of the deformation of such disturbances by the large–scale flow. The goal of this work is to identify where recumbent folding could occur and how it might affect the stratigraphy in ice cores. Due to limited knowledge of the seed processes, it has been most productive to start with a fold, and to seek constraints on its origin.

Chapter 1 is presents foundations for analysis, summarizes previous work, and outlines the basic model of folding. Precores and the deformation gradient tensor, F, are two tools that I use to evaluate what disturbances could be overturned. The precores are core–relative isochrones, which can be derived from conventional stratigraphic isochrones. They give the orientation at upstream points of segments which are vertical in an ice core. F, which can be calculated with a differential equation along a particle path, is a general tool for deforming any small disturbance. I apply these tools to the question of where observed dips and folds (in the GISP2 ice core) could have originated.

This folding model is extended in Chapter 2 with the addition of a probabilistic component. By describing the initial disturbance generation in terms of a disturbance injection probability distribution, I can calculate an overturn probability distribution at points downstream. F is used to define the the set of overturnable injection events. A number of different injection patterns are examined.

An example of the use of precores is given in Chapter 3. By overlaying precores and an offset Raymond bump, I show that a suitable stop–start pattern of divide migration can result in recumbent folding downstream. By tracking layers with a time dependent ice sheet geometry, I look at what effect the rate of divide migration has on this folding.

2

Stratigraphic disturbance by
- soft or hard anisotropic lumps
- special divide dynamics
- bed bumps

Observed disturbances in ice cores
- GRIP and GISP2 discrepancies
- dips, stripes and folds
- deep inverted layers
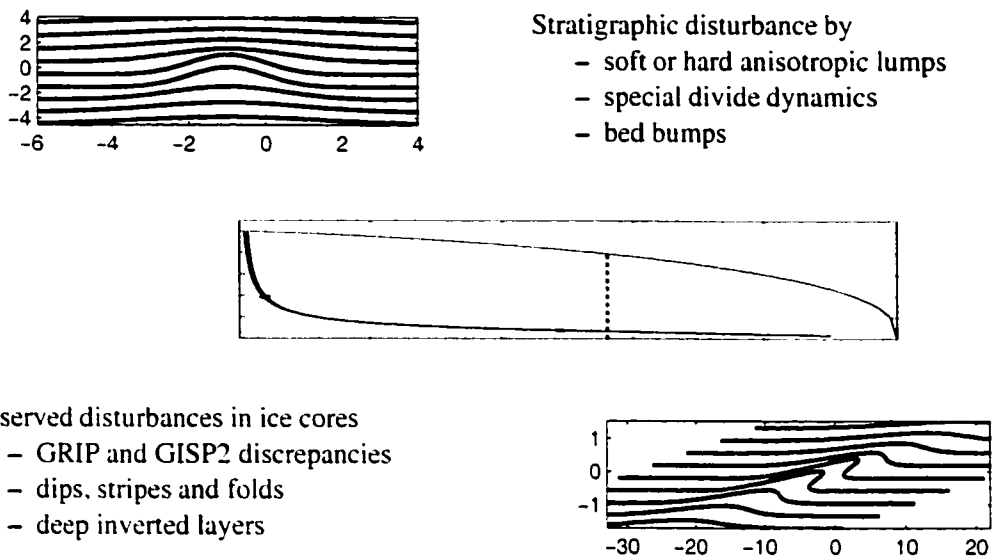
Figure 0.1: Large–scale flow deforms open disturbances into recumbent folds

In Chapter 4, the $\mathbf{F}$ tensor is used to examine the change in the vertical thickness of disturbed layers as they are deformed by the large–scale flow. After identifying key patterns of change from a simple disturbance. I look at thickness variations in more general wiggles, including the divide arching analyzed in Chapter 3.

Appendix A is a detailed description of the flowband velocity model used in this work (a summary is included in Chapter 1). Appendices B, C, and D add other calculation details to the main chapters. Appendix E describes a generalization of Mohr circles to nonsymmetric linear operators such as the velocity gradient and the deformation gradient tensors. Related topics such as the vorticity number, segment rotation rate, and matching rotation angles are also discussed. Appendix F is a preliminary look at folding over an undulating bed. Notation is summarized in Appendix G.

Chapter 1

RECUMBENT FOLDING IN ICE SHEETS - PART 1:
A CORE–REFERENTIAL STUDY

Abstract

To better understand apparent stratigraphic disturbances in ice cores such as GISP2, we examine how ice sheet flow can transform gentle open folds into order–disturbing recumbent folds. The initial disturbances in the stratigraphy must have their roots in transient dynamic processes and local rheological inhomogeneities, but the kinematics of even a simple ice flow model can deform these disturbances enough to alter paleoclimatic interpretation of an ice core. The vorticity number of the local velocity gradient of the flow suggests which structures can be passively overturned, but analyzing the finite strain along particle paths gives a more complete picture. We examine the finite strain relative to a hypothetical core location. Core–relative isochrones predict which stratigraphic disturbances will appear as obviously overturned layers in a core. Further insight is gained by calculating the deformation gradient tensor along particle paths and deriving its effect on segments of different slope. These calculations suggest that observed 20° dips in the GISP2 core are rotating on a time scale of a few hundred years and could result from dynamically produced distortions with much smaller slopes in the stratigraphy upstream. The time during which they are obviously overturning is small because the rotation rate is high. Once overturned they are flattened further and may be hard to recognize, especially in the small cross–section of a core.

1.1 Introduction

Underlying the paleoclimatic interpretation of ice cores is the assumption that a core samples the ice in the order in which it was deposited. Some post–depositional modification in the ice stratigraphy, such as thinning of annual layers, is anticipated and can be included in the interpretation of the climatic signal. Unanticipated thinning would introduce errors in some climatic signals, such as the

accumulation rate, but actual alteration in the order of some of the stratigraphic layers in the core sample affects all of the climatic signal they carry.

The suggestion that the GRIP ice core showed evidence of major climatic shifts in part of the Eemian interglacial period (GRIPmembers, 1993) proved to be particularly controversial when the nearby GISP2 core lacked the corresponding oxygen isotope oscillations (Grootes et al., 1993). It was suggested that one or both of the cores had been altered by folding or other forms of mixing. Further research found evidence for inverted stratigraphy close to the bed by comparing the water isotope signal with the atmospheric dissolved gases signal (Fuchs and Leuenberger, 1996). A detailed examination of visible stratigraphy showed dips of up to 20°, and even a few small overturned folds (Alley et al., 1995). A small–scale structure, called 'stripes', was also identified in the GISP2 core (Alley et al., 1997).

Interaction of contrasting layers has been been proposed as a cause of such folding (Dahl-Jensen et al., 1997). Layering in anisotropic ice directly under the divide, where it is subject to vertical compression appears, in theory, to be unstable (Castelnau et al., 1998; Azuma and Goto-Azuma, 1996). Recumbent Folding observed at the terminus of the Barnes Ice Cap has been attributed to advancing or retreating margins (Hudleston, 1976). Banding developed under one flow pattern could be passively deformed and folded when subjected to a different flow.

The GRIP core was drilled close to the current summit divide of the Greenland ice sheet in the hope of observing a maximum possible thickness of undisturbed ice. The GISP2 core was placed 10 ice thicknesses (30 km) to the west to give a complementary sample of near flank flow ice. But if the divide has moved around during last glacial cycle (Cuffey and Marshal, 2000) it may be best to consider both locations as near–divide sites. Other cores, such as Dye3, Camp C, and Byrd, have been drilled on clearly flank positions.

1.1.1   A Passive Shearing Model of Folding

To understand how stratigraphic layers in an ice sheet could be reordered, Waddington et al. (sub) (Waddington et al., 1995; Jacobson and Waddington, 1996) have studied the kinematics of forming recumbent folds from gentle disturbances in otherwise steady state stratigraphy. These initial disturbances could have their roots in some transient dynamic process, most likely involving local rhe-
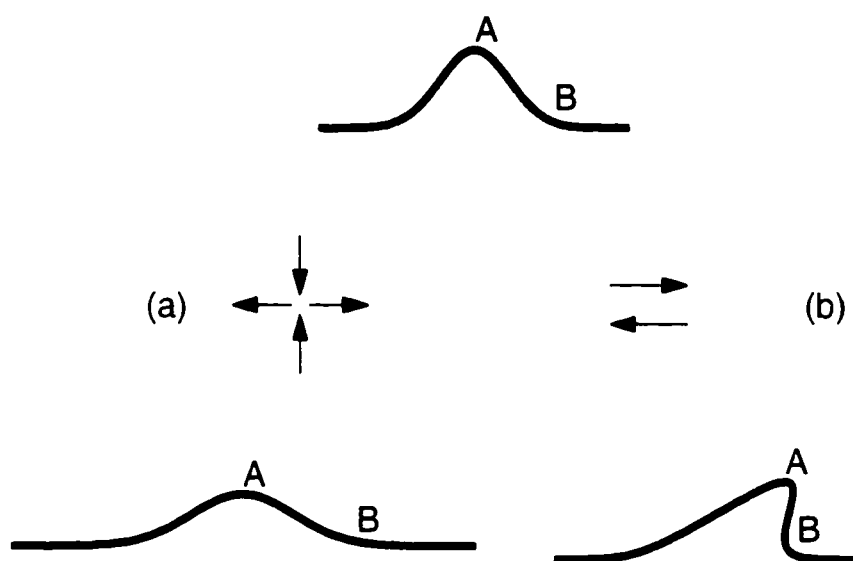
Figure 1.1: The deformation of a disturbed layer under (a) pure shear and (b) simple shear. Pure shear, with vertical compression, flattens the disturbance. Simple shear steepens (and overturns) the A–B edge while leaving the disturbance amplitude unchanged.

ological inhomogeneities. See Waddington *et al.* (sub) for further evaluation of possible processes that could generate wiggles.

The deformation in an ice sheet in plane strain can be represented as a combination of vertically compressive pure shear and bed–parallel simple shear. The pure shear thins and stretches the stratigraphic layers. It also flattens disturbances in these layers. The simple shear, on the other hand, 'catches' these wiggles and deforms them into order–disrupting recumbent folds. These two effects are illustrated in Figure 1.1, where the contrasting rotations of the A–B edge are highlighted. When we discuss the angle and rotation of a segment, it is the behavior of just such a portion of a disturbance that we have in mind.

Waddington *et al.* (sub) used this tradeoff between stretching and shearing to determine where disturbances of any given slope would be flattening and where they would be overturning. They

assessed the plausibility of several proposed disturbance sources, and applied their stability limit estimates to the Dye 3, GRIP, GISP2 and Siple Dome ice core sites. Their simple approach was based entirely on the strain rate at a point, e.g. the point at which a disturbance might be created by localized inhomogeneous flow. As they noted, their assessment gave an optimistic view of stratigraphic integrity, because it neglected variations in strain rate experienced by disturbances as they moved (a) over undulating bedrock, and (b) into deeper regions with stronger bed–parallel shear strain rates. They were able to estimate the time required for disturbances to overturn, and the distance that disturbances would move during this time, but only for disturbances that were already rotating strongly at the point of injection. They suggested that finite strain calculations, following disturbances as they moved along particle paths, would produce better assessments of the behavior of marginally unstable disturbances, and would greatly advance understanding of this passive folding process. This paper analyzes those finite strains to understand features of folding that could not be addressed by Waddington *et al.* (sub).

One measure of the mixture of pure and simple shear is the kinematic vorticity number, $W_k = \bar{\omega}/\bar{\varepsilon}$ (Means *et al.*, 1980). This is defined so that for pure shear $W_k = 0$, and $W_k = 1$ for simple shear. $\bar{\omega}$ is the rotation rate of the principal axes, and $\bar{\varepsilon}$ is the difference in their strain rates, $\dot{\varepsilon}_{max} - \dot{\varepsilon}_{min}$. In Hudleston and Hooke (1980) this is the Index of Simple Shear, *Iss*. Under pure shear the principal axes do not rotate, while under simple shear their rotation rate equals the strain rate.

The vorticity number for a simple ice sheet flowband model[1] is shown in Figure 1.2. Near the surface of the ice sheet vertical compression dominates so W_k is close to 0. This is also true directly under the divide where the horizontal flow is negligible. Elsewhere on the flank the proportion of simple shear increases with depth and W_k approaches unity.

In pure shear (as in Figure 1.1(a)), vertical and horizontal segments do not rotate, while segments on either side of vertical rotate toward horizontal. Under simple shear, all segments, except those parallel to the plane of shear, rotate in the same direction (clockwise in Figure 1.1(b)). In mixed pure and simple shear ($0 < W_k < 1$), there is some angle, $\theta_r \approx \cos^{-1} W_k$, between vertical and horizontal that is not rotating, and which separates the clockwise rotating segments from the anti–clockwise ones (Bobyarchick, 1986). The contours in Figure 1.2 have also been labeled with this angle.

---

[1]Our model geometry and notation are explained in Section 1.2.2.
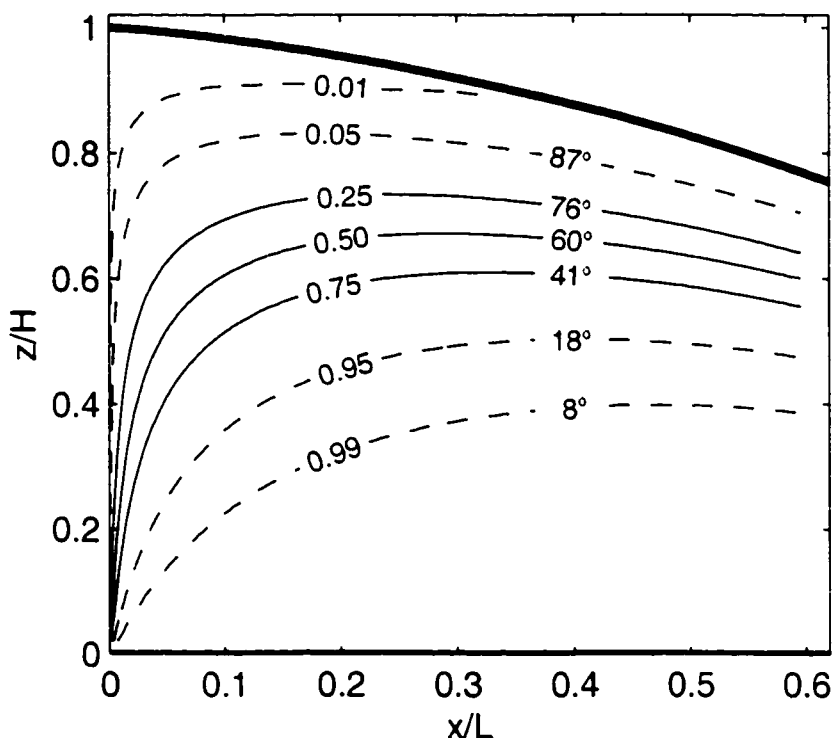
Figure 1.2: The kinematic vorticity number. W_k, and the critical wiggle angle. θ_r, for a simple ice sheet model. The left hand number on each contour. W_k, is a measure of the relative magnitudes of pure and simple shear. Pure shear dominates near the surface and under the divide (W_k close to 0) while simple shear dominates else where (W_k close to 1). The right hand number. θ_r is the segment angle that is not rotating at this point in the flow ($\cos^{-1} W_k$).

The critical wiggle segment slope. $m_{crit} \approx \Sigma^{-1}$. in Waddington *et al.* (sub) is approximately the tangent of θ_r. Their dimensionless shear number. Σ. is a variant on the vorticity number.

The bump in Figure 1.1 with the A–B segment at about 41° would be flattening if it occurred above the 41° contour in Figure 1.2. But if it was below this contour, the A–B segment would be steepening (rotating clockwise).

This no–rotation angle. θ_r. is not simply a divider between segments that rotate one way versus the other. As a segment moves along a particle path. W_k increases and θ_r decreases. The effect on the segment rotation can be seen by considering a segment with an angle equal to θ_r at time t on the path. At this point it is not rotating. At $t + dt$. a short time later, it will have practically the same angle. but
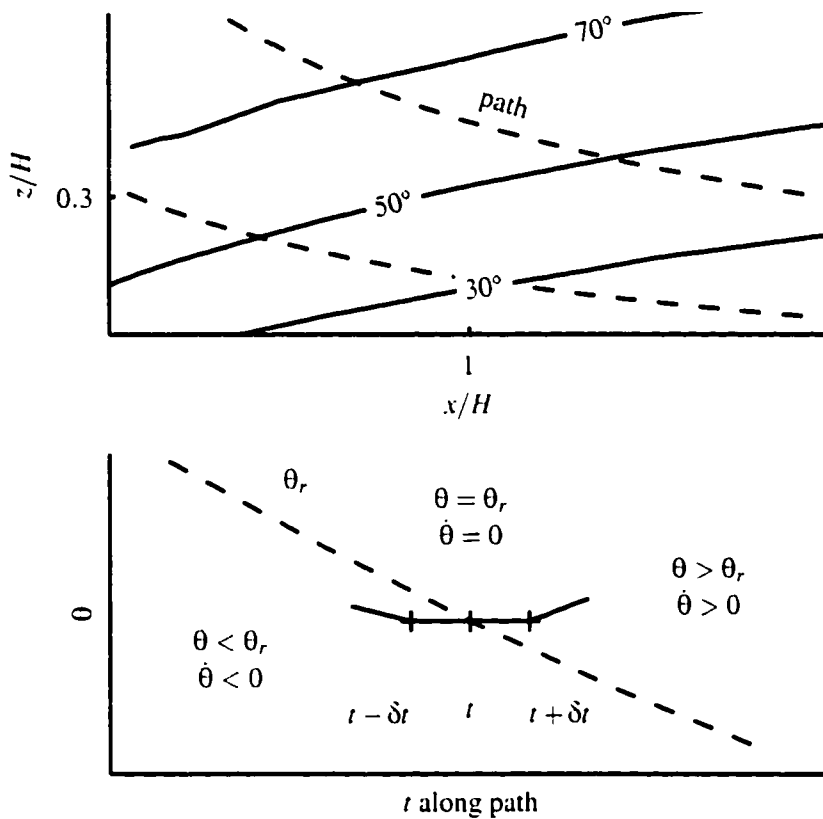
Figure 1.3: The change in leading edge rotation direction at θ_r, where $\dot{\theta} = 0$.

will be further along the path, where θ_r will be smaller. Since it is now steeper than θ_r its rotation is clockwise (steepening) away from θ_r. But at an earlier time, $t - dt$, the local θ_r was larger than the segment angle, which means, that the segment was rotating anti–clockwise (flattening) toward θ_r. In effect the θ_r angle is a turn–around point. Segments rotate anti–clockwise until they reach the local θ_r, at which point, they stop rotating, and start rotating in the other direction.

1.1.2 Observation Points

Since segments can change their direction of rotation, we need to look at the evolution of a disturbance over a finite interval along a path in order to gain a more detailed understanding of the folding

process than that which the first analysis of θ_r by Waddington *et al.* (sub) provides. This requires choosing meaningful end points for such an interval.

The obvious choice for the starting point is where the disturbance originated, assuming, of course, that there is a point where the transient dynamics generating the disturbance ceases to be significant and we can focus on the kinematics. In this paper we ignore the complexities of this transition. But since we do not have a comprehensive theory of how and where this disturbance injection might occur, we will limit our study to examining the effect of injection at a variety of positions.

We have found it equally productive to specify the interval end point, with an observed or hypothetical fold, and ask what sort of disturbance might have been its precursor. In particular we look at a vertical set of observation points, such as might be sampled in an ice core.

To study this kinematic folding, we use a flowband model to calculate the velocity and its gradient at all points, and use this to calculate particle paths. The model captures the transition in vorticity number, without unnecessary complexities. Then we define and explore the notion of core–relative isochrones, and show their relevance to the folding question. Next we calculate the deformation gradient and show how it ties in with these isochrones, giving us more general information on segment rotation. Finally we address the question of how much information is needed to predict where observed folds might have originated.

1.2 Flowband Model

After defining some terminology for dealing with disturbances and angles, we will describe a simple flowband model of an ice sheet. This model calculates the velocity at points in the flowband as a function of position and model geometry. Using this velocity field, we can calculate the velocity gradient, W_k and θ_r. We can also calculate particle paths and finite strain along these paths.

1.2.1 Disturbance Notation

A prototypical upward disturbance with key terms is depicted in Figure 1.4. Such a wiggle might be the result of stratigraphic layers draping around a transient rheologically harder lump (Waddington *et al.*, sub). Of particular interest is the *leading edge*, (the A–B edge in Figure 1.1) which is the portion of this disturbance which would overturn when sheared in the direction of flow. We will
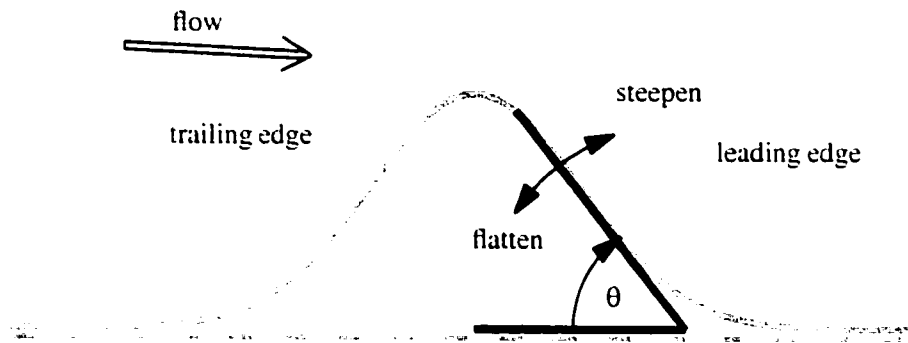
Figure 1.4: Prototypical disturbance, illustrating our notation, including *leading edge, trailing edge,* and θ. Segment slope is measured relative to horizontal (pointing upstream). Not shown is the slight slope (relative to horizontal) of the undisturbed stratigraphy. One could imagine a disturbance such as this forming around a rheologically stiffer 'lump' in the ice. Such a lump would also disturb the layers below it.

also refer to the *trailing edge,* the portion that will flatten under both pure and simple shear. If the disturbance were inverted (that is, a dip) the edge on the upstream side of the disturbance would be the edge at risk of folding[2].

We will use θ for the angle of a segment, measuring it relative to the horizontal axis pointing in the upstream direction (to the left in our prototype). This choice of angle orientation means that the initial angle of a leading edge will be in the 0 to 90° range, and will increase to 90° and beyond when the leading edge overturns. A trailing edge will start in the 90 to 180° range and rotate toward 180°.

For the purposes of this paper we ignore the distinction between horizontal and the slope of undisturbed stratigraphy. Near the center of an ice sheet, the slope of stratigraphy over a flat bed is negligible, on the order of 0.5° or less.

---

[2]We do not yet have a terminology that applies equally well to both upward and downward disturbances. For now *leading* and *trailing edges* are best understood in the context of this prototypical upward disturbance.
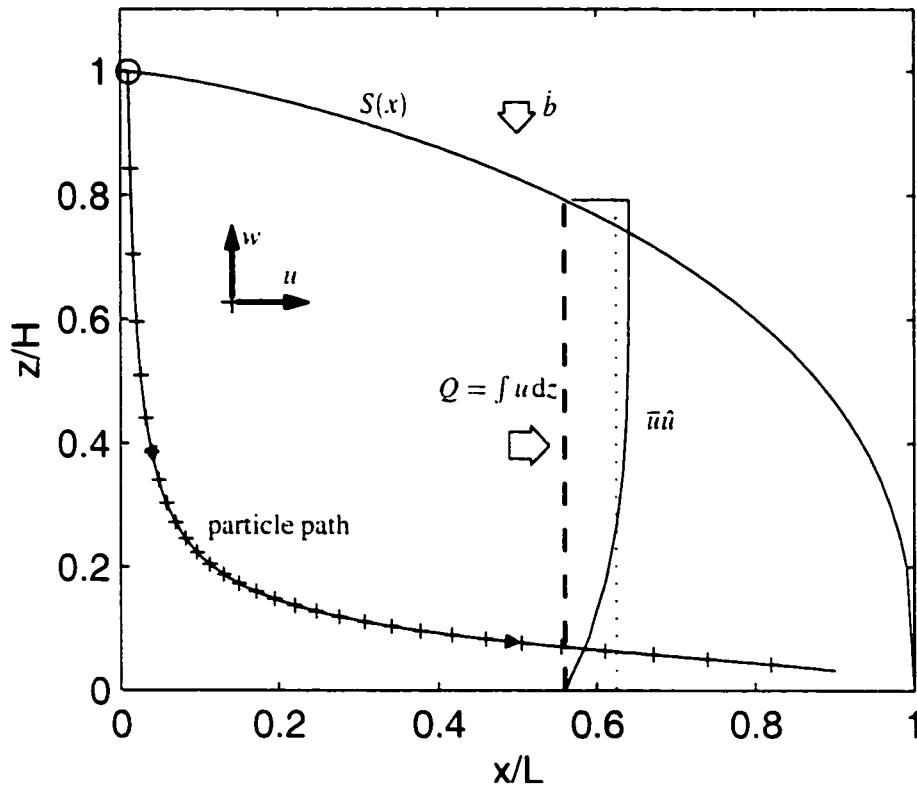
Figure 1.5: Flowband geometry and notation.

1.2.2 Velocity Model

We use a simple flowband model, with enough detail to capture the change in the vorticity number along particle paths but without complicating details. We are most interested in the central portion of an ice sheet where surface slopes are small and the bed is likely to be frozen. The principal variables are depicted in Figure 1.5.

The coordinate system is aligned with the direction of flow. The horizontal coordinate in this direction is x. z is the vertical coordinate. The corresponding velocity components are u and w (positive upward). Perpendicular to these is y, with its velocity component, v, being zero by definition.

The geometric inputs to our velocity model are the surface profile, $S(x)$, and the bed profile, $B(x)$. The flowband ice equivalent thickness is $h(x) = S - B$.

The transverse geometry can be expressed in terms of a relative flowband width, and used to

calculate the transverse spreading rate, $\partial_y v$, as a function of u and x.

We also specify the flux, $Q(x)$, through the flowband cross–section at x. Dividing by the thickness gives a depth–averaged horizontal velocity, $\bar{u}(x) = Q/h$.

Rounding out the inputs is an expression for the vertical profile (shape function) of the horizontal velocity, $\hat{u}(x, z)$. The source of this function is a dynamic model that includes momentum conservation and ice rheology. The horizontal velocity can then be written as:

$$u(x, z) = \bar{u}\, \hat{u}(x, z) \tag{1.1}$$

Since the integral of u over the depth h equals the flux, the integral of $\hat{u}$ over z must equal h. The vertical velocity can be derived from this by incompressibility:

$$w(x, z) = -\int_B^z (\partial_x u + \partial_y v)\, dz + w(x, B) \tag{1.2}$$

We simplify the calculations with a number of assumptions, which can be selectively relaxed to explore their effect on the results. Few are essential to this analysis, but they allow us to keep the description simple while retaining the features of the flow that are key to folding. The resulting model was first proposed by Vialov (1958) (see also Reeh (1988)).

We assume that the base is flat, $B(x) = 0$, and that the ice is frozen to the bed, so $u(x, B) = w(x, B) = 0$. The flowband width is uniform, so that all the gradient terms in the y direction vanish. This approximates the flow on an ice ridge or a highly elongated dome. The velocity gradient is then

$$\mathbf{L} = \nabla \mathbf{v} = \begin{bmatrix} \partial_x u & \partial_z u \\ \partial_x w & \partial_z w \end{bmatrix} \tag{1.3}$$

We assume that the ice sheet surface is in steady state. The flux $Q(x)$ through a cross–section must equal the net accumulation upstream. If we also assume that the accumulation rate, $\dot{b}$, is uniform in space, the flux is $Q(x) = \dot{b}x$.

The uniform accumulation assumption requires that we specify the length or span of the flowband, L, in order to determine the model geometry. In effect we specify a calving front that can handle any flux. The conditions at such a terminus are not realistic, but they do not adversely affect the model a short distance inland. This length L could also be thought of as a virtual or effective length.

If an ice sheet terminates in an ice stream (such as Siple Dome does) or a narrow ablation zone, the terminus profile would be different, but this model would still be useful from some distance inland back to the divide.

To specify $\hat{u}$ and S, we assume that the ice is isothermal, and use the shallow ice approximation (Hutter, 1983; Paterson, 1994, p. 262) with Glen's flow law. This flow law assumes that the deviatoric stress, σ', and strain rate, $\dot{\varepsilon}$, are related by $\dot{\varepsilon} = A\sigma'^3$, where A is a temperature–dependent flow parameter. Since in a typical ice sheet the length is much larger than the thickness, the shearing component, $\partial_z u$, is the largest term of the velocity gradient over much of the flowband and the flow law can be written as:

$$\partial_z u \approx 2\dot{\varepsilon}_{xz} \approx 2A\sigma'^3_{xz} = -2A(\rho g)^3 S'^3 h^3 \hat{d}^3 \qquad (1.4)$$

$$\hat{d} = \frac{S-z}{h} \qquad \text{normalized depth} \qquad (1.5)$$

$$\sigma'_{xz} = -\rho g S' h \hat{d} \qquad \text{shear stress} \qquad (1.6)$$

S' is the surface gradient. Integrating this upward from the bed gives the horizontal velocity:

$$u = -2A(\rho g)^3 S'^3 h^3 \int_0^z \hat{d}^3 \, dz$$

$$= -\tfrac{1}{2}A(\rho g)^3 S'^3 h^4 \left(1 - \hat{d}^4\right) = \bar{u}\hat{u}(\hat{d}) \qquad (1.7)$$

$$\hat{u}(\hat{d}) = \tfrac{5}{4}\left(1 - \hat{d}^4\right) \qquad (1.8)$$

In this case $\hat{u}$ is a function of the normalized depth only.

The corresponding vertical velocity (using (1.2)) is:

$$w = -b\hat{w}(\hat{d}) + uS'\left(1 - \hat{d}\right) \qquad (1.9)$$

$$\hat{w}(\hat{d}) \equiv \int_{\hat{d}}^1 \hat{u}(\hat{d}) \, d\hat{d} = 1 - \tfrac{5}{4}\hat{d} + \tfrac{1}{4}\hat{d}^5 \qquad (1.10)$$

A surface profile consistent with this $\hat{u}(\hat{d})$ can be derived from the steady state expression for the flux:

$$Q(x) = bx = \int_B^S u(x,z) \, dz = -\tfrac{2}{5}A(\rho g)^3 S'^3 h^5 \qquad (1.11)$$

This can be rewritten as a differential equation in S', which can be solved numerically. In the simple

case of a flat bed and uniform accumulation, it can be solved analytically giving:

$$S(x) = H \left(1 - \left(\frac{x}{L} \right)^{4/3} \right)^{3/8}$$

(1.12)

The maximum thickness, $H = h(0)$, is related to the other parameters (L, b, and A) by:

$$H = \left(\frac{20bL^4}{A(\rho g)^3} \right)^{1/8}$$

(1.13)

The horizontal coordinate, x, scales with L, while the vertical coordinate and ice sheet thickness scale with H. With a typical H/L ratio of $1/50$, the surface slope, S' (for $x < 0.5L$) is small. The time scale is set by $T = H/b$. The velocities, u and w, scale with L/T and H/T ($= b$) respectively.

The velocity gradient, $\mathbf{L}$ (1.3) scales as

$$\begin{bmatrix} 1 & L/H \\ H/L & 1 \end{bmatrix} \frac{1}{T}$$

(1.14)

Since L is much larger than H, the $\partial_z u$ term clearly dominates. The $\partial_x w$ term is $(H/L)^2$ times smaller, and can, in many cases, be assumed to be zero.

1.2.3 Segment Rotation Rate

With a velocity model we can calculate the velocity gradient, and from that the rotation rate, $\dot{\theta}$, of a segment with an angle of θ

$$\dot{\theta} = \partial_z u \sin^2 \theta - (\partial_x u - \partial_z w) \sin \theta \cos \theta - \partial_x w \cos^2 \theta$$

(1.15)

When W_k is small (mostly pure shear), the $(\partial_x u - \partial_z w)$ term dominates, resulting in rotation away from vertical for most angles. In most of the ice sheet $\partial_z u$ dominates, producing a positive $\dot{\theta}$ for most angles except a small set close to $0°$ (horizontal upstream). At some points over an uneven bed, it is possible for $\partial_z w$ to be sufficiently negative that $\dot{\theta} > 0$ for all segment angles. At such points $W_k > 1$.

When $\partial_x w$ is negligible, the segment is not rotating ($\dot{\theta} = 0$) if $\tan \theta \approx (\partial_x u - \partial_z w)/\partial_z u$. In this case the vorticity number can be written as:

$$\begin{aligned} W_k = \frac{\bar{\omega}}{\bar{\varepsilon}} &= \frac{\partial_z u - \partial_x w}{\sqrt{(\partial_z u + \partial_x w)^2 + (\partial_x u - \partial_z w)^2}} \\ &\approx \frac{\partial_z u}{\sqrt{\partial_z u^2 + (\partial_x u - \partial_z w)^2}} \\ &\approx \cos \left(\tan^{-1} \frac{\partial_x u - \partial_z w}{\partial_z u} \right) = \cos \theta_r \end{aligned}$$

(1.16)

confirming the relationship between W_k and θ_r shown in Figure 1.2.

In general there are two segment angles that do not rotate; they merge into one for simple shear. $\cos^{-1}W_k$ is the sum of angles of these two non–rotating segments. For small $\partial_x w$, our θ_r approximation is valid because one of these is practically horizontal. Waddington *et al.* (sub) refine this idea of a non-rotating segment by calculating the segment that is not rotating relative to the isochrone at a point. However this requires knowing the slope of the isochrones, which must be calculated from particle paths.

1.2.4   Particle Paths

We calculate particle paths by solving the pair of differential equations:

$$\dot{x} = u(x,z) \qquad \dot{z} = w(x,z) \tag{1.17}$$

Paths can start at any point in the ice sheet, and run either forward or back in time. Each point along a path is defined by a triplet of values, $[x,z,t]$. For a steady state geometry, only relative times are important. We solve these differential equations numerically with the ODE routines provided with MATLAB (Shampine and Reichelt, 1997).

In velocity and particle path calculations, the horizontal and vertical coordinates can be rescaled independently. But the slope and finite deformation calculations (next section) retain a dependence on the H/L ratio. For most of our examples we use an ice ridge with dimensions comparable to Siple Dome, West Antarctica, with a 1/50 ratio. We also examine a Greenland–like ridge with a 1/100 ratio (Table 1.1).

1.3   Precores

A conventional isochrone is the set of glacial ice of the same age, where age is the time since the ice accumulated at the surface. We can equally well construct isochrones relative to another set of initial points such as the set of vertically aligned points at a possible core site (located at $x = C$). Such isochrones would show where the ice currently in the core was located at earlier times. Such a set of core–relative isochrones, which we call *precores*, are shown in Figure 1.6 for a core at $C/L = 0.2$.

Figure 1.7 illustrates why precores are relevant to the problem of turning open folds into recumbent folds. If a disturbance originates at point (p) with a leading edge angle of 24°, this edge will be
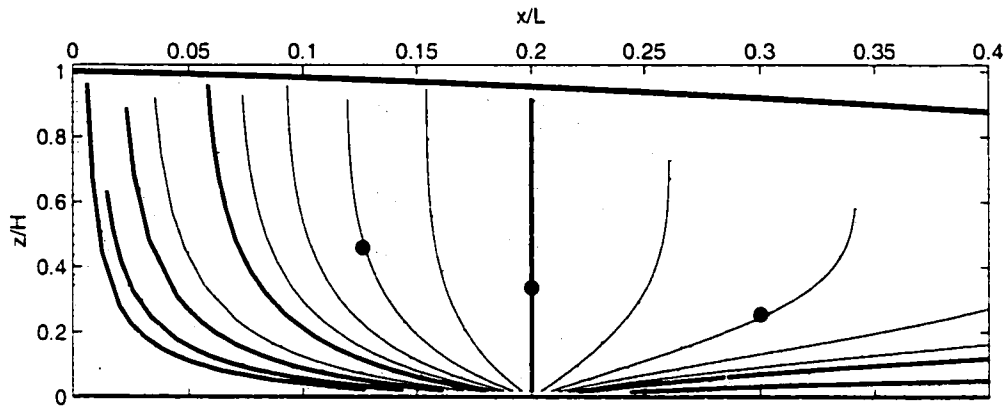
Figure 1.6: Precores for an ice sheet with an H to L ratio of 1 : 50 and a core at $C = 0.2L$ (10H). The heavier lines are at 1T intervals. Selected particle paths are drawn as dotted lines.
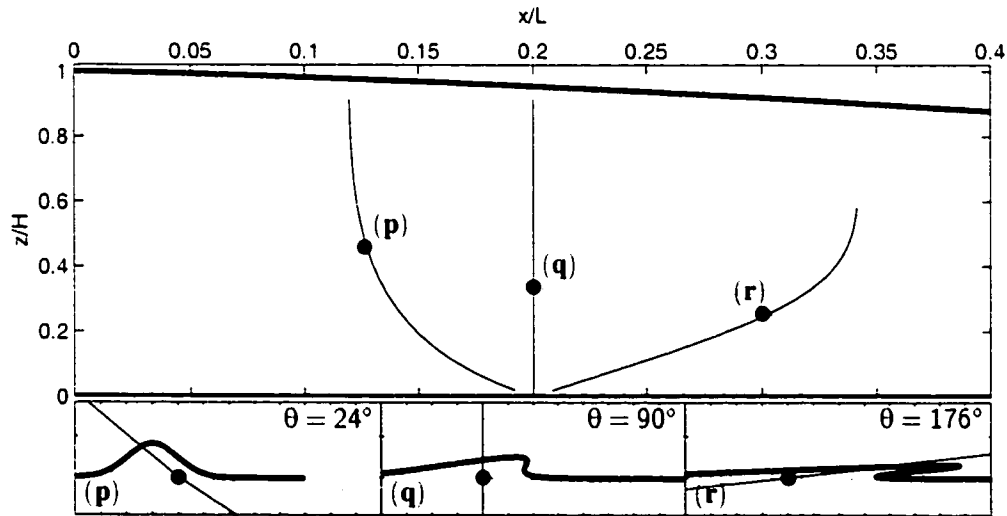
Figure 1.7: The relation of precores to the folding of a sample disturbance. A particle path (dotted) is shown with three precores (solid). The precores are at 0.4T before and after the core at $C = 0.2L$ (10H). The small figures underneath show a representative disturbance at these three points, (p), (q), and (r). These three plots have the same scale, but a different aspect ratio from the larger plot. The particle path and precore through the center point is included on each subplot. The number in the upper right corner is the angle of the precore at that point.

17

Table 1.1: Characteristic Geometry Parameters

parameter	Siple Dome	Greenland
L (km)	50	300
H (m)	1000	3000
H/L	1/50	1/100
b (myr^{-1})	0.1	0.3
$T = H/b$ (yr)	10.000	10.000
A (kPyr^{-3}s^{-1})	5.6×10^{-16}	3.3×10^{-16}

near vertical when the disturbance reaches point (q) at $x = 0.2L$. This disturbance would appear as an obvious fold-in-progress in a core sample taken at this point (provided that is small enough to fit in the core cross-section). Further downstream at point (r) it will appear as a nearly horizontal $176°$ segment.

A graphical way of using these precores would be to overlay them with plots of representative disturbances. If a portion of the disturbance is steeper than the corresponding precore, it will be overturned at the core location. Portions that are not as steep will not be overturned in this core, though overturning further downstream is still possible.

The upper panel in Figure 1.8 contours the angles of the precores shown in Figure 1.6, while the lower panel shows the angles along selected particle paths for segments that have an angle of $90°$ at $x = C$. The rotation through vertical is abrupt for deep paths, and much more gradual for paths near the surface. This contrast in rotation rates is largely a result of the larger vorticity number at depth, though the lower velocity near the bed makes the contrast stronger when plotted against distance (x) than against time.

In the lower panel of Figure 1.8, the angle at point (p) is close to the minimum along its particle path. This means that a segment with a slope angle of $24°$ is not rotating at this point in the flowband. In the upper plot of the same figure, the same property is seen in the fact that the angle contour is
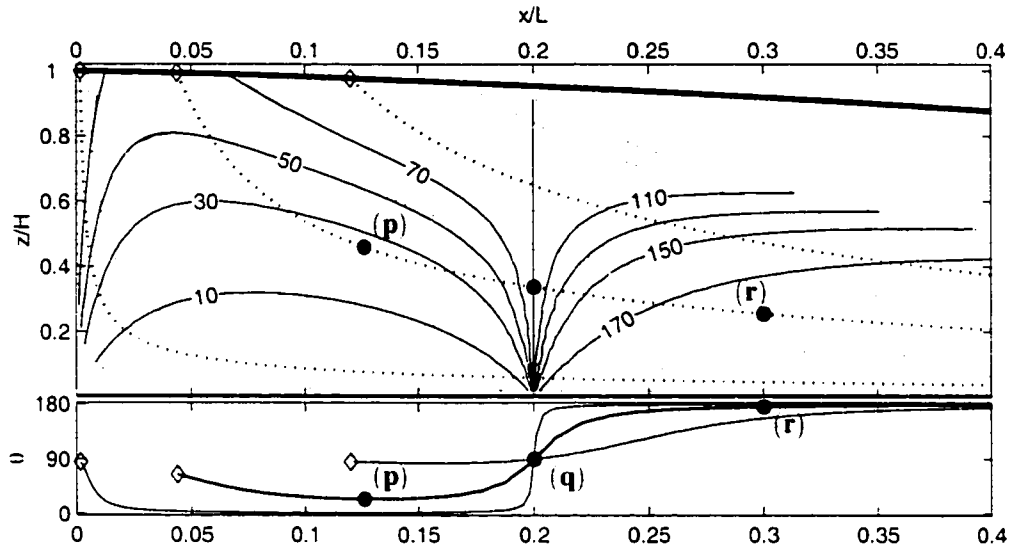
Figure 1.8: The upper plot shows contours of the precore angles, θ_f, in degrees. The lower plot shows these angles along selected particle paths (marked with o at the surface). (p), (q), and (r) points in Figure 1.7 are also shown.

parallel to the particle path at this point. At this point, $\theta_r \approx 24°$.

Consider a segment with an angle of 60° near the surface on the same particle path (the middle diamond). As it moves downstream, it will be flattened (angle decreasing) until it reaches point (p). At this point it starts rotating in the other direction. It passes through vertical at (q) and continues rotating toward horizontal in the downstream direction. Disturbances can be flattened when the vorticity number is small (dominant pure shear), but farther along the path the vorticity number grows to the point that the flattening changes to steepening and overturning.

The slope angle of the precore at a point is the threshold for segments that are obviously folding when they get to the core site. We will denote this *finite strain threshold* as θ_f. It is a function of the particle path and the core locations. Segments that are steeper than θ_f will overturn prior to reaching C. Segments with a smaller θ will not overturn before they get to C. and might never do so. This threshold is lower than the velocity gradient-based wiggle stability angle, θ_r (Waddington *et al.*, sub), for points upstream from its minimum ($\theta_f < \theta_r$). Further downstream the opposite is true.

Note that θ_r at a point depends only on the velocity gradient at that point, while θ_f is a function
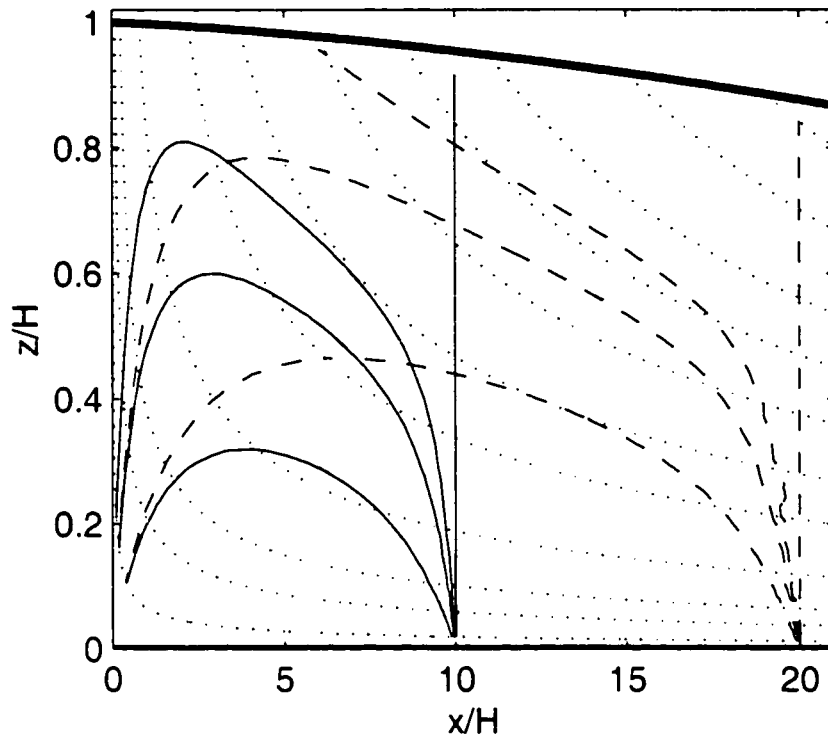
Figure 1.9: Precore slope angle contours ($\theta_f = 10°, 30° \,\& \, 50°$) for two core locations. $10H$ (solid lines) and $20H$ (dashed lines). The gray line marks where $\theta_r = \theta_f$.

of both the chosen core location, C, and the current point.

1.3.1   Precore Scale Dependence

Precores are an easy tool for determining what disturbances could appear as overturned folds in an ice core. All that is needed is a flow model that can calculate particle paths and travel times along those paths. The paths are determined by the flowband geometry which in our simple example is determined by L and H. The core location C determines shape of the precores. The time scale T for the ice sheet affects the contour interval of the precores (as it does stratigraphic isochrones) but does not change their shape. We can gain further insight into precores and the folding potential by looking at how the precore angles vary with these scaling factors.

Figure 1.9 shows how the precore angles vary with the core location C (while keeping H/L con-

Table 1.2: The effect of flowband geometry on precore slope angles

H/L	C/L	C/H	scale
1/50	0.2	10	reference
1/100	0.1	10	equivalent
1/100	0.2	20	1/2
1/50	0.4	20	1/2
1/50	0.02	1	10

stant). The solid set of lines with the core at $10H$ are a subset of the contours in Figure 1.8. The dashed set are for a core at $20H = 0.4L$. The gray lines mark where these angle contours are parallel to the particle paths, that is where $\theta_f = \theta_r$.

For the inner portion of this simple ice sheet, the precore shapes are controlled primarily by the location of the core. specifically the C/H ratio. Here (out to about $0.4L$) the surface slope is small (specifically $S'(1 - \hat{d}) \ll 0$), and the vertical velocity is dominated by the $b\hat{w}(\hat{d})$ term (1.9). The contours of θ_f versus z/h and x/H show little variation when H/L is varied, as long as C/H is held constant.

On the other hand if we keep the core position. C/L, constant relative to the length, the slope of a precore scales with the H/L ratio. If the length L of the modeled ice sheet is doubled, the precore slopes are halved. Since the slope is the tangent of the angle, the angles for precores in two different sets of model geometries are related by:

$$\tan(\theta_2) = \frac{H_2}{L_2}\frac{L_1}{H_1}\tan(\theta_1) \tag{1.18}$$

Figure 1.10 illustrates this H/L dependence for a vertical section through point (p) in Figure 1.8 (Table 1.2).

The finite perpendicular material line (FPM) of Grasemann and Vannay (1999) is similar to our precores. They show that currently inverted metamorphic zones in rock could have originated with
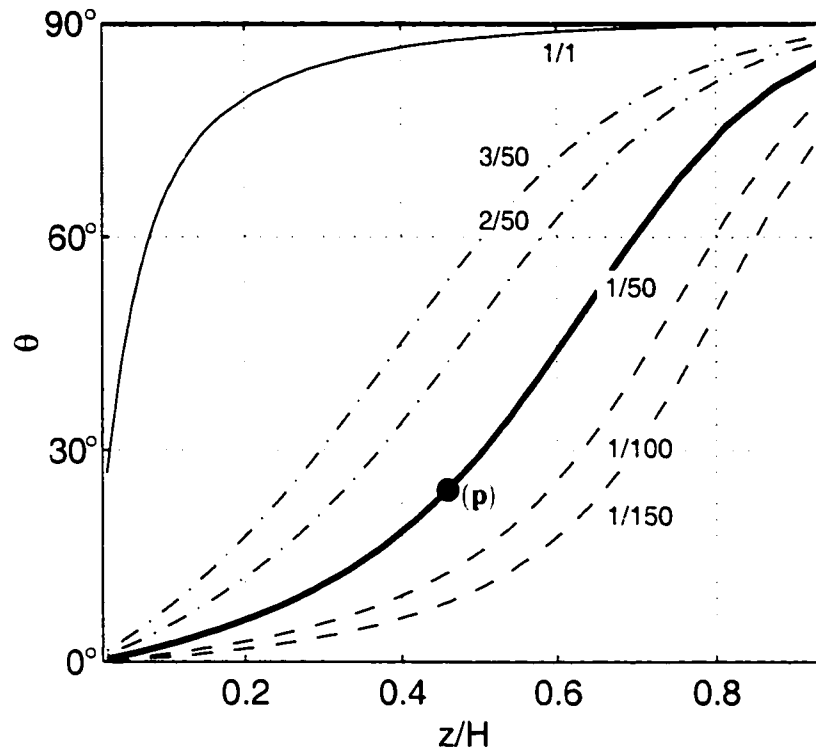
Figure 1.10: The scaling of precore angles with variations in the H/L ratio. The heavy solid line shows the angles along a vertical transect through point (p) on Figure 1.7. In this case $H/L = 1/50$ and $C/L = 0.2$. The dashed lines show the equivalent angles for other H/L ratios (keeping $C/L = 0.2$). The curves are related by Eq. (1.18).

tilted. but otherwise normal (cold over hot) metamorphic isotherms. The FPM is the pre–deformation alignment of a set of rocks sampled in the currently deformed terrane.

1.4 Deformation Gradient Tensor

Precore angles can be calculated from the finite difference slopes of the precores defined by a finite number of particle paths. A more general approach is to calculate the deformation gradient tensor along the particle paths. and use this to rotate segments aligned with the core. This tensor can also be used to calculate the deformation of any disturbance that is small relative to the scale of inhomogeneity in the strain field.

Let d**X** (with components dX and dZ) be a small segment at a reference point such as (p) in Fig-
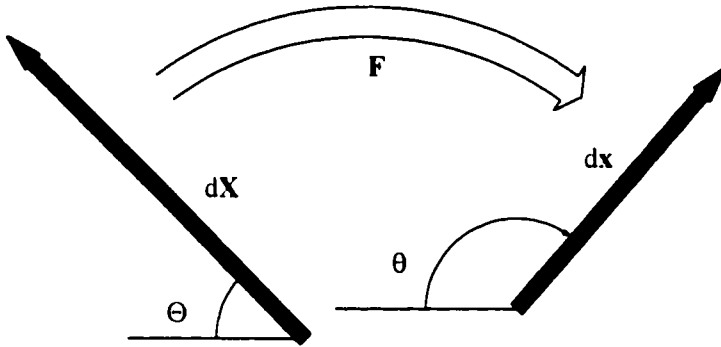
Figure 1.11: The deformation gradient tensor **F** acts on **dX** (at the *reference* time) producing **dx** (at the *current* time).

ure 1.7. The corresponding deformed segment. **dx** at point (**q**), can be expressed as a linear function of **dX**:

$$dx = F_{\langle (p)(q) \rangle} \cdot dX \tag{1.19}$$

where $F_{\langle (p)(q) \rangle}$ is a tensor mapping **dX** onto **dx**. The bracketed subscripts denote the *reference* and *current* points. When it is clear which points we are referring to, we will just write **F**. The component $F_{xx} = \partial x / \partial X$ maps a horizontal segment (or the horizontal component of a segment). dX, onto a horizontal segment. dx. F_{xz} maps dZ onto dx (vertical to horizontal). In terms of the tensor components, (1.19) is:

$$\begin{bmatrix} dx \\ dz \end{bmatrix} = \begin{bmatrix} F_{xx} dX + F_{xz} dZ \\ F_{zx} dX + F_{zz} dZ \end{bmatrix} \tag{1.20}$$

The tensors for the deformations shown in Figure 1.1 are:

$$\text{(a) } F = \begin{bmatrix} 3/2 & 0 \\ 0 & 2/3 \end{bmatrix} \text{ and (b) } F = \begin{bmatrix} 1 & 1 \\ 0 & 1 \end{bmatrix} \tag{1.21}$$

We are interested in the rotation of layer segments. If Θ is the angle of the segment at the reference point, then the current angle. θ satisfies:

$$\tan(\theta) = \frac{dz}{-dx} = \frac{-F_{zx} + F_{zz} \tan(\Theta)}{F_{xx} - F_{xz} \tan(\Theta)} \tag{1.22}$$

(The negative signs result from defining angles relative to the $-x$ coordinate.)

F can be calculated from closely spaced particle paths. much as finite strain is calculated in the field or laboratory; however we can also calculate it using a set of differential equations.

$$\dot{F} = L \cdot F \tag{1.23}$$

L in (1.3) is the gradient of the velocity relative to the current segment. while $\dot{F}$ is gradient of the velocity relative to the original segment. We can get a rough idea of where this comes from by writing

$$\frac{d}{dt}\left(\frac{\partial x}{\partial X}\right) = \frac{\partial}{\partial X}\frac{dx}{dt} = \frac{\partial v}{\partial X} = \frac{\partial v}{\partial x}\frac{\partial x}{\partial X}$$

See (Malvern, 1969, sec. 4.5) for details.

We solve (1.23) for F when we calculate a particle path (1.17), using I as its initial value. These form a differential equation system of six variables (x, z and the four strain terms). L is calculated with an eight point finite difference to maximize continuity. The error tolerances have to take into account the widely differing magnitudes of the variables. The result is a series of F tensors, one for each point along the particle path, relating dx at that point to dX at the path start.

The components of such a series of tensors are shown in Figure 1.12. The particle path is shown in panel (a). In (b) and (c) the reference point is at the surface. The diagonal components. F_{xx} and F_{zz} start at 1. while the two shear components. F_{zx} and F_{xz}. start at 0. F_{zx} remains too close to zero to plot with the other components (it is slightly negative. with some increase in magnitude near the terminus).

The determinant of F is just the Jacobian determinant (Malvern, 1969, (4.5.25)) relating an infinitesimal deformed volume at the current point to the undeformed volume at the reference point. Since ice is incompressible. this determinant must be equal to one at all points along the particle path.

$$1 = |F| = F_{xx}F_{zz} - F_{zx}F_{xz} \tag{1.24}$$

While $F_{zx}F_{xz}$ is small. $F_{zz} \approx 1/F_{xx}$. When $x/L < 1/3$. F_{xx} is approximately linear in x. (See Appendix B.1 for details.) This also means that $F_{zz} \approx x_0/x$. so that the height of a disturbance decreases inversely with the distance traveled away from the divide. A disturbance observed at $10H$ would be half as high as it was at $5H$. regardless of the observation depth or slope.
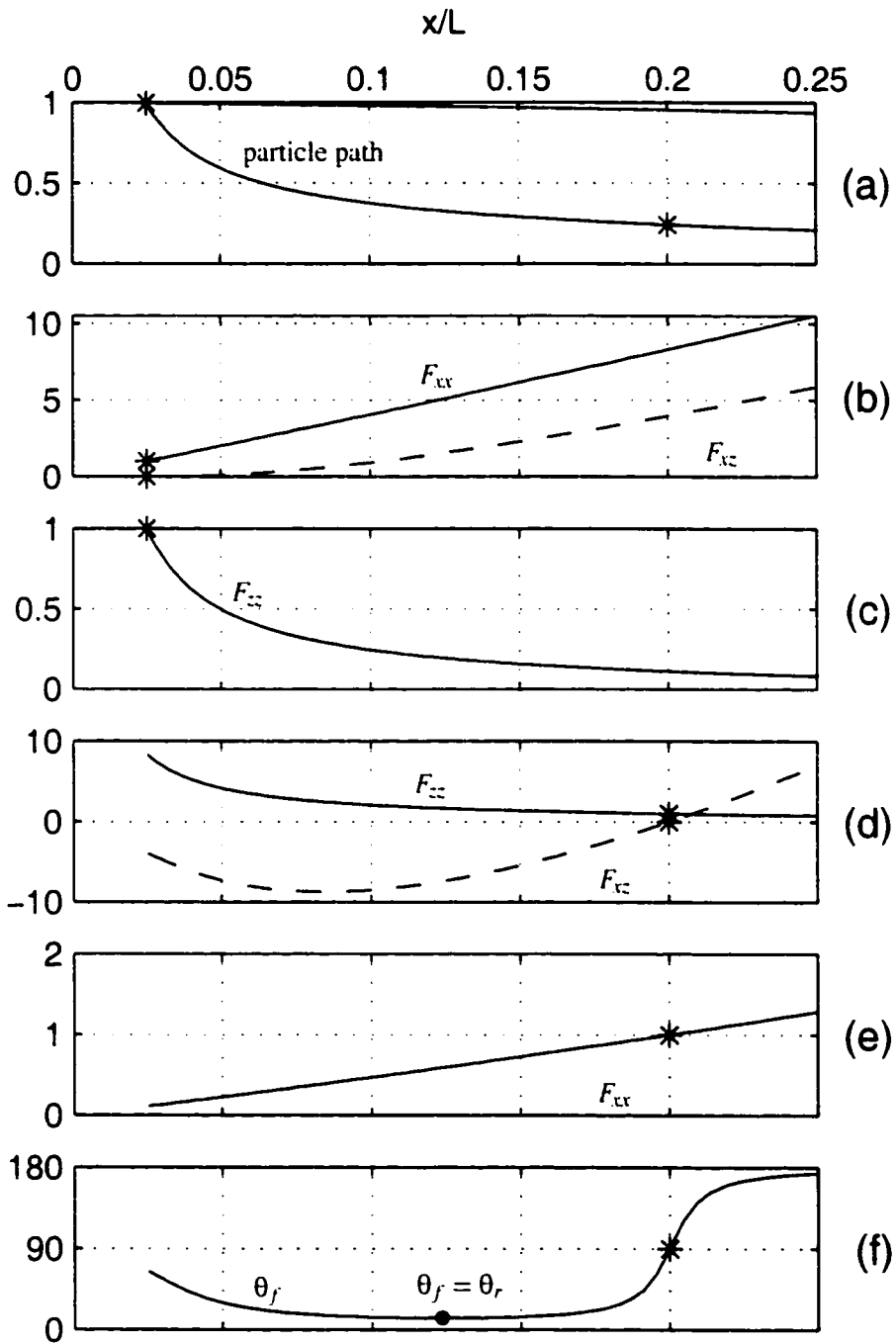
Figure 1.12: **F** components along a particle path (a). In (b) and (c) the reference point (*) is at the surface; in (d) and (e) it is at the core. $C = 0.2L$. (f) $\theta_f = \tan^{-1}(-F_{zz}/F_{xz})$.

1.4.1 Change of Reference Point

The reference point of $\mathbf{F}$ can be changed. Taking the inverse, $\mathbf{F}^{-1}_{((\mathbf{p})(\mathbf{q}))}$, interchanges the reference and current points, $(\mathbf{p})$ and $(\mathbf{q})$, in effect undoing the strain.

$$dX = \mathbf{F}^{-1}_{((\mathbf{p})(\mathbf{q}))} \cdot d\mathbf{x} = \mathbf{F}_{((\mathbf{q})(\mathbf{p}))} \cdot d\mathbf{x} \qquad (1.25)$$

We use such an inverse to shift the reference point from the surface, $(\mathbf{s})$, to the core, $(\mathbf{q})$.

$$\mathbf{F}_{((\mathbf{q})(\mathbf{p}))} = \mathbf{F}_{((\mathbf{s})(\mathbf{p}))} \cdot \mathbf{F}^{-1}_{((\mathbf{s})(\mathbf{q}))} \qquad (1.26)$$

The components for such a shifted set of $\mathbf{F}$ tensors are shown in Figure 1.12(d and e).

Since a segment aligned with the core at $(\mathbf{q})$ (Figure 1.7) is vertical, its angle at other points on the particle path was calculated from (1.22) and shown in Figure 1.12(f). This is the precore slope angle, θ_f, contoured in Figure 1.8.

$$\tan\theta_f = -\frac{F_{zx}0 + F_{zz}\,dZ}{F_{xx}0 - F_{xz}\,dZ} = \frac{F_{zz}}{-F_{xz}} \qquad (1.27)$$

The minimum point of θ_f along a path, where $\theta_f = \theta_r$, is a consequence of the variation of the velocity gradient, $\mathbf{L}$, along the path. As $\mathbf{L}$ changes, θ_r decreases, leading to the change in rotation direction for certain segments (section 1.1.1). On the other hand, the rapid change in θ_f while it passes through 90° (at the core), does not depend on $\mathbf{L}$ changing. This rapid rotation through vertical occurs even when $\mathbf{L}$ is assumed to be constant (see Appendix B.3).

1.4.2 Patterns of Segment Deformation

Figure 1.13 shows the history of a fan of segments along a particle path. On the left the path is near the surface and pure shear dominates. Segments rotate in both directions toward horizontal. Segments around vertical are under compression (the shaded region) while near–horizontal ones are under extension. θ_r starts out at 90°. As the proportion of simple shear increases, the set of angles under compression shifts to angles less than 09°. All segments with an angle less than that of the particle path itself, θ_p, continue to rotate toward 0°.

Of particular interest when considering folding are the segments that are steeper than θ_p, but less than vertical. We call these *flippers* because they initially flatten but then stop rotating and *flip* in the other direction. Smaller angles flip further downstream, but some just 'run off of glacier' and so may never flip.
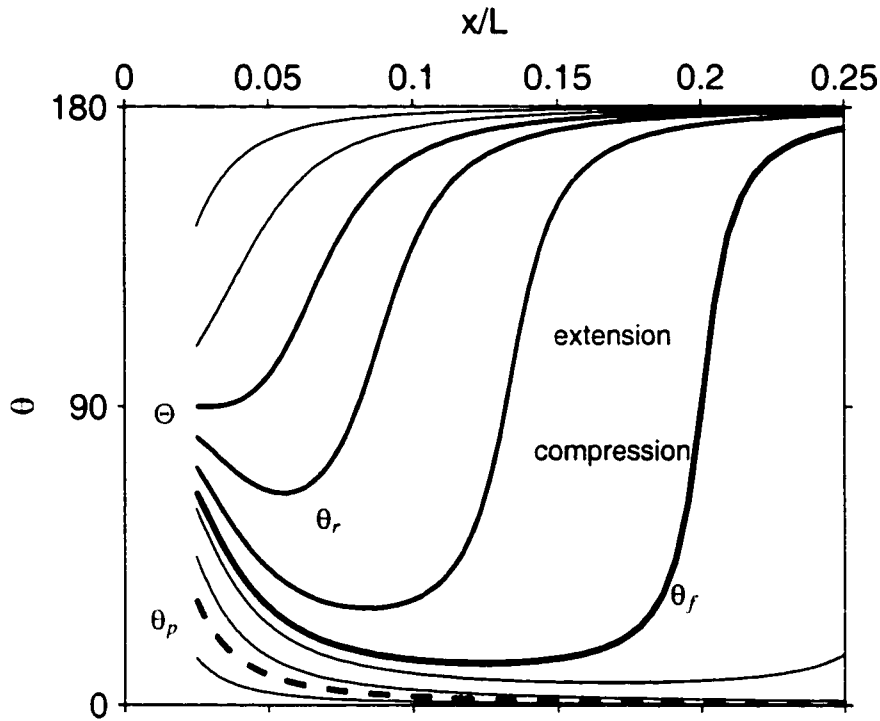
Figure 1.13: Rotation of segments of various initial slope Θ along a particle path (Figure 1.12(a)). The line marked θ_f is the precore angle for a core at $C = 0.2L$. The heavy dashed line is the angle of the particle path. θ_p. Shading marks where segments are undergoing shortening. The darker gray line marks the angles. θ_r. that are not (momentarily) rotating.

1.5 Some Applications

Even if disturbances are regularly generated along a particle path. and subsequently overturned, the likelihood of recognizing them in a core is low. While moving through vertical is an essential part of folding. disturbances spend little time in this configuration. Much more time is spent around θ_r, where the rotation rate is low. The flattening and extension of recumbent folds further reduces the likelihood of identifying them in the small cross–section of an ice core.

Here we have treated the stratigraphic layers as simple one dimensional lines. Actual layers have a finite thickness. which in the undisturbed orientation. is reduced by the vertical compression. If a portion of a layer is disturbed and overturned. it will be shortened as it rotates through vertical. At the

same time, by incompressibility, it must undergo a corresponding thickening. We also expect that the dynamic processes that create such a disturbance in the first place will alter layer thicknesses. The tools we have described here can be used to examine how shearing redistributes mass within these altered layers.

1.5.1 Predicting the Origin Site of Observed Folds

We can also start with an observed structure in a core, and attempt to predict where it originated and what its shape was. The amount of information that we can deduce about the original disturbance depends on how much information we can glean from the deformed structure in the core. We may have to make some assumptions about the source. For example, if we assume that gentle wiggles are more likely than steeper ones, then the point where the θ_f curve is minimum is the most likely point of origin of the disturbance.

In cores such as GISP2, stratigraphic layers with 5° to 20° of tilt have been observed (Alley *et al.*, 1995). With our deformation model, we can project these tilted layers upstream and downstream from the observed location at $9H$. Figure 1.14(a) shows the angle history of the leading edge of an recumbent fold at depth of $0.8H = 2400$ m in the core. Its core angle is slightly past vertical (100°). For comparison, a segment that clearly has not yet overturned (5°) in the core is plotted. Panel (b) is similar but for a 20° segment at $0.88H = 2640$ m depth. Because the azimuthal orientation of the core is unknown, we show the history for segments that tilt 20° in both the upstream and downstream directions. During their prior history, the minimum angles are practically the same for both segments (about 5°). The most likely point of disturbance is a broad region around $5H$. For similar segments at a depth of $0.92H$, the minimum angle is closer to 3°.

The time scale $T = H/\dot{b}$ for these computations is 10,000 years (Table 1.1). The age of the core observation point in Figure 1.14(a) is 25,000 years. The time from minimum value to overturn is about 700 years. In (b) at a deeper level the age is 40,000 years, the time from minimum value to overturn is about 1000 years, and time it takes to rotate from 20° to 160° about 200 years. These depth age figures do not take into account the much lower accumulation rate during glacial times, so they are smaller than measured core ages. However, the overturn times fall well within the current interglacial period, so the deformation causing folding is not affected by the earlier accumulation
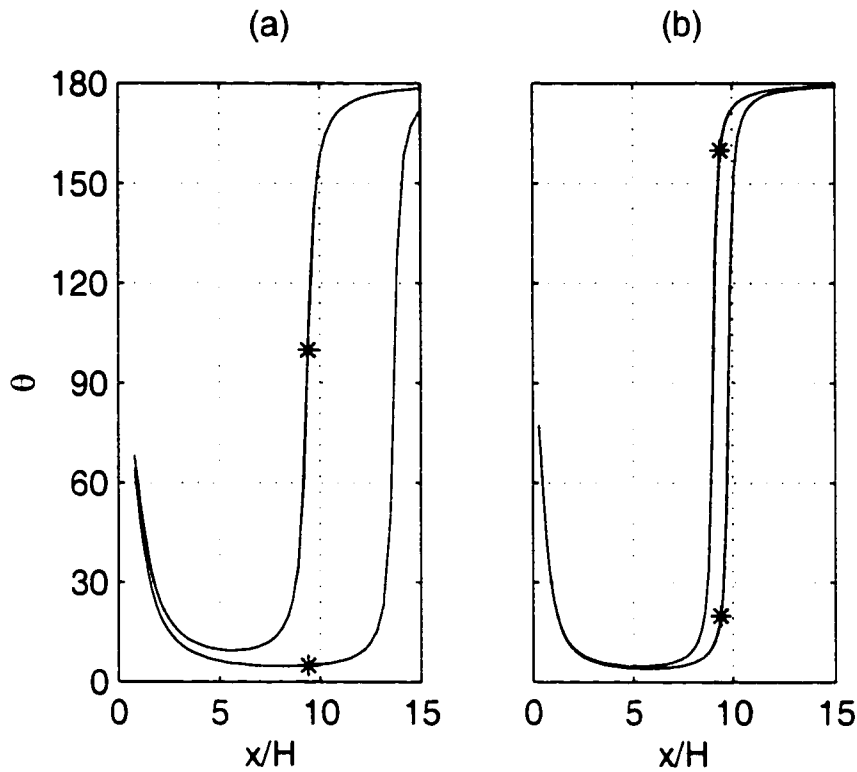
Figure 1.14: Predicted history of observed disturbances in a core at 9.4H ($\approx$ GISP2). (a) 100° slightly overturned segment at a depth of 0.8H (10° minimum value). For comparison a gentle 5° segment has also be plotted. (b) 20° and 160° segments at 0.88H depth. (5° minimum values).

rates.

Figure 1.15 shows a similar case with a different flowband model. The bed approximates the radar profile from the Greenland summit (Castelnau *et al.*, 1998; Jacobel and Hodge, 1995). The velocity profile $\tilde{u}(x, \tilde{d})$ has been adapted from a finite element flowband model (Nereson *et al.*, 1998; Bolzan *et al.*, 1995). Most of the difference between the two figures, once the bed slope is accounted for, can be attributed to the polythermal nature of the finite element model.

We could also constrain the disturbance location if we knew the initial shape. If the disturbance is the result of layers draping over a transient 'hard lump' (Figure 1.4) it might be reasonable to assume that the disturbance before shearing was symmetrical as depicted at point (p) in Figure 1.7. If we observe the fold at point (q) (in a core), and measure the angles of the leading edge and trailing
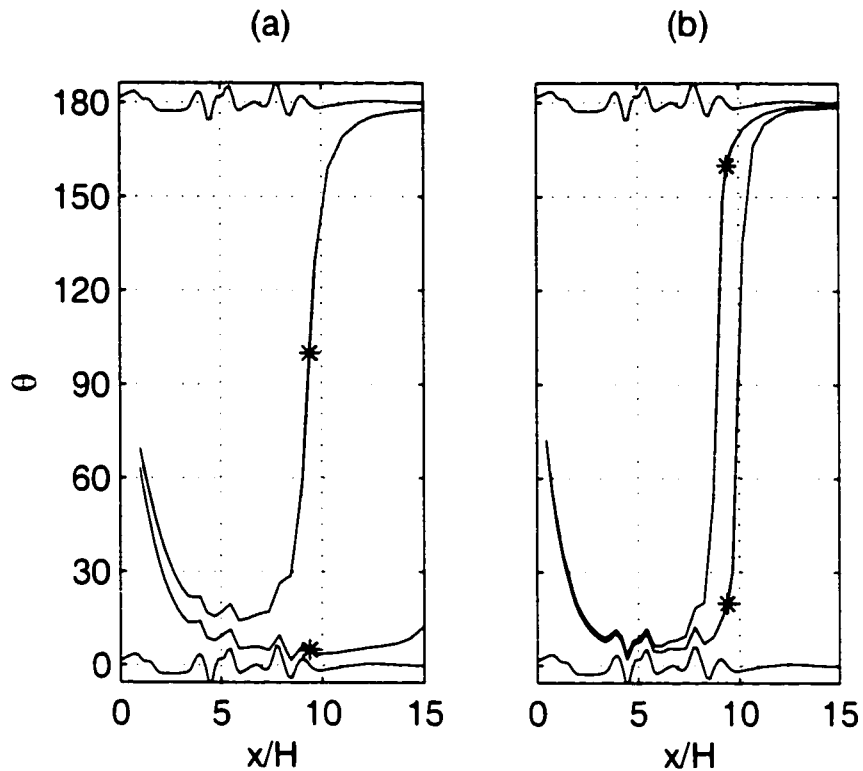
Figure 1.15: Same as Figure 1.14 but with bed and velocity profiles that better approximate Greenland summit area. Minimum values are (a) 15°. (b) 2 – 4°. Relative to the bed slope these minima are (a) 15° and (b) 5 – 6°. The bed slope angle is plotted at the top and bottom (centered on 180 and 0°).

edge, we can constrain the location of point (**p**). i.e. run the wiggle backwards from the core until its shape becomes symmetrical.

We can approximate a fold of height Δz and width Δx (and trailing edge slope of $\Delta z/\Delta x$) at (**q**) by a right triangle with a set of points with relative positions (Figure 1.16(a)):

$$\left\{ \begin{bmatrix} 0 \\ 0 \end{bmatrix}, \begin{bmatrix} 0 \\ \Delta z \end{bmatrix}, \begin{bmatrix} -\Delta x \\ 0 \end{bmatrix} \right\}$$

(1.28)

The relative positions at an earlier time would be (using (1.20)):

$$\left\{ \begin{bmatrix} 0 \\ 0 \end{bmatrix}, \begin{bmatrix} F_{xz}\Delta z \\ F_{zz}\Delta z \end{bmatrix}, \begin{bmatrix} -F_{xx}\Delta x \\ -F_{zx}\Delta x \end{bmatrix} \right\}$$

(1.29)
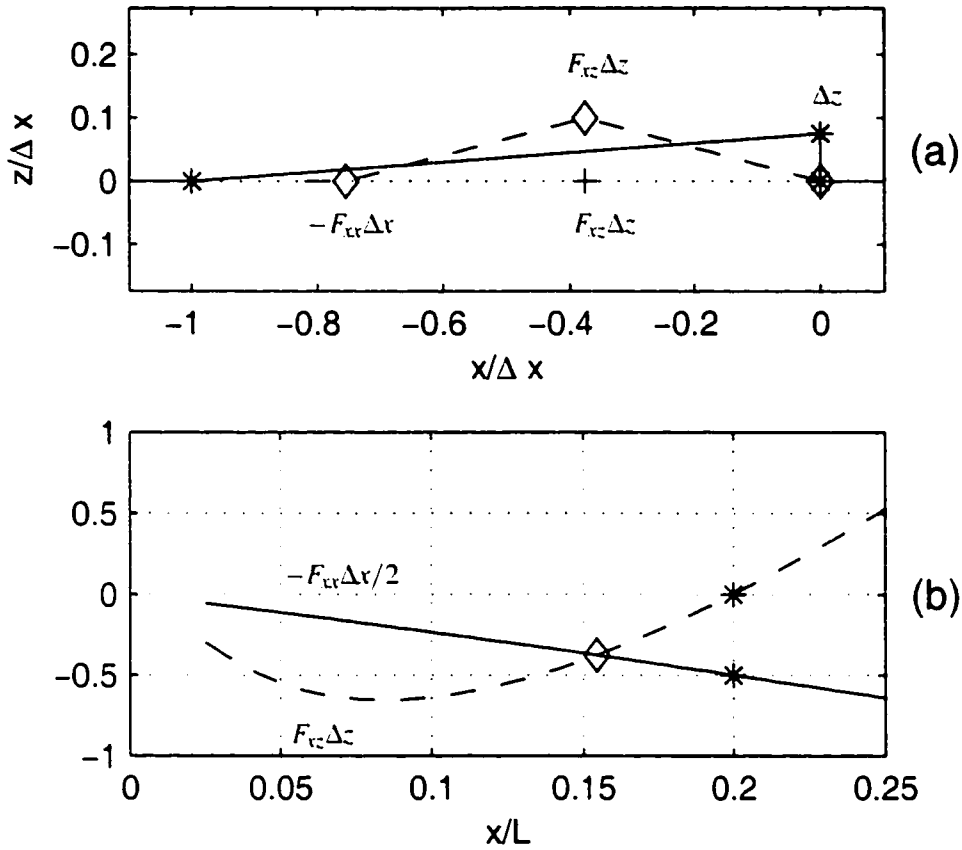
Figure 1.16: (a) An overturning disturbance (∗) and a possible symmetric predecessor (◇). (b) The time at which $F_{xz}\Delta z$ equals $-F_{xx}/2$ (◇).

Here we assume that $-F_{zx}\Delta x \approx 0$. If $F_{xz}\Delta z = -F_{xx}\Delta x/2$ as shown in Figure 1.16(b), the earlier disturbance is a symmetrical triangle with height $F_{zz}\Delta z$. For smaller $\Delta z/\Delta x$, the symmetric injection time is earlier (e.g. in Figure 1.7 (q), this slope is 0.04, versus 0.075 in Figure 1.16). It is possible, if $\Delta z/\Delta x$ is too small, that no point satisfies this constraint. In this case, the observed fold could not have originated with a symmetric wiggle.

1.6 Conclusions

The kinematics of large-scale ice sheet flow can deform gentle open folds into order disrupting re-cumbent folds. To extend the results of Waddington et al. (sub) to disturbances that are injected near

their no rotation stability points, and to relate disturbances in the cores to injection sites in the presence of spatially variable strain rates, we have used three concepts; θ_r the strain rate stability angle, θ_f the finite strain threshold angle, and precores, the core relative isochrones.

From the velocity gradient at a point, we calculate W_k, the kinematic vorticity number which measures the relative mix of pure and simple shear, and θ_r, the angle that is not rotating at that point. Segments steeper than θ_r are rotating toward vertical and overturning, while gentler ones are being flattened. But because segments move along paths into regions of higher W_k, segments that were not rotating will begin to overturn, i.e. the θ_r criterion of Waddington *et al.* (sub), while it is an approximate indicator of stability against recumbent folding, is still optimistic about downstream stratigraphic integrity.

By calculating the finite strain deformation gradient tensor, **F**, along a particle path, we see how a disturbance segment rotates over a finite interval. Given our limited understanding of the dynamic processes that could give rise to the initial disturbances, the most useful form of the angle rotation function specifies a vertical segment at a reference (observation) point, and calculates the corresponding angle at other points along the path. We have called this the finite strain threshold angle, θ_f. At any point this is the angle of the segment that will be in the process of overturning when it reaches the reference point.

θ_r is a minimum angle on the θ_f curve, i.e. the gentlest segment that will overturn at the reference point. A segment can flatten for a period, then reach the local θ_r and proceed to steepen and overturn. Since this minimum is broad, it gives little indication of how soon the overturn will occur. For that, the full θ_f calculation in this paper is needed.

For a more complex flowband model, such as the one illustrated in Figure 1.15, θ_r is harder to use. The θ_f curve has multiple θ_r (zero rotation) points when there are bed undulations. These remain, in a modified form, even when angles are specified relative to steady state isochrones. Again, the θ_f calculation in this paper is required.

Precores, or core–relative isochrones, extend the concept of the θ_f curve to multiple particle paths. The zero time isochrone is defined along a hypothetical ice core, and upstream precores give the location of the core ice at earlier times. They also give the slope of segments that will be vertical in the core. A θ_f curve with its reference point on the core gives the precore slope angle along its path. Thus the precores and the θ_f contours are a graphical way to show how steep disturbances

must be to be overturned in the core.

While the probability of a core containing a fold increases downstream. this fold may be harder to recognize. The interval during which a fold is obviously overturning is small because of the rapid rotation of the overturning edge. Once a segment is overturned, it continues to rotate toward the undisturbed isochrones. Since ice lacks reliable 'up' indicators (Alley et al., 1995). the fold will merge back into the otherwise undisturbed stratigraphy.

Although our examples used steady flow and a flat bed, our approach is equally applicable to transient ice sheets on rough beds. Other processes such as shear band development. or various three dimensional effects can also disrupt stratigraphy. In that sense our calculations may still err on the optimistic side when assessing stratigraphic integrity. Our analysis identifies scale parameters for processes that could generate initial disturbances. A process that cannot generate an adequate disturbance can be ruled out as a core-disrupting process.

Chapter 2

RECUMBENT FOLDING IN ICE SHEETS - PART 2:
A PROBABILITY MODEL

Abstract

To better understand apparent stratigraphic disturbances in ice cores such as GISP2, we use a two stage model of folding to predict where overturned folds are likely to occur. In this model, a transient dynamic process injects a gentle open fold with a probabilistically described shape at a probabilistically described time along a particle path. These injection probability distributions encode our limited knowledge regarding how stratigraphy could be disturbed. The large–scale kinematics of a flowband model of ice sheet flow gives a rotation function that relates the slope of a disturbance segment to its slope at an observation point. The probability of observing an overturned fold is the injection probability density integrated over all segments that could rotate through vertical by the observation time.

We examine the consequences of a number of injection density patterns, both along a specific particle path and across a range of independent paths. In general, overturn probabilities increase downstream along a path as the injection probability increases and gentler segments can be overturned. If the injection is concentrated along an isochrone, the overturn probability will also have a maximum along an isochrone. If the near–divide disturbances can occur deep in the ice, the overturn probability near the bed is higher. Our model cannot produce folding right at the divide. Disturbances injected near the divide must move a few ice thickness away to be overturned.

2.1 Introduction

The interpretation of the paleoclimatic signal in ice cores is based on the assumption that the observed layering in the core is in correct stratigraphic order. Post depositional processes that could fold or otherwise alter the order of these stratigraphic layers would introduce significant errors in the

interpretation, particularly if these disturbances could not be readily identified.

In Chapter 1 we modeled the formation of overturned folds in ice sheet stratigraphic layers as a two stage process. Initially the flat stratigraphy is locally disturbed, to form gentle open folds. Then the kinematics of the large–scale flow shears these folds, overturning certain segments. The initial disturbance of stratigraphy must originate in transient dynamic processes and local rheological inhomogeneities. While various processes have been suggested (e.g. Waddington *et al.* (sub), Castelnau *et al.* (1998)), specifics about what disturbance angles they can produce, and the location where they could occur remain sketchy. As a consequence we found it more productive to start with observed structures in a hypothetical ice core, and calculate how they might have looked upstream. This imposes constraints on the disturbance processes, particularly on the magnitude of a disturbance they must produce.

In this paper we use this same kinematic model of folding, together with probability theory, to investigate where folding is most likely. This probabilistic model of folding allows us to explore various hypotheses and intuitions regarding the dynamic disturbance processes.

We also use the disturbance notation (such as *leading* and *trailing edge*) that is discussed in section 1.2.1 and Figure 1.4.

2.1.1 A Passive Shearing Model of Folding

In Chapter 1 we used a simple ice sheet flowband model to calculate particle paths and the finite strain deformation gradient tensor along those paths. This tensor expresses how segments of various slopes rotate as they move down a path. In this paper, we extend this analysis by defining an injection probability distribution and its related density. This injection density, together with the deformation gradient tensor, enables us to calculate the probability that an overturned leading edge will be observed at a specified point downstream.

We illustrate these calculations with numerical examples using a Vialov ice sheet flow model. The initial set of examples focuses on probabilities along one particle path. This allows us to examine the effect of the injected segment angle distribution on the observed angle probability.

Our second set of examples compares the probability patterns across paths. The focus here is more on the spatial or temporal variability in the injection process. We look at injection patterns that

are uniform across the flowband, patterns that are concentrated along isochrones, and patterns that are limited to the divide zone. In appendix C we discuss alternative measures of probability, and the feasibility of testing these results.

2.2 Deterministic Model of Folding

2.2.1 Velocity Model

We use the plane strain steady state flowband model of ice flow in Chapter 1. This model draws heavily on Vialov (1958) and Reeh (1988).

The coordinates of our flowband model are x, horizontal in the downstream direction, and z vertical; u and w are the corresponding velocity components. The cross-flow coordinate and velocity are y and v. The bed is flat and the surface is $S(x)$.

By aligning x with the flow and assuming constant flowband width and plane strain, the cross-flow coordinate, velocity and strain rate terms are zero. The velocity depends on flowband geometry, flux assumptions, and rheological assumptions. Its components, u and w, are related by incompressibility.

$$u(x,z) = \bar{u}(x)\, \hat{u}(z/S(x)) \tag{2.1}$$

$$w(x,z) = -\int_0^z \partial_x u \; dz \tag{2.2}$$

When we assume steady state and uniform accumulation b, the depth averaged downstream velocity is $\bar{u}(x) = bx$. The vertical profile of the horizontal velocity, $\hat{u}(z/S)$, is based on the shallow ice approximation with Glen's flow law, and involves the fourth power of the normalized depth, $1 - z/S$.

We denote the length or span of the flowband by L, and its maximum thickness (at the divide, $x = 0$) by H. In the examples in this paper, the H/L ratio is $1/50$, approximating the profile of Siple Dome in Antarctica. Our time scale, $T = H/b$, is 10,000 years.

With the flowband geometry and this velocity model, we calculate particle paths using the set of differential equations, $\dot{x} = u(x,z)$ and $\dot{z} = w(x,z)$, and a starting point, (x_0, z_0). Each point, $(x(t),z(t))$, on a path is described as a function of the initial point and travel time.

2.2.2 Finite Strain and Segment Rotation

Along a path, we also calculate the deformation gradient tensor, $F(t_1.t_2)$. This tensor describes how a small structure at the point defined by time t_1 is strained when it moves to the t_2 point on the path. See Chapter 1 and Malvern (1969)[sec. 4.5] for details.

If $[dx_1.dz_1]'$ is a small segment at time t_1, then at t_2 the deformed segment is

$$\begin{bmatrix} dx_2 \\ dz_2 \end{bmatrix} = \begin{bmatrix} F_{xx}(t_1.t_2)\ dx_1 + F_{xz}(t_1.t_2)\ dz_1 \\ F_{zx}(t_1.t_2)\ dx_1 + F_{zz}(t_1.t_2)\ dz_1 \end{bmatrix} \qquad (2.4)$$

The segment angles at t_1 and t_2 satisfy

$$\tan\theta_1 = \frac{dz_1}{-dx_1} \qquad (2.5)$$

$$\tan\theta_2 = \frac{F_{zx}(t_1.t_2) - F_{zz}(t_1.t_2)\tan\theta_1}{-F_{xx}(t_1.t_2) + F_{xz}(t_1.t_2)\tan\theta_1} \qquad (2.6)$$

Here we define angles relative to horizontal upstream ($-x$ direction) (Figure 1.4).

Using (2.6) we can define an *angle rotation function* in which the strained segment's angle is a function of the initial angle and the respective times. This function also has an inverse giving the angle at t_1 as a function of the angle at t_2.

$$\theta_2 = \gamma(\theta_1.t_1.t_2) \qquad (2.7a)$$

$$\theta_1 = \gamma^{-1}(\theta_2.t_1.t_2) \qquad (2.7b)$$

In practice, the inverse function has the same form as the forward function except that it uses the matrix inverse of F, in effect reversing the strain.

Figure 2.1 illustrates how segments rotate while moving along a particle path. Three patterns of rotation are worth noting. If its angle is greater than $90°$ (vertical), a layer rotates toward $180°$ (horizontal downstream). If its angle is small enough, it rotates toward $0°$ (horizontal upstream). Larger angles in the first quadrant first rotate toward a minimum, then turn around and rotate to vertical and beyond. It is this set of 'flippers' that is of particular interest in studying folding.

Even in a simple flowband model such as this, the stratigraphy is not exactly parallel to the flat bed. In addition, the F_{zx} component of the deformation gradient tensor is slightly negative, which means that $\gamma(0°.t_1.t_2)$ is not zero. However these deviations from horizontal are so small that we
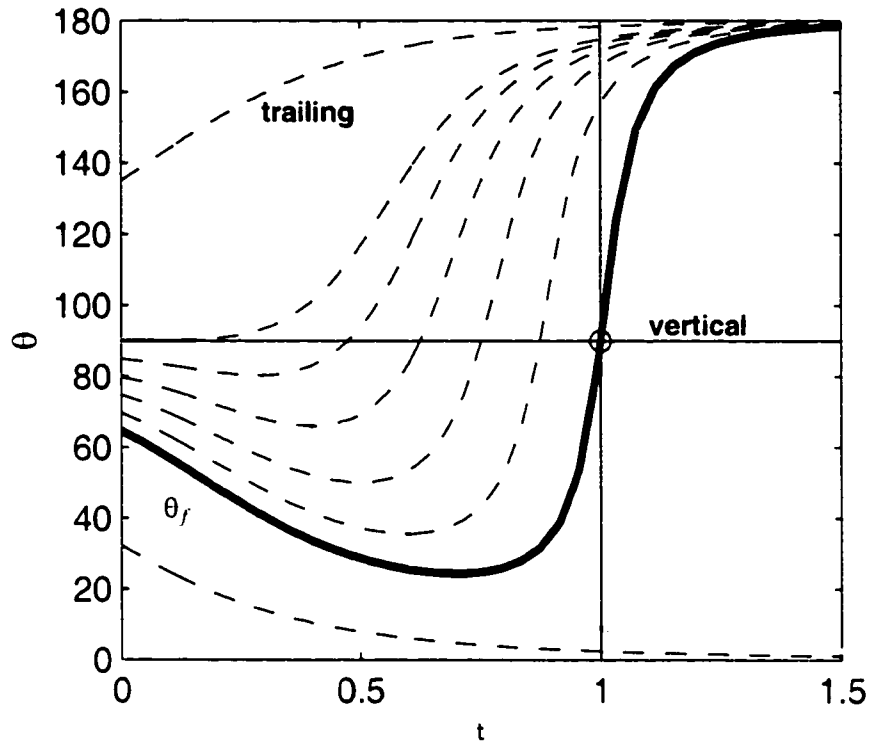
Figure 2.1: The evolution of a set of angles along a particle path. $\gamma(\theta.t_1.t_2)$ (dashed), plotted against travel time. The heavy solid line is $\theta_f = \gamma^{-1}(90°.t_1.1)$, the history for an angle that is vertical at $t_2 = 1$. The gray line passes through the minimum point of each rotation curve.

can ignore them, and treat all angles as though they are measured relative to the steady state stratigraphic isochrones. In a flow model with significant bed slope, we would need to distinguish between horizontal and the isochrone slope.

2.2.3 Precores

The inverse angle rotation function when θ_2 is vertical is of sufficient interest to warrant its own symbol.

$$\theta_f(t_1.t_2) = \gamma^{-1}(90°.t_1.t_2) \tag{2.8}$$

The lower panel in Figure 2.2 shows $\theta_f(t.t_c)$ for several particle paths, where t_c is the time on each path where $x(t_c) = 10H$. These are the angle history curves of segments that would be vertical in a
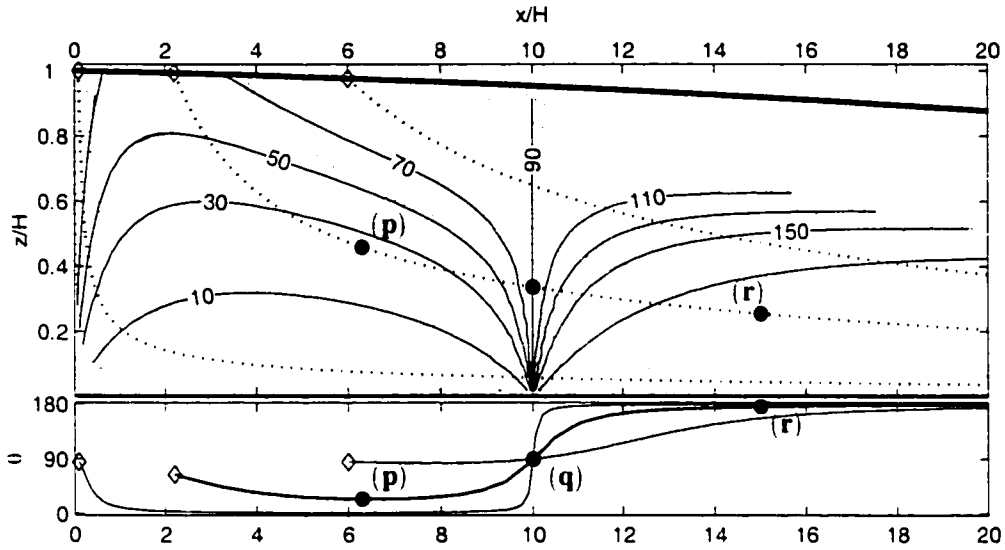
Figure 2.2: (upper) Particle paths (*dotted*) and contours of $\theta_f(t.t_c)$, the precore slope angle in degrees, plotted along the inner portion of an ice sheet flowband. The ice divide is on the left ($x/H = 0$). (lower) $\theta_f(t.t_c)$ along selected particle paths (marked with ○ at the surface). Corresponding points on both panels are marked (p), (q), (r). The values of θ_f at these points are $24°$, $90°$, and $176°$.

hypothetical ice core drilled at 10 ice thicknesses from the divide. At the core they are aligned with the core. At times earlier than t_c, the $\theta_f(t.t_c)$ function gives the angle of the segment that will become vertical when it moves to the core location.

The set of all points that are t_1 travel time upstream from the core location can be thought of as the t_1 isochrone relative to the core. In Chapter 1 we called these isochrones *precores*. The upper panel plots contours of the slope angle of the precores, which is $\theta_f(t.t_c)$. These contours can be used to determine whether a particular disturbance will be an overturn fold when it reaches the core. For example, if the leading edge of a disturbance at point (p) has angle of $30°$, it will rotate beyond $90°$ at point (q). By point (r) it will be within a few degrees of horizontal.

The flowband framework, the ability to calculate the velocity, particle paths and F, and the angle rotation function are necessary prerequisites for the probability model. The flat bed, uniform accumulation, steady state, L, H, the constant flowband width, and the shallow ice rheology are specific to our examples.

2.3 A Probabilistic Model of Segment Overturning

2.3.1 The Probability Variables

When a layer segment is observed to have a disturbed orientation θ_2 at time t_2, the inverse angle rotation function (2.7b) identifies the required injection angle θ_1 at any injection site upstream along the particle path. However, (2.7b) cannot tell us which of those locations is the actual source point, or even which point is most likely to have been the source. When constructing a probability model of folding, we need to distinguish between the probability of injecting a particular disturbance, and the probability of observing a disturbance in a core. The two probabilities have different properties and need different variables. Our task is to relate the two.

In the following we will frequently refer to an *injected segment*. Such a reference is shorthand for *the leading edge segment of an injected disturbance*. Even this is a simplification, since an actual disturbance in the stratigraphy will involve multiple layers which are rotated over a continuous range of angles. The *leading edge* is the steepest portion which will overturn first[1].

In our model, a layer observed at time τ on a particular path is said to be *folded* (or overturned) if it contains a segment with angle ϕ greater than or equal to 90°, and that segment was a leading edge (with an angle θ less than 90°) of a disturbance injected at some earlier time t. This terminology is summarized in Table 2.1.

We are describing a random phenomenon where some process injects a disturbance at one point and angle on the path. That disturbance is later observed at another angle. The observation point is defined in this problem, but injection time and angle, as well as the observed angle are described in terms of probabilities. We will refer (with some mathematical informality) to these as *random variables* (Parzen, 1960, sec. 4.3, 7.1).

The link between the injected angle and the observed angle is the angle rotation function (2.7a) $\phi = \gamma(\theta, t, \tau)$, and its inverse, $\theta = \gamma^{-1}(\phi, t, \tau)$.

The travel distance along the path, or some other measure of position on the path, could be used instead of the times, t and τ. When looking across paths, the injection and observation points can be specified either in terms of the x, z coordinates, or in terms of a particle path and travel time along it.

---

[1] Though much of this analysis applies, with some wording changes, to any section of a disturbance.

Table 2.1: Injection and Observation Variables

	angle	time	distribution	density
Injection			$P(\theta_a.t_a)$	$p(\theta_a.t_a)$
variables	θ	t		
parameters	θ_a	t_a		
fixed values	θ_{fix}	t_{fix}		
Observation			$Q(\phi_a.\tau)$	$q(\phi_a.\tau)$
variable	ϕ			
parameters	ϕ_a	τ		

2.3.2 The Injection Probability

The starting point for deriving the overturn probability is the specification of the probability of an injection. For continuous random variables, probabilities are usually defined on intervals rather than at individual values. One way of defining an *injection probability distribution* is

$$P(\theta_a.t_a) \equiv P\{\theta.t \ : \ \theta_a \leq \theta \leq 90° \ \& \ t \leq t_a\} \tag{2.9}$$

This is the probability of the event in which a disturbance segment is injected at time t less than or equal to t_a, and at an angle θ between θ_a and vertical. It is a function of two jointly distributed random variables, θ and t.

We can derive a joint *probability density* from this distribution by differentiation[2].

$$p(\theta.t) \equiv -\frac{\partial^2}{\partial\theta\partial t}P(\theta.t) \tag{2.10}$$

---

[2]Strictly speaking, θ is a random variable, and θ_a is a parameter defining a set of θ values. Maybe the differentiation variable should be θ_a.

The probability distribution can, in turn, be expressed as an integral of the density.

$$P(\theta_a, t_a) = \int_0^{t_a} \int_{\theta_a}^{90^\circ} p(\theta, t) \, d\theta \, dt \tag{2.11}$$

It is also convenient to define two individual probability density functions

$$P_a(\theta_a, t) \equiv \frac{\partial}{\partial t} P(\theta, t) = \int_{\theta_a}^{90^\circ} p(\theta, t) \, d\theta \tag{2.12}$$

and

$$P_t(\theta, t_a) \equiv -\frac{\partial}{\partial \theta} P(\theta, t) = \int_0^{t_a} p(\theta, t) \, dt \tag{2.13}$$

$$p(\theta, t) = \frac{\partial}{\partial t} P_t(\theta, t) = -\frac{\partial}{\partial \theta} P_a(\theta, t)$$

While formally, we are defining the density as a derivative of the probability distribution, in our examples, we will start with the joint density and assume that it is the product of two or more independent densities. That is, $p(\theta, t) = g(\theta) f(t)$ or $p(\theta, t) = g(\theta) f_x(x(t)) f_z(z(t))$. We have chosen these forms because they are convenient to work with, rather than because they correspond to particular injection scenarios.

The upper bound of 90° on θ restricts our attention to a leading edge segment which can overturn. The probability distribution could be extended to include angles up to 180° (or below 0°) (see Appendix C.1). The angle rotation functions can handle these angles just as well.

2.3.3 The Overturn Probability

The event in which an injected disturbance has overturned by observation time τ on a path, can be defined as the event in which the disturbance segment was injected with an angle θ less than vertical and was later (at τ) observed (at angle ϕ) at vertical or beyond[3].

$$Q(90^\circ, \tau) \equiv P\{\phi, \theta, t : \phi \geq 90^\circ \ \& \ \theta \leq 90^\circ \ \& \ t \leq \tau\} \tag{2.14}$$

If an injection occurs at $\theta \geq \theta_f(t) = \gamma^{-1}(90^\circ, t, \tau)$, it will be observed at time τ with angle $\phi \geq 90^\circ$. The overturn probability can then be expressed as:

$$Q(90^\circ, \tau) = P\{\theta, t : \theta_f(t) \leq \theta \leq 90^\circ \ \& \ t \leq \tau\}$$

$$= \int_0^\tau \int_{\theta_f(t)}^{90^\circ} p(\theta, t) \, d\theta \, dt = \int_0^\tau P_a(\theta_f(t), t) \, dt \tag{2.15}$$

---

[3]We will often omit the τ argument in this and other functions if we are not focusing on its variation.
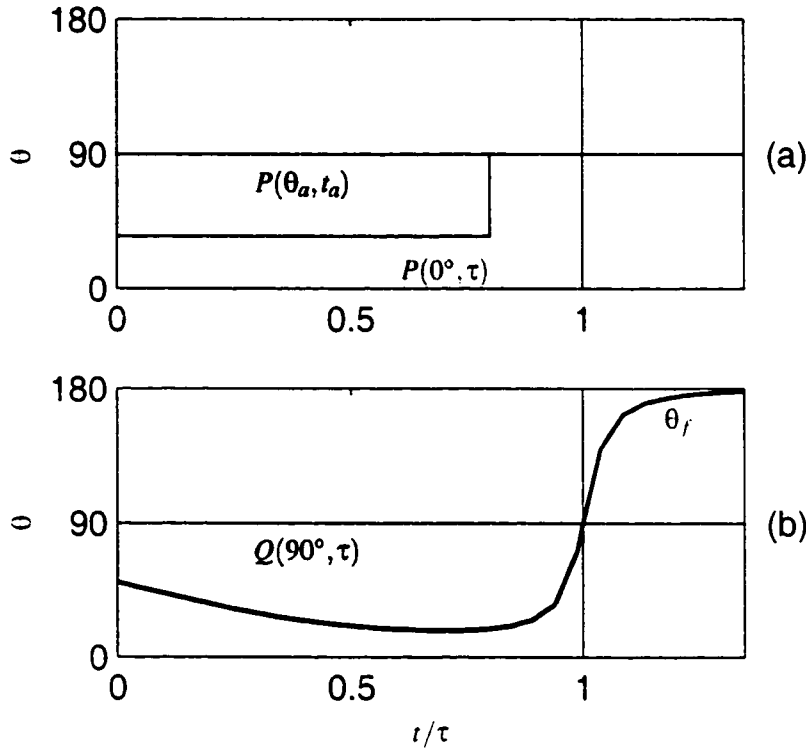
Figure 2.3: Integration areas for $P(\theta_a.t_a)$ and $Q(90°.\tau)$. (a) $P(\theta_a.t_a)$ can be obtained by integrating $p(\theta.t)$ over the rectangle defined by $0 \le t \le t_a$ and $\theta_a \le \theta \le 90°$. (b) $Q(90°.\tau)$ is obtained by integrating $p(\theta.t)$ over the area bounded by $\theta_f(t.\tau)$. This is a subset of the area covered by $P(0°.\tau)$ (which equals $Q(0°.\tau)$).

The integration area bounded by $\theta_f(t)$ is illustrated in Figure 2.3. It is a subset of the rectangular integration area for $P(0°.\tau)$.

We can define a more general *observation probability distribution* by using a ϕ_a threshold in place of $90°$.

$$Q(\phi_a.\tau) \equiv P\{\phi.\theta.t : \phi \ge \phi_a \ \& \ \theta \le 90° \ \& \ t \le \tau\}$$

$$= \int_0^\tau \int_{\theta_a(t)}^{90°} p(\theta.t)\,\mathrm{d}\theta\,\mathrm{d}t = \int_0^\tau P_a(\theta_a(t).t)\,\mathrm{d}t \tag{2.16}$$

where $\theta_a(t) = \gamma^{-1}(\phi_a.t.\tau)$.

The choice of $90°$ as the overturn threshold angle is convenient but not crucial since the rotation through vertical is rapid. The more general observation distribution can be used to calculate the prob-

ability of observing near–vertical angles. For example, $P\{90° \le \phi \le 160°\} = Q(160°) - Q(90°)$. Such a segment would stand out as one that is in the process of overturning, while one much closer to 180° could be indistinguishable from undisturbed stratigraphy.

An *observation probability density* can be calculated by taking the derivative of $Q(\phi_a, \tau)$ with respect to the angle.

$$q(\phi_a, \tau) = -\frac{\partial}{\partial\phi_a} Q(\phi_a, \tau) \tag{2.17}$$

$$= -\frac{\partial}{\partial\phi_a} \int_0^\tau P_a(\theta_a(t), t)\, dt = -\int_0^\tau \frac{\partial}{\partial\phi_a} P_a(\theta_a(t), t)\, dt$$

$$= -\int_0^\tau \frac{\partial}{\partial\phi_a} \int_{\theta_a(t)}^{90°} p(\theta, t)\, d\theta\, dt = -\int_0^\tau \frac{\partial\theta_a}{\partial\phi_a} \frac{\partial}{\partial\theta_a} \int_{\theta_a}^{90°} p(\theta, t)\, d\theta\, dt$$

$$= \int_0^\tau p(\theta_a, t) \frac{\partial\theta_a}{\partial\phi_a}\, dt$$

This density is the cumulative injection density along the $\theta_a(t) = \gamma^{-1}(\phi_a, t, \tau)$ curve modified by how the injection angle varies with respect to the observation angle. $\partial\theta_a/\partial\phi_a$ is, in a sense, the width of the $\gamma^{-1}(\phi_a, t, \tau)$ function. In Figure 2.3 the integration area for $q(90°)$ can be pictured as the infinitesimal width of the θ_f curve.

We need to keep in mind that $Q(\phi_a, \tau)$ is a function of τ in a different sense than ϕ_a. ϕ is a random variable, so that integrals and derivatives across this value transform between probability densities and distributions. τ on the other hand, is a parameter which defines where the observation is being made. It is shorthand for all the parameters that define where the observation occurs, including the specification of path and flowband. This means that $\partial Q/\partial\tau$ is not a probability density.

We can also define a conditional overturn probability:

$$Q_c(\tau) = \frac{Q(90°, \tau)}{Q(0°, \tau)} = \frac{Q(90°, \tau)}{P(0°, \tau)} \tag{2.18}$$

This is the overturn probability relative to the probability of there being any injected disturbance up to the observation time. We have found that in some cases $Q_c(\tau)$ is easier to understand than $Q(90°, \tau)$ (Appendix C.2).

2.4 Examples Along a Path

We start exploring this relation between injection probability and overturn probability along one particle path. Fixing first the injection time and then the injection angle allows us to isolate the effects

44
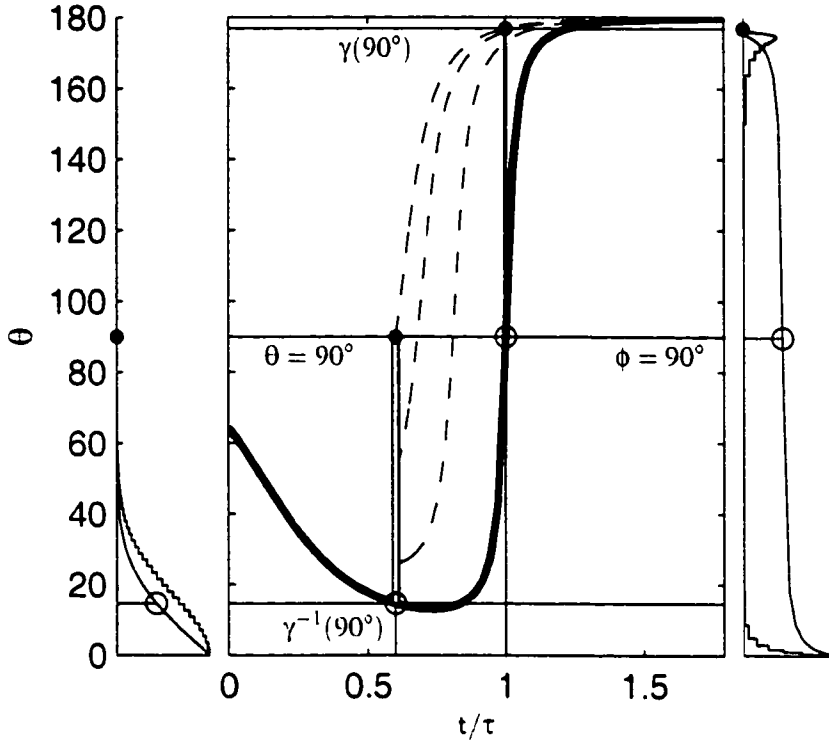
Figure 2.4: Injection and overturn probabilities for the injection angle and fixed injection time. (left) The injection $p(\theta)$ (*stepped*) and $P_a(\theta)$ (*line*) against θ. Each is scaled for maximum resolution. (right) Observed $q(\phi)$ (*stepped*) and $Q(\phi)$ (*line*) against ϕ. The probabilities at $\phi = 90°$ and $\theta = \gamma^{-1}(90°)$ are marked with $-\circ$. (center) θ_f (*heavy line*) and several other $\gamma(\theta)$ (*dashed*) curves that map θ onto ϕ. The vertical gray bar at $t/\tau = 0.6$ marks the injection angle range that contributes to the $Q(90°)$ overturn probability.

of angle and time on the overturning process. We also pay attention to how the overturn probability varies with the overturn threshold ϕ_a and the observation time τ.

2.4.1 Known Injection Time, Probabilistic Angle

Fixing the injection time (t_{fix}) allows us to focus on how the injection angle affects the overturn probability. Formally, the time can be fixed by using the Dirac delta function. $\delta(t - t_{fix})$, which is zero everywhere except when $t = t_{fix}$.

$$p(\theta,t) = g(\theta)\,\delta(t - t_{fix}) \qquad (2.19)$$

The probability distributions, (2.12), (2.11), and (2.16), become

$$P_a(\theta_a, t) = \int_{\theta_a}^{90^\circ} g(\theta)\, \delta(t - t_{fix})\, d\theta = \delta(t - t_{fix}) \int_{\theta_a}^{90^\circ} g(\theta)\, d\theta = \delta(t - t_{fix})\, P_a(\theta_a) \tag{2.20}$$

$$P(\theta_a, t_a) = \int_0^{t_a} \delta(t - t_{fix})\, P_a(\theta_a)\, dt = \begin{cases} P_a(\theta_a) & \text{for } t_{fix} \le t_a \\ \\ 0 & \text{if } t_{fix} > t_a \end{cases} \tag{2.21}$$

$$Q(\phi_a, \tau) = \int_0^{\tau} \delta(t - t_{fix}) P_a(\theta_a(t))\, dt = \begin{cases} P_a(\theta_a(t_{fix})) & \text{for } t_{fix} \le \tau \\ \\ 0 & \text{if } t_{fix} > \tau \end{cases} \tag{2.22}$$

$$\theta_a(t_{fix}) = \gamma^{-1}(\phi_a, t_{fix}, \tau)$$

Figure 2.4 illustrates how the injection probability density maps onto the observation probability. The injection density (*stepped region in the left panel*) is a portion of a normal (Gaussian) probability density function located at time $t_{fix} = 0.6\tau$. This choice is based on the assumption that small angle disturbances are more likely than large angle disturbances. We will use this same angle density in the following examples (except when the injection angle is fixed).

$$g(\theta) = \begin{cases} \frac{c_1}{\sigma\sqrt{2\pi}} \exp\left(-\frac{1}{2}\left(\frac{\theta}{\sigma}\right)^2\right) & \text{for } 0^\circ < \theta < 90^\circ \\ \\ 0 & \text{elsewhere} \end{cases} \tag{2.23}$$

$$\sigma = 0.1\pi \text{ radians} = 18^\circ$$

The constant, c_1, scales $g(\theta)$ so that its integral over all injection angles, $P_a(0^\circ)$, is the total probability of a disturbance being injected at this time. This could be unity if we are considering the probability of injecting a leading edge, and one half if we count both leading and trailing edges. Technically we should also be concerned about the nonzero value of $g(90^\circ)$, but since this is 5σ away from 0° any adjustments to c_1 are negligible. Since our focus is on the process and patterns of folding, we will not fix c_1. Plots of densities and distributions are scaled to give the best resolution and the numerical ticks are omitted.

$g(\theta)$ and its integral $P_a(\theta)$ do not have to be continuous at all angles. 0° is the most obvious place where we might want to make these functions discontinuous, either to rule out a 0° disturbance, or to express the probability that no disturbance occurs at this time.
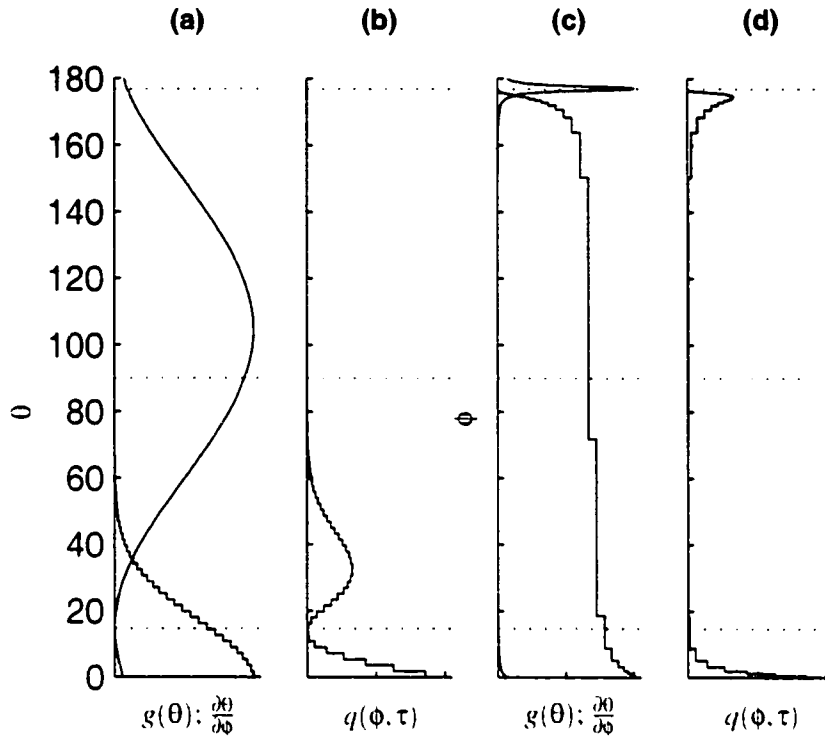
Figure 2.5: Density components from Figure 2.4.

In (a) and (b) the vertical scale is θ, the injection angle. In (c) and (d) the vertical scale is φ, the observation angle. (b) and (d) plot $q(\phi, \tau)$, the observation density, which is the product (2.24) of the two components shown in (a) and (c), $g(\theta)$ (*stairs*) and $\partial\theta/\partial\phi$.

In this case where the injection can occur at only one time, the overturn distribution is a composite function of the injection distribution and the inverse angle rotation function (2.22), $Q(\phi_a) = P_a(\gamma^{-1}(\phi_a))$. This is illustrated in Figure 2.4 where $P_a(\theta)$ is plotted on the left panel, and $Q(\phi)$ on the right. The center panel plots $\theta = \gamma^{-1}(\phi)$ and indicates the range of injection angles that can overturn.

While we have omitted the numerical scales on the right and left panels, it is easy to calculate the overturn probability relative to the total injection probability. In this example, $\gamma^{-1}(90°. t_{fix}. \tau) \approx 15°$. With $\sigma = 18°$, the cumulative normal distribution value is 0.8, which translates to 0.4 of the $P(0°. t_{fix})$ value. Here there is no distinction between the total injection probability and the probability so far, as long as $t_{fix} \leq \tau$.

The observation density (2.17) simplifies to:

$$q(\phi_a.\tau) = \int_0^\tau g(\theta_a(t))\, \delta(t - t_{fix})\, \frac{\partial \theta_a(t)}{\partial \phi_a}\, dt$$

$$= g(\theta_a(t_{fix}))\, \frac{\partial \theta_a(t_{fix})}{\partial \phi_a} \qquad \text{for } t_{fix} \le \tau \tag{2.24}$$

Figure 2.5 shows how the injection density relates to the observation density. The injection density, $p(\theta)$ (*stepped*), in (a) is the same as in Figure 2.4(left). $\partial\theta/\partial\phi$ (*smooth curve*) has a maximum value at the center where a segment rotates (through vertical) the fastest. Here the widest range of injection angles contributes to a given interval of observed angles.

The peak of the product of these two terms is around $30°$ (in b) where both components are below their maximum values, but are not close to zero. The peak around $0°$ is a product of the large $p(\theta)$ value and a small rise in the derivative's value. These small angles are flattened rather than overturned.

When these same values are plotted against the observed angle in (c) and (d), the range of values for $\theta > 30°$ is compressed into a small region above $\phi = 170°$, while the θ around $13°$ are spread out around $\phi = 90°$. The product in (d) corresponds to the observed density plotted in Figure 2.4(right).

Note that the probability of observing an angle greater than $\gamma(90°)$ is zero. This is because we have restricted ourselves to leading edges. Even if trailing edges were included there would be a gap around $\gamma(90°)$ as long as the injection density is negligible around $90°$. This separation between flattened trailing edges and overturned leading edges becomes blurred when the injection can occur over a range of times (compare the appendix Figure C.1 and Figure C.1).

2.4.2 Known Injection Angle, Probabilistic Time

If instead we fix the injection angle and let the time be the random variable, the injection density can be written with a Dirac delta function on the angle:

$$p(\theta.t) = \delta(\theta - \theta_{fix})\, f(t) \tag{2.25}$$

The corresponding distribution over θ (2.12) is

$$P_a(\theta_a.t) = \int_{\theta_a}^{90°} \delta(\theta - \theta_{fix})\, f(t)\, d\theta = \begin{cases} f(t) & \text{if } \theta_a \le \theta_{fix} \\[2mm] 0 & \text{if } \theta_a > \theta_{fix} \end{cases} \tag{2.26}$$
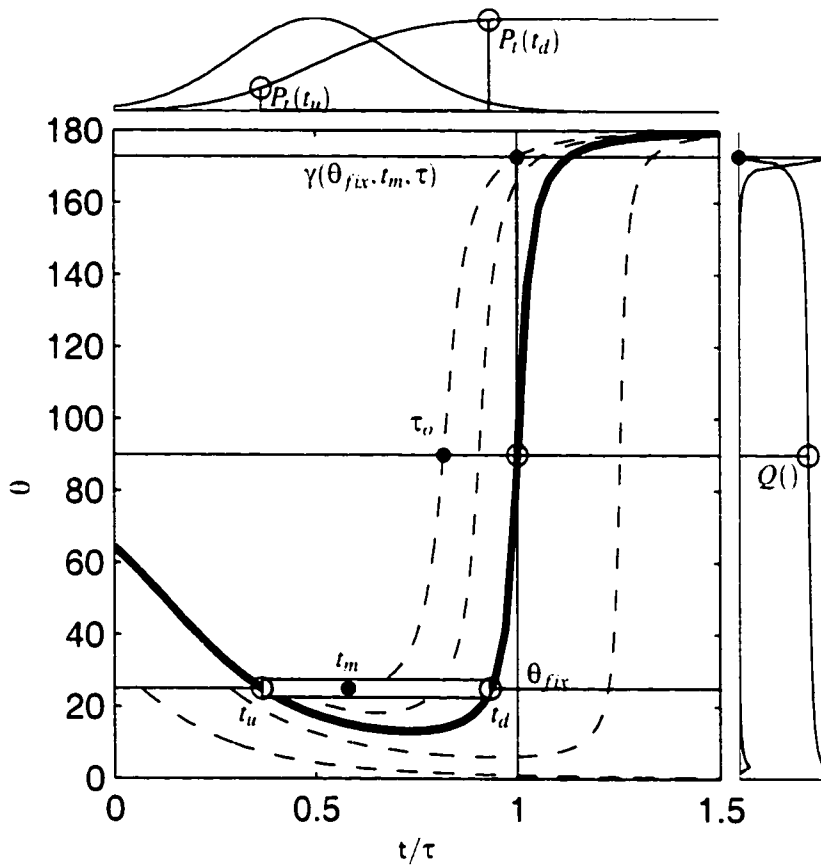
Figure 2.6: Known injection angle ($\theta_{fix} = 25°$), probabilistic injection time. (top) The injection density $f(t)$ (*shaded*) and the injection distribution $P_t(t)$ versus t. (right) The corresponding observation distribution $Q(\phi)$ (*line*) and density $q(\phi)$ (*shaded*). The circles on the two panels mark the terms in $Q(90°) = P_t(t_d) - P_t(t_u)$. (center) The injection region that contributes to $Q(90°)$ is the gray bar between the t_u and t_d points on the $\theta_f(t, \tau)$ curve. A segment injected at t_m is the first one to overturn (at time τ_o).

The overturn probability (2.16) simplifies to:

$$Q(\phi_a.\tau) = \int\limits_{\theta_a(t)\leq\theta_{fu}} f(t)\,dt$$

(2.27)

For our simple flowband geometry, $\{\theta_a \leq \theta_{fix}\}$ is true on a simple interval, $[t_u.t_d]$. The end points are either equal to 0 and τ, or to points in between at which $\gamma^{-1}(\phi.t.\tau) = \theta_{fix}$. The observation integral over the interval becomes:

$$Q(\phi.\tau) = \int_{t_u}^{t_d} f(t)\,dt = P_t(t_d) - P_t(t_u)$$

(2.28)

where $P_t(t)$ is defined in (2.13). It is possible, that for some values of τ this interval is empty, in which case, no segment injected at θ_{fix} will have rotated past ϕ by τ.

For more complex geometries, such as when the flowband bed is not flat, the $\gamma^{-1}(\phi_a.t.\tau)$ function will have a more complex shape, and the $\{\theta_a \leq \theta_{fix}\}$ set may be broken into multiple intervals.

The observation density is

$$q(\phi.\tau) = f(t_d)\,\frac{\partial t_d}{\partial\phi} - f(t_u)\,\frac{\partial t_u}{\partial\phi}$$

(2.29)

Figure 2.6 illustrates how the injection distribution, $P_t(t)$, maps onto the observation distribution, $Q(\phi)$. The injection density is a normal density function in time, with a mean at $t = 0.5\tau$ (*shaded area in top panel*). The known injection angle is $\theta_{fix} = 25°$. As before, several $\gamma^{-1}(\phi.t.\tau)$ curves are plotted in the central panel, with $\theta_f(t)$ highlighted. The times where $\theta_f = \theta_{fix}$ are marked as t_u and t_d. A disturbance segment injected at θ_{fix} in the interval between these two times will appear as an overturned segment at τ. The probability of this event is marked with a circle on the right panel ($Q()$), which is the difference of the two $P_t(t)$ points marked in the upper panel (2.28).

The overturn probability for other observation angles, $Q(\phi)$, can be calculated using the corresponding $\gamma^{-1}(\phi)$ curves. These curves sample different portions of the injection density, with distinct values of t_u and t_d. The left–most curve equals θ_{fix} at only one time, marked t_m. Here, $t_u = t_d$. Corresponding to t_m is the observation time τ_o, which is the earliest time at which a segment injected at

θ_{fix} can rotate through vertical. Both of these times are functions of the injection angle.

$$90° = \gamma(\theta_{fix}, t_m, \tau_o)$$

$$\theta_{fix} = \gamma^{-1}(90°, t_m, \tau_o)$$

$$Q(90°, \tau_o) = P_t(t_d) - P_t(t_u) = 0$$

$$Q(90°, \tau) = 0 \qquad \text{for } \tau \le \tau_o \tag{2.30}$$

At τ, $\phi = \gamma(\theta_{fix}, t_m, \tau)$ is the steepest that a segment injected at θ_{fix} can be. The observation density at this ϕ is a spike, because the sensitivity of t_u and t_d to ϕ is greatest at t_m where $\gamma^{-1}(t)$ is tangent to the $\theta = \theta_{fix}$ line (2.29).

We can divide the interval between t_u and t_d into two regions. $R_u = [t_u, t_m]$ and $R_d = [t_m, t_d]$. A segment injected in R_u will flatten before overturning. A segment injected in R_d starts overturning immediately. The earlier in R_u that an injection occurs, the later it overturns. The instantaneous rotation rate of a segment injected at t_m is zero, but becomes positive immediately.

As in the fixed time example (of the previous section), it is possible that a segment will not overturn by τ, resulting in a minor increase in $q(\phi)$ around 5°. For a more uniform $f(t)$, this spike is more prominent, but still secondary. Its value also increases when θ_{fix} is smaller and less likely to overturn.

The injection density that we have used here varies slowly over time, thus most of the shape of $q(\phi)$ is attributable to $\partial t_u / \partial \phi$ and $\partial t_d / \partial \phi$ (2.29). It is possible to construct an injection density that produces quite different observation densities. An injection density that is concentrated around t_u will result in a relatively high density for ϕ around vertical because $P_t(t)$ will vary most right where $\theta_f = \theta_{fix}$. On the other hand, if the injection density is small at t_m, the principal spike in the observation density will be more symmetric.

Figure 2.7 illustrates how the observation density (plotted as black bars) varies with the observation time, τ. Note that up to $t = t_m(t_{fix}) \approx 0.6T$ a newly injected segment starts out being flattened, and does not start steepening until after t_m. A segment injected after t_m starts steepening immediately. The probability of observing a near–vertical segment decreases further downstream, largely because the higher rotation rate.

In earlier figures, times have been plotted relative to the observation time, τ. In this, and following figures, we plot results for multiple observation times using a reference time, T, that is either the
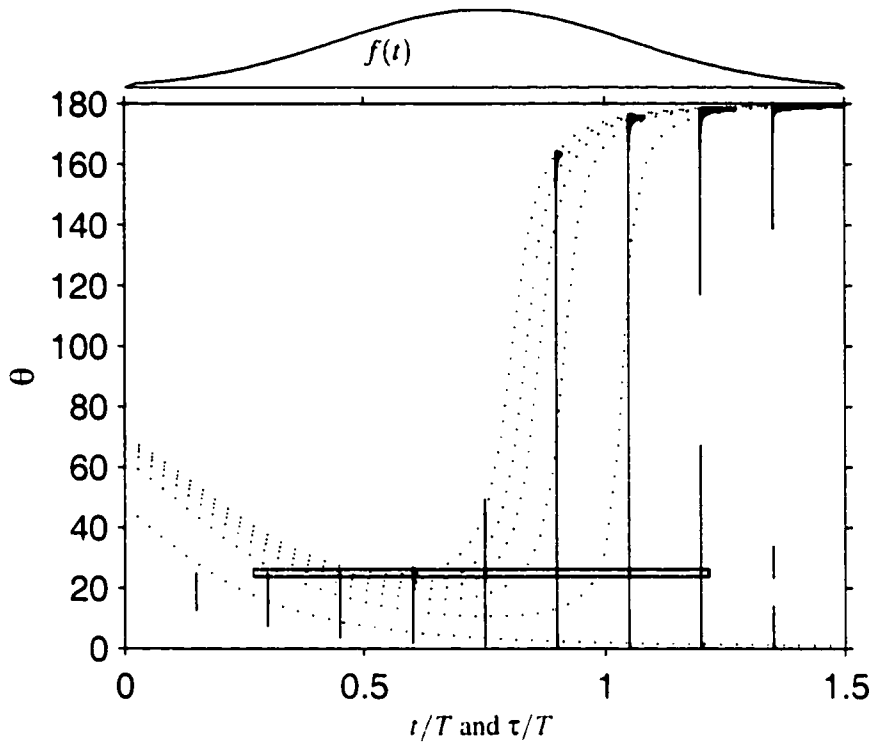
Figure 2.7: The observation density, $q(\phi, \tau)$ for a range of observation times, τ, along a particle path. The injection density, $f(t)$, is plotted in the upper panel. The region of significant injection density is also marked as the gray bar in the bottom panel at $\theta_{fix} = 25°$. The filled vertical lines correspond to the shaded $q(\phi)$ curve in Figure 2.6 (right). They are plotted at the individual observation times. These density curves have been left blank when the density is small.

flowband time scale, b/H, or the time at the 'core' (at $10H$ or $20H$) for this path. While there is some room for confusion in this usage, the numerical values of time are not important for our purposes.

2.4.3 Both Angle and Time as Random Variables

Now we return to the case where both the injection angle and the time are random variables (2.16). In Figure 2.8, the injection density $p(\theta, t)$ is indicated by the dashed contours centered on $\theta = 0°$ and $t/T = 0.5$. This density is the product of a normal density in θ (as in Figure 2.4) and a normal density in t, i.e. $p(\theta, t) = g(\theta)f(t)$. The observation density $q(\phi, \tau)$ is plotted as filled contours[4].

---

[4] The contour intervals for the injection and observation densities do not match.
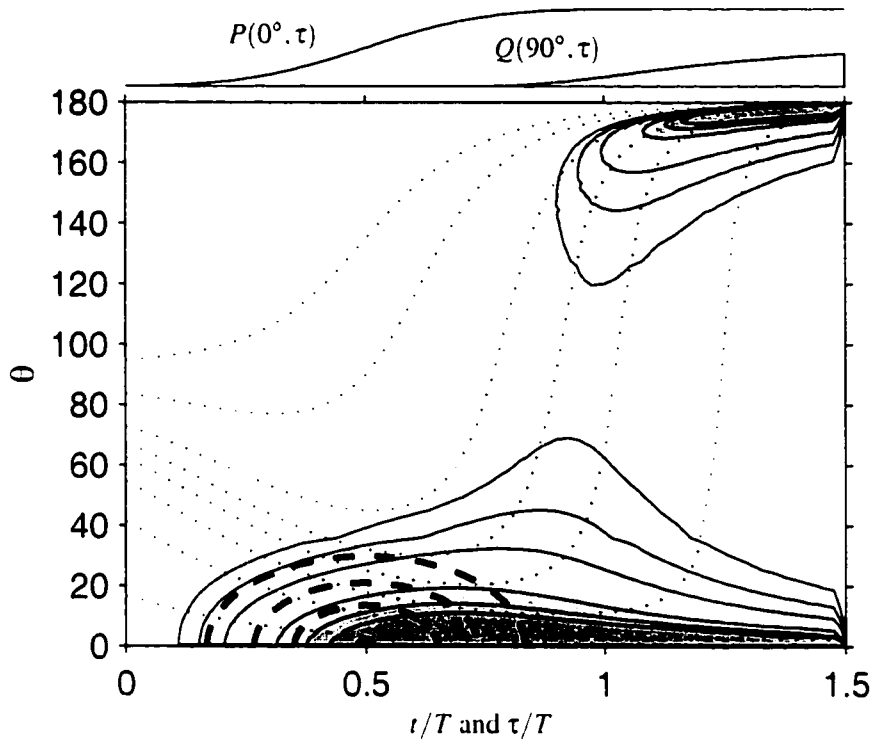
Figure 2.8: Injection density. $p(\theta.t)$ contours (*dashed*) and observation density. $q(\phi.\tau)$ contours (*filled*). $p(\theta.t)$ is normal in both angle and time. with peak density at $\theta = 0°$ and $t = 0.5T$. (upper) Overturn probability. $Q(90°.\tau)$ and the cumulative injection distribution. $P(0°.\tau)$.

The overturn probability distribution. $Q(90°.\tau)$ in the upper panel is the integral of the contoured density above $90°$. We have also plotted the total probability of injecting a segment up to time τ. $Q(0°.\tau) = P(0°.\tau)$. Their ratio is $Q_r(\tau)$ (which is about one half at $1.5T$).

In Figure 2.8 the observation density at $90°$ has a maximum around $\tau/T = 1$. This is the point where we are most likely to see a near-vertical segment. This maximum is the result of two trends. the increased cumulative injection probability and the increased rotation rate. The later (in time) that a $\gamma^{-1}(\phi)$ curve passes through vertical. the higher its cumulative injection probability is. because it has sampled more of the injection density space. especially the higher density small angles. But the overturning rate also is higher. reducing the time a segment spends around $90°$.
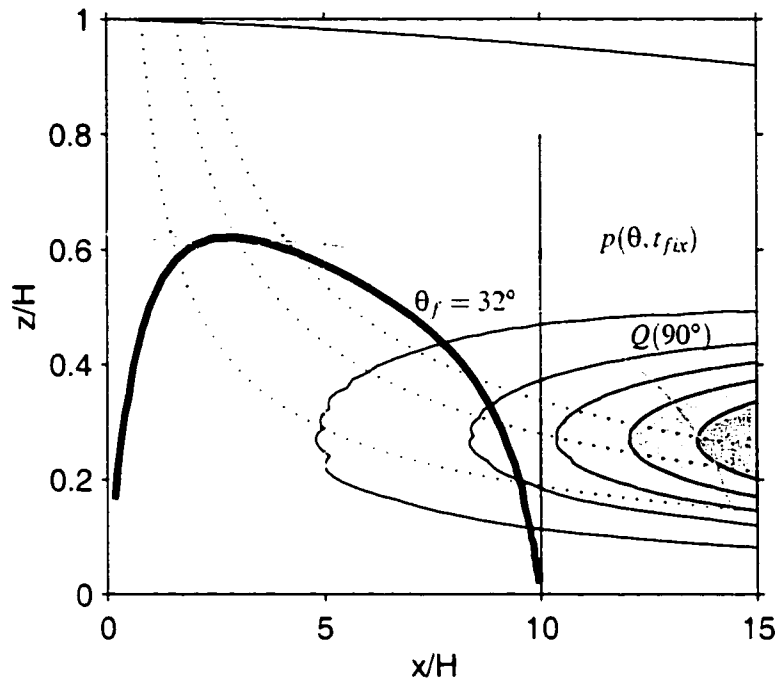
Figure 2.9: The relation between overturn probability. $Q(90°)$ (*filled contours*). and θ_f precores (*contours*) when injection is at t_{fix}. The injection density. $p(\theta, t) = \delta(t - t_{fix})g(\theta)$. plots as an isochrone (*gray band* near $z/H = 0.6$). The precore contours ($51°$. $32°$. and $17°$) for cores at 5. 10. and $15H$. just touch the injection isochrone. Particle paths (*dotted*) connect the peaks of the precores and center lines of the probability contours.

2.5 Probabilities Across a Range of Paths

Up to this point. we have focused on the overturning along one particle path. Extending this to cover a range of paths. just requires evaluating the same probabilities along a representative set of paths. treating each path independently. But displaying the probabilities requires some changes. Since we need to deal with points in two dimensional space ($\mathbf{x} = [x, z]$). we will pay less attention to the angular variations in the probability densities and distributions. We will continue to use an injection density of the form $g(\theta)f(\mathbf{x})$. but will plot just the $f(\mathbf{x})$ portion. Similarly. we will focus on the overturn probability. $Q(90°, \mathbf{x})$ (as opposed to the observation density).

2.5.1 Fixed Injection Time, Probabilistic Injection Angle

Figure 2.9 shows $Q(90°)$ for the case when the injection time is known and constant across all particle paths. This was illustrated for one path and observation time in Figure 2.4. The location of this injection plots as an isochrone (*gray band*) ($t = t_{fix}$).

Along each particle path, the overturn probability increases downstream, but along a vertical transect across paths (such as in an ice core), the probability increases to around $z/H = 0.25$, and then decreases.

At first glance, this maximum in $Q(90°)$ at an intermediate depth may be surprising, but comparison with the θ_f (precore angle) contours (Figure 2.2), gives an idea of what is happening. In Figure 2.9 we have plotted θ_f contours for three core locations (5, 10, and 15H), ones which just touch the injection isochrone. A segment injected at $\theta_f = 32°$ at the tangent point of the middle contour (*bold*), will be vertical in the core at 10H (these points are connected by a particle path). On other paths, an injected segment will have to be steeper, if it is to become vertical at this core location. The smaller this θ_f value is at t_{fix}, the larger $P_a(\theta, t_{fix})$ is, and the larger $Q(90°)$ will be.

A segment injected on paths closer to the divide, will be subject to more vertical compression before being sheared, so it is less likely to overturn, while a segment injected further downstream, will not have traveled long before reaching the core location.

For other core locations, this minimum θ_f value is different and occurs on different paths. The vertical maxima in $Q(90°)$ (across core locations) appear to lie along an isochrone, though we cannot show mathematically that this must be the case.

2.5.2 Fixed Angle, Probabilistic Injection Position

The precore (θ_f) contours also provide insight in the case when the injection angle is fixed and the injection time is a random variable. As shown in Figure 2.6, the injection region that contributes to the overturn probability at τ, is the interval where the θ_f curve is below the injection angle, $\{\theta_f(t) \leq \theta_{fix}\}$. We described this interval by its two end points, t_u and t_d, further dividing it into two regions by the t_m time, R_u and R_d. A segment injected at θ_{fix} in R_u initially flattens before overturning, while one injected in R_d starts overturning immediately.

Since t_u and t_d are times where $\theta_f(t) = \theta_{fix}$, in the flowband space (x, z) they are the θ_{fix} precore
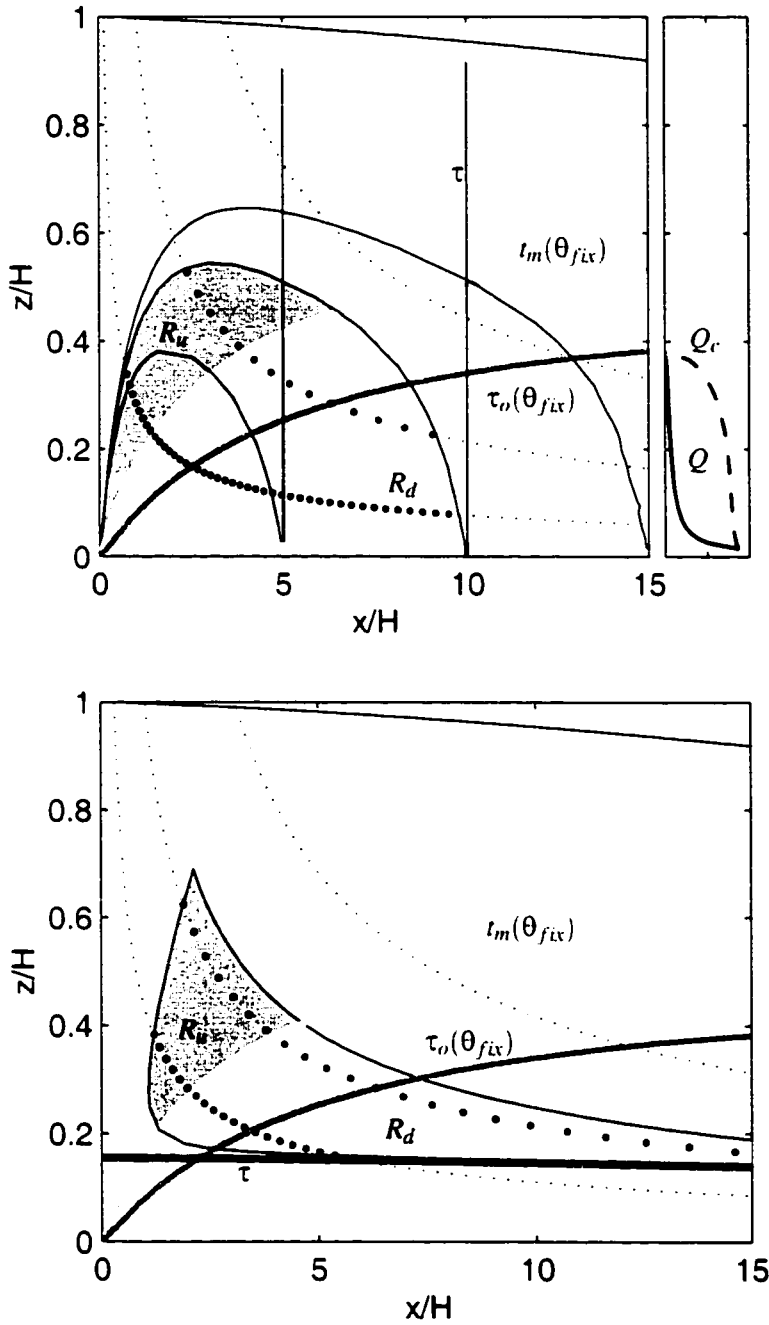
Figure 2.10: (upper) The R_u and R_d regions for observation points along a vertical core. Their boundaries lie on the $\theta_f = \theta_{fix}$ precore angle contour.

(lower) The R_u and R_d regions for observation points along an isochrone (the τ line at $0.15H$).

angle contours when the observation points lie along a vertical core. This is illustrated in Figure 2.10 for cores at 5. 10. and 15H. The R_u and R_d regions for a core at 15H are shaded. while the boundaries of these regions for the other cores are outlined.

The boundary between the two regions. $t_m(\theta_{fix})$. depends only on the injection angle. and not on the observation point. The $\tau_o(\theta_{fix})$ curve where a $t_m(\theta_{fix})$ segment reaches vertical. is the earliest that a segment injected at θ_{fix} can overturn (2.30). Thus $Q(90°)$ must be zero above this curve.

On several of the particle paths crossing these regions. we have plotted dots at regular time intervals (500 years). Their spacing is much closer deep in the ice. reflecting the lower velocity and thinner stratigraphic layers at depth. If the injection density is uniform in time. the number of these dots along a path in the R_u and R_d regions is an indicator of the overturn probability at the core. Specifically. $Q(90°.\tau_c) \propto t_d - t_u$. The conditional overturn probability (2.18) is $Q_c(\tau_c) = (t_d - t_u)/\tau_c$. The shape of these two probability distributions is shown in right panel of Figure 2.10. The growth of Q_c below τ_u is more abrupt than for $Q(90°)$.

More generally. if we know the cumulative injection probability. $P_t(\theta_{fix}.t)$ (2.13). along the t_u and t_d boundaries. we can calculate $Q(90°.\tau)$ from the difference (2.28).

Figure 2.10(lower) presents the same information as Figure 2.10(upper) but the observation points are along an isochrone. The $t_m(\theta_{fix})$ and $\tau_o(\theta_{fix})$ curves are the same. but the R_u and R_d regions have a quite different shapes. The principal for determining their boundaries is the same.

2.5.3 Probabilistic Angle and Position

In Figure 2.11 the injection density is Gaussian in angle and injection time. $p(\theta.x) = g(\theta)f(t)$. as in Figure 2.8. The contours in panel (a) are for the $f(t)$ portion. They are aligned with stratigraphic isochrones because the density is the same for all particle paths. The overturn probability contours in panel (b) are similar to those shown in Figure 2.9 for just one injection time.

Figure 2.12 is similar to Figure 2.11. but the injection density is binormal in the x and z coordinates.

$$p(\theta.t) = g(\theta)\, f_1(x(t))\, f_2(z(t))$$ (2.31)

The overturn probability pattern is similar. because the injection density is still concentrated along an isochrone (there is considerable vertical exaggeration in these plots).

(a) Injection density

(b) Overturn Probability
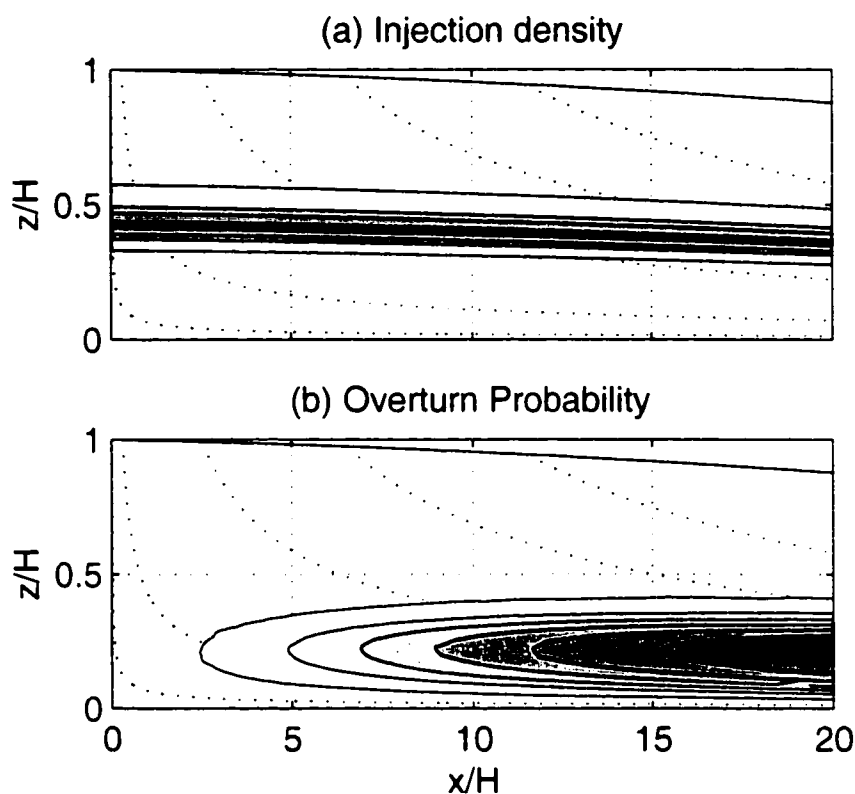
Figure 2.11: (a) Contours of an injection density, $f(t)$, that is Gaussian in travel time. These contours are aligned with isochrones. (b) Contours of the overturn probability, $Q(90°.\tau)$. The pattern is similar to fixed injection time case plotted in Figure 2.9. Contour levels are not the same in the two panels.

Figure 2.12(a) includes contours of the probability of observing an angle in the range of $90°$ to $160°$. Such a segment would be obviously overturned. This region is a narrow band on the upstream side of the larger overturn range. Further downstream, an overturned segment is more likely to have rotated beyond $160°$.

In Figure 2.13 the injection region is concentrated under the divide (on the far left). Because the injection density is significant near the bed, the overturn probability is high close to the bed. A segment injected at depth near the divide, enters the zone of dominant simple shear before it is flattened very much. Further downstream, the paths with the highest injection density approach the bed, taking with them, the overturn probability contours.

(a) Injection density

(b) Overturn Probability
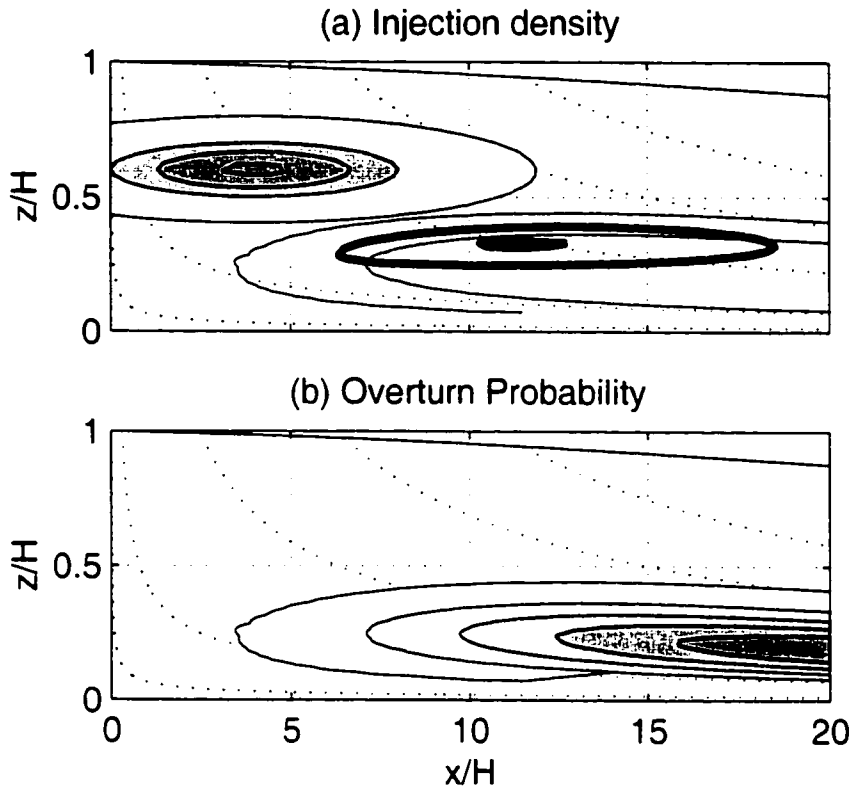
Figure 2.12: Overturn probability for binormal injection density in x and z coordinates. $p(\theta, x) = g(\theta)f(x)f(z)$. Panel (a) also has contours (*heavy lines*) where the probability of observing an overturned segment in the $90 - 160°$ range is largest.

Figure 2.14 combines the injection densities from Figure 2.12 and Figure 2.13. Such a pattern might occur if two distinct processes could disturb the stratigraphy. The combined injection density is just the sum of the two simpler ones. The overturn probability is evaluated in the same manner as before. This summation of injection densities is valid if they are both small enough so that the probability of one injection process modifying an already injected disturbance is very low.

Even though the peak density in the two injection zones is comparable, the divide injection produces a much higher peak overturn probability. Again, the precore contours help us understand the difference. For the $10H$ core, the $30°$ precore contour crosses the upper injection zone, while the $10°$ contour crosses a significant portion of the divide injection zone.

In Figure 2.15 the injection density is uniform in time across the flowband, with the Gaussian an-

(a) Injection density

(b) Overturn Probability
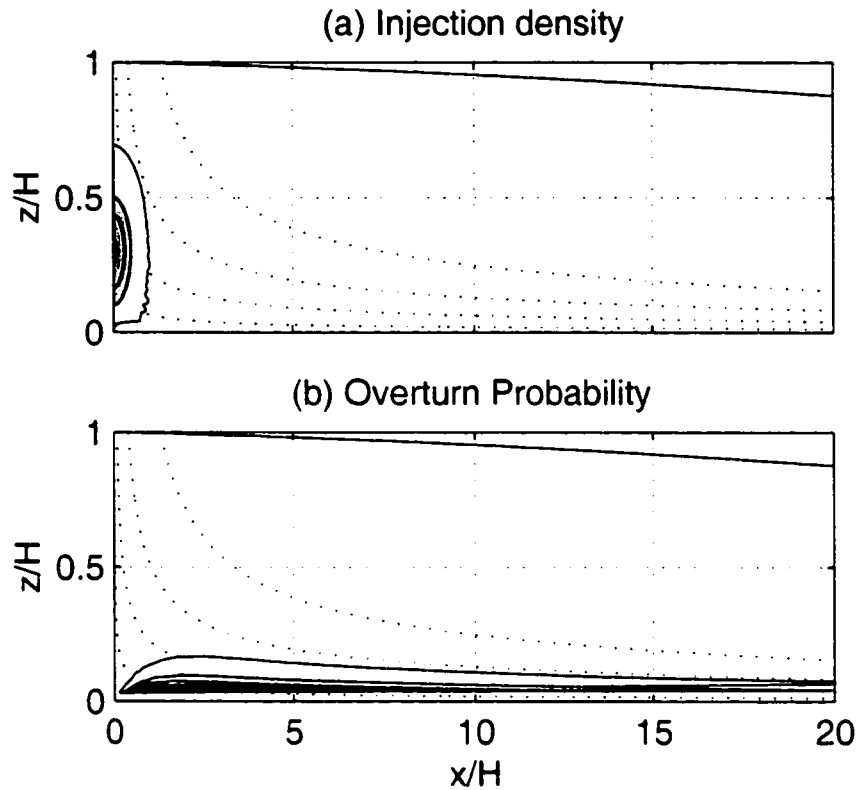
Figure 2.13: Overturn probability contours for an injection region directly under the divide. The injection density is binormal in x and z, with the x mean at $0H$, and the z mean at $0.3H$. Probabilities have not been evaluated all the way to the bed.

gle distribution as before. As in divide injection case (Figure 2.13) the overturn probability is largest at the bed. but because injections can occur on all paths. the depth range of overturning increases downstream (as in the isochrone case. Figure 2.11).

2.6 Conclusion

We have modeled the case in which a disturbance characterized by a segment angle θ, is injected at time t on a particle path. and observed at time τ at angle ϕ. The injection angle and time are random variables (specified in terms of a probability distribution). The observation time is a parameter. while the observation angle is a random variable, whose probability distribution is determined by the model. It is important to make a clear distinction between the injection variables and the observation

(a) Injection density

(b) Overturn Probability
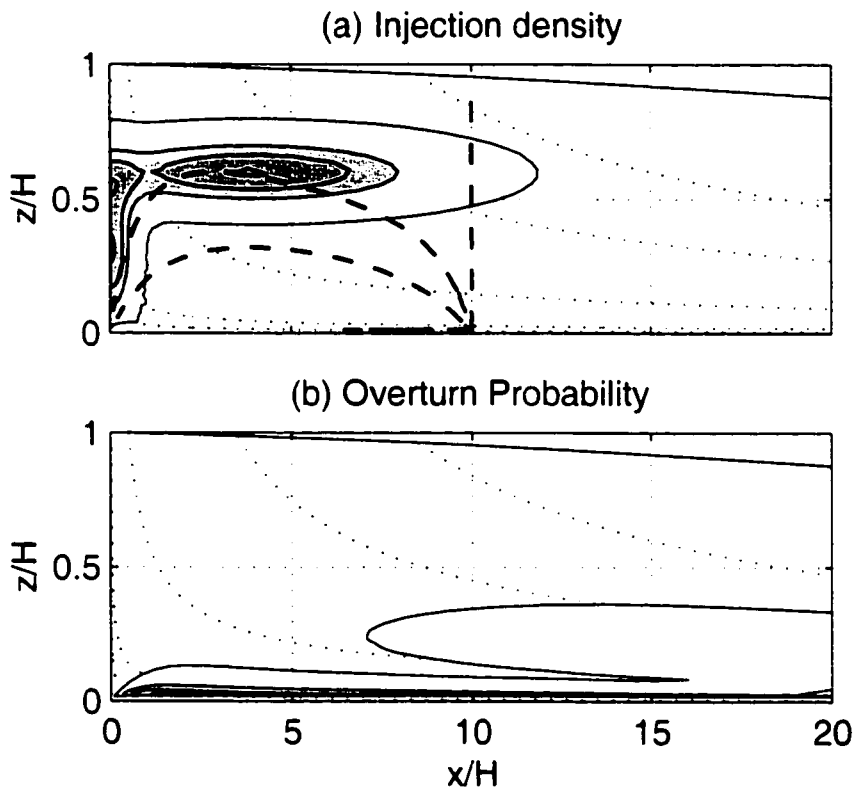
Figure 2.14: Overturn probability for a two zone injection density. The injection pattern in (a) is the combination of the patterns from Figure 2.12 and Figure 2.13. Panel (a) includes the 10 and 30° precore contours (dashed) from Figure 2.2. The 30° contour cuts across the upper injection region, while the 10° contour crosses a portion of the divide region.

(a) Near vertical

(b) Overturn Probability
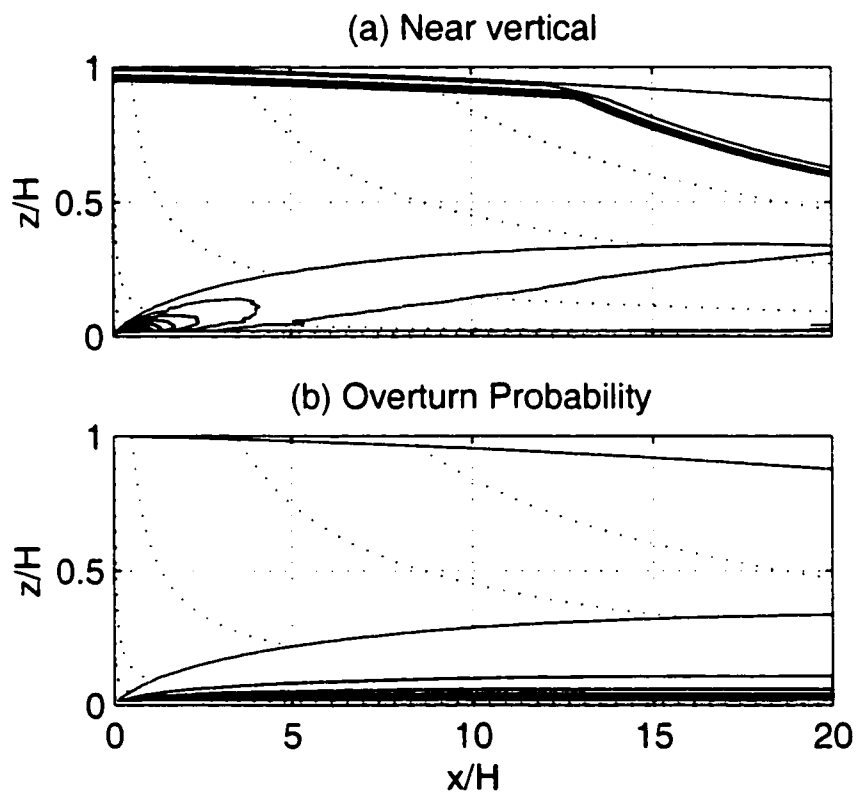
Figure 2.15: Overturn probability for a uniform (in travel time) injection density. (a) The outer area is the region in which $p(\theta, x) = g(\theta)$ is uniform in time. The inner shaded contours show the probability of observing an overturned segment in the $90 - 160°$ range. (b) plots contours of $Q(90°)$.

variables, and to also clearly identify which are random variables and which are parameters.

The overturn probability is the injection density integrated over the subset of angles that can rotate through vertical by the observation time. This set is bounded by an inverse angle rotation function, the same one that is associated with the precore angle contours. This probability is a special case of a more general observation angle distribution.

Focusing on one injection point, illustrates how the injection angle probabilities are translated into observation densities by the kinematic strain. Fixing the angle and letting the injection time be variable, highlights the range of points that can contribute to a fold. In particular, an injected segment might be flattened for a while before it is overturned.

When trying to understand overturn probability patterns across paths, it is important to keep in mind that the probabilities are evaluated independently along each path. At the scale we are considering, disturbances on one path do not affect those on neighboring paths. The overturn probability increases along the path as the total injection probability increases and gentler angles can be overturned. These principles are built into the folding model, but are easily forgotten when looking at probability contours on a flowband cross-section.

The precores that we developed in Chapter 1, have also proven valuable in connecting overturn patterns with injection patterns. In general, the shallower that the precore angle is at an injection point, the higher the overturn probability will be on the same particle path at the core.

We have observed in our examples, two basic patterns of overturn probability. If the injections are most likely along a particular isochrone, the overturn probability will also have its maximum along an isochrone, with increasing value downstream. The overturn probability drops off close to the bed in ice that comes from near the divide, because disturbances injected close to the divide experience significant vertical compression before they move far enough from the divide to be sheared.

On the other hand, if the injection densities are high at depth near the divide, the overturn pattern has its highest probabilities close to the bed. While our model cannot produce folding right under a fixed divide, the folding potential can be significant within a few ice thicknesses of the divide.

Except when comparing the overturn probability to the total injection probability up to the observation point, we have not attempted to put absolute numbers on the probabilities. Such numbers would require greater specificity regarding the total injection probability along each path than we are

able to provide at this point.

The observation probability, as we have defined it, is not directly amenable to statistical verification, even if we had larger samples than the currently available ice cores. A probability cast in terms of the number of folds per unit volume might be better from a statistical point of view, but it would require a better definition of the shape and independence of folds. Working with statistical data could also introduce a size dependence into the problem. The statistics for small folds that can be readily identified in a small ice core cross-section, may or may not, be correlated with probabilities for larger folds.

Finally, we need to keep in mind that the injection probabilities are not directly observable. With a greater knowledge of the injection processes, we might be able to identify precursor structures, such as rheological inhomogeneities. We might also be able to better distinguish between a newly injected disturbance and one that has been around for a while. All of this assumes, though, that the distinction between the dynamic disturbance process, and the kinematic overturning process is real and discernible. At this stage in our research this distinction is primarily a modeling convenience. We expect that a dynamic model capable of producing the initial disturbances, will also handle the large-scale flow deformation.

Chapter 3

RECUMBENT FOLDING OF DIVIDE ARCHES IN RESPONSE
TO UNSTEADY ICE DIVIDE MIGRATION

Abstract

An arching in stratigraphic layers directly under the flow divide of ice sheets has been observed in several ice domes, and is predicted by models of ice sheet flow. We examine the possibility that such a divide bump could be the seed for recumbent folding if the divide moves. By overlaying a portion of a well developed divide stratigraphic arch with a set of precores (core–relative isochrones), we model the case where the divide moves rapidly to a new position, leaving the original divide strati-graphic arch in a flank position. A divide offset of as little as two ice thicknesses can result in the overturning of the deepest layers as they move ten or more thicknesses further downstream. The maturity of the initial divide arching is more important than the speed of the divide movement. The divide must remain at one location long enough for the arch to develop in the stratigraphic column. After the move, the original divide layers must remain on the flank long enough to be overturned. If the location of a ice sheet summit is not sufficiently constrained, as appears to be the case in Green-land, a mature arch might not develop, and this type of folding would not occur. The most likely place to find this type of folding might be the flank of an ice ridge bounded by variable ice streams.

3.1 Introduction

Arching of stratigraphic layers directly under an ice divide has been observed with ground–penetrating radar in several ice sheets (Conway et al., 1999; Nereson et al., 1998; Vaughan et al., 1999), and pre-dicted by models of steady state ice sheet flow (Raymond, 1983; Hvidberg, 1996). Divide movement has also been modeled (Anandakrishnan et al., 1994; Marshal and Cuffey, 2000), and inferred from observed layering (Nereson et al., 1998). This movement has been suggested as a reason why no arch is observed at the Greenland summit (Hempel and Thyssen, 1992; Hvidberg et al., 1997; Hindmarsh,

1996).

Waddington *et al.* (sub) looked at stratigraphic folding near ice sheet centers as a two stage process. Initially the flat stratigraphy is locally disturbed, forming gentle open folds. Then the kinematics of the large–scale flow shears these folds, overturning certain segments. In Chapter 1 we built on this by modeling the kinematic deformation over finite intervals along particle paths. Missing from that work is a comprehensive model of the transient dynamic processes that could generate the initial disturbances. In this paper we evaluate the possibility that a divide arch might be a seed for kinematic folding if the divide moves. As discussed in some detail in Waddington *et al.* (sub) and Chapter 1, the flow at depth and away from the divide is increasingly dominated by shear which tends to overturn deviations from the steady state stratigraphy.

The changing geometry of an ice sheet was proposed by Hudleston (1976) as a cause for folds observed at the margin of the Barnes Ice Cap. Advance or retreat of the ice sheet margin could change the flow around bed–parallel stratigraphy enough to shear it some distance further downstream. We show that a similar analysis can be applied to layers high above the bed and near the ice sheet center.

Models of ice sheets using power law rheology produce distinctive velocity patterns within a few ice thicknesses of the divide (Raymond, 1983).Since the effective viscosity of a power law material increases with decreasing deviatoric stress, the ice deeper under the divide tends to be more viscous than elsewhere. Calculations of isochrones in thermo–mechanical finite element models of ice sheet divides produce a distinctive arching of stratigraphy in a region approximately two ice thicknesses wide (Hvidberg, 1993, 1996; Hvidberg *et al.*, 1997). This has been called a *Raymond Bump* (Vaughan *et al.*, 1999).

Nereson *et al.* (1998, 1997) and Nereson (1998) observed an arch in ground–penetrating radar layers under Siple Dome (Antarctica), and estimated the rate of divide movement from the inclination in the axis of this arch. They also examined the possibility that the arch was the result of reduced accumulation due to wind scouring over the divide. While their work favored the rheological explanation, they could not rule out low accumulation as the cause. In this paper we start with a rheologically produced divide arch, but our approach would also apply to an arch caused by differential accumulation.

3.1.1 Overview

In Chapter 1 we used a kinematic model of ice sheet flow to show that a gentle open disturbance of the stratigraphic layers could be deformed into an overturned fold that would disrupt the order of the layers in an ice core. We introduced the concept of *precores*, or core–relative isochrones, which predict the slope of segments that could overturn at a particular observation 'core'.

In this paper we modify that flowband model to replicate the velocities calculated by a finite element model that produces the divide arches in steady state ice sheets. This allows us to calculate both conventional stratigraphic isochrones and precores. By overlying shifted divide stratigraphy over precores, we show that a moving divide can be the source of folds some distance downstream.

By further modifying our model to handle an evolving geometry, we track the evolution of stratigraphic layers as the divide moves smoothly for a limited distance. This allows us to look at the effect of the divide movement velocity on the folding potential.

We are not attempting to model folding that could be observed in a core drilled at the summit of an ice sheet. While the seed disturbance for this folding is created at a divide, the folding itself occurs well downstream, though it is conceivable that the divide could migrate over such a folded region.

3.2 Geometry and Velocity Model

The coordinates of our flow model are x, horizontal aligned with the flow, and z, vertical. The corresponding velocity components are u and w. Although this is not essential to our approach, for simplicity we assume plane strain, with a constant flowband width, so that strain rates perpendicular to the flowband are zero. The surface and bed functions, $S(x)$ and $B(x)$ (Figure 3.1), approximate the geometry of the north flank of Siple Dome, Antarctica (Nereson, 1998). With a net accumulation, $b = 0.1 \, \mathrm{m \, yr^{-1}}$, and divide thickness $H = 1000$ m, the model characteristic time is $T = H/b = 10,000$ years. The position of the divide, x_{div}, where the flux is zero, is initially at $x = 0$.

The velocity components are calculated from

$$u(x,z) = \bar{u}(x)\hat{u}(x,z) \tag{3.1}$$

$$w(x,z) = -\int_B^S \partial_x u \, dz \tag{3.2}$$
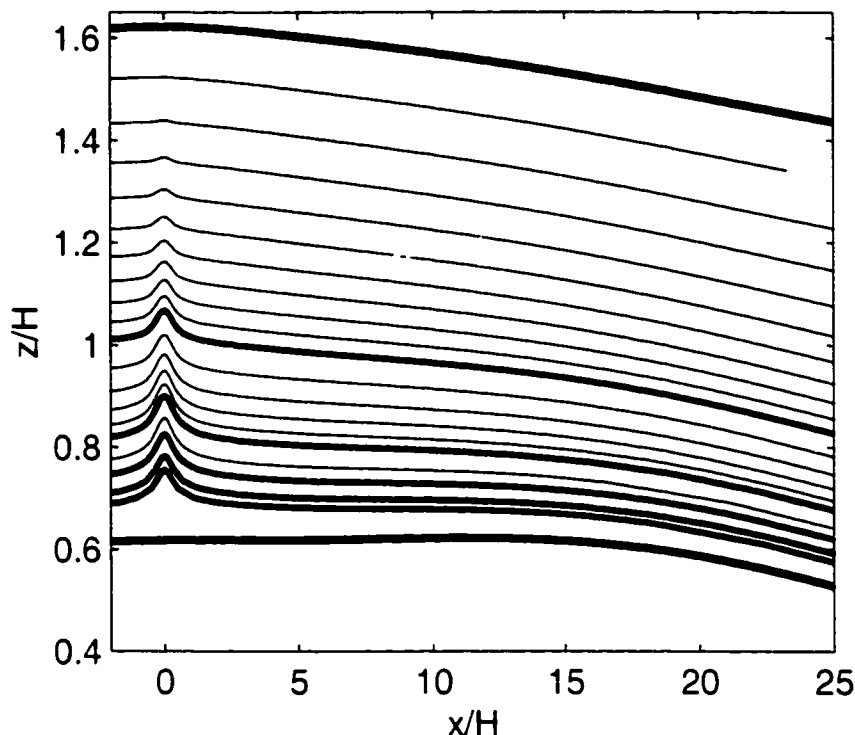
Figure 3.1: Mature divide isochrones. The heavier lines are at $1T$ (10.000 year) intervals. The flow-band bed and surface approximate the north flank of Siple Dome, Antarctica. Divide thickness, H, is about 1000 meters.

$\bar{u}$ is the mean velocity derived from standard assumptions about the flux and the flowband thickness (Reeh, 1988, 1989). $\hat{u}$ is a velocity shape function derived from a dynamic flow model. It is primarily a function of $\hat{z} = (z - B)/(S - B)$, the normalized height. The vertical velocity (3.2) is derived from the horizontal velocity by incompressibility ($\partial_x u + \partial_z w = 0$). Velocity at the bed is zero (frozen bed). Particle paths are calculated numerically using the pair of differential equations in position, $\dot{x} = u$, and $\dot{z} = w$.

In Chapter 1 the horizontal velocity profile, $\hat{u}(x, \hat{z})$ is based on the shallow ice approximation (Appendix A). Here we use a finite element flowband model (Nereson et al., 1998) to get a polynomial approximation to $\hat{u}$ at the divide and at $10H$ downstream. For other x we use a weighted average

68

of these two profiles.

$$\hat{u}(x,\hat{z}) = \eta(x)\hat{u}_d(\hat{z}) + (1 - \eta(x))\hat{u}_f(\hat{z}) \tag{3.3}$$

The weighting, $\eta(x)$ is a function of the distance from the divide, and is chosen to maximize the fit between $\hat{u}(x,\hat{z})$ in this model and the source finite element model. For details on this flowband model see appendix A, and appendix A.1.4 for details on the polynomial velocity profiles.

The flank and divide profiles are compared in Figure A.3. The flank profile, $\hat{u}_f(\hat{z})$, has greater curvature at depth than the shallow ice approximation, $\hat{u}_I(\hat{z}) = 1 - (1 - \hat{z})^4$ (Hutter, 1983; Paterson, 1994, p. 262), because the finite element ice is polythermal, with warmer, softer ice near the bed. The divide profile, $\hat{u}_d(\hat{z})$, on the other hand, has greater curvature near the surface when compared to $\hat{u}_I(\hat{z})$ because the full strain rate tensor is included when evaluating the ice viscosity.

When the surface and bed slopes are small, the vertical velocity, $w(x,z)$, is dominated by a $-b\hat{w}$ term (A.23) (Reeh, 1988). The flank $\hat{w}_f$ is nearly linear except close to the bed, while the divide $\hat{w}_d$ is smaller and more curved (almost quadratic) in the lower two thirds of the ice. This means that $w(x,z)$ decreases faster with depth under the divide than on the flank. The produces the arch in the isochrones directly under the steady divide.

Our flowband geometry and coordinate system are illustrated in Figure 3.1 and Figure A.1.

3.3 Fold Potential Assessed with Precores

Conventional isochrones plot the age of glacial ice since it accumulated at the surface. These are contours of constant time, starting with time, $t = 0$, at points on the ice surface. Figure 3.1 shows the isochrones for our model. Note the arching under the divide.

As discussed in Chapter 1, we can also calculate isochrones relative to another set of reference points, such as the vertically aligned points at a possible core site. These contours of constant time would show where the ice sampled in the core could have been found at earlier times. We call these core–relative isochrones, or *precores*. Precores for a core at $20H$ are plotted in Figure 3.2.

The lower set of panels in this figure illustrates how precores help us assess the potential of observing recumbent folds in a core. The fold at point (q) (the core) has a near vertical *leading edge*, which should be stand out as a fold–in–the–making if observed in a core sample. About $0.4T$ earlier,
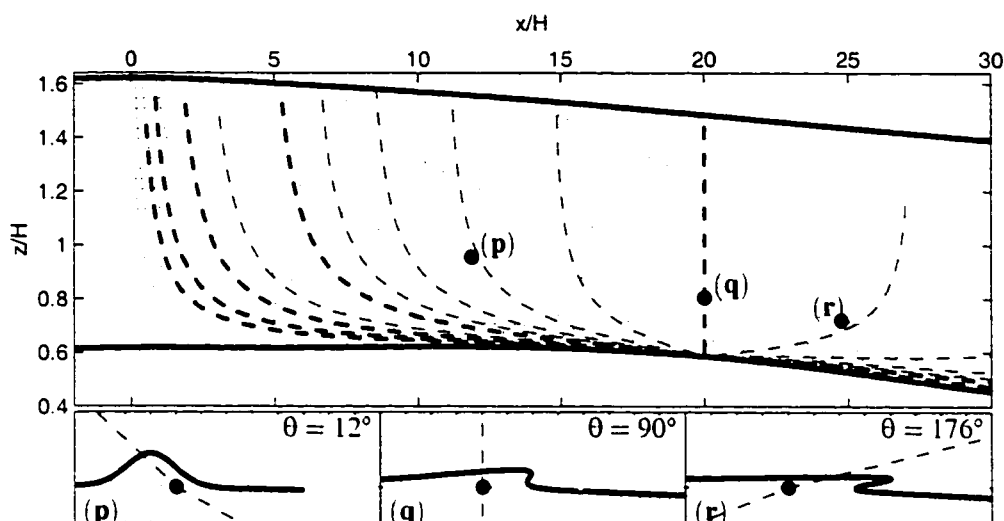
Figure 3.2: Precores (*dashed*) for a core at $20H$ (*vertical line*). The heavier lines are at $1T$ intervals. Selected particle paths are drawn as dotted lines. The three lower panels illustrate the change in shape of a disturbance at three points, (p), (q), and (r), along a particle path. The leading edge of the fold at each point is aligned with the corresponding pr ·core.

this structure would have been a symmetric open fold at point (p), with a leading edge angle of $12°$. This is the same slope as the precore at (p). The precores show the orientation at each point along a flowpath of a segment that will be vertical at this core. A segment that is steeper than the precore will rotate past vertical before it reaches the core, while a gentler segment will not reach vertical.

Here we define the angle θ of a segment relative to horizontal upstream. We use the term *leading edge* to refer to the portion of a fold that rotates through vertical when it is deformed into an order–disrupting Z fold, as illustrated in the (p), (q), and (r) sequence. If a layer disturbance was a trough instead, the overturnable edge would 'trail', but we still call it the leading edge.

One way to evaluate whether a disturbance in the stratigraphy could disrupt the order of layers further downstream would be to superimpose that disturbance on a plot of the precores. Any portion of the disturbance that is steeper than the precore at that point will rotate past vertical by the time it is carried to the core location.

Consider a divide that is at $5H$ long enough to develop a mature divide Raymond Bump, and then moves rapidly to $0H$. The original divide stratigraphy is now $5H$ away from the divide, and subject
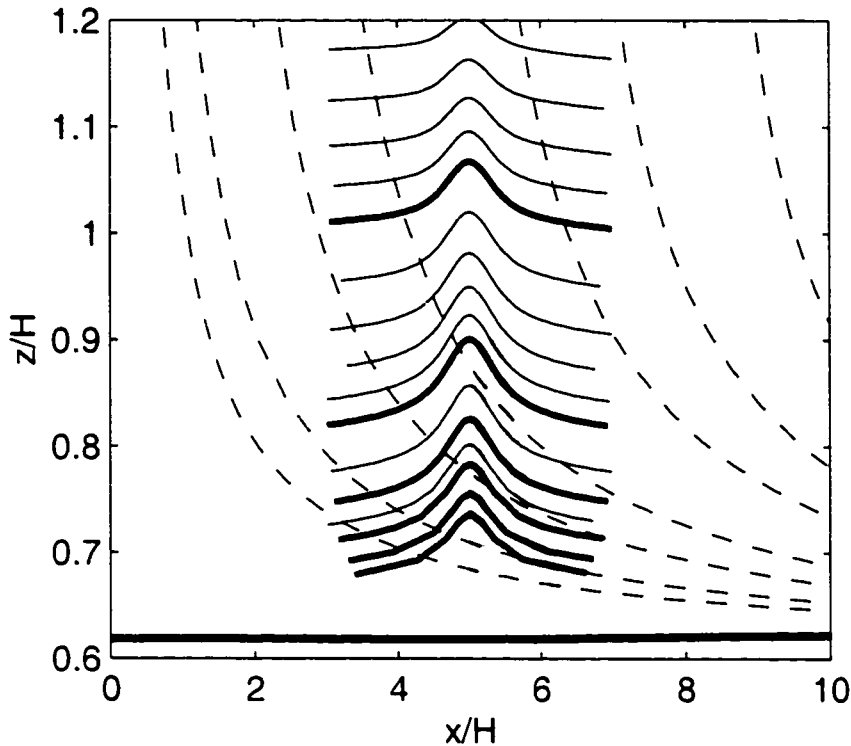
Figure 3.3: Offset (5H) surface-relative divide isochrones (*solid*) overlayed on precores (*dashed*) for a core at 20H. The grey band outlines the area in which the isochrones are steeper than the precores, indicating that they will fold by time they reach the core. This is a portion of the flowband shown in Figure 3.2 with the bed (*heavy line*) at about $z/H = 0.6$.

to a much different strain rate than that which formed the arching. How will the stratigraphy evolve now that it is in a flank position, and moves further downstream?

In Figure 3.3 we show a portion of the precores from Figure 3.2 together with the arched portion of the isochrones from Figure 3.1. These isochrones have been offset 5H, approximating a rapid move of the divide from 5H to 0H. The precores are based on flow when $x_{div} = 0H$. The region where the isochrones in the arch are steeper than the precores is outlined in gray. These portions of the isochrones will rotate through vertical as they move downstream to the core site at 20H.

Figure 3.4 shows contours of the slope angle of the precores and isochrones in Figure 3.3. The precore angle contours are roughly horizontal, with the gentlest angles at the bottom ($\theta = 0°$). The isochrone slope contours outline the steepest sides (shoulders) of the 5H offset divide bump. As
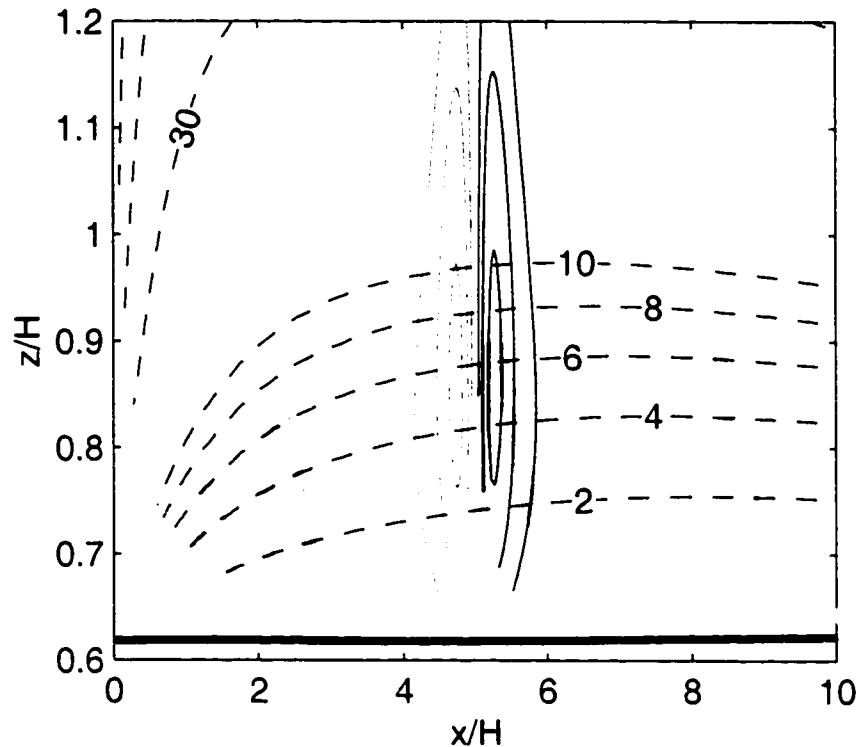
Figure 3.4: Slope angle contours of the isochrones and precores in Figure 3.3. Precore angle contours in degrees (*dashed lines*) are roughly horizontal. The isochrone angle contours (*thin lines*) are vertically aligned about *x* = 5*H*, with the leading edge angles on the right (2° intervals). Gray bands show where precore and isochrone angles match for divide offsets of 1. 2. 5. and 8*H*.

before, a gray band outlines the region where the isochrones are steeper than the precores and therefore will be overturned in the core. Along this band, the precores and the isochrones have the same slope. At the top of this overturnable region the slope angle is about 7°. We also show the overturnable region for divide offsets of 1.2, and 8*H*, for which the overturnable angle range is similar. For the smaller divide moves, the overturnable isochrones are deeper (older) while for the larger divide move, shallower isochrones can be overturned.

While details of these overturnable regions, including their shape, extent, and angle range, are sensitive to the transition from a divide to a flank velocity profile, the existence of zones in which layers can be overturned is a robust feature of sudden divide offsets.

Figure 3.5 shows the evolution of two of the arch isochrones. These were calculated by tracking
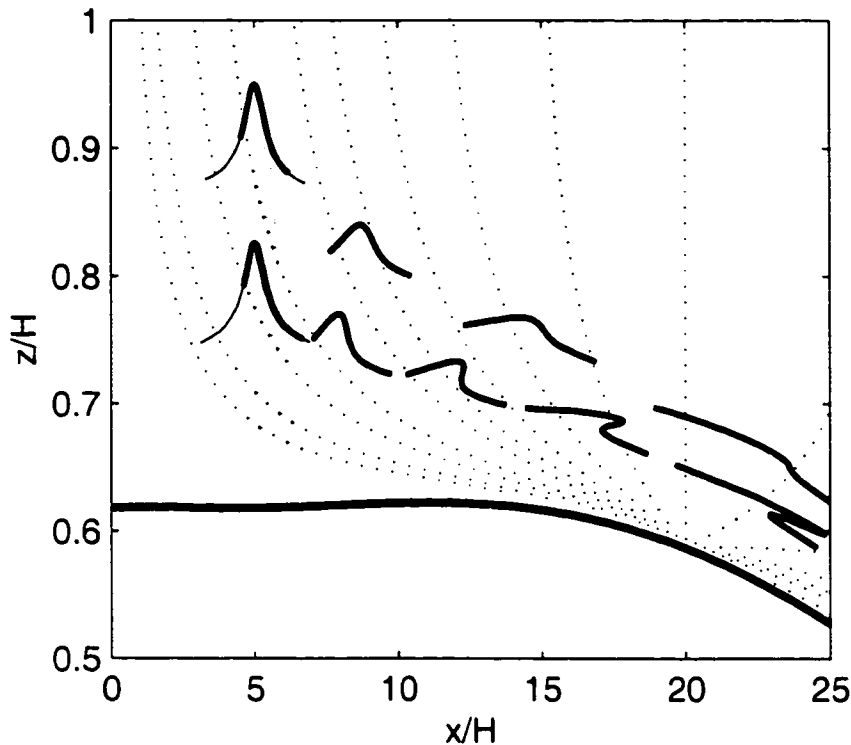
Figure 3.5: The history of two divide arch isochrones after the divide has been offset by $5H$. Ages at the time of the divide move are $1.6T$ (*upper*) and $3T$ (*lower*). The $1.6T$ isochrone is above the potential folding zone, and does not show signs of folding until well past $20H$. The $3T$ one is overturning by $12H$. The layers are plotted at $0.5T$ intervals.

a number of particles starting at the arch, using freshly offset divide flow field. The upper isochrone, with an initial age of $1.6T$ (at the time of the sudden divide offset), does not overturn by $20H$, though it could overturn further downstream. The $3T$ isochrone is well within the overturning zone, and its leading edge becomes vertical by $12H$.

3.4 Folding with Gradual Divide Movement

Overlaying precores and divide isochrones identifies the portions of the stratigraphic layers that can overturn if the divide moves, but it does not indicate how fast the divide movement must be. This technique simulates essentially instantaneous motion. If the movement is slow enough, the stratigraphy should adjust to the new flow pattern without any overturning.

Whereas Nereson *et al.* (1998) and Nereson and Waddington (2001) found the shape of layers with steady divide motion, here we will include the transients associated with (a) starting from a stationary divide at time T_1, and (b) stopping the divide migration at a later time, T_2.

To look at the effect of the divide movement speed on the folding potential, we make the divide position, $x_{div}(t)$, a function of time, and redefine the surface profile, $S(x - x_{div})$, and the flux, $Q(x - x_{div})$, to be functions of the distance from the divide. Then we can calculate particle paths for an ice sheet with a changing geometry. The flux at the divide is 0, and the surface at the divide is a maximum with a zero gradient. The blending function, $\eta(x - x_{div})$ (3.3) (A.32), for the divide and flank velocity profiles is also a function of this distance from the divide.

We assume that the bed is flat ($B(x) = 0$) and that the surface assumes the simple analytical profile derived from the shallow ice approximation (Chapter 1 and (A.25)). Although the actual surface evolution may not follow this simple form exactly, we expect that any differences in the resulting flow histories have at most a small effect on the pattern of layer overturning.

Our divide movement function has the form:

$$x_{div}(t) = \begin{cases} 5H & \text{for } t < T_1 \\ 5H - V_{div}t & \text{for } T_1 < t < T_2 \\ 0H & \text{for } t > T_2 = T_1 + \Delta T \end{cases}$$

The divide arch isochrones can be generated and folded in a seamless manner by starting a set of particles at the surface between $4.75H$ and $5.25H$ at time $t = 0$. At a later time their subsequent positions define an isochrone. From $t = 0$ to $t = T_1$, the layer develops the standard Raymond Bump centered at x_{div}. At $t = T_1$ the divide position starts migrating, and at T_2 it stops. We continue to track the particles for $t > T_2$.

Figure 3.6 shows the evolution of this layer for four offset speeds, V_{div}. In all cases, the divide starts to move at $T_1 = 3T$. The shape of the divide bump at the end of the move (T_2) is highlighted. The current divide position, $x_{div}(t)$, is marked on each isochrone and under it on the bed with a 'o'. In Figure 3.6(a) the divide moves very fast (the T_1 and T_2 isochrones are indistinguishable), and the layer overturns at $x \approx 12H$, similar to the $3T$ isochrone in Figure 3.5.

In Figure 3.6(b), the divide migration speed is 50 times slower, yet the leading edge of the former Raymond Bump becomes vertical only a few H further downstream ($\approx 14H$). At this point it is also
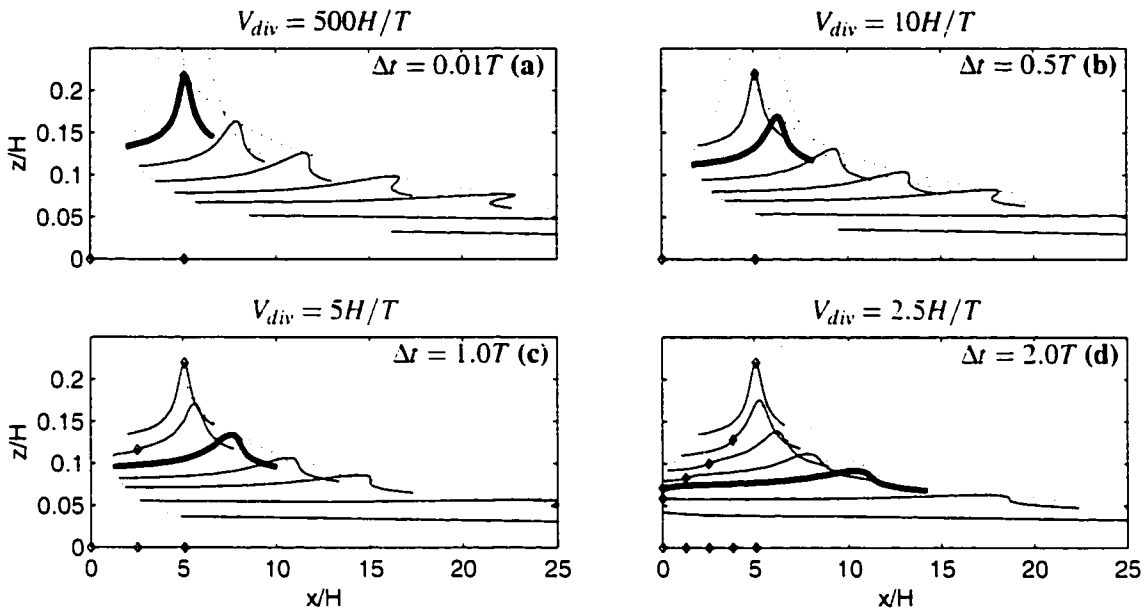
Figure 3.6: Folding of an isochrone when a divide moves to a new position at various rates. The divide is at $5H$ from $t = 0T$ to $3T$ to build a near-steady state arch. It then moves at speed V_{div} to $0H$. The isochrone at the end of this move (Δt elapsed time) is highlighted. Isochrones are plotted at 3.0, 3.5, 4.0, 4.5, 5.0, 6.0, and 8.0T. V_{div} is expressed in $H/T = b = 0.1\,\mathrm{m\,yr^{-1}}$. Divide position is marked with 'o' on the isochrones and x axis. The dotted lines are paths for three of the initial points (the two ends and the center).

0.5T older and a bit deeper than the overturning isochrone in Figure 3.6(a). Panel (c) continues this pattern. There is, in effect, a trade off between shearing the arch sooner (with a high V_{div}) and moving it deeper before shearing (with a lower V_{div}). This trade off also means that it is difficult to evaluate the effect of the offset speed without also varying the depth and age of the divide arch.

In Figure 3.6(d) the divide move is slow enough that it does not overturn until close to $20H$. The moving divide also leaves a raised 'plateau' behind it. Once it stops at $0H$ (at $5T$), it starts producing a new divide bump (the raised segment on the lowest isochrone, $8T$).

Figure 3.7 shows the effect of an even slower divide speed, $V_{div} = 1H/T$. By $6T$ the divide has moved only to $2H$. This speed is slow enough to produce a second arch even before the divide stops moving. The original arch has not overturned by $8T$ and $25H$.

In these examples the divide moves only to $0H$. If it continued to move in the same direction
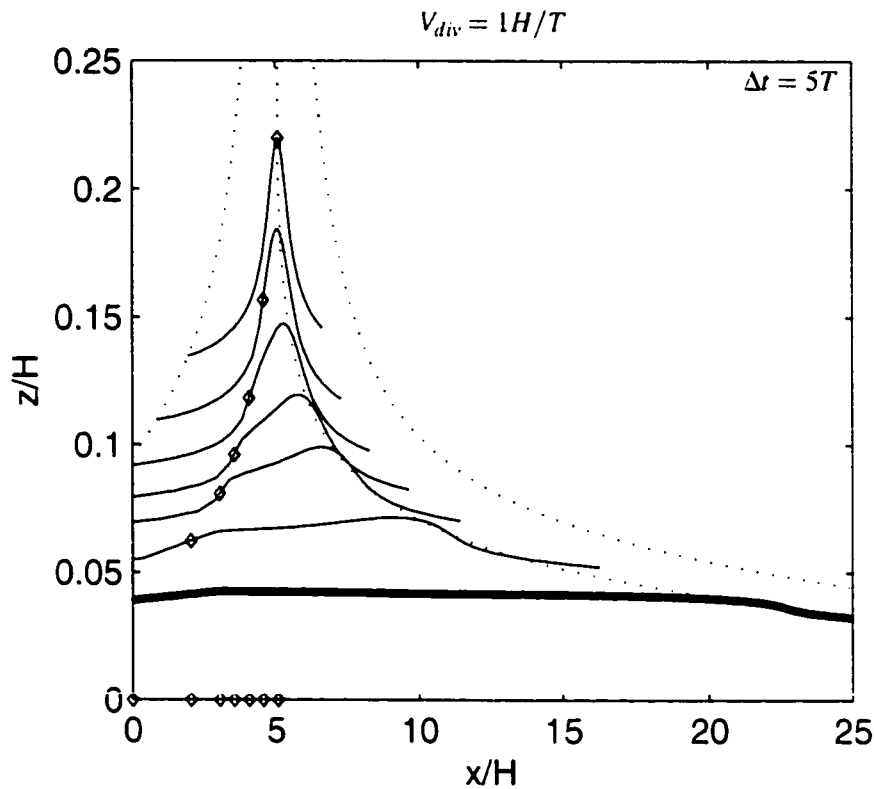
Figure 3.7: Evolution of a layer under a slowly moving divide. As in Figure 3.6 the divide movement starts at $3T$ at $x = 5H$ (the topmost isochrone), and moves at a constant velocity to the left, stopping at $x = 0H$ at $8T$ (the bottom–most isochrone (*heavy line*)). Isochrones are at 3.0, 3.5, 4.0, 4.5, 5.0, 6.0, and $8.0T$. The current divide position is marked by '◇' on the relevant isochrone and at the base.

(to the left) the velocity and shearing of the former divide bump would increase. The same qualitative picture holds, but the profiles would be shifted further downstream and become even more overturned. Conversely if the divide moves back (to the right) the velocity and shear of the bump will decrease. But unless the divide moves beyond its original position, the bump will remain on the flank, and will continue to overturn.

3.5 Folding Prospects at Various Domes

It was the discrepancy between the GRIP and GISP2 ice cores from Greenland that brought the issue of possible folding in ice sheets to prominence (Grootes *et al.*, 1993; Alley *et al.*, 1995). However

this divide does not appear to be a good candidate for the folding mechanism that we analyze in this paper, because there is evidence of too much divide movement. Radar profiles of the current summit show little sign of arching, raising questions about its current stability (Hempel and Thyssen, 1992; Hvidberg et al., 1997; Hindmarsh, 1996). The position of this divide is sensitive to the dynamics of the whole ice sheet (Anandakrishnan et al., 1994), and may, even under stable climatic conditions, be subject to an inherent topological instability Nye (1990, 1991).

Modeling of the whole Greenland ice sheet over last glacial cycle produced a bimodal pattern in the divide location, with a separation of about 70km between dominant glacial and interglacial positions (Cuffey and Marshal, 2000; Marshal and Cuffey, 2000). Movement within the 20km model grid size is less well constrained, but the glacial position appears to be more stable. While it might possible to construct a divide movement scenario that would fit with this reconstruction, and would produce folding at the current near-summit ice cores, it would be quite contrived.

The examples we have presented assume plane strain, which models the flow off of a ridge or elongated dome. With axisymmetrical flow, overturning of a divide arch may still be possible, but the critical angles will be different due to presence of lateral spreading. Since the footprint of an orphaned dome arch would be quite small (only a few H in diameter), there is little chance that the earlier divide, the current divide and the observation point (core) will line up.

The clearest examples of Raymond Bumps in radar profiles are at the West Antarctic ridges such as Siple Dome (Nereson and Raymond, 1997; Nereson et al., 1998), Roosevelt Island (Conway et al., 1999), and Fletcher Promontory (Vaughan et al., 1999). These are highly elongated domes, with ridge-like flow (plane strain) on their flanks. Their boundaries are strongly controlled by bed topography and the surrounding ice streams and ice shelves.

Fletcher Promontory has a well developed divide arch that is attributed to divide rheology. The tilt of the arch crest suggests a divide movement rate of $2b$. The Raymond Bump at Roosevelt Island is (perhaps) the best developed arching observed to date. However this arching is probably the result of the thinning of a much thicker ice sheet over the past several thousand years. Its position is well defined by bedrock platform and the surrounding ice shelf, so there is little likelihood of significant divide movement in the past or future.

The arching at Siple Dome is less mature, possibly because the current divide movement is on the order of $5b$ (Nereson and Raymond, 1997; Nereson et al., 1998). However this dome is bounded by

active and relic ice streams (ref), so there is the possibility that this divide has experienced the kind of stop–start motion that our model requires. If produced, recumbent folds are more likely to be found well down on the current flanks of the dome than near the summit. Furthermore the current geometry of Siple Dome may not be relevant when considering the possibility this folding. Our folding requires times on the order of $3T$ to develop a mature divide arch, and several more T to overturn it. With T of around 10.000 years ($H = 1000m$, and $\dot{b} = 0.1m/a$), $3 - 5T$ is right in the middle of the last glacial period. It may be that recumbent divide arches, if they exist in Antarctica, are the result of movement of divides that existed during the last glacial maximum, but are not evident now.

3.6 Conclusion

Arching in the stratigraphic layer under a divide is a potential source of recumbent folding on the flanks of an ice dome. But the arching must go through three stages: development, divide offset, and folding. The divide has to be fixed long enough for the bump to develop, with times on the order of several $T = H/\dot{b}$. Then there must be a period of relatively rapid divide movement, followed by a period in which the orphaned arch remains on the flank. The initial movement puts the arch into a new flow regime. The following stable period is needed to actually overturn it. The fold appears some distance down the flank of the new geometry. Such a fold would found under a divide only if the divide jumped back post its old position. Divide movement is a possible mechanism for producing folds in ice sheet stratigraphy, but it is not a promising explanation for folds at or near a current divide.

Chapter 4

THICKNESS CHANGES IN RECUMBENT FOLDED LAYERS

Abstract

Our previous work on kinematic folding in ice sheets focused on the overturning of steepest seg-ments of a disturbance. Here we examine the deformation of two dimensional structures with length and thickness. Portions of deformed stratigraphic layers with different initial slopes are stretched by different amounts as they rotate. Because mass is conserved, they also experience different amounts of thinning. Parts of a disturbance thin at a higher rate than the undisturbed stratigraphy, while oth-ers thin at a slower rate even when they are flattened. The deformation of an overturning segment is more complicated. It is shortened and thickened as it rotates toward vertical. Further rotation pro-duces stretching and thinning. An ice core that penetrates a fold may encounter sections that are much thinner or thicker than undisturbed stratigraphy, as well as passing through a particular layer two or more times.

4.1 Introduction

Waddington *et al.* (sub) introduced a model of folding in ice sheets in which a transient dynamic pro-cess disturbs the stratigraphy, producing gentle open folds. These can then be passively overturned by the strong shear that characterizes the large–scale flow of the ice. In Chapter 1 we elaborate on this process by calculating the finite strain along particle paths, and applying this to segments of var-ious slopes, seeking to determine how steep a disturbance must be to overturn. We focused on the *leading edge* of an upward disturbance, the steepest portion that would overturn first. However when the same finite strain is applied to a more complicated disturbance such as illustrated in Figure 4.1(a), it is apparent that more is involved in folding than just overturning simple segments. Since different layers have different initial slopes, their leading edges overturn at different times. Even when the top and bottom of a layer are similar, the trailing edge thins, while the overturning leading edge thickens.
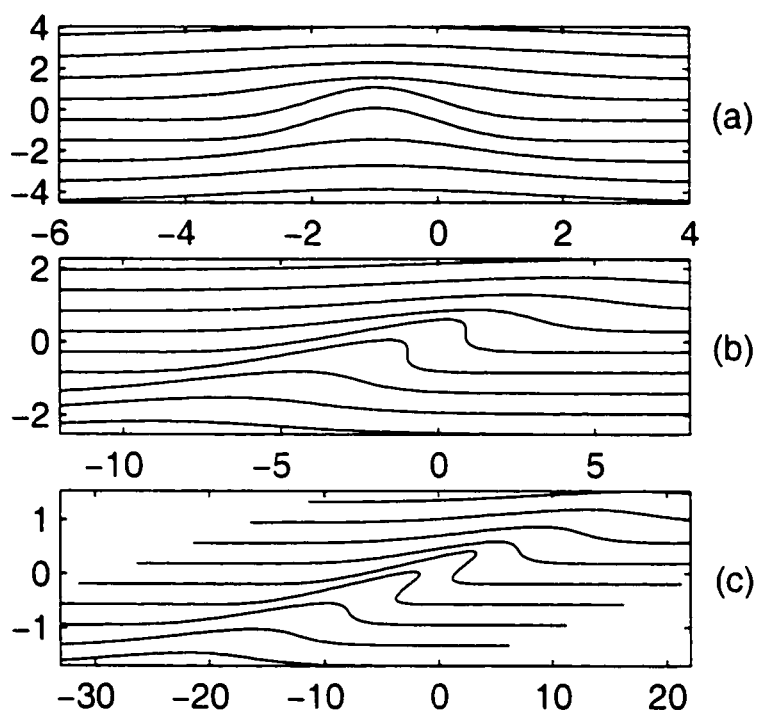
Figure 4.1: The deformation of a set of layers with variable amounts of initial disturbance (a). The area of each layer is the same. Panels (b) and (c) display the same disturbance at successive points along a particle path.

In this paper we quantify the changes in layer thickness that occur as the disturbed layers deform.

4.2 Overview

We apply a velocity model and deformation gradient tensor to a simple straight–sided disturbance. With this simple geometry we derive algebraic expressions for the thickness and width of various portions of the layer as the fold overturns. We then generalize this disturbance by imposing a variable initial layer thickness, and using smooth Gaussian curves in place of straight segments. By finding a large number of particle paths, we can also look at the thickness changes for large structures, such as the offset divide arches modeled in Chapter 3. Finally we look at the observed folded layers associated with *stripes* in the GISP2 ice core (Alley *et al.*, 1997).

4.3 The Deformation Gradient Tensor

As described in Chapter 1, we use a plane strain flowband model of an ice sheet to calculate the ice velocity and particle paths. x and z are the horizontal and vertical coordinates. The bed is flat, and the surface profile is assumed to be in steady state. By keeping track of travel times along a set of particle paths, we can derive a set of steady state isochrones, which coincide with stratigraphic layers.

In our passive strain model of folding, we assume that some unspecified process disturbs a portion of this steady state stratigraphy. We assume that the factors contributing to this displacement, such as anisotropy or rheological contrasts, are transient, and do not affect subsequent deformation of the disturbance. The disturbance is then passively deformed by the large–scale flow, with some portions overturned by shear, and other parts flattened by vertical compression.

We can track the kinematic deformation of the steady state stratigraphy and any disturbance in two ways. One way involves calculating a large set of particle paths starting at various points in the structure we are studying. We used this when studying the possible folding of offset divide arches in Chapter 3. However, if we can assume that the structure is small compared to variations in the strain field, a second powerful tool, the deformation gradient tensor, is available. This tensor assumes that the strain is homogeneous in a small neighborhood around a particular particle path. With a sequence of tensors that can be calculated at the same time as the particle path, it is possible to study the deformation of an arbitrary small structure (Chapter 1).

If x_0 is a small structure (or vector or segment) at the *reference* point, then the same structure after homogeneous strain, at the *current* point, is a linear function of its original configuration.

$$x_1 = F \cdot x_0 \tag{4.1}$$

where F is the deformation gradient tensor describing this strain. This can be written in terms of the x, z coordinate system.

$$\begin{bmatrix} x_1 \\ z_1 \end{bmatrix} = \begin{bmatrix} F_{xx}x_0 + F_{xz}z_0 \\ F_{zx}x_0 + F_{zz}z_0 \end{bmatrix} \tag{4.2}$$

If the reference and current points are the same, F is the identity tensor, with F_{xx} and F_{zz} being unity, and the other terms being zero. As the current point moves downstream, the F_{xx} and F_{xz} terms grow, while $F_{zz} \approx 1/F_{xx}$. For an ice sheet with a flat bed, the F_{zx} term is a small negative number.

Waddington *et al.* (sub) distinguish between slopes relative to horizontal (the large–scale coordinate system) and the local steady state isochrone. Their principal measure of fold susceptibility is the slope of the segment that momentarily is not rotating relative to this isochrone, m_{crit}. In Chapter 1 we glossed over this distinction because our focus was on the rotation of segments through vertical, in which case, angle differences on the order of a tenth of a degree are negligible. However, for the purposes of looking at layer thicknesses during folding, it is convenient to work with angles relative to the isochrones. With the vertical exaggeration used in Figure 4.1(c), the layers would have a notable tilt if plotted relative to horizontal rather than the local isochrone.

For this reason, in this paper we use a variant on F that operates in a reference frame that rotates with the steady state isochrone.

$$\hat{F} = R(\phi_{iso})^t \cdot F \cdot R(\theta_{iso})$$

$$(4.3)$$

where θ_{iso} is the steady state isochrone angle at the reference point. The corresponding steady state isochrone angle at the current point, ϕ_{iso}, can be derived by applying F to a segment with a θ_{iso} angle (Chapter 1) (1.22). $R(\theta)$ is the familiar rotation tensor[1].

$$R(\theta) = \begin{bmatrix} \cos\theta & \sin\theta \\ -\sin\theta & \cos\theta \end{bmatrix}$$

$$(4.4)$$

The result of applying $\hat{F}$ to a segment that is parallel to the reference isochrone will be a segment aligned with the current isochrone. The folded layers shown in Figure 4.1(b) and (c) are the result of applying a $\hat{F}$ tensor to the disturbance in panel (a). Undisturbed steady state stratigraphy would plot as horizontal lines in all three panels.

Plotting folds with respect to the isochrones rotates the true verticals and horizontals by θ_{iso}. When the axis scale is 1 : 1 and the bed is flat, this effect is barely noticeable. With strong vertical exaggeration, the true horizontal rotation becomes obvious, but the rotation of the true vertical is even less noticeable.

---

[1] The signs here are appropriate for angles defined relative to horizontal upstream, i.e. the $-x$ axis.
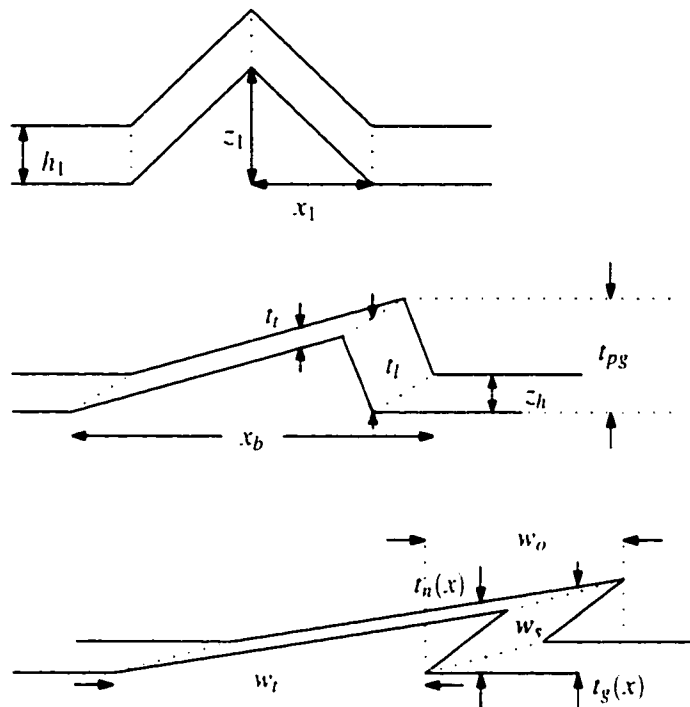
Figure 4.2: Layer geometry notation as summarized in Table 4.1. Relative values are marked with outside arrows and gray bands. Note that the band for $t_g(x)$ is continuous, while that for $t_n(x)$ is in two parts.

4.4 Folding a Parallelogram Disturbance

In Chapter 1 (Figure 1.4) we took as our prototypical disturbance a symmetric inverted 'V'. a simplification of the draping of stratigraphic layers around a transient hard lump in the ice. In this simplest form the disturbance has two straight edges. In a flow with strong shear. one of these will rotate through vertical and overturn if it is steep enough. We label this the *leading edge*. The other edge is the *trailing edge*. It just flattens. rotating toward horizontal downstream.

In this section. we give this disturbance a uniform vertical thickness as illustrated in Figure 4.3(a). Initially it is symmetric. with a rise of z_1. and a width of $2x_1$. The vertical thickness of the layer is h_1. These parameters and other measures of strained thickness and width are summarized in Figure 4.2

Table 4.1: Layer geometry notation for a parallelogram disturbance. See Figure 4.2 and Figure 4.3.

	initial state
h_1	layer thickness
z_1	disturbance rise
x_1	disturbance half width
$\mathbf{x}_l$	leading edge vector
$\mathbf{x}_t$	trailing edge vector
$\mathbf{x}_h$	initial thickness vector
	deformed state
x_l, z_l	$\hat{\mathbf{F}} \cdot \mathbf{x}_l$ components
x_t, z_t	$\hat{\mathbf{F}} \cdot \mathbf{x}_t$ components
x_h, z_h	$\hat{\mathbf{F}} \cdot \mathbf{x}_h$ components
x_b	base width. $x_t - x_l + x_h$
	thickness relative to z_h
p	peak ratio. $1 + x_1 / h_1$
t_l	leading segment
t_t	trailing segment
$t_g(x)$	gross thickness at x
$t_n(x)$	net thickness at x
t_{pg}	maximum gross thickness
t_{pn}	maximum net thickness
	width relative to x_b
w_g	total. gross width
w_t	thinned
w_o	overlapping
w_s	stem
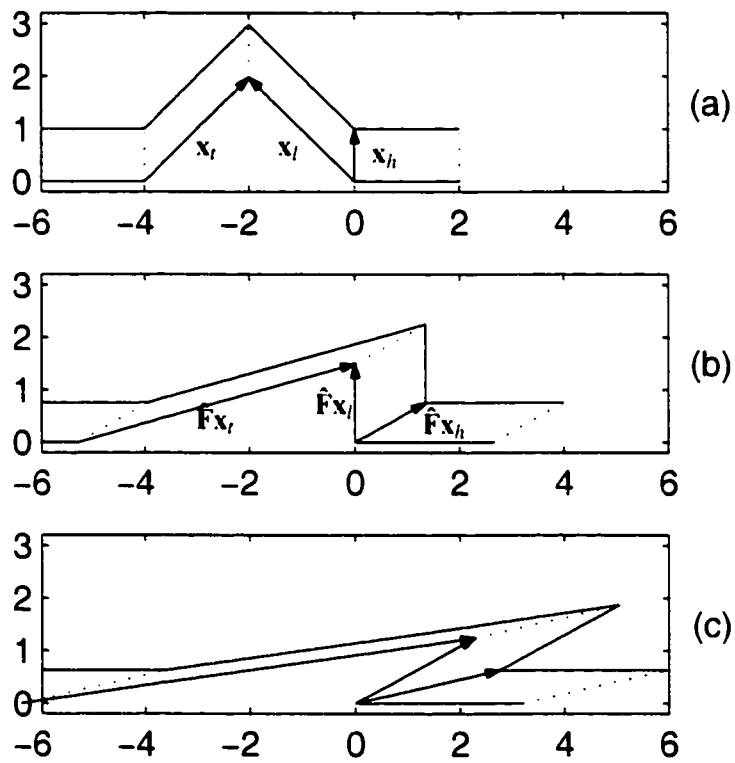
Figure 4.3: Overturning of a parallelogram disturbance. (a) Initial symmetric disturbance. (b) Leading edge becomes vertical. (c) Overturned fold.

and Table 4.1.

This disturbance can be thought of as being made up of two parallelograms, which we will refer to as the leading and trailing parallelograms. The essential geometry of these segments can be encapsulated with three vectors, x_l, x_t, and x_h. x_h is the initial thickness vector, which tracks the shearing of an initially vertical line through the layer.

$$x_h = [0, h_1] \qquad x_l = [-x_1, z_1] \qquad x_t = [x_1, z_1] \tag{4.5}$$

The corners of the leading and trailing parallelograms are at

$$\{[0,0], x_l, x_h, x_l + x_h\} \tag{4.6}$$

$$\{[0,0], x_t, x_h, x_t + x_h\} + [-2x_1, 0]. \tag{4.7}$$

When the strain represented by $\hat{F}$ is applied these parallelograms, these vectors become

$$\hat{F} \cdot x_h = [x_h, z_h] = [F_{xz}, F_{zz}] \, h_1$$

$$\hat{F} \cdot x_l = [x_l, z_l] = [-F_{xx}x_1 + F_{xz}z_1, F_{zz}z_1] \tag{4.8}$$

$$\hat{F} \cdot x_t = [x_t, z_t] = [F_{xx}x_1 + F_{xz}z_1, F_{zz}z_1]$$

Figure 4.3(b, c) show this strained fold at two successive points on the path[2]. The three $\hat{F}$ tensors are:

$$\begin{bmatrix} 1 & 0 \\ 0 & 1 \end{bmatrix} \quad \begin{bmatrix} 1.32 & 1.34 \\ 0 & 0.76 \end{bmatrix} \quad \begin{bmatrix} 1.60 & 2.77 \\ 0 & 0.63 \end{bmatrix} \tag{4.9}$$

We focus on those aspects of this fold deformation that would be most apparent in a vertical ice core, especially a core that has a small cross-section compared to the extent of the disturbance. One important property of a fold is the thickness of the deformed layer. It is most useful to view this relative to the thickness of the steady state stratigraphy at the sample point. A related parameter is the width of various portions of the fold. This too should be viewed relative to a reference undisturbed width. This width is a measure of the probability of the core encountering a particular part of the fold.

---

[2]Figure E.6 shows the finite strain Mohr circles for this overturning.
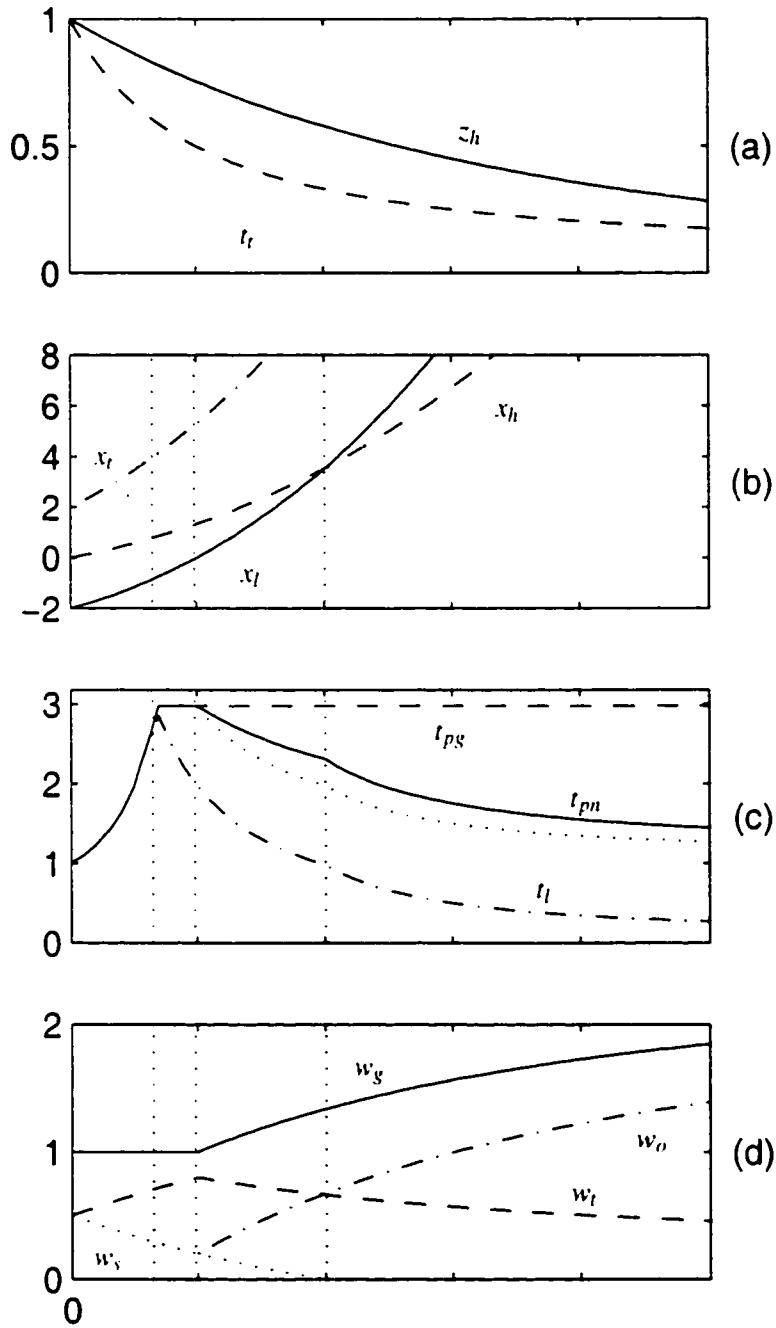
Figure 4.4: Thicknesses and widths at selected points on a disturbance through time (horizontal axis).

(a) Layer thickness. $z_h = F_z h_1$ (*solid*), and the relative trailing thickness, t_t (*dashed*).

(b) x_l (solid). x_h (dashed). and x_t (*dot dashed*). $x_l = \{-x_h, 0, x_h\}$ (*vertical grid*).

(c) Relative thicknesses. In this example the peak ratio. $p = 3$.

(d) Widths relative to x_b.

4.4.1 Fold Thickness

Before calculating the thickness of a folded layer all along its length, it is instructive to look at how the thickness at selected points on the fold varies as the folding progresses. Because our initial disturbance is defined by a few select vectors and parameters, we can focus on how these affect the evolving thickness and width.

The undisturbed layer thickness evolves as $z_h = F_{zz}h_1$. The height of the *peak* of the disturbance, which initially is given by $h_1 + z_1$, decreases at the same fractional rate as the undisturbed layer thickness, so the peak height relative to z_h remains constant.

$$p = \frac{F_{zz}(h_1 + z_1)}{z_h} = 1 + \frac{z_1}{h_1} \qquad (4.10)$$

This p differs from our other measures of thickness in that it is the (relative) distance between the highest and the lowest points of the disturbance. These two points are not vertically aligned until the leading edge steepens enough to bring the peak over undisturbed stratigraphy (when $x_l = -x_h$).

The trailing edge parallelogram has an initial base width of x_1. When strained, this becomes $F_{zz}x_1$. But the total strain of x_t parallel to the steady state isochrone is $x_t = F_{xx} x_1 + F_{xz} z_1$. Since the trailing parallelogram stretches more than the corresponding undisturbed stratigraphic layer, it must also thin at a greater rate in order to preserve area. As a result, the relative thickness of the trailing parallelogram is the ratio of these two stretches.

$$t_t = \frac{F_{xx} x_1}{x_t} \qquad (4.11)$$

It can be expressed in several other ways.

$$t_t = \frac{z_h x_t - x_h z_t}{z_h x_t} = \left(1 + \frac{F_{xz}}{F_{xx}} \tan \theta_t \right)^{-1} \qquad (4.12)$$

Appendix D.1.1 gives more details on the trailing edge calculation. z_h and t_t are plotted in Figure 4.4(a). t_t does not depend on the initial layer thickness, h_1, nor the z_1/h_1 ratio, but rather just on the strain and initial trailing edge angle, θ_t.

This calculation is contingent on $x_t > x_h$, because it assumes that the top and bottom edges of the trailing parallelogram overlap. This is true early in the strain when x_h is still nearly vertical and x_h small. It remains true for all strains if the layer is thin enough, specifically if $z_1 \geq h_1$. But if the

disturbance amplitude is smaller than the layer thickness ($z_1 < h_1$) it is possible for x_h to become larger than x_t with large F_{xz}. In this case, we would have to use a different parallelogram geometry to calculate the rotated layer thickness.

This is not a strong limitation. Unless we are examining disturbances in single annual layers, we can always focus on a thinner set of layers. In addition, folds at the scale of the finest observable stratigraphy probably will be observable in their entirety in a typical ice core, and the type of analysis that we are doing here may not be needed. This analysis should be most valuable when trying to understand folds that are larger than the ice core samples.

Thickness calculations for the leading parallelogram are more complicated because it can rotate through vertical and overlap the undisturbed segment. Details of these calculations can be found in Appendix D.1.2.

Early in the deformation, the expression for the relative thickness of the leading parallelogram is similar to that for the trailing one.

$$ t_l = \frac{z_h \, x_l - x_h \, z_l}{z_h \, x_l} = \frac{-F_{xx} \, x_1}{x_l} \tag{4.13} $$

But because $x_l < 0$, t_l is greater than unity, and increases as the leading edge gets steeper (that is, as x_l decreases), t_l reaches a maximum when $x_l = -x_h$, and decreases as the rotation proceeds further (Figure 4.4(c), *dashed line*). The thickness picture becomes more complicated at this point because the leading edge starts overlapping with portions of the undisturbed layer and the trailing parallelogram.

When we talk about the combined thickness of overlapping segments, we need to distinguish between two ways of measuring the thickness at a particular x. The *net* thickness $t_n(x)$, is the sum total of the relative thicknesses of the pieces that overlap. The *gross* thickness $t_g(x)$, is the distance (relative to z_h) between the upper- and lower-most edges of these pieces. The two measures are the same if the structure involves only one piece (such as the t_t measure), or if the overlapping pieces are vertically contiguous, but the net thickness will be less than the gross thickness if there are gaps between the overlapping pieces. The distinction between $t_n(x)$ and $t_g(x)$ is illustrated in Figure 4.2.

If a folded layer has a distinct chemical signature, the gross thickness measures the relative distance between the first and last encounters with this signature in a core, while the net thickness is the relative length of core with this signature, which may not be in one piece.

For this parallelogram fold, it is instructive to look at the maximum values (over the length of the fold) of these two measures.

$$t_{pn} = \max_x t_n(x)$$ (4.14)

$$t_{pg} = \max_x t_g(x)$$ (4.15)

t_{pn} and t_{pg} are plotted in Figure 4.4(c). Their calculation depends on the value of x_l relative to x_h. x_l and x_h are plotted in Figure 4.4(b); vertical lines mark where $x_l/x_h = -1.0$. and 1. Note that these neat boundaries are a special feature of this simple disturbance. which has parallel and straight top and bottom edges.

Until $x_l = -x_h$, the thickest portion of the fold is the leading parallelogram. so $t_{pn} = t_l$. When $x_l = -x_h$, t_{pn} reaches its maximum, p, along the vertical diagonal of the leading parallelogram. With further rotation, t_l decreases. but t_{pn} remains at the maximum. When the leading edge rotates beyond vertical ($x_l \geq 0$), gaps develop in the maximum vertical section through the fold. The gross thickness t_{pg}, remains equal to p. but t_{pn} starts to decline. Eventually the net thickness becomes $t_{pn} = 1 + t_l + t_t$. the undisturbed layer plus the two small contributions from the flattened and thinned trailing and leading parallelograms.

4.4.2   Fold Width

Another aspect of a disturbance that varies as it is deformed. is the width of the thinned and thickened portions. Initially in our example (Figure 4.3(a)), the leading and trailing parallelograms have the same base width. but by the time the leading edge becomes vertical, the thinned trailing parallelogram is much wider than the leading parallelogram (b). With further rotation, the width of the overturned leading segment increases. In (c) a randomly placed core would be roughly as likely to encounter the overlapping portion of the fold as the non-overlapping part of the trailing parallelogram.

As with the thickness. it is useful to look at fold widths relative to the width of the equivalent undisturbed parallelogram. In our example. the disturbance has an initial width $2x_1$ and height h_1. During deformation. its bottom length is $2F_{xx}x_1$. but since it has been sheared. a better measure of its width (or footprint) includes $F_{xz}h_1$. This is our *base* or reference width. x_b.

$$x_b = x_t - x_l + x_h = 2F_{xx}x_1 + F_{xz}h_1$$ (4.16)

w_t is width or footprint relative to x_b of the portion of the thinned trailing edge that does not overlap the leading edge. Before the leading edge overturns, w_t is just the footprint of the trailing parallelogram, x_t/x_b. After overturning we have to subtract the width of the overlapping leading parallelogram, $w_t = (x_t - x_l)/x_b = 2F_{xx}x_l/x_b$. w_o is the width of the overlapping region, where the trailing and leading parallelograms overlap with the undisturbed portion. Before overturning, w_o is zero. After overturning, w_o is the sum of x_l and x_h.

During the early stages of overturning, $t_n(x) = t_g(x)$ in the central portion of the overlapping region. The width of this *stem* of the fold is $w_s = (x_h - x_l)/x_b$ until the leading edge rotates so far that $x_l > x_h$. The remaining part of the overturn structure might be called the *points*.

For $x_l \leq 0$, the disturbance has the same footprint as the undisturbed layer, so the *gross width*, $w_g = 1$. For $x_l \geq 0$, $w_g = w_t + w_o$ increases as the peak of the disturbance moves beyond the footprint of the undisturbed layer. These width measures are plotted in Figure 4.4(d). See Appendix D.1.4 for details.

4.4.3   Flattening Leading Edge

In Chapter 1 we observed that a leading edge can flatten before moving into a region where the shear becomes strong enough to overturn it. While the focus of this paper is on the layer thickness as a disturbance overturns, thickness variations also occur even when the leading edge is flattening.

Appendix D.1.3 presents the same initial disturbance as in Figure 4.2, but starts it further upstream where the simple shear is weaker. Most of the deformation we show falls in the $x_l \leq -x_h$ category. During this time, the leading edge angle decreases. Thus the trailing parallelogram thins and the leading one thickens even as it flattens.

This means that kinematic strain cannot remove all evidence of a disturbance. Such strain preserves the relative vertical position. Structures are spread out, and many angles reduced, but evidence of the original disturbance (which is not kinematic) will remain in the form of layer thickness variations.
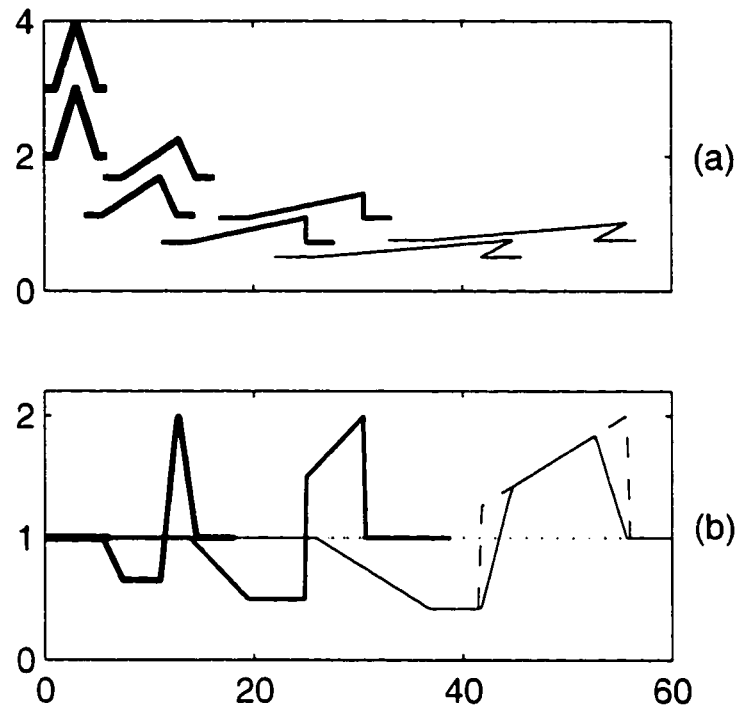
Figure 4.5: (a) Simple similar (class 2) disturbance (as in Figure 4.3) at several stages of strain (the line width varies with stage). (b) The net relative thicknesses $t_n(x)$ (*solid line*) and the gross thicknesses $t_g(x)$ (*dashed*). The horizontal scale is the same on both panels.

4.5 Layer Thickness Examples

To calculate the thickness of more complicated disturbances, we define the top and bottom surfaces of a layer as piecewise linear functions. Then we can find the thickness all along the fold at specific stages of the strain, though it is harder to track specific thickness properties as we did in the previous section.

With a pair of piecewise linear functions, the vertical thickness of an open fold at a particular x can be found by interpolating the height (z) and taking the difference. When the layer overturns the calculation is a bit more complicated, since the interpolation needs to return multiple z values for each boundary function. This is best done by dividing the function into pieces that are monotonic in x. Taking pair–wise differences of the layer crossings gives the thickness of each of the layer pieces
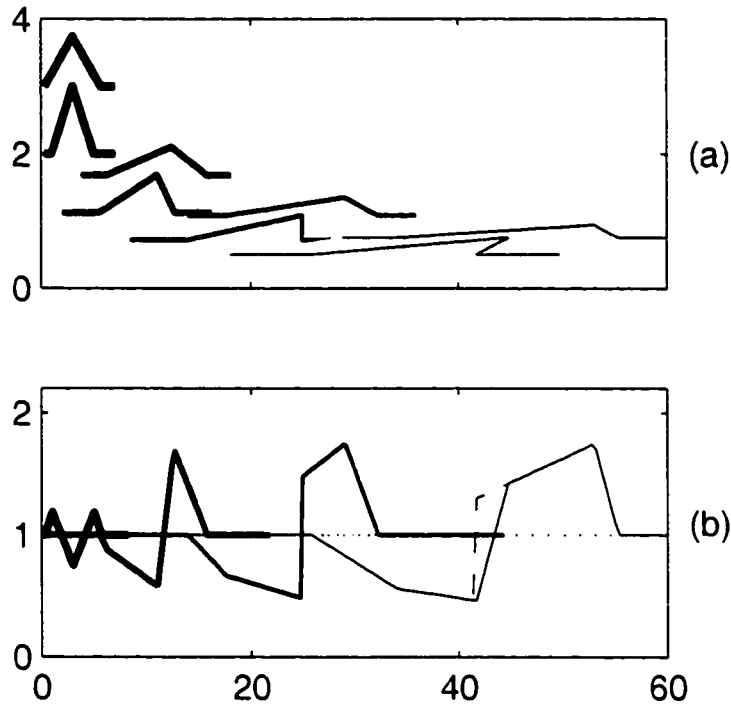
Figure 4.6: Same case as Figure 4.5 except that the initial disturbance is not similar. The layer thickness at the fold hinge is less than on the flanks. This evident in the 'M' shaped thickness profile in panel (b).

that the vertical section encounters. The sum of these differences gives the net thickness, $t_n(x)$. The difference between the largest and smallest heights gives the gross thickness, $t_g(x)$.

These two thickness measures are plotted in Figure 4.5(b) for several successive stages of folding as shown in panel (a). Until the leading edge overturns, $t_n(x) = t_g(x)$ at all points on the disturbed layer. With overturning, a difference develops between these measures in the thickened portion of the fold. The maximum gross thickness (t_{pg}) at each strained stage is the peak ratio p (4.10), which is the same for the three stages. If we had plotted an earlier strained stage, t_{pg} would be less than p (as shown in the left–most side of Figure 4.4(c) where $x_l < -x_h$). The flat minimum thickness at each stage is t_t, the thickness of the thinned trailing segment.

Assuming that the disturbed layer initially had an uniform thickness is a simplifying assumption. When we generate a multilayer disturbance such as illustrated in Figure 4.1(a), it becomes apparent

that we need layers of variable thickness to make the transition between undisturbed layers and disturbed ones. Furthermore, if a section of a layer forms a transient 'hard lump' that resists vertical compression (relative to its neighbors), it must also resist horizontal extension. This means that adjacent portions of the layer might be thinned more than normal. Conversely, we expect the layers immediately above such a lump to be thinner than the undisturbed layers, with material shifting to the flanks of the disturbance.

Figure 4.6 shows a simple inverted 'V' disturbance in which the top of the layer is displaced less than the bottom. To conserve area, the disturbance in the top surface must span a greater horizontal distance than the disturbance in the bottom surface. The leading edge parallelogram in earlier figures is now replaced by a general quadrilateral that preserves area.

The thicknesses in Figure 4.6(b) differ from those in Figure 4.5 in several ways. The initial thickness (*heaviest line on the left*) varies with *x*, being thicker on the flanks of the disturbance, and thinnest at its peak. The averaged thickness is the same as before. When strained, the trailing edge thickness decreases more gradually, with a minimum adjacent to the junction with the leading edge. The upper leading edge is gentler than the lower one, and does not overturn as soon.

One way of producing a smoothly curved version of this last disturbance is to use a Gaussian curve. By using the same normalization for the top and bottom curves, but different spreads (σ) we can produce an area–preserving disturbance with a thinner hinge and wider area, as shown in Figure 4.7. After strain, the thicknesses resemble a smoothed version of Figure 4.6(b).

4.5.1   Precores

Precores, or core relative isochrones, were introduced in Chapter 1 as a tool for predicting what disturbances would overturn by the time they were observed at a downstream core site. Figure 4.8 shows the deformation of a more complex up–and–down fold. A precore (*dashed line*) is drawn across the initial disturbance to show the orientation of material which is vertically aligned in the strained version. In the second wiggle, the precore cuts across the initial disturbance at three points, just as the vertical line does in the overturned fold.
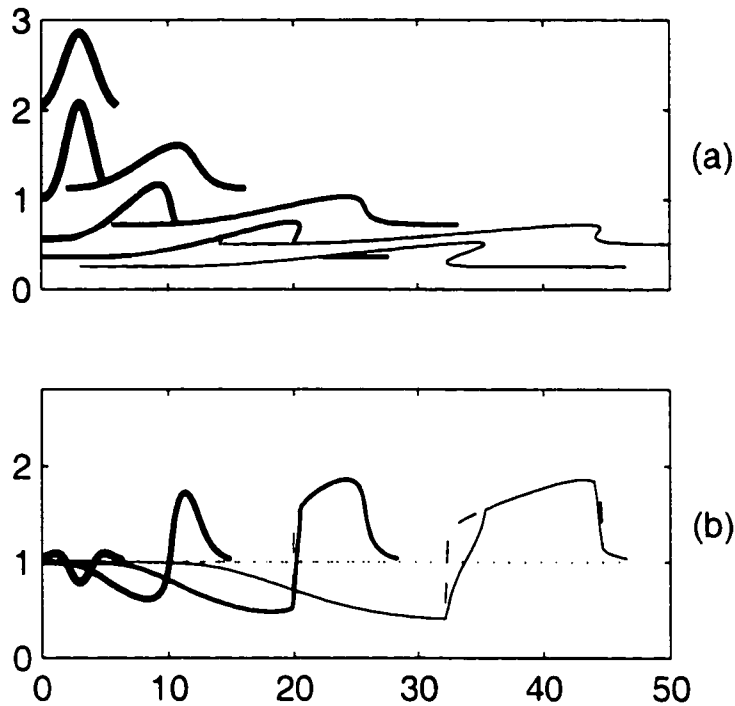
Figure 4.7: Layer thickness for a Gaussian disturbance with variable initial thickness. (a) The upper and lower edges of the disturbance have a Gaussian shape, but the upper one has a larger spread σ and smaller amplitude. The resulting layer thickness at the hinge of the disturbance is less than 1, while the thickness on the flanks is greater than 1. (b) The relative layer thickness at the successive stages.

4.6 Moving Divide Layers

In Chapter 3, we studied the deformation of large-scale disturbances using a large set of particle paths, as opposed to assuming that the disturbance is small compared to the scale of variations in the strain field. In Figure 4.9 we extend this analysis by tracking a pair of (non-steady state) isochrones. In panel (b) we plot the vertical distance between these two surfaces. In this case, the thickness is scaled by a constant, the maximum ice sheet thickness, rather than the evolving layer thickness remote from the fold.

The ice sheet dimensions are roughly those of Siple Dome, Antarctica, with a time scale (T) of 10.000 years. The first layer plotted on the left is approximately $3T$ old and its bounding isochrones
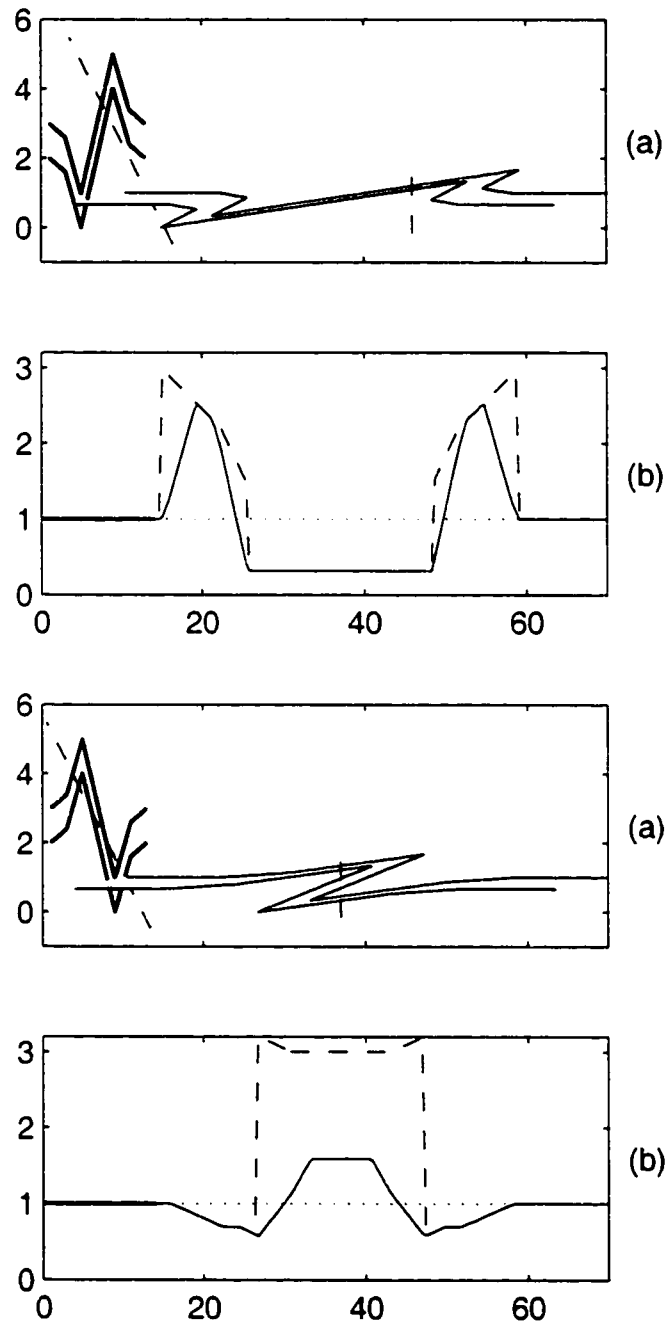
Figure 4.8: (upper) Folding of an up–and–down fold. A precore (*dashed line*) in (a) on the initial disturbance becomes vertical in the second stage.

(lower) The initial fold is just the inverse of the disturbance in the upper panel. but its thickness pattern is substantially different after overturning.
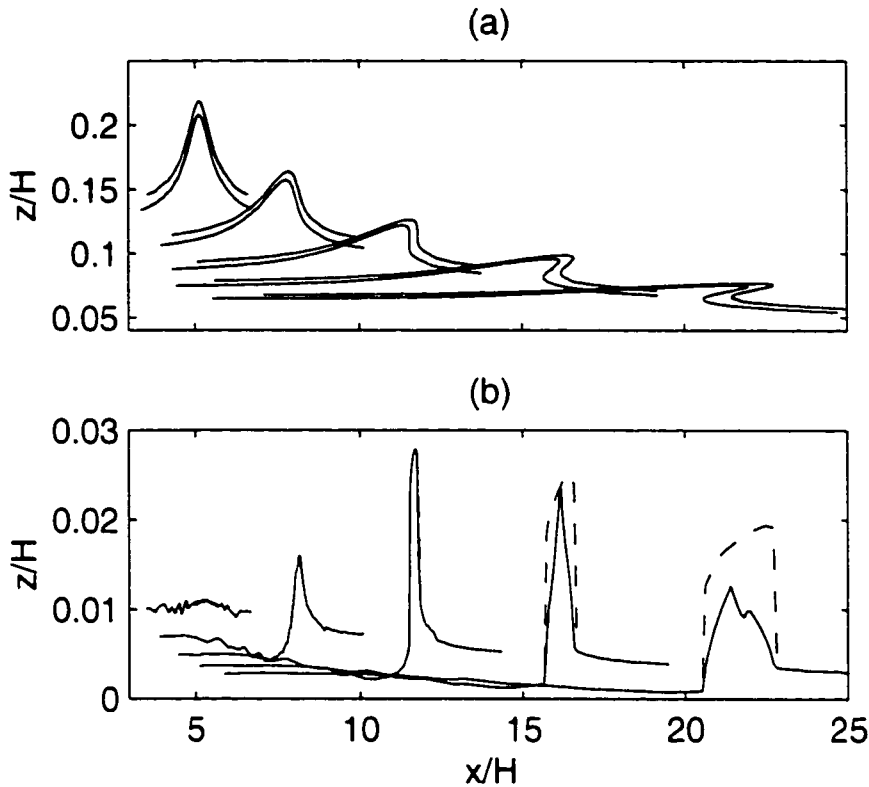
Figure 4.9: Folding of arched isochrones when the divide moves. (a) A pair of isochrones (0.2T apart) at successive time steps. (b) The net (*solid*) and gross (*dashed*) vertical distance between these isochrones. The scenario is described in Figure 3.6 in Chapter 3. The divide is at $x = 5H$ from $t = 0T$ to 3T. Then in 0.01T it moves to $x = 0H$, putting the well–developed divide arch in a flank position. The isochrones are plotted at 3.0, 3.5, 4.0, 4.5 and 5.0T. Note the vertical exaggeration.

are 0.2T apart. The layer thickness is approximately uniform at this point. Up to this time, the strain has been predominately the pure shear that characterizes the near–divide flow of an ice sheet. After the divide moves from 5H to 0H, bed–parallel simple shear dominates at the old divide location, overturning the layer. The thickness changes are similar to those already described, with a thinning of the trailing edge, and a thickening of the overturning leading edge.

After 5T, the stem has disappeared ($x_l > x_h$). The net thickness has an 'M' shaped peak, with a decrease in thickness at the middle of the fold. We do not see this feature in our other examples. Its occurrence here may be the the result of the large disturbance–amplitude to layer–thickness ratio, but we have not studied this.

4.7 Stripes

A few folds and tilted layers have been observed in the Greenland ice cores (Alley et al., 1995). In Chapter 1 we calculated the possible angle history of some of these tilted layers (Figure 1.14). Using the same flowband geometry, we can do the same for the stratigraphic layers sketched in Figure 2 in Alley et al. (1997). This is one of the few published examples of a fold in an ice core, and is associated with a unique striped pattern of grain anisotropy. These layers are shown (slightly simplified) in Figure 4.10(c). By running a particle path through the sample location ($9H$ from the divide and $0.17H$ up from the bed), we can calculate what this small fold would have looked like at points upstream (panels (a) and (b)) and will look like at a point downstream (panel (d)). The points on the particle path were chosen to approximate the orientation of the main stripe in [Figure 4] of Alley et al. (1997).

At this depth and distance from the divide, the shear strain clearly dominates, with a vorticity number of $W_k = 0.998$ (Figure 1.2). The shearing component of $\hat{F}$ is approximately ± 2 (F_{xz}) for these panels, in contrast to a horizontal extension (F_{xx}) of only 1.05. For a similar amount of shear (rotation of the stripe), Alley et al. (1997)[Figure 4] seem to assume there is more vertical compression.

While our model does not include the grain anisotropy that is crucial to the hypothesis outlined in Alley et al. (1997), it does point to a possible problem with this explanation. It may be difficult to produce the observed offset in these layers without rotating the stripe considerably more than their Figure 4 suggests.

In their hypothesis, a stripe of specially oriented grains acts as a shear plane, allowing one side to move down relative to the other.

One issue that has not been addressed, is, what happens to the ice above and below the 'dropped' section. The layers below must thin at an above–average rate, while the section above must thin at a slower rate. There must also be a compensatory thickness change above and below the portion that does not drop. In contrast to the formation of grabens at the earth's surface, there is no atmosphere or magma to flow to or from the fallen block. In other words, having a roughly vertical fault is not enough to produce a vertical displacement.

One possibility is that the displacement along the stripe occurs further upstream, where the stripe had a much gentler slope (e.g. angles around $20°$). In such an orientation, the simple shear and pure shear would work in concert to produce slip along the stripe. The offset would involve as much

(a) x=8.5 H

F=[0.94–2.60; 0.00 1.07]

(b) x=8.6 H

F=[0.96–1.83; 0.00 1.05]

(c) x=9 H

F=[1.00 0.00; 0.00 1.00]

(d) x=9.4 H

F=[1.05 1.94; 0.00 0.96]
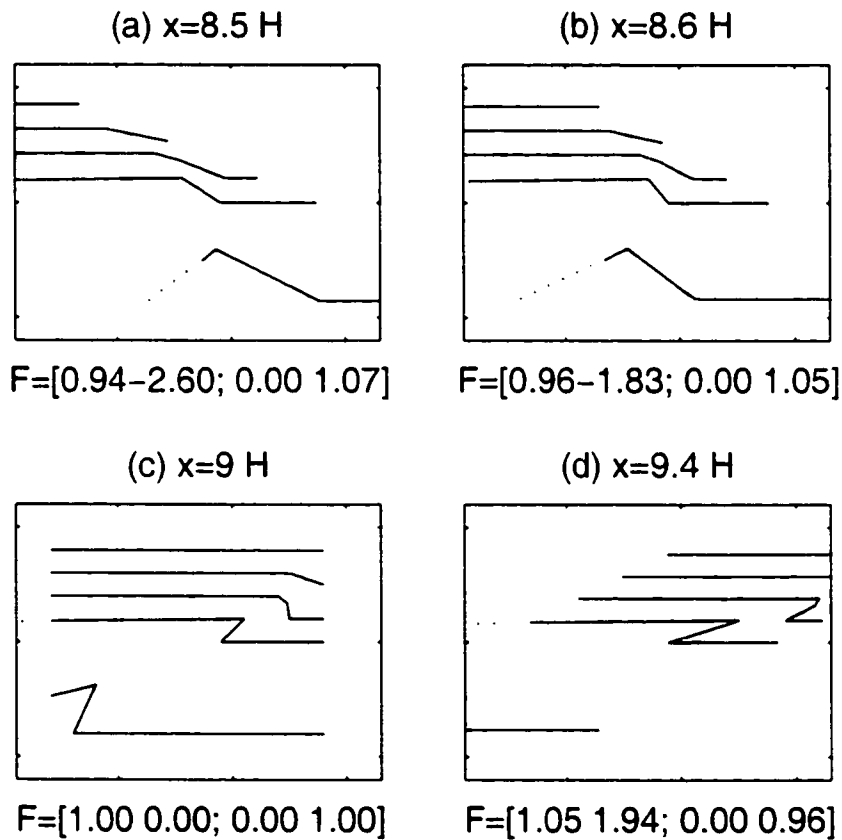
Figure 4.10: Possible kinematic folding of a *stripe* in the GISP2 core. Panel (c) shows the layers as observed in the core (Alley *et al.*, 1997)[Figure 2]. Panels (a) and (b) show the layers at two points upstream. and (d) at a point downstream. The panels are labeled with the x position. and the deformation gradient tensor $\hat{F} = [F_{xx}F_{xz}; F_{zx}F_{zz}]$ that produces the. The gray bands outline the stripes. The horizontal and vertical axis scales are equal. and the same in all panels.

or more horizontal relative movement as vertical movement. This may be easier to achieve while maintaining continuity. We might also note that Figure 4.10(a) resembles the extensional kink band case illustrated in Figure 20.28B of Ramsay and Huber (1983)[Vol.2, p. 427]. In that illustration, two stripes converge toward the bottom.

Our kinematic analysis suggests that there is significant stretch along the axis of the main stripe, particularly as it rotates beyond vertical. The length of the stripe (bounded by the two parallel gray bands) doubles from panel (b) to (c). If the grains in this stripe have their basal planes aligned with the stripe, such stretch should be easily accommodated.

There may be some uncertainty in the thickness of the thick bottom layer in Figure 4.10(c). On the left of the panel it is three times as thick as the upper layers, and on the right four times. This difference in thickness from left to right may not be real, since it is hard to track layers through the fold at the bottom left of the relevant photograph. We have projected the slight downward dip in the bottom line in panels (a) and (b), trying to see if the thickness difference is of the trailing versus leading edge type. This probably is not the case.

4.8 Conclusion

Our previous work focused on the overturning of a stratigraphic disturbance, which can alter the order of stratigraphic layers in a vertical sample. The disturbance was treated as a line, or in the simplest case, as a segment with only one property, its orientation. Real disturbances are two (or actually three) dimensional objects. Thus, when subjected to a finite strain, they also stretch and their thickness changes.

From a detailed examination of a simple disturbed layer made up of parallelograms, it is evident that some portions (which we have been calling trailing edges) are thinned as they rotate toward horizontal. On the other hand, the leading edge (which we focused on earlier) thickens (relative to undisturbed stratigraphy) regardless of whether it is flattened or steepened by the shearing flow. But it also important to note that the relative vertical position of the parts of a disturbance is not altered by the finite strain[3].

---

[3]We have not looked at how this statement must be qualified if the structure is not small relative to the scale of inhomogeneities in the strain field.

Our work suggests that, even if a disturbance is flattened rather than folded, the layer thickness in the disturbed region can still be altered. The thickness variation may even be greater with no overturning than with overturning. Variations in the initial angles and strain components are precisely what determine whether there is overturning or not.

THESIS CONCLUSION

The focus of this work has been on how steady, large–scale flow in an ice sheet can turn seemingly minor disturbances in the stratigraphy into recumbent folds that disturb the stratigraphic order. Such folds could introduce errors into paleoclimatic interpretations of ice cores, particularly if the folds are not detected.

One of the more significant conclusions of this work is that it may be difficult to detect recumbent folds in the small cross–section of a typical ice core. Because steep segments rotate rapidly through vertical in the strongly shearing flow that is characteristic an ice sheet, obviously overturning folds will be identifiable for only short distances along a particle path. Once a fold has overturned it will merge with the undisturbed stratigraphy as it is flattened and stretched. Since there are few, if any, up–down stratigraphic markers in glacial ice, distinguishing a short length of subhorizontal overturned stratigraphy from a neighboring undisturbed segment may be impossible.

One of my earliest discoveries when looking at the finite strain of disturbances, was that gentle disturbances can be flattened for a while, and then be steepened and overturned when they move deeper in the ice where the flow has a higher vorticity number. This turn around occurs at the critical wiggle slope identified by Waddington et al. (sub). But looking at the effect of this strain on layers of finite thickness shows that even during flattening, variations can develop in the vertical thickness of stratigraphic layers. This is because the large–scale kinematic strain shears one layer relative to another, but does not alter their vertical order. When a transient dynamic process displaces a portion of a stratigraphic layer vertically relative to its neighbors, the kinematics cannot reverse the displacement. It can only alter the the relative horizontal position of the pieces. These thickness variations suggest that even without overturning, we need to be cautious when making deductions from layer thicknesses in ice cores.

This relative horizontal displacement is nicely captured by the precores. At a hypothetical core, the precore is vertical, aligned with the core and with the leading edge of a fold caught in the midst of overturning. Anything that an upstream precore cuts across, will become vertical before it reaches

the core. A precore can be used as a quick-and-dirty tool for identifying overturnable disturbances, as well as a means of visualizing the sequence of disturbed layers that the particular core will sample.

I have made some progress in identifying where folding can occur in an ice sheet; however, little is known about the processes that could disturb the steady state stratigraphy in the first place. My folding model cannot produce folds directly under a divide, but neither have I shown that folding is impossible there. Disturbances that originate close to a divide are the best source for folds deep in an near–divide core. In steady state flow, the likelihood of encountering folded stratigraphy increases downstream. Perhaps the only surprising result of my probabilistic model is the conclusion that, if for some reason, the disturbance process is concentrated at a particular depth, then the overturn probability is also greatest at a deeper, but intermediate depth.

In dealing with overturn probabilities, I have focused on spatial patterns, without trying to put specific numbers on the probabilities. This probability work needs more statistical grounding, possibly by expressing the probabilities in terms of the number of disturbances per unit volume, or by tying the probabilities to observed dips and folds in cores.

I have had some success in deriving simple scale–independent measures of folding potential. The underlying tools of finite strain calculation, whether using the deformation gradient tensor, or tracking points along multiple particle paths, can be used with more realistic and case–specific models of ice flow.

My calculation of the rotational history of 20° dips observed in the GISP2 ice core puts these layers in the midst of overturning. Since at deeper levels much gentler dips could be overturned, it would be desirable to have a more detailed inventory of stratigraphic dips, and their azimuths, for this and other cores. With such information it may be possible to calculate a disturbance probability, even if obvious folds are not visible. Of course, small folds, such as those associated with anisotropic stripes, deserve further analysis and modeling.

In this work, disturbed stratigraphic layers are only passive markers in the large–scale flow. I have assumed that any rheological inhomogeneities that could have given rise to the disturbance in the first place have disappeared, or at least, are not significant when simple shear dominates the deformation. The closest I have come to modeling the transition from the dynamic disturbance phase of folding to the kinematic overturning phase, is my work on orphaned Raymond Bumps. Even in this case, the processes that control the critical divide movement are external to the model. Overall

my work has focused on the second stage of a two part model of folding. I have assumed that there are processes that are capable of disturbing the stratigraphy enough for the large–scale flow to act on it. An important goal of future work will be to explore the initial dynamic processes that disturb layers. One way that my work will contribute to the development of disturbance models is to give an idea of how big these disturbances must be. Ultimately I expect the sharp distinction between dynamics and kinematics will be blurred.

BIBLIOGRAPHY

Alley, R. B., Gow, A. J., Johnsen, S. J., Kipfstuhl, J., Meese, D. A., and Thorsteinsson, T. (1995). Comparison of deep ice cores. *Nature*, 373, 393–394.

Alley, R. B., Gow, A. J., Meese, D., Fitzpatrick, J. J., Waddington, E. D., and Bolzan, J. (1997). Grain–scale processes, folding and stratigraphic disturbance in the GISP2 ice core. *Journal of Geophysical Research*, 102(C12), 26819–30.

Anandakrishnan, S., Alley, R. B., and Waddington, E. D. (1994). Sensitivity of the ice–divide position in Greenland to climate change. *Geophysical Research Letters*, 21(6), 441–444.

Azuma, N. and Goto-Azuma, K. (1996). An anisotropic flow law for ice–sheets and its implications. *Annals of Glaciology*, 23, 202–208.

Baylis, W., editor (1996). *Geometric (Clifford) Algebras in Physics, Mathematics and Engineering*. Birkhauser, Boston.

Bobyarchick, A. R. (1986). The eigenvalues of steady flow in Mohr space. *Tectonophysics*, 122, 35–51.

Bolzan, J. F., Waddington, E. D., Alley, R. B., and Meese, D. A. (1995). Constraints on Holocene ice-thickness changes in central Greenland from the GISP2 ice-core data. *Annals of Glaciology*, 21, 33–39.

Castelnau, O., Shoji, H., Milsch, H., Mangeney, A., Duval, P., Miyamoto, A., Kawada, K., and Watanabe, O. (1998). Anisotropic behavior of GRIP ices and flow in Central Greenland. *Earth and Planetary Science Letters*, 154(1–4), 307–22.

Conway, H., Hall, B., Denton, G., Gades, A., and Waddington, E. (1999). Past and future grounding–line retreat of the West Antarctic Ice Sheet. *Science*, 286, 280–283.

Cuffey, K. M. and Marshal, S. J. (2000). Substantial contribution to sea–level rise during the last interglacial from the Greenland ice sheet. *Nature*, **404**, 591–594.

Dahl-Jensen, D., Thorsteinsson, T., Alley, R., and Shoji, H. (1997). Flow properties of the ice from the GRIP ice core – the reason for folds? *Journal of Geophysical Research*, **102**, 26831–40.

Fuchs, A. and Leuenberger, M. (1996). $\delta^{18}O$ of atmospheric oxygen measured on the GRIP Ice Core document stratigraphic disturbances in the lowest 10% of the core. *Geophysical Research Letters*, **23**(9), 1049–1052.

Grasemann, B. and Vannay, J. (1999). Flow controlled inverted metamorphism in shear zones. *Journal of Structural Geology*, **21**, 743–750.

GRIPmembers (1993). Climate instability during the last interglacial period recorded in the GRIP ice core. *Nature*, **364**, 203–207.

Grootes, P., Stuiver, M., White, J., Johnsen, S., and Jouzel, J. (1993). Comparison of oxygen isotope records form the GISP2 and GRIP Greenland ice cores. *Nature*, **366**, 552–554.

Gull, S., Doran, C., and A.N.Lasenby (1996). Dynamics. In W.E.Baylis, editor, *Geometric (Clifford) Algebras in Physics*, Boston. Birkhauser.

Hempel, L. and Thyssen, F. (1992). Deep radio–echo soundings in the vicinity of GRIP and GISP2 drill sites, Greenland. *Polarforschung*, **62**(1), 11–16. published 1993.

Hestenes, D. (1986). *New Foundations for Classical Mechanics*. Reidel, Dordrecht.

Hestenes, D. and Sobczyk, G. (1984). *Clifford Algebra to Geometric Calculus : a Unified Language for Mathematics and Physics*. D. Reidel, Dordrech.

Hindmarsh, R. C. A. (1996). Stochastic perturbation of divide position. *Annals of Glaciology*, **23**, 94–104.

Hudleston, P. J. (1976). Similar folds, recumbent folds and gravity tectonics in ice and rocks. *Journal of Geology*, **85**, 113–122.

Hudleston, P. J. and Hooke, R. L. (1980). Cumulative deformation in the Barnes Ice Cap and implications for the development of foliation. *Tectonophysics*, **66**, 127–146.

Hutter, K. (1983). *Theoretical glaciology; material science of ice and the mechanics of glaciers and ice sheets*. D. Reidel Publishing Company/Tokyo, Terra Scientific Publishing Company.

Hvidberg, C. S. (1993). *A thermo–mechanical ice flow model for the centre of large ice sheets*. Ph.D. thesis, University of Copenhagen.

Hvidberg, C. S. (1996). Steady–state thermomechanical modelling of ice flow near the centre of large ice sheets with the finite–element technique. *Annals of Glaciology*, **23**, 116–123.

Hvidberg, C. S., Dahl, J. A., and Waddington, E. D. (1997). Ice flow between the Greenland Ice Core Project and Greenland Ice Sheet Project 2 boreholes in central Greenland. *Journal of Geophysical Research*, **102**, 26851–9.

Jacobel, R. W. and Hodge, S. M. (1995). Radar internal layers from the Greenland Summit. *Geophysical Research Letters*, **22**(5), 587–590.

Jacobson, H. P. and Waddington, E. W. (1996). Finite strain and folding in ice sheets. *EOS Trans. AGU, Fall Meeting Suppl.*, **77**, S.

Lasenby, J., Lasenby, A., and C.J.L.Doran (1996). A unified language for the 21st century. *Phil. Trans. R. Soc. Lond. A*.

Lister, G. and Williams, P. (1983). The partitioning of deformation in flowing rock masses. *Tectonophysics*, **92**, 1–33.

Malvern, L. E. (1969). *Introduction to the Mechanics of a Continuous Medium*. Prentice-Hall Series in Engineering of the Physical Sciences. Prentice-Hall, Inc., Englewood Cliffs.

Marshal, S. J. and Cuffey, K. M. (2000). Peregrinations of the Greenland Ice Sheet divide in the last glacial cycle: implications for central Greenland ice cores. *Earth and Planetary Science Letters*, **179**, 73–90.

McRobie, F. and Lasenby, J. (1999). Simo-Vu Quoc rods using Clifford Algebra. *Int. J. Numer. Meth. Engng.*, **45**, 377–398.

Means, W., Hobbs, B., Lister, G., and Williams, P. (1980). Vorticity and non–coaxiality in progressive deformations. *Journal of Structural Geology*, 2(3), 371–378.

Nereson, N. and Waddington, E. (2001). Isochrones and isotherms beneath migrating ice divides. in review.

Nereson, N. A. (1998). *The flow history of Siple Dome and Ice Streams C and D, West Antarctica: Inferences from geophysical measurements and ice flow models*. Ph.D. thesis, University of Washington.

Nereson, N. A. and Raymond, C. F. (1997). Recent Migration of Siple Dome Divide Determined from 1994 Radio-Echo Sounding Measurements. *Antarctic Journal of the U.S.* (in press).

Nereson, N. A., Hindmarsh, R. C. A., and Raymond, C. F. (1997). Sensitivity of the divide position at Siple Dome to boundary forcing. *Annals of Glaciology*.

Nereson, N. A., Raymond, C. F., Waddington, E. D., and Jacobel, R. W. (1998). Migration of the Siple Dome ice divide, West Antarctica. *Journal of Glaciology*, 44, 643–652.

Nye, J. (1990). Interpreting the field evidence of past ice sheets: structural stability and genericity. *Annals of Glaciology*, 14, 208–210.

Nye, J. (1991). A topological approach to the strain–rate pattern of ice sheets. *Journal of Glaciology*, 39, 10–14.

Parzen, E. (1960). *Modern Probability Theory and Its Applications*. John Wiley & Sons, Inc.

Passchier, C. (1988). The use of Mohr circles to describe non–coaxial progressive deformation. *Tectonophysics*, 149, 323–338.

Paterson, W. S. B. (1994). *The Physics of Glaciers*. Pergamon Press, Oxford, 3rd edition.

Ramberg, H. (1975). Particle paths, displacement and progressive strain applicable to rocks. *Tectonophysics*, 28, 1–37.

Ramsay, J. G. and Huber, M. I. (1983). *The techniques of modern structural geology, vol 1: strain analysis*. Academic Press, London.

Raymond, C. F. (1983). Deformation in the vicinity of ice divides. *Journal of Glaciology*, **29**(103), 357–373.

Reeh, N. (1988). A flow line model for calculating the surface profile and the velocity, strain rate, and stress field in an ice sheet. *Journal of Glaciology*, **34**(127), 46–54.

Reeh, N. (1989). The age–depth profile in the upper part of a steady–state ice sheet. *Journal of Glaciology*, **35**(121), 406–417.

Shampine, L. F. and Reichelt, M. W. (1997). The MATLAB ODE suite. *SIAM Journal on Scientific Computing*, **18**(1), 1–22. also in MATLAB documentation.

Treagus, S. (1990). The Mohr diagram for three–dimensional reciprocal stretch vs rotation. *Journal of Structural Geology*, **12**(3), 383–395.

Vaughan, D. G., Corr, H. F. I., Doake, C. S. M., and Waddington, E. D. (1999). Distortion of isochronous layers in ice revealed by ground–penetrating radar. *Nature*, **398**, 323–326.

Vialov, S. S. (1958). Regularities of glacial shield movement and the theory of plastic viscous flow. *International Association of Hydrological Sciences*, **47**, 266–275.

Waddington, E. D., Bolzan, J. F., and Alley, R. A. (1995). The origin of folding in ice cores. *EOS*, **76**(17), S177.

Waddington, E. D., Bolzan, J. F., and Alley, R. B. (sub). Potential for stratigraphic folding near ice sheet centers. *Journal of Glaciology*. submitted.

Appendix A

FULL VELOCITY MODEL DESCRIPTION

A.1 General Model

This flowband model is essentially that developed by Vialov (1958) and expanded by Reeh (1988). The polynomial form of the velocity profile draws from Nereson et al. (1998), Nereson (1998), and Nereson and Waddington (2001).

The orthogonal coordinates are aligned with the flow of ice. x is the horizontal coordinate in the direction of flow. z is the vertical coordinate, and y is transverse to the flow. The corresponding velocity components are u, w, and v. Because of the alignment of the coordinates, $v = 0$. I also assume that the shearing components of strain in the y direction are zero (that is, there is no twisting), but leave open the possibility that $\partial_y v$ is not zero.

The ice sheet is describe by several functions of horizontal position:

$B(x)$ the base

$S(x)$ the flowband surface

$Q(x)$ flux through cross–section (per unit width)

$\upsilon(x)$ flow band width (relative)

The thickness or height of the flowband is $h(x) = S - B$ (omitting the obvious dependence on x to simplify notation). These functions, in particular the surface and flux, could also vary with time, but the ice velocity field depends only on the current geometry. Later in section A.1.4 I describe a limited generalization that allows the divide position to change with time.

For the simplest model the base is flat ($B(x) = 0$). Otherwise I specify its elevation at a set of points (taken for example from radar data) and interpolate to other points. For the surface, I use either an analytical or a numerical solution to the steady state thickness equation, or interpolate it from field data. Flux can also be interpolated, though as a default, I assume that the accumulation
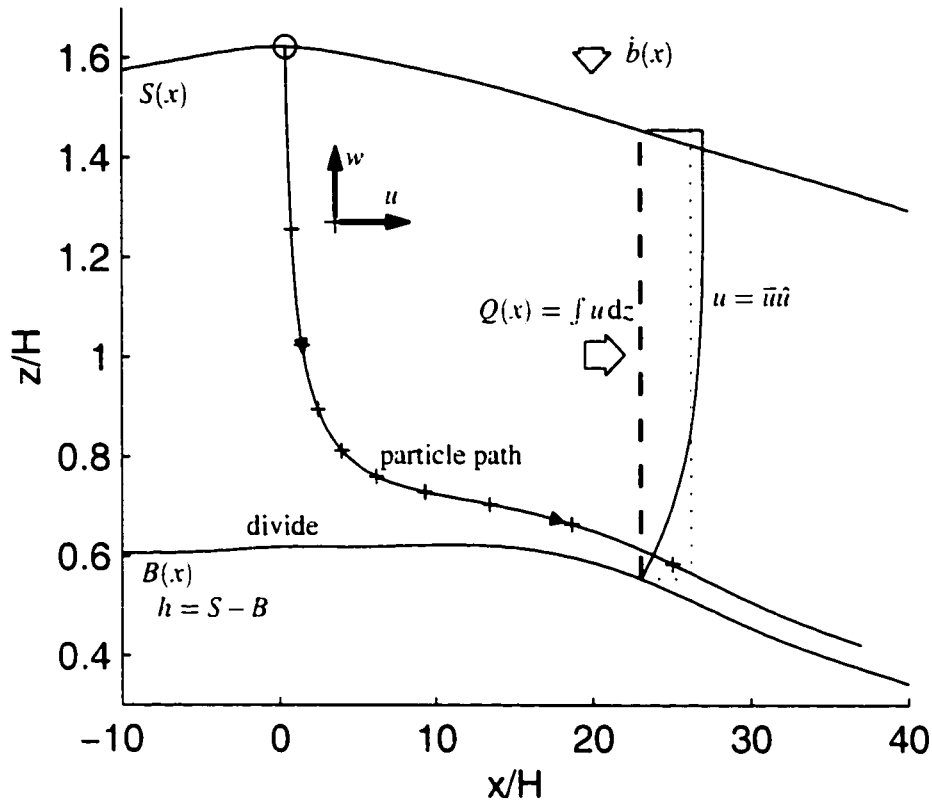
Figure A.1: Flowband geometry and notation.

rate is uniform and the flux is linear with x.

The flowband width, $\upsilon(x)$, is not an absolute measure, but rather a relative one. At any point x, I am concerned with how the width compares with that upstream and the rate of change of the width. In my default geometry this width is uniform, $\upsilon(x) = \upsilon$, modeling the plane strain flow off of a ridge or a highly elongated dome. For an axisymmetric dome, it is a linear function of x, $\upsilon(x) = \upsilon x$.

One way $\upsilon(x)$ enters the velocity calculations is through the lateral strain rate[1] .

$$\partial_y v = u(x,z)\frac{\upsilon'}{\upsilon} \tag{A.1}$$

For ridge flow this is 0, while for a dome it is u/x.

---

[1] Here I am using the prime to denote the derivative with respect to x, $\upsilon' = d\upsilon/dx$.

Under these assumptions the velocity gradient tensor has only four or five nonzero terms.

$$\mathbf{L} = \nabla \mathbf{v} = \begin{bmatrix} \partial_x u & 0 & \partial_z u \\ 0 & \partial_y v & 0 \\ \partial_x w & 0 & \partial_z w \end{bmatrix} \tag{A.2}$$

It is convenient to work with normalized forms of the vertical coordinate

$$\hat{d} = \frac{S-z}{h} \quad \text{relative depth} \tag{A.3}$$

$$\hat{z} = 1 - \hat{d} \quad \text{relative height} \tag{A.4}$$

$$\partial_z \hat{d} = -\frac{1}{h} \tag{A.5}$$

$$\partial_x \hat{d} = \frac{1}{h}\left[S'(1-\hat{d}) + B'\hat{d}\right] = \frac{1}{h}\left[S' - h'\hat{d}\right] \tag{A.6}$$

Rounding out the basic inputs is an expression, $\hat{u}(x,\hat{d})$, for the vertical profile (shape function) of the horizontal velocity. The source of this function should be a dynamic model that includes momentum conservation and ice rheology. The horizontal velocity can then be written as:

$$u(x,z) = \bar{u}(x)\,\hat{u}(x,\hat{d}) \tag{A.7}$$

where the mean (depth averaged) horizontal velocity is

$$\bar{u}(x) = \frac{Q}{h} \tag{A.8}$$

Deriving u from $\bar{u}$ (A.7) requires that the integral of $\hat{u}(x,\hat{d})$ over the normalized thickness be unity.

$$Q(x) = \int_B^S u(x,z)\,dz = \bar{u}h \int_1^0 \hat{u}(x,\hat{d})\,d\hat{d} = \bar{u}h$$

This integral of $\hat{u}$ [2] is important enough to warrant its own symbol [3].

$$\hat{w}(x,\hat{d}) = \int_{\hat{d}}^1 \hat{u}(x,\hat{d})\,d\hat{d} = \int_0^{\hat{z}} \hat{u}(x,\hat{z})\,d\hat{z} \tag{A.9}$$

---

[2] I am being a bit sloppy with all my semidefinite integrals, assuming that $\int_0^x f(x)\,dx$ is just as clear as $\int_0^x f(\xi)\,d\xi$ without introducing yet another symbol.

[3] While it is common to use symbols like ϕ for the velocity shape function, I have found it preferable to use that symbol for a segment angle, paralleling the my use of θ. My use of $\hat{u}$ and $\hat{w}$ suggests that these shape functions are normalized versions of the respective velocity components. An alternative to $\hat{w}$ might be $\hat{q}$, since it is the profile of $q(x,z)$.

$$\hat{w}(x.0) = 1 \qquad \partial_{\hat{d}}\hat{w} = -\hat{u}$$

It is also convenient to define a 'partial flux', the flux passing below the point $(x.z)$.

$$q(x.z) = \int_B^z u(x.z)\,dz = Q(x)\hat{w}(x.\hat{d}) \tag{A.10}$$

$\hat{w}(x.\hat{d})$ is, in effect, the vertical profile of the partial flux.

The vertical velocity can be derived from this by incompressibility.

$$0 = \partial_x u + \partial_y v + \partial_z w$$

$$w(x.z) = -\int_B^z (\partial_x u + \partial_y v)\,dz + w(x.B) \tag{A.11}$$

$w(x.B)$ is the vertical velocity at the base, that is, the net accumulation rate at the base. If it is negative (net melting) I would also expect that there is basal sliding, $u(x.B) > 0$. Here I assume that the ice is frozen to bed so that both of these basal velocity components are zero.

Given $u(x.z)$, the vertical velocity, $w(x.z)$, could be calculated from (A.11) using direct numerical differentiation and integration, but finding particle paths from the velocity is much faster if the integration can be done analytically. I first expand the horizontal gradient of $u(x.z)$

$$\partial_x u = \bar{u}'\,\hat{u} + \bar{u}\,\partial_x\hat{u} + \bar{u}\,\partial_{\hat{d}}\hat{u}\,\partial_x\hat{d} \tag{A.12}$$

Then substituting (A.12) and (A.1) into (A.11) gives

$$w = -h\int_{\hat{d}}^1 (\partial_y v + \partial_x u)\,d\hat{d}$$

$$= -\bar{u}h\hat{w}\frac{v'}{v} - \bar{u}'\,h\hat{w} - \bar{u}h\int_{\hat{d}}^1 \partial_x\hat{u}\,d\hat{d} - \bar{u}\int_{\hat{d}}^1 \partial_{\hat{d}}\hat{u}\,[S' - h'\hat{d}]\,d\hat{d}$$

$$= -q\frac{v'}{v} - \bar{u}'\,h\hat{w} - Q\,\partial_x\int_{\hat{d}}^1 \hat{u}\,d\hat{d} + \bar{u}S'\hat{u} - \bar{u}h'\int_1^{\hat{d}} \hat{d}\,\partial_{\hat{d}}\hat{u}\,d\hat{d}$$

$$= -q\frac{v'}{v} - \bar{u}'\,h\hat{w} - Q\partial_x\hat{w} + \bar{u}S'\hat{u} - \bar{u}h'(\hat{w} + \hat{d}\,\hat{u})$$

$$= -q\frac{v'}{v} - \bar{u}'\,h\hat{w} - Q\partial_x\hat{w} + u[S' - h'\hat{d}] - \bar{u}h'\hat{w} \tag{A.13}$$

This expression[4], which uses several derivatives with respect to x, can be expressed in other ways.

---

[4] I am a little bothered that I have to expand on $h\partial_x\hat{d} = [S' - h'\hat{d}]$ to solve this, while the following derivation using $q(x.z)$ does not need this expansion. But is there any other way of getting the h' term? Also this derivation is somewhat sloppy about what happens at the $\hat{d} = 1$ end of the definite integrals. Since I am assuming a frozen bed with $\hat{u}(1) = \hat{w}(1) = 0$ this does not matter in this case.

Using $Q = \bar{u}h$ and $Q' = \bar{u}'h + \bar{u}h'$ gives

$$w = -Q'\hat{w} + u\left[S'(1-\hat{d}) + B'\hat{d}\right] - Q\partial_x\hat{w} - q\frac{\upsilon'}{\upsilon} \tag{A.14}$$

The $Q'\hat{w}(x.\hat{d})$ term dominates near the divide, where the surface velocity is approximately equal to the accumulation rate.

The $uh\partial_x\hat{d} = u\left[S'(1-\hat{d}) + B'\hat{d}\right]$ term adds the effect of the surface and bed slopes. For small $\hat{d}$ the surface slope dominates, while the bed slope dominates at depth.

The $Q\partial_x\hat{w}$ term accounts for the horizontal variation in the $\hat{u}(x.\hat{d})$ profile (if any), while $q\frac{\upsilon'}{\upsilon}$ adds the effect of the flowband width variation.

The relation between the two velocity components can be derived from consideration of the partial flux along a particle path. The total flux below point $(x.z)$ in the flowband is $q(x.z)\upsilon(x)$. Along a particle path this must be preserved. This means that if I vary $(x.z)$ along $(u.w)$, this quantity will not vary. Its directional derivative in the direction of flow is zero.

$$0 = \mathbf{v} \cdot \nabla\{q(x.z)\upsilon(x)\} = (u\partial_x + w\partial_z)(\upsilon Q\hat{w})$$

$$= u\upsilon\left(Q'\hat{w} + Q\partial_x\hat{w} + Q\hat{w}\frac{\upsilon'}{\upsilon} - Q\hat{u}\partial_x\hat{d}\right) + w(\upsilon u)$$

$$0 = \left(Q'\hat{w} + Q\partial_x\hat{w} + Q\hat{w}\frac{\upsilon'}{\upsilon} - Q\hat{u}\partial_x\hat{d}\right) + w$$

$$w = -Q'\hat{w} - Q\partial_x\hat{w} - Q\hat{w}\frac{\upsilon'}{\upsilon} + Q\hat{u}\partial_x\hat{d} \tag{A.15}$$

This uses $\partial_{\hat{d}}\hat{w} = -\hat{u}$ and

$$d(q\upsilon) = (Q'\hat{w}\upsilon + Q\upsilon\partial_x\hat{w} + Q\hat{w}\upsilon')\,dx + Q\upsilon\partial_{\hat{d}}\hat{w}\left(\partial_x\hat{d}\,dx - \frac{1}{h}dz\right)$$

$$= \upsilon\left(Q'\hat{w} + Q\partial_x\hat{w} + Q\hat{w}\frac{\upsilon'}{\upsilon} - Q\hat{u}\partial_x\hat{d}\right)\,dx + \upsilon\left(Q\hat{u}\frac{1}{h}\right)dz$$

The tangent to the particle path (flow line?) satisfies $0 = -w(x.z)\,dx + u(x.z)\,dz$.

Given the prominence of the derivatives of these geometric inputs in the calculation of the vertical velocity, and even more so, the importance of the velocity derivatives in calculating the finite strain, differentiation should be as smooth and consistent as possible. Where analytical expressions for both the variable and its derivative are available, it is best to use both. If the variable is defined by

a set of points. I prefer to use a spline interpolation to calculate both its value and its derivative. Numerical derivatives based on linear interpolation are too discontinuous for my purposes, especially when calculating velocity gradients.

A.1.1 The Shallow Ice Approximation

I can specify the geometry functions, in particular the velocity profile, $\hat{u}(x, \hat{d})$ and the surface, $S(x)$, in two ways. One way is to adopt these functions from a combination of field data and a more complete dynamic flowband model (appendix A.1.4). The other is make a number of assumptions and derive simpler analytical functions.

An analytical value for $\hat{u}$ can be derived by assuming that the ice is isothermal, and using the shallow ice approximation (Hutter, 1983; Paterson, 1994) with Glen's flow law. This flow law assumes that the deviatoric stress, τ, and the strain rate, $\dot{\varepsilon}$, are related by $\dot{\varepsilon} = A\tau^n$. A is a temperature–dependent flow parameter, and $n = 3$ is the flow law exponent. Since in a typical ice sheet, the horizontal extent is much larger than the thickness, the shearing component, $\partial_z u$, is the largest term of the velocity gradient (A.2), over much of the flowband. The flow law can then be approximated by:

$$\partial_z u \approx 2\dot{\varepsilon}_{xz} \approx 2A\tau_{xz}^n = -2A(\rho g)^n S'^n h^n \hat{d}^n \tag{A.16}$$

$$\tau_{xz} = -\rho g S' h \hat{d} \qquad \text{shear stress} \tag{A.17}$$

S' is the surface gradient. Integrating this upward from the bed ($\hat{d} = 1$) gives the horizontal velocity:

$$u = -2A(\rho g)^n S'^n h^n \int_B^z \hat{d}^n \, dz$$

$$= -\tfrac{2}{n+1}A(\rho g)^n S'^n h^{n+1} \left(1 - \hat{d}^{n+1}\right) = \bar{u}\hat{u}(\hat{d})$$

$$\bar{u}(x) = -\tfrac{2}{n+2}A(\rho g)^n S'^n h^{n+1} \tag{A.18}$$

$$\hat{u}(\hat{d}) = \tfrac{n+2}{n+1}\left(1 - \hat{d}^{n+1}\right) \tag{A.19}$$

$$\hat{w}(\hat{d}) \equiv \int_{\hat{d}}^1 \hat{u}(\hat{d}) \, d\hat{d} = 1 - \tfrac{n+2}{n+1}\hat{d} + \tfrac{1}{n+1}\hat{d}^{n+2} \tag{A.20}$$

The $\tfrac{n+2}{n+1} = \tfrac{5}{4}$ scaling on $\hat{u}$ is needed so that $\hat{w}(0) = 1$. In this case $\hat{u}$ and $\hat{w}$ are functions of the normalized depth only, and $\partial_x \hat{w} = 0$.

A.1.2 Steady State

A surface profile consistent with this $\hat{u}(\hat{d})$ can be derived from the steady state expression for the flux:

$$Q(x) = -\tfrac{2}{n+2}A(\rho g)^n S'^n h^{n+2} = -C_x S'^n h^{n+2} \tag{A.21}$$

The flow parameter, C_x, could be generalized to include a depth averaged temperature dependence and slow variation in x (Reeh, 1988). The expression for $\hat{u}$ would not as simple as (A.19) in this case.

In steady state, the accumulation upstream from a point equals the flux through the flowband cross–section at this point. Allowing for variation in the flowband width, this flux is

$$Q(x) = \frac{1}{\upsilon(x)} \int_{x_{dn}}^x b(\xi)\upsilon(\xi)\,d\xi \tag{A.22}$$

x_{div} is the flowband divide where the flux is zero.

The flowband width can be combined with the flux gradient term, giving a different expression for the vertical velocity (Reeh, 1988).

$$Q' = -\frac{\upsilon'}{\upsilon^2} \int_{x_{dn}}^x \upsilon(\xi)\dot{b}(\xi)\,d\xi + \frac{1}{\upsilon}\upsilon\dot{b} = -\frac{\upsilon'}{\upsilon}Q + \dot{b}$$

$$w = -\dot{b}\hat{w} - q(x,z)\,\partial_x\hat{w} + uh\partial_x\hat{d} \tag{A.23}$$

The flux expression (A.21), can be written as a differential equation in $S(x)$.

$$S' = \left(-\frac{Q}{C_x}\right)^{1/n} \left(\frac{1}{S-B}\right)^{-(n+2)/n} \tag{A.24}$$

This can be solved numerically for a general bed geometry, flowband width, and flux (Anandakrishnan et al., 1994). Care has to be taken with the sign of flux, and the sign of $(S-B)$.

A.1.3 Steady State, Uniform Accumulation Geometry

The steady state flux (A.22) can be further simplified by assuming that the accumulation, $\dot{b}(x)$, is uniform, and the flowband width is a simple function of length, $\upsilon(x) = \upsilon x^{m-1}$. Then $Q(x) = \dot{b}x/m$. For a ridge with uniform width ($m = 1$), $Q = \dot{b}x$, while for dome, $m = 2$, υ is linear in x, and $Q = \dot{b}x/2$.

The uniform accumulation assumption requires that I specify the length or horizontal extent of the flowband, L, in order to determine the model geometry. A uniform accumulation together with

a finite length implies that the terminus is a calving front that can handle any flux. The conditions at such a terminus are not realistic, but they do not adversely affect the model a short distance inland. L could also be thought of as a virtual or effective length. If an ice sheet terminates in an ice stream (such as Siple Dome does) or a narrow ablation zone, the terminus profile would be different, but this model would still be useful from some distance inland back to the divide.

In the simple case of a flat bed and uniform accumulation, the $S(x)$ differential equation (A.24) can be solved analytically giving:

$$S(x) = H \left(1 - \left(\frac{x}{L} \right)^{\frac{n+1}{n}} \right)^{\frac{n}{2(n-1)}}$$

(A.25)

The derivation of (A.25) is:

$$Q(x) = \dot{b}x/m = -C_x S'^n S^{n+2} \qquad C_x \equiv \frac{2}{n+2} A (\rho g)^n$$

$$C_1 x^{\frac{1}{n}} = -S' S^{\frac{n-2}{n}} \qquad C_1 \equiv (\dot{b}/m C_x)^{\frac{1}{n}}$$

$$C_1 x^{\frac{1}{n}} \, dx = -S^{\frac{n-2}{n}} \, dS$$

$$\frac{C_1 n}{n+1} \left(x^{\frac{1+n}{n}} - \text{Const} \right) = -\frac{n}{2(n+1)} S^{\frac{2(1-n)}{n}}$$

$$\text{if } S(L) \equiv 0 \qquad \text{Const} = L^{\frac{1+n}{n}}$$

$$S^{\frac{2(1-n)}{n}} = 2C_1 L^{\frac{1+n}{n}} \left(1 - \left(\frac{x}{L} \right)^{\frac{1+n}{n}} \right)$$

$$S = H \left(1 - \left(\frac{x}{L} \right)^{\frac{1+n}{n}} \right)^{\frac{n}{2(1-n)}}$$

$$H^{2(1+n)} = 2^n C_1^n L^{1+n} = \frac{2^{n-1}(n+2)\dot{b} L^{1+n}}{m A (\rho g)^n}$$

The maximum thickness, $H = h(0)$, in this solution is related to the other parameters (L, $\dot{b}$, m, and A) by:

$$H = \left(\frac{2^{n-1}(n+2)\dot{b} L^{n+1}}{A(\rho g)^n m} \right)^{\frac{1}{2(n-1)}}$$

(A.26)

x scales with L, while z and S scale with H. With a typical H/L ratio of $1/50$ or smaller, the surface slope, S' (for $x < 0.5L$) is small. The time scale is set by $T = H/\dot{b}$. The velocities, u and w, scale with L/T and H/T ($= \dot{b}$), respectively.

For an axisymmetric dome, $m = 2$, and flux is half the ridge flow. By replacing the rectangular accumulation area of the ridge case with a pie shaped piece, the effective integrated upstream accumulation rate is halved. The steady state surface height is decreased by a factor of $2^{1/8}$.

A.1.4 Moving Divide Details

To explore the effect of a moving ice divide, I have extended the above velocity model by specifying the divide position as a function of time, and redefining the geometry variables

$$x_1 = x - x_{div}(t) \tag{A.27}$$

$$S(x_1) \qquad b(x_1) \qquad Q(x) = Q(x_1) = \int_0^{x_1} b(x)\,dx \tag{A.28}$$

The flowband width, if not uniform, should also be a function of x_1.

The weighting functions (A.32) for blending divide and flank velocity profiles are also a function of this distance from the divide.

The surface function (A.25), is derived assuming steady state, uniform accumulation, flat bed, isothermal, and shallow ice Glen's flow law rheology. The velocity profiles (Figure A.2) are derived from a finite element model, with polythermal ice. All of the strain rate terms are included in the effective strain rate in the FEM.

A.2 Polynomial Velocity Profiles

Another source of model geometry and velocity profiles is a more complete dynamic flow model. While such a model could itself could be used to calculate velocity gradients, particle paths, and deformation gradient tensors, a kinematic model such as I have described has been preferred when studying alternative scenarios. An example would be the study of divide movement (Nereson, 1998; Nereson et al., 1998). Potential advantages of a kinematic (or semi-dynamic) model include calculation speed, ease of varying the geometry, and smoother varying values. To some degree, these advantages are disappearing as computing speeds increase.

The bed, surface and flux data from another model or field data can be used in a model such as this in a piecewise linear form, though, because of the importance of gradients such as $S'(x)$ and $B'(x)$ I have found that a smoother interpolation such as splines is preferable. This is especially true

when calculating the velocity gradient and deformation gradient tensors which use derivatives of the velocity.

The velocity profiles, $\hat{u}(x,\hat{z})$ and $\hat{w}(x,\hat{z})$, can also be derived from another model. Whereas the shallow ice profiles, (A.19) and (A.20), assume that the ice is isothermal and that $\partial_z u$ dominates throughout, profiles taken from a finite element model can include the effect of the ice temperature and the full effective strain rate.

In the following, the d and f subscripts identify the divide and flank profiles respectively. I also use the normalized height, $\hat{z}$ (A.4), instead of the normalized depth, $\hat{d}$.

Nereson et al. (1998) (also Bolzan et al. (1995); Nereson (1998)) fitted Chebyshev polynomials, $T_n(\xi)$, to the horizontal velocity at two x points of a finite element model, one near the divide, and the other ten ice thickness down the flank. These profiles, $\hat{u}_d(\hat{z})$ and $\hat{u}_f(\hat{z})$ are plotted in Figure A.2(a). The isothermal laminar flow approximation, $\hat{u}_l(\hat{z})$ (A.19), is included for comparison. The curvature at depth is greater for $\hat{u}_f$ than for $\hat{u}_l$ because the finite element model is polythermal, with warmer, softer ice at the base. The curvature of $\hat{u}_d$ in the upper ice is greater because it takes into account the effect of pure shear in softening the ice. The corresponding vertical velocity profiles can be calculated by algebraic 'integration' of the polynomial coefficients. $\hat{w}_d(\hat{z})$ and $\hat{w}_f(\hat{z})$ are plotted in Figure A.2(b).

The velocity profiles at x are weighted sums of the divide and flank profiles.

$$\hat{u}(x,\hat{z}) = \sum_{j=d,f} \eta_j(x)\hat{u}_j(\hat{z}) \qquad (A.29)$$

$$\hat{w}(x,\hat{z}) = \sum_{j=d,f} \eta_j(x)\hat{w}_j(\hat{z}) \qquad (A.30)$$

$$\partial_x \hat{w}(x,\hat{z}) = \sum_{j=d,f} \eta'_j(x)\,\hat{w}_j(\hat{z}) \qquad (A.31)$$

The blending weights are based on the distant from the divide, $x_1 = x - x_{div}(x,t)$. Initially, working from Nereson et al. (1998), I used a weighting function that is the sum of several Gaussian curves, with σ_i and c_i parameters.

$$e_i = c_i e^{-(x_1/\sigma_i)^2}$$

$$\eta_d = \sum e_i \qquad\qquad \eta_f = 1 - \eta_d \qquad (A.32)$$

$$\eta'_d = \sum -2e_i x_1/\sigma_i^2 \qquad \eta'_f = -\eta'_d \qquad (A.33)$$
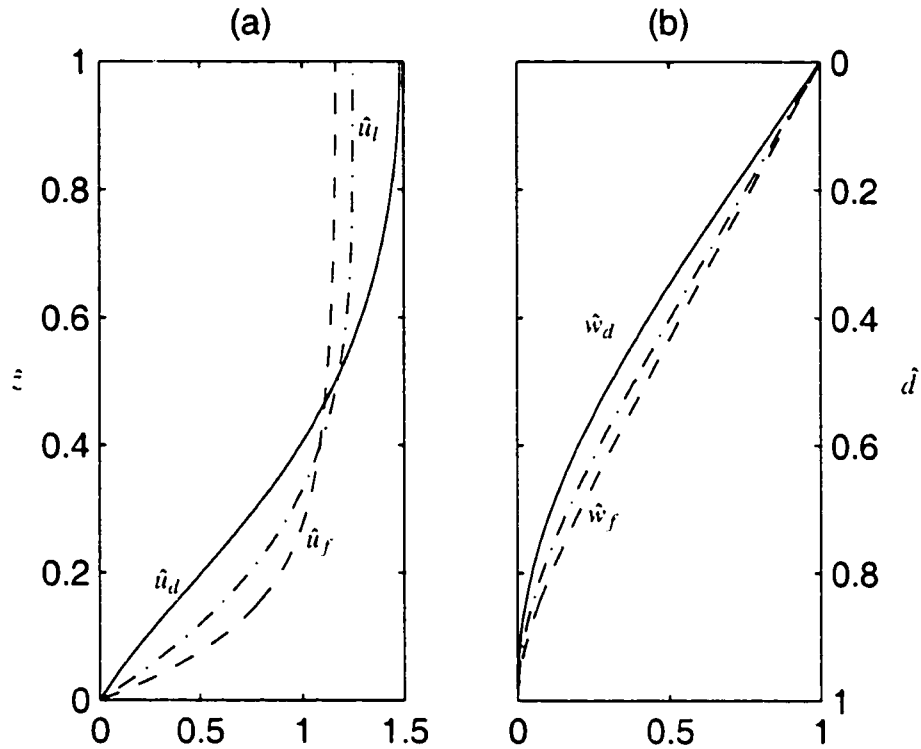
Figure A.2: Divide and flank velocity shape functions. (a) divide $\hat{u}_d$ (solid), flank $\hat{u}_f$ (dashed), isothermal shallow ice $\hat{u}_l$ (dot dashed). (b) corresponding integrals, $\hat{w}(\hat{z})$ (A.9) .

Since the velocity profile varies with x, the $\partial_x \hat{w}(x,\hat{z})$ term is nonzero, and needs to be included when evaluating $w(x,z)$ (A.13).

Currently, I am following Nereson and Waddington (2001) and using a different form of this weighting function that gives more consideration to how the weighting figures in the calculation of $w(x,z)$. Near the divide, the bed and surface slopes are negligible. If we also assume that the accumulation is uniform ($Q = bx$), the equation for $w(x,z)$,(A.14), simplifies to

$$w = -\dot{b}(\hat{w}+x\partial_x \hat{w}) = -\dot{b}\sum_{j=d,f}[\eta_j(x)+x\partial_x\eta_j(x)]\hat{w}_j(\hat{z}) \qquad (A.34)$$

This $\eta_j(x)+x\partial_x\eta_j(x)$ is an effective weighting function from $w(x,z)$, and should stay in the 0 to 1 range. With the η_d in (A.32), $\eta+x\eta' = \sum e_i(1-2x_1/\sigma_i^2)$, which has the possibility of going negative.
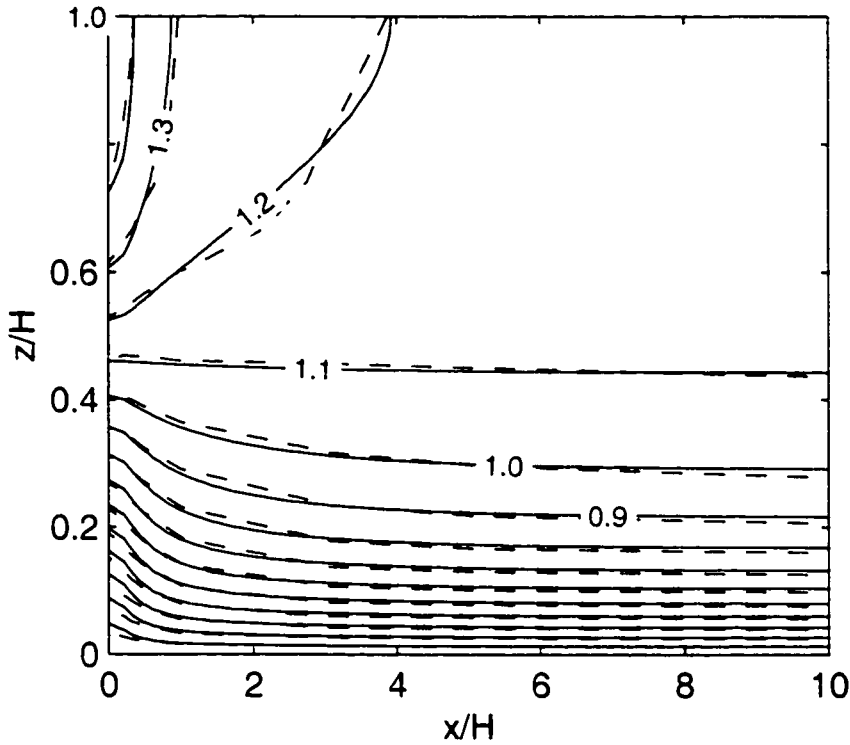
Figure A.3: $\bar{u}(x, z)$ contours: comparison of profiles used in this model (*solid*) and profiles from finite element model (*dashed*). Contours are at 0.1 intervals.

A better behaved weighting function is based on $\mathrm{erf}(x)/x$.

$$\sigma = [0.2, 0.5, 1.0]H \qquad c = [0.7, 0.2, 0.1]$$

$$x_i = \frac{x_1}{\sqrt{2}\sigma_i} \qquad \eta_d(x) = \sum_i c_i \frac{\sqrt{\pi}}{2} \frac{1}{x_i} \mathrm{erf}(x_i)$$

The effective weighting for $w(x, z)$ in this case is a reasonable looking Gaussian.

$$\eta_d(x) + x \partial_x \eta_d(x) = \sum_i c_i \exp\left(-x_i^2\right)$$

Here I use several c_i and σ_i to better control the transition from divide to flank[5].

The quality of the approximation of $\bar{u}(x, z)$ is shown in Figure A.3, where both the approximation and the underlying finite element profiles are contoured.

---

[5]Nereson and Waddington (2001) use only one set of σ.

A.2.1 Profile Refinements

I use the cosine version of the Chebyshev polynomial evaluation. Denoting the $\tilde{u}$ (either divide or flank) coefficients by a_n, and the corresponding $\tilde{w}$ ones by A_n, then

$$\xi = \frac{2\tilde{z} - \tilde{z}_l - \tilde{z}_u}{\tilde{z}_u - \tilde{z}_l} \tag{A.35}$$

$$T_n(\xi) = \cos(n\cos^{-1}\xi) \tag{A.36}$$

$$\tilde{u}(\tilde{z}) = \tfrac{1}{2}a_0 + \sum_{n=1,m} a_n T_n(\xi) \qquad \tilde{w}(\tilde{z}) = \tfrac{1}{2}A_0 + \sum_{n=1,m} A_n T_n(\xi)$$

The first few Chebyshev polynomials are

$$T_0(\xi) = 1 \qquad T_1(\xi) = \xi \qquad T_2(\xi) = 2\xi^2 - 1 \qquad T_3(\xi) = 4\xi^3 - 3\xi$$

$\tilde{z}_l$ and $\tilde{z}_u$ (A.35) are the lower and upper bounds of $\tilde{z}$, and serve to map $\tilde{z}$ on to the Chebyshev polynomial range. $[-1\ 1]$. Initially I used $\tilde{z}_l = 0$ and $\tilde{z}_u = 1$, which is the normal range for $\tilde{z}$. However, because the Chebyshev polynomials all approach their bounds (± 1) with a slope of 1 or greater, this means that $\tilde{u}(\tilde{z})$ oscillates at both bounds.

Because the surface of the ice sheet is stress free, ideally $\partial_{\tilde{z}}\tilde{u}$ should be 0 for $\tilde{z} = 1$[6]. One way to achieve this with the Chebyshev polynomials is to calculate the coefficients with $\tilde{z}_u = 2$, and reflect the profiles about $\tilde{z} = 1$ (e.g. $\tilde{u}(\tilde{z}) = \tilde{u}(2 - \tilde{z})$ for $\tilde{z} > 1$). This makes both $\tilde{u}$ and $\tilde{w}$ symmetric about $\tilde{z} = 1$. At this point, $\xi = 0$, and T_n has zero slope for odd n. This also the removes the oscillations near the surface.

Another advantage of this extended $\tilde{z}$ range is that it gives computationally reasonable velocity values for points above the flowband surface. It is easier to evaluate particle paths near the surface if the differential equation solver can smoothly project the path above the surface. Without this range extension, the above surface velocities are highly unpredictable, since the Chebyshev polynomials head off to $\pm\infty$ outside the ± 1 range.

The derivation of $\tilde{u}_d$ from finite element model data warrants some additional comments. Strictly speaking, at the divide $u(x_{div}, \tilde{z}) = 0$ because $Q(x_{div}) = \bar{u}(x_{div}) = 0$. This would be true if the finite element model had a symmetry boundary at the divide. However, if the model spans the divide, it is likely that the nodes nearest the divide will have small, but nonzero horizontal velocities. A profile

---

[6]this is true for the shallow ice profile. (A.19)

taken from these nodes may be quite noisy. One way around this is to average the velocity data for a couple of sets of nodes around the divide. Another option is to start with the vertical velocity profile, which should be quite close to $\hat{w}(x_{div}, z)$, and calculate $\hat{u}(x_{div}, z) = \partial_z \hat{w}$.

A.2.2 Divide Arching Explanations

A common explanation of the Raymond Bump focuses on the deep divide ice being subjected to a low deviatoric stress, and hence being stiffer, and behaving like a hard lump. But what is it stiffer than? It is stiffer than the flank ice, but it is not stiffer than the corresponding ice in the shallow ice approximation. It may be more accurate to say that the shallow ice model does not produce a divide arch because it makes the near surface ice too stiff, especially near the divide. On the other hand, the linear ice model ($n = 1$) does not produce a divide arch because it makes the deep divide ice too soft. When saying some ice is stiffer or softer, we need to be careful what we are comparing it to.

Another thing to be aware of when trying to explain the divide arch is the interaction between the velocity profiles and the steady state surface and flux assumptions. The steady state shallow ice surface $S(x)$ (A.25) has a zero slope at $x = 0$, and a zero curvature, $d^2S(x)/dx^2$. For $n = 1$, this curvature is nonzero, but for $n = 3$ it is zero. This means that the $n = 3$ divide is flat but sharp. It needs to be sharp to move the required flux away from the divide with ice that gets infinitely stiff right at the divide. I suspect, though have not proven, that a steady state profile with $n = 3$ and using the full strain rate tensor in the viscosity calculation will not be as sharp as the shallow ice version. It may even have a nonzero curvature at the divide. This may be difficult to prove if the only model that can implement this full rheology is a discrete approximation one (like finite elements).

Appendix B

CORE REFERENTIAL STUDY DETAILS

B.1 The Approximate Linearity of F_{xx} Along a Path

For our simple geometry, where $\bar{u} = bx/h$, the position $x(t)$ along a flowpath can be expressed as the exponential of an integral.

$$\dot{x} = u = \frac{bx}{h}\bar{u} \qquad \frac{x(t)}{x(0)} = \exp\left(\int_0^t \frac{b}{h}\bar{u}\,dt\right) \tag{B.1}$$

See (1.1) in section 1.2.2. This is not a simple exponential in time, since $\bar{u}$ decreases along the flow-path, making x more linear than would be expected from a simple exponential.

The F_{xx} term of F, as a function of time along a path, can be approximated by a similar exponential. Starting with the differential equation for F (1.23)

$$\dot{F}_{xx} \approx \partial_x u\, F_{xx} \qquad \partial_x u \approx \frac{b}{h}\bar{u} \tag{B.2}$$

$$F_{xx}(t) \approx \exp\left(\int_0^t \partial_x u\,dt\right) \approx \frac{x(t)}{x(0)} \tag{B.3}$$

Here we assume that $F_{zx}, \partial_x w, \partial_x \bar{u}$, and h' are small. All these hold best in the inner third of our ice sheet model.

B.2 The Determinant of F

Using (1.20) and the algebra of differential forms

$$dx\,dz = (F_{xx}\,dX + F_{xz}\,dZ)\,(F_{zx}\,dX + F_{zz}\,dZ)$$

$$= F_{xx}F_{zz}\,dX\,dZ + F_{xz}F_{zx}\,dZ\,dX$$

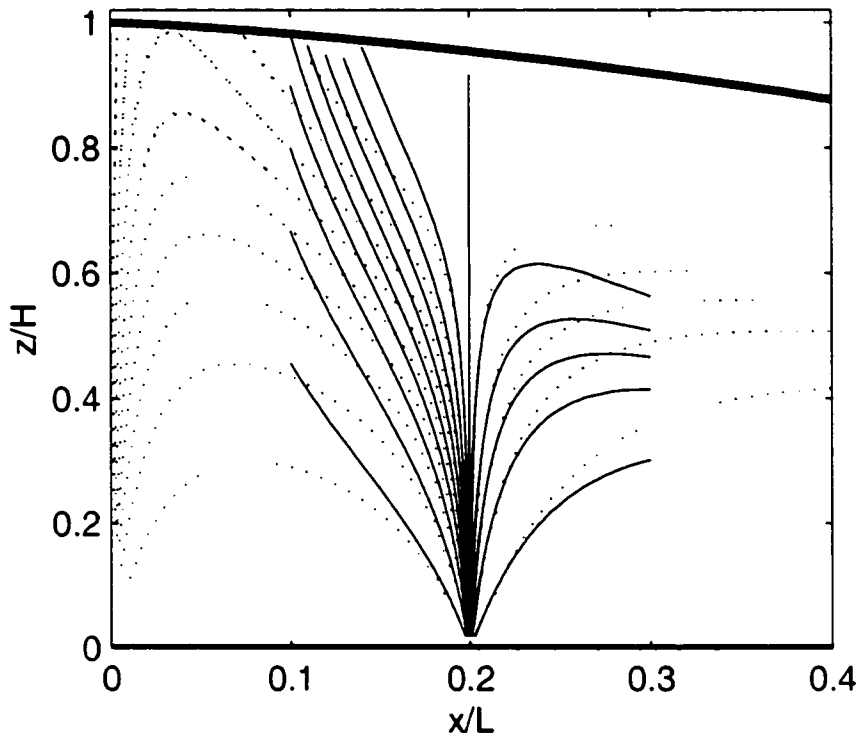$$= |F|\,dX\,dZ$$

$$\int_v dx\,dz = \int_V |F|\,dX\,dZ$$

Figure B.1: Precore slope angles (*solid*) calculated from the 'constant strain rate' approximation, using rates at the core location (10H). Precore slope contours (*dotted*) are included for comparison

This uses the basic differential form products. $dx^2 = 0$; $dz^2 = 0$; $dxdz = -dzdx$. This is for the plane strain, constant flowband width case. If the flowband width can vary, we would have to include a $dy = F_{yy}dY$ term.

B.3 Homogeneous Strain Rate Approximation

Over a short distance along a particle path, we can assume that the velocity gradient matrix is approximately constant. It is then possible to get an analytical expression for **F** as a function of time (Ramberg, 1975)[equations 33, 38]. In the neighborhood of the core, the equations are ($t = 0$ at the

core) (again using (1.23))

$$\mathbf{L}_{(r)} = \begin{bmatrix} \partial_x u & \partial_z u \\ \partial_x w & \partial_z w \end{bmatrix} \approx \begin{bmatrix} \varepsilon & \tau \\ 0 & -\varepsilon \end{bmatrix}$$

$$\mathbf{F}(t) \approx \begin{bmatrix} e^{\varepsilon t} & \dfrac{\tau}{2\varepsilon}(e^{\varepsilon t} - e^{-\varepsilon t}) \\ 0 & e^{-\varepsilon t} \end{bmatrix}$$

$$\tan\theta_f \approx \frac{F_{zz}}{-F_{xz}} \approx \frac{\varepsilon}{\tau}\frac{-2}{e^{2\varepsilon t}-1}$$

This approximation captures the rapid rotation of the precores angles near the core. Further away the variation in the velocity gradient must be taken into account. A similar approximation is used in Waddington *et al.* (sub) to estimate segment overturn times.

Appendix C

PROBABILITY MODEL DETAILS

C.1 The Separation between Trailing and Leading Edges

Figure C.1(left) plots the observation density for the fixed time case as plotted in Figure 2.4, with the addition of a similar injection density for the trailing edge ($\theta > 90°$) at $t = t_{fix}$ (the upper dashed contour). The leading edge density (lower dashed contours) splits into two observation parts, flattened and overturned. The trailing edge injection density (upper dashed contours) becomes a flattened observation density close to 180°. In this case, the flattened trailing edge and the overturned leading edge regions remain distinct, though increasingly, both are compressed into a narrow angle range near 180°.

When the same dual injection angle density is run with a Gaussian injection time (Figure C.1(right)), the distinction between overturned leading edge and flattened trailing edge densities is blurred. For any one injection time the distinction is sharp, but each injection time puts the division at a different place [1].

C.2 Conditional Probability

Figure C.2 shows how the observation density changes when it is calculated relative to the injection probability so far. The injection density is Gaussian in angle and time (as in Figure 2.8), but the variance in the time density is large, approximating a uniform density in time.
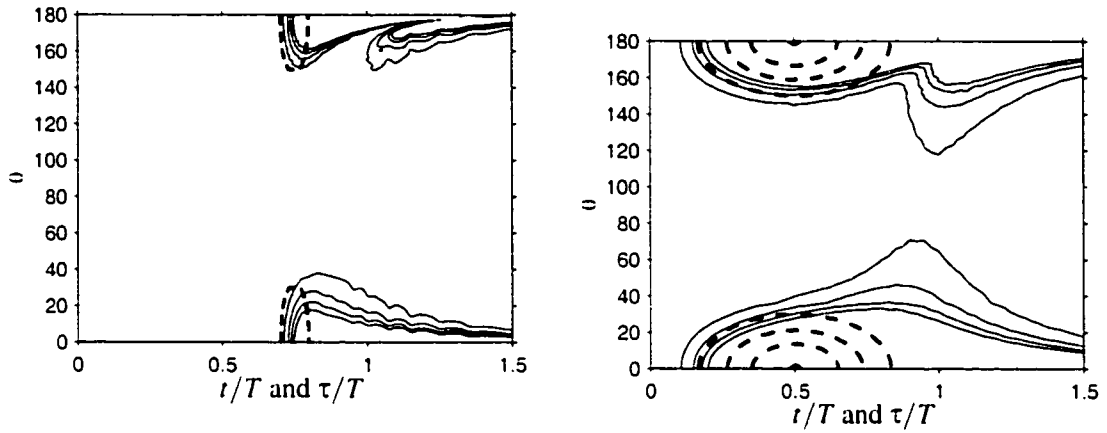
Figure C.1: Injection density contours (*dashed*) and observation density contours (*solid*) for an injection angle density that includes both leading (*lower set*) and trailing edges (*upper set*). Contours as in Figure 2.8.

(left) Injection at a fixed time, $t_{fix} = 0.75T$.

(right) Injection and observation density contours as in Figure 2.8.

C.2.1 $Q_c(\tau)$ and $\tau_o(\theta)$

Figure C.3(a) displays the conditional overturn probability, $Q_c(\tau)$ (2.18). Overlaying this are contours of $\tau_o(\theta_a)$ (*dashed*). As illustrated in Figure 2.6 and Figure 2.10 this time is the first observation point (on a path) at which a segment injected at θ_a will rotate to 90°. Conversely, θ_a is the smallest angle that will overturn by $\tau_o(\theta_a)$. It is the lowest point on the $\theta_f(t, \tau_o)$ curve.

In (2.15) we evaluated the double integral for Q, first over injection angle, and then over time. We could instead start with the injection time.

$$Q(90°, \tau) = \int_{0°}^{90°} \int_{\theta_f(t) \le \theta} p(\theta, t) \, d\theta \, dt = \int_{0°}^{90°} (P_t(t_d) - P_t(t_u)) \, d\theta \tag{C.1}$$

---

[1] It is tempting to argue that if we could get a large enough statistical sample of segment angles, we might be able to distinguish between trailing edges and overturned leading ones if the injection point were fixed. But the conditions that would have to be satisfied for this to be true are so stringent that it probably is not feasible.
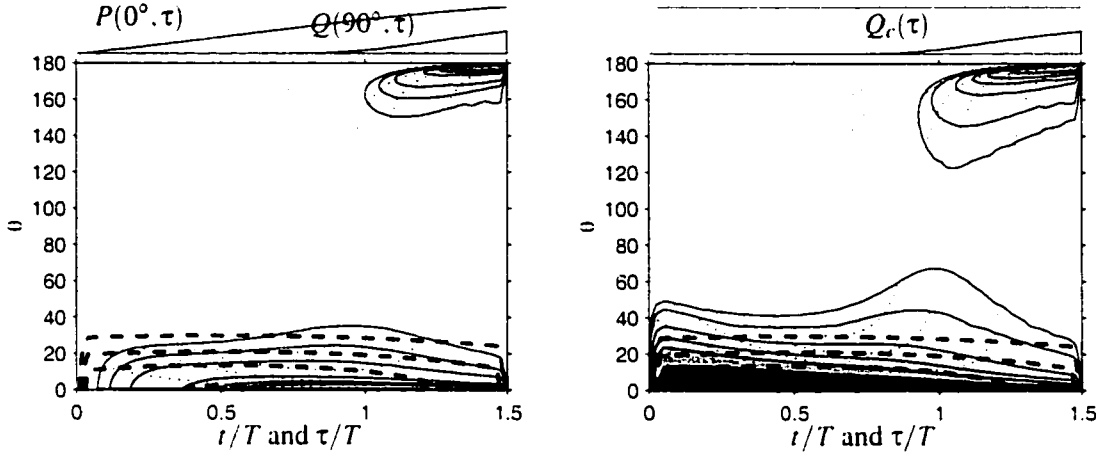
Figure C.2: Comparison of $Q(90°,\tau)$ and $Q_c(\tau)$ with injection density that is nearly uniform in time. (left) Injection and observation probabilities as in Figure 2.8, except the variance over time is large. $p(\theta,t)$ (*dashed contours*); $q(\phi,\tau)$ (*filled contours*).
(right) Same but the observation probabilities are relative to the total injection probability so far. $q(\phi,\tau)/P(0°,\tau)$ (*filled contours*).

For an uniform injection density (in time) the injection distribution becomes:

$$p(\theta,t) = g(\theta) \tag{C.2}$$

$$P_a(\theta_a,t) = P_a(\theta_a) = \int_{\theta_a}^{90} g(\theta)\,d\theta \tag{C.3}$$

$$P(\theta_a,t_a) = \int_0^{t_a} P_a(\theta_a)\,dt = t_a P_a(\theta_a,t_a) \tag{C.4}$$

$$P_a(0°) = 1 \qquad P(0°,t_a) = t_a \tag{C.5}$$

The overturn distribution is

$$Q(90°,\tau) = \int_{0°}^{90} g(\theta)\,(t_d(\theta,\tau) - t_u(\theta,\tau))\,d\theta \tag{C.6}$$

and the conditional distribution is

$$Q_c(\tau) = \int_{0°}^{90} g(\theta)\frac{t_d(\theta,\tau) - t_u(\theta,\tau)}{\tau}\,d\theta = \int_{0°}^{90} g(\theta)Q_{1h}(\theta,\tau)\,d\theta \tag{C.7}$$

where $Q_{1h}(\theta,\tau)$ is the conditional overturn probability for a fixed injection angle, θ as evaluated at the end of section 2.5.2. This overturn probability is the integral of the probability due to individual injection angles (evaluated over the range of possible injection times) weighted by the probability
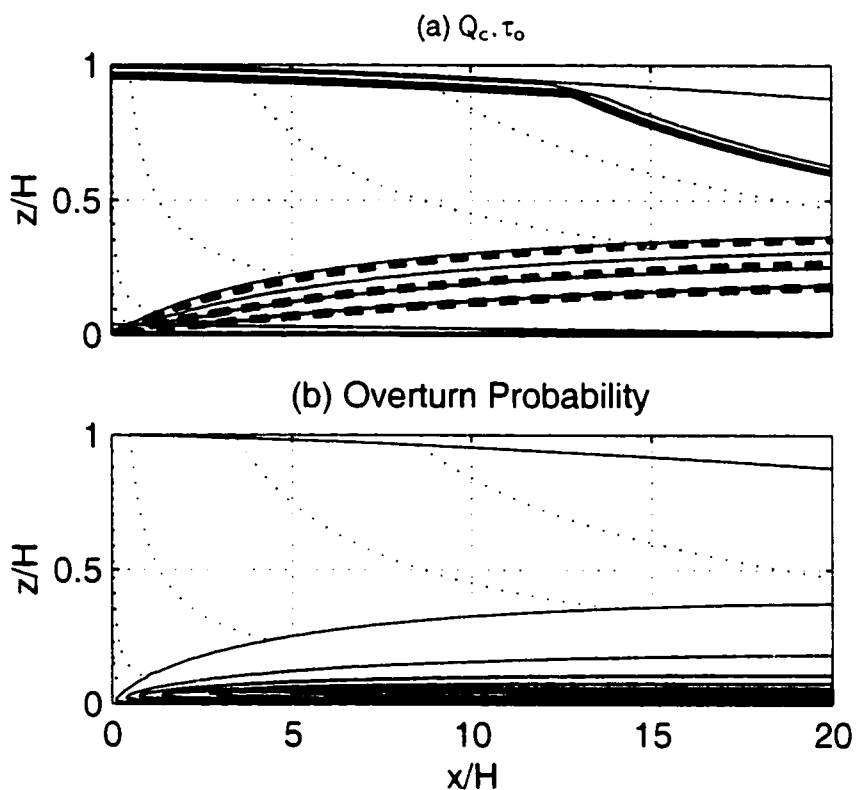
Figure C.3: Uniform injection density in time as in Figure 2.15. (a) Contours of Q_c (*shaded*); τ_o contours (*heavy dashed lines*). (b) $Q(90°)$ contours (*shaded*)

density for each angle. Since the conditional probability for a given injection angle increases abruptly under the τ_o, it is not surprising that the contours of τ_o approximately parallel those of $Q_c(\tau)$.

This analysis suggests, but does not prove, that the overturn probability pattern is dominated by the injection density over time. The details about the angle density may be less important. Evaluating the fixed injection angle case for just a few angles may be enough to approximate the effect of the whole injection density.

C.3   Unresolved Probability Issues

C.3.1   Scaling the Injection Density

In Chapter 2 we built the injection probability distribution from mathematically simple probability densities with angle and position random variables. The injection angle is either fixed or has a Gaussian distribution with a mean of $0°$. Our position random variable. the travel time along a specific path. is either fixed. uniform. or Gaussian in distribution. But functions such as these only define how the density varies over angle and time. leaving considerable room for scaling of the values.

Perhaps the easiest way to scale probability densities is to equate the total probability distribution (the integral of the density over all possible outcomes) to unity. The problem then becomes one of choosing the possible range of the random variables. As discussed in section 2.4.1 we can restrict θ to the $0°$ to $90°$ range (a leading edge). or let it span up to $180°$ (which includes both leading and trailing edges). Its probability distribution can also account for the probability that no disturbance occurs at a point.

Similarly the range of possible injection times does not have clear limits in the downstream direction. The usefulness of our ice sheet flow model decreases as we approach the terminus. so we have not tried to calculate paths and probabilities much beyond 30 ice thicknesses. Nor have we pushed the limits of the travel times for paths particularly close to the divide. The wide range in possible travel times along various particle paths complicates any attempt to define a uniform injection density across paths.

Because of this difficulty in assigning meaningful scaling factors to injection densities. we have omitted the axis ticks and contour levels when plotting both injection and observation densities and distributions. It is easier. though. to be specific about the values of the conditional probability as defined in $Q_c(\tau)$ (2.18).

C.3.2   Injections per Unit Volume

Another approach to setting probability levels is to cast them in terms that are more amenable to statistical testing. For example. we could talk about the number of independent injections or folds per unit volume. Translating between this measure of probability and what we have been using should. in theory. be simple; just shrink the 'unit' volume down until only the count of 0 or 1 injections remains

significant. But there are a number of complications that need to be considered, such as (1) how we define the unit volume, (2) what do we count as a disturbance or fold, and (3) how independent must the disturbances be.

If a core sample has multiple independent folds, they will be small relative to the sampled section (which is on the order of several centimeters) and should be readily identifiable. Such small folds would not disrupt the layer counting because their effect on layers should be obvious. Larger folds that are only partially visible in a sample are more likely to cause errors in the stratigraphic interpretation. If only the central portion of a wide overturned fold is visible in the sample, the folding might not be recognized, and the corresponding stratigraphic sequence could end up being counted multiple times. When working with the deformation gradient tensor, both large and small structures are deformed in the same way (as long as they are small relative to the velocity field variations), but the rheological inhomogeneities that could give rise to the disturbances in the first place might not be so scale invariant. The statistics for millimeter sized disturbances might not help in predicting the presence of disturbances ten centimeters long.

The cleanest interpretation of our probability mathematics is that, at most one disturbance will be injected along a path and be observed at the observation time. The injection probability densities that we have used imply this, though we might be able to construct an injection probability that would include the possibility of one injection modifying an earlier one. But if the segments under consideration are truly infinitesimal, it is reasonable to assume that the probability of the second injection occuring right on top of the first (in time and space) is very low.

Instead of counting the number of disturbances per volume, we might measure the fraction of the volume that is disturbed. This would require three (or more) random variables, the angle, position, and volume (or cross–sectional area) of a disturbance. The volume specification might involve the number of stratigraphic layers and a measure of its length. We would also need a measure of how much of the volume is overturned at an observation point. The region does not have one angle; rather there will be a transition from the undisturbed stratigraphy to the most disturbed portions near the center. As the structure is sheared, the steepest portion overturns first, while the periphery flattens. As the deformation proceeds, more and more of the volume is caught up in the fold, changing the proportion that is overturned.

Appendix D

THICKNESS CHANGES DETAILS

D.1 Leading and Trailing Parallelogram Mathematics

In the (slowly) rotating frame aligned with the steady state isochrone, $\hat{F}$ has the matrix form:

$$\begin{bmatrix} F_{xx} & F_{xz} \\ F_{zx} & F_{zz} \end{bmatrix} = \begin{bmatrix} \alpha & \beta \\ 0 & 1/\alpha \end{bmatrix} \tag{D.1}$$

The F_{zx} term is 0 because a segment aligned with the isochrone at the reference point remains aligned with the isochrone at the current point.

$$\begin{bmatrix} 0 \\ z \end{bmatrix} = \hat{F} \cdot \begin{bmatrix} 0 \\ 1 \end{bmatrix}$$

The F_{zz} term is the reciprocal of the F_{xx} term because, under plane strain, area is conserved and $|\hat{F}| = 1$.

In the reference configuration, x_h, x_l, and x_t are vectors defining a symmetric disturbance as illustrated in Figure 4.3(a). h_1 is the layer thickness, z_1 is the amplitude of the disturbance, and $2x_1$ is its width[1].

$$
\begin{array}{lll}
x_h = [0, h_1] & \theta_h = 90^\circ & |x_h| = h \\[2mm]
x_l = [-x_1, z_1] & \theta_l = \tan^{-1}\left(\dfrac{z_1}{x_1}\right) & |x_l| = \sqrt{x_1^2 + z_1^2} \\[2mm]
x_t = [x_1, z_1] & \theta_t = -\theta_l & |x_t| = |x_l|
\end{array}
\tag{D.2}
$$

When strained by $\hat{F}$ these become

$$\hat{F} \cdot x_h = [F_{xz}, F_{zz}] \, h_1$$

$$\hat{F} \cdot x_l = [-F_{xx}x_1 + F_{xz}z_1, F_{zz}z_1]$$

---

[1] Following Chapter 1 we define angles relative to $-x$ axis.

$$\hat{\mathbf{F}} \cdot \mathbf{x}_t = [F_{xx}x_1 + F_{xz}z_1, F_{zz}z_1]$$

The strained angles and lengths are

$$\phi_h = -\tan^{-1}\left(\frac{F_{zz}}{F_{xz}}\right) \qquad\qquad |\hat{\mathbf{F}} \cdot \mathbf{x}_h| = h_1 \sqrt{F_{xz}^2 + F_{zz}^2}$$

$$\phi_l = \tan^{-1}\left(\frac{F_{zz}z_1}{F_{xx}x_1 - F_{xz}z_1}\right) \qquad |\hat{\mathbf{F}} \cdot \mathbf{x}_l| = \sqrt{(-F_{xx}x_1 + F_{xz}z_1)^2 + (F_{zz}z_1)^2}$$

$$\phi_t = -\tan^{-1}\left(\frac{F_{zz}z_1}{F_{xx}x_1 + F_{xz}z_1}\right) \qquad |\hat{\mathbf{F}} \cdot \mathbf{x}_t| = \sqrt{(F_{xx}x_1 + F_{xz}z_1)^2 + (F_{zz}z_1)^2} \qquad \text{(D.3)}$$

For the special situation in Figure 4.3(b), $\hat{\mathbf{F}} \cdot \mathbf{x}_l$ is vertical, so $0 = -\alpha x_1 + \beta z_1$. This implies that $z_1 = \alpha/x_1$ and $\beta = \alpha x_1/z_1 = \alpha\cot\theta_l$.

$$\hat{\mathbf{F}} \cdot \mathbf{x}_h = [\beta, 1/\alpha]\, h_1 \qquad\qquad \phi_h = -\tan^{-1}\left(\frac{1}{\alpha\beta}\right)$$

$$\hat{\mathbf{F}} \cdot \mathbf{x}_l = [0, 1/\alpha]\, z_1 = [0, 1/\beta]\, x_1 \qquad \phi_l = 90°$$

$$\hat{\mathbf{F}} \cdot \mathbf{x}_t = [2\alpha, 1/\beta]\, x_1 \qquad\qquad \phi_t = -\tan^{-1}\left(\frac{1}{2\alpha\beta}\right) \qquad \text{(D.4)}$$

D.1.1 Trailing Parallelogram Thickness

One of the more compact ways of deriving an expression for the vertical thickness of the trailing parallelogram uses the notion of a directed area from geometric algebra (Hestenes, 1986) (also Appendix E). The directed area of the parallelogram defined by two vectors, $\mathbf{x}_1$ and $\mathbf{x}_2$ is

$$\mathbf{x}_1 \wedge \mathbf{x}_2 = (x_1\mathbf{e}_1 + z_1\mathbf{e}_2) \wedge (x_2\mathbf{e}_1 + z_2\mathbf{e}_2)$$

$$= (x_1 z_2 - z_1 x_2)\, \mathbf{e}_1\mathbf{e}_2 \qquad\qquad \text{(D.5)}$$

where the $\wedge$ (wedge) product is a generalization of the anti-commutative tensor cross product. $\mathbf{e}_1$ and $\mathbf{e}_2$ are orthonormal vectors, and $\mathbf{e}_1\mathbf{e}_2 = \mathbf{e}_1 \wedge \mathbf{e}_2$ is the unit bivector, or unit directed area.

The area of the initial trailing parallelogram defined by $\mathbf{x}_t$ and $\mathbf{x}_h$ (D.2) is

$$\mathbf{x}_t \wedge \mathbf{x}_h = (x_1 h_1)\, \mathbf{e}_1\mathbf{e}_2. \qquad\qquad \text{(D.6)}$$

After deformation the area is the same,

$$(\hat{\mathbf{F}} \cdot \mathbf{x}_t) \wedge (\hat{\mathbf{F}} \cdot \mathbf{x}_h) = (x_t z_h - z_t x_h)\, \mathbf{e}_1\mathbf{e}_2. \qquad\qquad \text{(D.7)}$$

134

If $x_t > x_h$, the upper and lower surfaces (the ones parallel to $\hat{F} \cdot x_t$) of the trailing edge overlap vertically. In this case an equivalent parallelogram can be defined by $\hat{F} \cdot x_t$ and the vertical vector $(t_t z_h)\, e_2$, where t_t is the relative vertical height. Its area is $(x_t t_t z_h)\, e_1 e_2$.

Equating the three parallelogram areas gives two expressions for t_t.

$$t_t = \frac{x_t z_h - z_t x_h}{x_t z_h} = 1 - \frac{z_t x_h}{x_t z_h} \tag{D.8}$$

$$t_t = \frac{h_1 x_1}{x_t z_h} = \frac{h_1 x_1}{x_t F_{zz} h_1} = \frac{F_{xx} x_1}{x_t} \tag{D.9}$$

In (D.9) $F_{xx} x_1$ is the stretched base of the undisturbed layer segment (with initial length x_1), and x_t is the base of the stretched trailing segment. The ratio of the two horizontal stretches is the inverse of the two vertical stretches because the area is unchanged.

The condition that $x_t > x_h$ implies that $F_{xx} x_1 > F_{zz}(h_1 - z_1)$. Early in the strain, this is satisfied because F_{xx} is close to 1 and F_{zz} close to 0. Further downstream F_{zz} can be larger than F_{xx}. However, if $h_1 \leq z_1$, this condition is satisfied regardless of how large F_{zz}/F_{xx} gets. In this detailed analysis, we assume that this is the case.

Examples with $h_1 > z_1$, suggest that the trailing segment still thins relative to the undisturbed layer, but not quite as much as given by Figure D.9.

This relative thickness can be expressed in several other ways

$$t_t = 1 - \frac{\tan \phi_t}{\tan \phi_h} = \frac{1}{z_h}\left(z_h - x_h \frac{z_t}{x_t} \right) \tag{D.10}$$

$$t_t = \left(1 + \frac{F_{xz}}{F_{xx}} \tan \theta_t \right)^{-1} \tag{D.11}$$

The last expression tells us that t_t depends on the strain (F_{xz}/F_{xx}), and the initial trailing edge angle (θ_t), but not on the layer thickness or the disturbance to thickness ratio.

D.1.2 Leading Parallelogram Thickness

The initial area for the leading parallelogram is

$$x_h \wedge x_l = (h_1 e_2) \wedge (-x_1 e_1 + z_1 e_2) = h_1 x_1 \, e_1 e_2 \tag{D.12}$$

x_h is on the left in this product, so that we go around the parallelogram in the positive, anti–clockwise direction, just as in the $e_1 \wedge e_2$ product.

After deformation by $\hat{\mathbf{F}}$ the leading edge area is

$$(\hat{\mathbf{F}} \cdot \mathbf{x}_h) \wedge (\hat{\mathbf{F}} \cdot \mathbf{x}_l) = (x_h z_l - z_h x_l)\, \mathbf{e}_1 \mathbf{e}_2 \tag{D.13}$$

As with the trailing edge we can calculate t_l from the area of an equivalent vertical–sided parallelogram, but because $\mathbf{x}_l$ can rotate through a wide angle range, we need to take care to choose the right base vector.

Initially in our examples, $x_l \leq -x_h$. A vertical line through this parallelogram connects the two $\mathbf{x}_l$ sides, but not the $\mathbf{x}_h$ sides (this is similar to the trailing edge case).

$$(t_l z_h \mathbf{e}_2) \wedge (x_l \mathbf{e}_1 + z_l \mathbf{e}_2) = -x_l t_l z_h\, \mathbf{e}_1 \mathbf{e}_2$$

$$t_l = -\frac{h_1 x_l}{x_l z_h} = \frac{-F_{xx} x_l}{x_l} \tag{D.14}$$

$$t_l = \frac{x_h z_l - z_h x_l}{-x_l z_h} = 1 - \frac{x_h z_l}{x_l z_h} \tag{D.15}$$

When the leading edge rotates close to vertical, specifically when $-x_h \leq x_l \leq x_h$, a vertical line connects the two $\mathbf{x}_h$ sides instead.

$$(x_h \mathbf{e}_1 + z_h \mathbf{e}_2) \wedge (t_l z_h \mathbf{e}_2) = x_h t_l z_h\, \mathbf{e}_1 \mathbf{e}_2$$

$$t_l = \frac{h_1 x_l}{x_h z_h} = \frac{F_{xx} x_l}{x_h} \tag{D.16}$$

$$t_l = \frac{x_h z_l - z_h x_l}{x_h z_h} \tag{D.17}$$

When the leading edge is vertical, $x_l = 0$ and $t_l = z_l / z_h$.

With further rotation, $x_h \leq x_l$, and the leading edge again is the correct base vector.

$$(-t_l z_h \mathbf{e}_2) \wedge (x_l \mathbf{e}_1 + z_l \mathbf{e}_2) = x_l t_l z_h\, \mathbf{e}_1 \mathbf{e}_2$$

$$t_l = \frac{h_1 x_l}{x_l z_h} = \frac{F_{xx} x_l}{x_l} \tag{D.18}$$

$$t_l = \frac{x_h z_l - z_h x_l}{x_l z_h} = -\left(1 - \frac{x_h z_l}{z_h x_l}\right) \tag{D.19}$$

There is a sign change here (compared to the trailing edge and initial leading edge cases) because $\hat{\mathbf{F}} \cdot \mathbf{x}_h$ lies to the SW of the $\hat{\mathbf{F}} \cdot \mathbf{x}_l$ vector. The corresponding vertical–sided parallelogram is defined by $-t_l z_h \mathbf{e}_2$ and $\hat{\mathbf{F}} \cdot \mathbf{x}_l$.

The full maximum fold thickness, t_{pg}, is a combination of this leading edge thickness, a portion of the overlapping trailing edge, and a portion of an undisturbed layer.

In the following, t_{lh} is t_l plus the thickness of the undisturbed stratigraphy directly underneath it. The maximum *net* thickness, t_{pn}, adds the thickness of the overlapping trailing edge, if any, to t_{lh}.

For $x_l \leq -x_h$, $t_{pn} = t_{pg} = t_l$.

When $x_l = -x_h$, $t_l = 1 - \dfrac{z_l \cdot x_h}{z_h \cdot x_l} = 1 + \dfrac{z_l}{z_h} = p$, the maximum thickness.

For a steeper leading edge, $-x_h \leq x_l \leq 0$. t_l starts decreasing, but due to a growing overlap, $t_{pn} = t_{pg} = p$.

When the leading edge is vertical, $x_l = 0$, $t_l = z_l/z_h$, and $t_{pn} = p$.

For $0 < x_l < x_h$, $t_{pg} = p$, and

$$t_{pn} = 1 + \frac{z_l \cdot x_t - x_l z_t}{z_h \cdot x_t} \tag{D.20}$$

For a well overturned leading edge, $x_h \leq x_l$, and $t_{pn} = 1 + t_l + t_t$.

D.1.3 Flattening Leading Edge

A case in which the leading edge flattens for a while until the shear becomes strong enough to overturn it is illustrated in Figure D.1 and Figure D.2.

Early in the strain, when the thickness of both segments of the parallel–sided fold is given by the spacing between the x_t and x_l vectors, it is

$$t_t = \frac{F_{xx} x_1}{F_{xx} x_1 + F_{xz} z_1} = 1 \bigg/ \left(1 + \frac{F_{xz}}{F_{xx}} \frac{z_1}{x_1} \right) \tag{D.21}$$

$$t_l = \frac{-F_{xx} x_1}{-F_{xx} x_1 + F_{xz} z_1} = 1 \bigg/ \left(1 - \frac{F_{xz}}{F_{xx}} \frac{z_1}{x_1} \right) \tag{D.22}$$

Under pure shear, $F_{xz} = 0$, and both t_t and t_l are one. For modest $F_{xz} > 0$, t_t is a bit less than one, while t_l is a bit larger than one. This is a consequence of the angles of the two segments, not their direction of rotation.

The first strained stage in Figure D.1 is a good example of a case in which $t_{pg} < p$. The relative height of the peak of the disturbance above the base line is p, but no part of the disturbed layer has this thickness. But at the second strained stage the disturbance peak has sheared enough that it is now above part of the undisturbed layer, so $t_{pg} = p$.
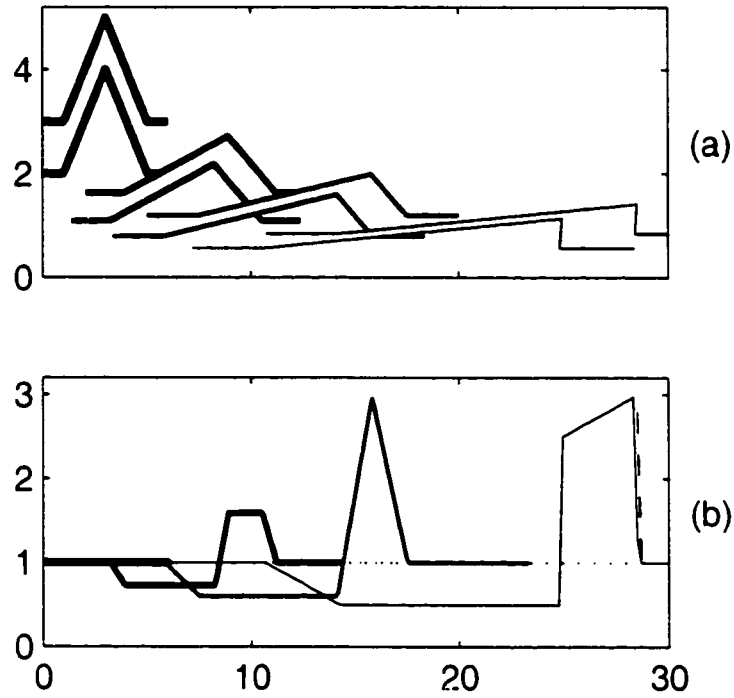
Figure D.1: Thickness variation of a flattening disturbance. The initial disturbance dimensions match those in Figure 4.3, but it occurs further upstream, and is subject to more pure shear. In the second and third snapshots, the leading edge has flattened before overturning in the fourth.

D.1.4 Fold Width Details

The reference, or base, width is

$$x_b = x_t + x_h - x_l = F_{xx} 2x_1 + F_{xz} h_1 \qquad (D.23)$$

This is the width of the undisturbed layer, including the shearing of its initial thickness, that is, the x component of $\hat{F} \cdot [2x_1 \ h_1]^t$.

The width calculations differ depending on whether the leading edge has overturned or not. Before overturning, $x_l \leq 0$ and

$$w_t = \frac{x_t}{x_b} \qquad \text{non–overlapping trailing segment} \qquad (D.24)$$

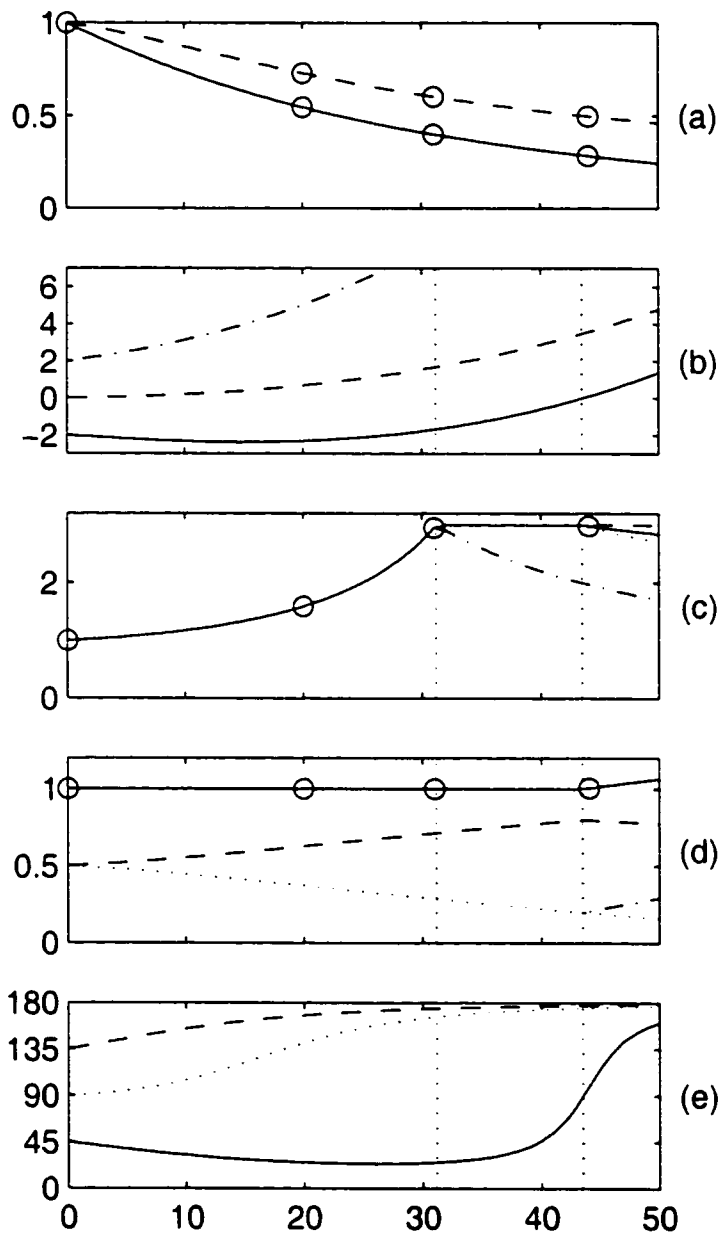$$w_o = 0 \qquad \text{overlapping region} \qquad (D.25)$$

Figure D.2: Trailing and leading edge variation over time for the disturbance in Figure D.1. Panels as in Figure 4.4. with the addition (e) of vector angles. $\hat{F} \cdot x_l$ (*solid*). $\hat{F} \cdot x_t$ (*dashed*), and $\hat{F} \cdot x_h$ (*dotted*). The leading edge initially flattens, and starts to steepen just before $x_l = -x_h$, about at time step 28.

$$w_s = \frac{x_h - x_l}{x_b} \qquad \text{thickening stem} \tag{D.26}$$

$$w_g = w_t + w_s = 1 \qquad \text{gross relative width} \tag{D.27}$$

If $x_l \geq 0$, the leading edge is overturned, and

$$w_t = \frac{x_t - x_l}{x_b} = 1 - \frac{x_h}{x_b} = \frac{2x_l F_{xx}}{x_b} \tag{D.28}$$

$$w_o = \frac{x_h + x_l}{x_b} = \frac{-F_{xx}x_1 + F_{xz}(h_1 + z_1)}{x_b} \tag{D.29}$$

$$w_s = \frac{x_h - x_l}{x_b} = \frac{F_{xx}x_1 + F_{xz}(h_1 - z_1)}{x_b} \qquad \text{until } x_l = x_h \tag{D.30}$$

$$w_g = w_t + w_o = \frac{x_t + x_h}{x_b} = 1 + \frac{x_l}{x_b} \tag{D.31}$$

$$= \frac{F_{xx}x_1 + F_{xz}(h_1 + z_1)}{x_b}$$

Several patterns in Figure 4.4(d) are peculiar to a subset of parameters. The fact that $w_o = w_t$ when $x_l = x_h$ is a consequence of our choosing $z_1 = x_1 = 2h_1$. When the leading edge overturns, w_o starts increasing while w_t decreases. They become equal when

$$2F_{xx}x_1 = -F_{xx}x_1 + F_{xz}(h_1 + z_1); \qquad \frac{F_{xz}}{F_{xx}} = \frac{3x_1}{h_1 + z_1}$$

With our initial dimensions, this condition is satisfied when $F_{xz} = 2F_{xx}$ and $x_l = x_h$.

In this example, before overturning w_t increases while w_s decreases as the disturbance moves downstream. This occurs because $h_1 < 2z_1$. If $h_1 = 2z_1$, the two relative widths would be the same.

$$w_t = \frac{F_{xx}x_1 + F_{xz}z_1}{2F_{xx}x_1 + F_{xz}h_1} = \frac{1}{2}\frac{F_{xx}x_1 + F_{xz}z_1}{F_{xx}x_1 + F_{xz}z_1} = \frac{1}{2}$$

If $h_1 > 2z_1$, it is w_s that increases.

D.2   Fold Classification

We have referred to some of our disturbances as *similar*. This is one of several ways that structural geologists classify folds.

Perhaps the two most significant classes are parallel folds and similar folds. In parallel folds the layer thickness perpendicular to the layer boundary is constant. These are typical of folded competent

layers in high contrast contexts. In similar folds, the thickness is constant parallel to the fold axis. The top and bottom boundaries of the layer are identical. One of the early papers on folding in ice sheets specifically discusses similar folds (Hudleston, 1976).

A more detailed classification of folds is based on the degree of curvature of the inner and outer arcs of the fold (Ramsay and Huber, 1983, Vol. 2). A related tool is the construction of dip isogons. These are lines that join points where the surfaces have an identical orientation, that is, lines connecting points of equal slope (slope contours).

In Class 1 folds, the inner arc curvature is greater than the outer. The dip isogons converge toward the inner arc. These folds are further sub-classified based on limb and hinge thicknesses perpendicular to the boundary. Parallel (concentric) folds are Class 1b, with equal hinge and limb thicknesses. Class 1c folds, with a larger hinge thickness, are attributed to flattening of parallel folds.

Class 2 folds are similar folds, with equal inner and outer arc curvatures. The dip isogons are parallel. In class 3 folds, the inner arc curvature is less than the outer.

Under homogeneous strain, dip isogon classes should remain the same. Isogons connect surface points with matching material angles. Under homogeneous strain, segments with the same angle rotate at the same rate. This means the isogons themselves are passive markers in the material, and are strained by the $\hat{F}$ just like the stratigraphic layer markers. If two isogons have the same orientation in the initial state, they retain that orientation after strain. In particular, similar folds (parallel isogons) remain similar.

In Figure D.3 the middle layer is Class 2, with parallel isogons. Above it, in the center, the fold is Class 1, with convergent isogons toward the fold core, and limbs thicker than the hinge. Below the fold is Class 3. The reverse bend on the flank is Class 3 above and Class 1 below.
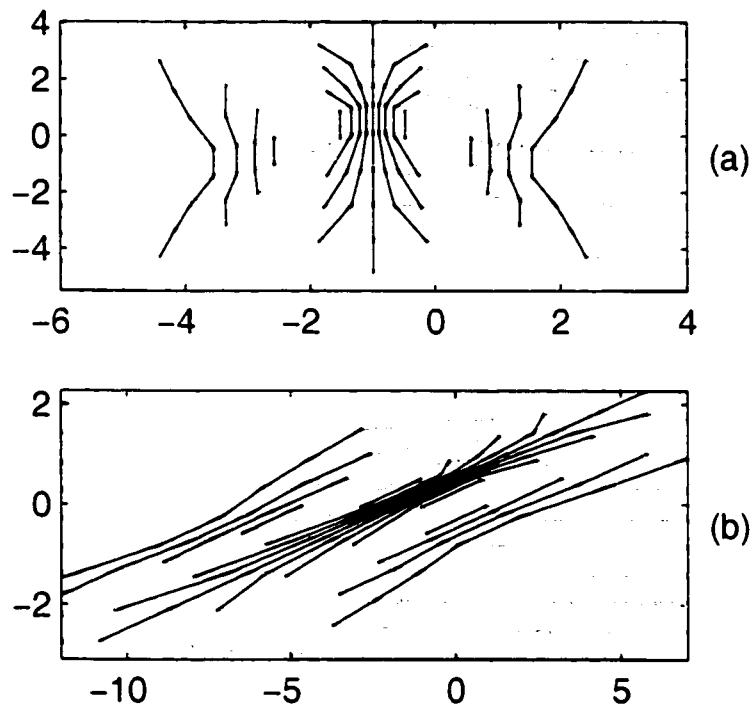
Figure D.3: Multiple layers with variable σ (*gray lines*) and dip isogons (*lines*). Under homogeneous strain, isogons deform with the stratigraphic layers.

Appendix E

MOHR/MEANS CIRCLES

E.1   Tensors and Mohr Circle

The Mohr circle is a well established tool for depicting deviatoric stress and strain rate tensors and solving for their eigenvalues (Malvern, 1969)[sec.3.5]. This application has been extended by structural geologists to nonsymmetric tensors such as the velocity gradient and deformation gradient (Means et al., 1980; Bobyarchick, 1986; Passchier, 1988). This generalized Mohr circle plots the relative effect of a linear operator (tensor) on vectors of various orientations.

Let $f\mathbf{x} = f(\mathbf{x})$ be the result of applying the linear operator f to the unit vector $\mathbf{x}$ in 2D (R^2). This vector can be written as the sum of two vectors, one parallel to the original $\mathbf{x}$ and the other perpendicular to it.

$$f\mathbf{x} = f\mathbf{x}_{\|} + f\mathbf{x}_{\perp} \tag{E.1}$$

If the point $(|f\mathbf{x}_{\|}|, |f\mathbf{x}_{\perp}|)$ is plotted for all orientations of $\mathbf{x}$, the points lie on a circle.

The result of applying the velocity gradient tensor, $\mathbf{L} = \nabla\mathbf{u}$, to a small unit displacement vector $\delta\mathbf{x}$, is a deformation rate vector $\delta\mathbf{u}$, whose components parallel and perpendicular to the displacement are its strain rate, $\dot{\varepsilon}$, and rotation rate, $\dot{\omega}$. The Mohr circle plots $\dot{\omega}$ versus $\dot{\varepsilon}$.

The application of the deformation gradient tensor, $\mathbf{F}$, to a small segment, $d\mathbf{X}$, produces a deformed segment, $d\mathbf{x}$. The Mohr circle representation of $\mathbf{F}$ plots the orientation and magnitude of $d\mathbf{x}$ relative to those of $d\mathbf{X}$. The Cartesian coordinates of this point are the magnitudes the parallel and perpendicular components of $d\mathbf{x}$ relative to $d\mathbf{X}$, while the polar coordinates are the stretch and rotation of $d\mathbf{x}$ relative to $d\mathbf{X}$, which are usually more useful.

In this chapter I attempt to explain this generalized Mohr circle using Geometric Algebra.

E.1.1 Geometric Algebra

Geometric Algebra (GA) unifies the scalars, vectors, and inner and outer products of vector algebra. Based on the work of Grassmann, Hamilton, and Clifford its principal recent developer is David Hestenes (Hestenes, 1986; Hestenes and Sobczyk, 1984). Good summaries can be found in Baylis (1996), Lasenby *et al.* (1996), and Gull *et al.* (1996). Perhaps the fullest application of GA to continuum mechanics is McRobie and Lasenby (1999). The use of Mohr circles to solve for eigenvalues and vectors of symmetric linear operators is described using GA in Hestenes (1986)[chap.5]. I build on this, extending it to nonsymmetric operators.

In GA, scalars, vectors and 'higher objects' can be added to form multivectors. The multivector of particular interest to us is the result of the *geometric product* of two vectors, which unites the dot and cross products of vector algebra.

$$x_1 x_2 = x_1 \cdot x_2 + x_1 \wedge x_2 \tag{E.2}$$

$x_1 \cdot x_2$ is the scalar dot product. The *wedge product*, $x_1 \wedge x_2$, is a *bivector*, the area swept out by the two vectors x_1 and x_2. While the dot product of vectors commutes, the wedge product, which is a generalization of the vector cross product, anti-commutes. Hestenes refers to this sum of a scalar and a bivector as a *spinor*.

While the geometric product can be formally defined in terms of its algebraic properties (Hestenes and Sobczyk, 1984), thinking of the product as the sum of the dot and wedge products of vectors is sufficient for our purposes. GA extends seamlessly to higher dimensions, but I will focus on R^2.

Ideally in GA one should be able to work without reference to any coordinate system, however given our familiarity with vector notation, it is convenient work with an orthonormal basis, two perpendicular unit vectors, which I call e_1 and e_2. Another vector can then be expressed as $x = x_1 e_1 + x_2 e_2$. The properties of e_1 and e_2 include

$$e_1^2 = e_2^2 = 1 \qquad e_1 e_2 = -e_2 e_1$$
$$(e_1 e_2)^2 = e_1 e_2 e_1 e_2 = -e_1 e_1 e_2 e_2 = -1$$
$$e_1 \cdot e_2 = 0 \qquad e_1 \wedge e_1 = 0$$

$e_1 e_2$ is the unit bivector. Because its square is the scalar -1, it is convenient to write it as i. This is

an allusion to the imaginary number $\sqrt{-1}$. There are significant similarities between GA spinors in R^2 and complex numbers.

In R^2, i is unique, and referred to as a pseudo-scalar. A general R^2 multivector is the sum of a scalar, vectors, and a bivector.

As with complex numbers, multiplying by i produces a rotation.

$$e_1 i = e_1 e_1 e_2 = e_2 \tag{E.3}$$

$$e_2 i = e_2 e_1 e_2 = -e_2 e_2 e_1 = -e_1 \tag{E.4}$$

The vector perpendicular to x is $xi = -x_2 e_1 + x_1 e_2$. This left multiplication by i results in clockwise rotation by $90°$. Right multiplication rotates it anticlockwise ($ie_1 = -e_2$).

The GA exponential $e^{i\phi}$ is similar to the complex exponential. If the angle between e_1 and x is ϕ, x can be expressed in terms of an *exponential*

$$x = e_1 \, r e^{i\phi} \tag{E.5}$$

Here the exponential is actually a spinor, a scalar plus a bivector. Multiplication of this spinor by a vector produces another vector.

$$e^{i\phi} = \cos\phi + i\sin\phi \tag{E.6}$$

$$x = r(\cos\phi \, e_1 + \sin\phi \, e_2) = r e_1 (\cos\phi + i\sin\phi) \tag{E.7}$$

More generally, $x r e^{i\phi}$ is a vector with an angle of ϕ (in the anticlockwise direction) relative to vector x, and length $r|x|$. When dealing with disturbance folding, it is convenient to talk about angles clockwise from upstream horizontal. If θ is such an angle, and e_1 is aligned with horizontal downstream, then a vector can be expressed as

$$x = -e_1 r e^{-i\theta}$$
$$= e_1 r e^{i\phi} = e_1 r e^{i(\pi-\theta)} = e_1 r e^{i\pi} e^{-i\theta} = r(-\cos\theta e_1 + \sin\theta e_2) \tag{E.8}$$

E.1.2   The Circle Representation of a Linear Operator

In GA the concept of linear operators is similar to that in linear algebra and tensor mathematics, with perhaps, an even greater effort to work without reference to a coordinate system where possible.

Let f be a *linear operator*. When applied to $\mathbf{x}$ the result is another vector which I denote $f\mathbf{x} = f(\mathbf{x})$[1]. Its linear property is expressed by $f(a\mathbf{x}_1 + b\mathbf{x}_2) = af(\mathbf{x}_1) + bf(\mathbf{x}_2)$.

Using the $\mathbf{e}_1$ and $\mathbf{e}_2$ basis, the effect of f on a vector can be expressed in a manner similar to tensor coordinate notation

$$f\mathbf{x} = (a x_1 + b x_2)\mathbf{e}_1 + (c x_1 + d x_2)\mathbf{e}_2 \tag{E.9}$$

The values of a, b, c, and d depend on the choice of basis. The operator could be defined in terms of these scalar components, or these components could be derived from the application of the operator to the basis.

$$f\mathbf{e}_1 = a\mathbf{e}_1 + c\mathbf{e}_2 \qquad f\mathbf{e}_2 = b\mathbf{e}_1 + d\mathbf{e}_2$$

$$\begin{bmatrix} a & b \\ c & d \end{bmatrix} = \begin{bmatrix} f\mathbf{e}_1 \cdot \mathbf{e}_1 & f\mathbf{e}_2 \cdot \mathbf{e}_1 \\ f\mathbf{e}_1 \cdot \mathbf{e}_2 & f\mathbf{e}_2 \cdot \mathbf{e}_2 \end{bmatrix} \tag{E.10}$$

To keep notation simple I assume in the following discussion that $\mathbf{x}$ is a unit vector ($\mathbf{xx} = 1$). The geometric product of $f\mathbf{x}$ and $\mathbf{x}$ is

$$f\mathbf{xx} = f\mathbf{x} \cdot \mathbf{x} + f\mathbf{x} \wedge \mathbf{x} \tag{E.11}$$

For our pair of basis vectors this product is

$$f\mathbf{e}_1 \mathbf{e}_1 = a\mathbf{e}_1 \mathbf{e}_1 + c\mathbf{e}_2 \mathbf{e}_1 = a - ic$$

$$f\mathbf{e}_2 \mathbf{e}_2 - b\mathbf{e}_1 \mathbf{e}_2 + d\mathbf{e}_2 \mathbf{e}_2 = d + ib \tag{E.12}$$

For $\mathbf{x}$ expressed in the same basis

$$f\mathbf{xx} = (a x_1^2 + (b + c)x_1 x_2 + d x_2^2) + i(-c x_1^2 + (a - d)x_1 x_2 + b x_2^2) \tag{E.13}$$

Since $x_1^2 + x_2^2 = 1$, this can also be written

$$f\mathbf{xx} = \left(\frac{a+d}{2} + \frac{b+c}{2}y_2 + \frac{a-d}{2}y_1 \right) + i\left(\frac{b-c}{2} + \frac{a-d}{2}y_2 - \frac{b+c}{2}y_1 \right) \tag{E.14}$$

where $y_1 \equiv x_1^2 - x_2^2 \qquad y_2 \equiv 2x_1 x_2$ \hfill (E.15)

---

[1] In GA a linear operator on vectors can be extended to multivectors, with its action on a pseudo-scalar providing a definition for the determinant, $|f|$.

y_1 and y_2 come from squaring $e_1 x = e^{i\phi}$.

$$e_1 x = e_1(x_1 e_1 + x_2 e_2) = x_1 + i x_2$$

$$e^{i2\phi} = (x_1 + i x_2)^2 = x_1^2 - x_2^2 + i2 x_1 x_2 = y_1 + i y_2$$

With $x_1 = \cos\phi$ and $x_2 = \sin\phi$ (E.15) are the familiar double angle sine and cosine formulas.

$f x x$ can be plotted in spinor space, with the scalar part ($f x \cdot x$) along the horizontal axis, and the bivector part ($f x \wedge x$) along the vertical axis. This is akin to plotting a point in complex space, on the real and imaginary axes. Since the y_1 and y_2 used in (E.14) satisfy $y_1^2 + y_2^2 = 1$, these $f x x$ points lie on circle. The points $f e_1 e_1$ and $f e_2 e_2$ define a diameter of this circle. Its center is $\frac{1}{2}(f e_1 e_1 + f e_2 e_2)$, and the radius is $\lambda_r = \frac{1}{2}|f e_1 e_1 - f e_2 e_2|$.

There are a couple of ways of interpreting this $f x x$ product. One is that it gives the magnitude of the components of $f x$ that are parallel and perpendicular to x.

$$f x = f x_{\parallel} + f x_{\perp} \tag{E.16}$$

$$= (f x) x x = (f x x) x = (f x \cdot x) x + (f x \wedge x) x$$

$$f x_{\parallel} = (f x \cdot x) x \qquad f x_{\perp} = (f x \wedge x) x \tag{E.17}$$

Changing the order of the product changes the sign of just the perpendicular (wedge) part.

An equivalent way of writing these components using tensor notation is

$$|f x_{\parallel}| = f x \cdot x \qquad |f x_{\perp}| = |f x \times x| \tag{E.18}$$

The exponential form of the $f x x$ spinor gives the magnitude, λ_r, and orientation (or rotation) of $f x$ relative to x, ϕ_x.

$$f x x = \lambda_r e^{i\phi_x} = \lambda_r \cos\phi_x + i\lambda_r \sin\phi_x$$

$$\lambda_r \cos\phi_x = f x \cdot x \qquad i\lambda_r \sin\phi_x = f x \wedge x \tag{E.19}$$

The product $f\mathbf{x}\mathbf{x}$ can be represented as several different combinations of spinors.

$$f\mathbf{x}\mathbf{x} = \lambda_c e^{i\Phi_c} + y_1\lambda_r e^{i\Phi_1} + y_2\lambda_r i e^{i\Phi_1}$$

$$= f\mathbf{e}_2\mathbf{e}_2 + x_1^2 2\lambda_r e^{i\Phi_1} + x_1 x_2 2\lambda_r i e^{i\Phi_1}$$

$$= f\mathbf{e}_2\mathbf{e}_2 + (x_1^2 + i x_1 x_2)2\lambda_r e^{i\Phi_1}$$

$$f\mathbf{e}_1\mathbf{e}_1 = \lambda_c e^{i\Phi_c} + \lambda_r e^{i\Phi_1}$$

$$f\mathbf{e}_2\mathbf{e}_2 = \lambda_c e^{i\Phi_c} - \lambda_r e^{i\Phi_1}$$

$\lambda_c e^{i\Phi_c}$ is the circle center. λ_r is the circle radius, while ϕ_1 is the angle of the diameter between $\mathbf{e}_1$ and $\mathbf{e}_2$. $2\lambda_r i e^{i\Phi_1}$ is the diameter perpendicular to this.

$$\lambda_c e^{i\Phi_c} = \tfrac{1}{2}((a+d) + i(b-c))$$

$$\lambda_r e^{i\Phi_1} = \tfrac{1}{2}((a-d) - i(c+b))$$

If f is the identity operator, $f\mathbf{x} = \mathbf{x}$, and $f\mathbf{x}\mathbf{x} = \mathbf{x}\cdot\mathbf{x} + \mathbf{x}\wedge\mathbf{x} = 1 + 0i$. Its Mohr circle is a point (1) on the horizontal (scalar) axis.

E.2 Velocity Gradient Tensor and Circle

For a velocity gradient tensor, $\mathbf{L}$, the linear operator is

$$d\mathbf{u} = \mathbf{L}\mathbf{x} = (\mathbf{x}\cdot\nabla)\mathbf{u}$$

$$= (x_1\partial_1 u_1 + x_2\partial_2 u_1)\mathbf{e}_1 + (x_1\partial_1 u_2 + x_2\partial_2 u_2)\mathbf{e}_2 \tag{E.20}$$

$$\mathbf{L}\mathbf{x}\mathbf{x} = \dot{\varepsilon} + i\dot{\omega} \tag{E.21}$$

$$= (\partial_x u x_1^2 + (\partial_z u + \partial_x w)x_1 x_2 + \partial_z w x_2^2) + i(-\partial_x w x_1^2 + (\partial_x u - \partial_z w)x_1 x_2 + \partial_z u x_2^2)$$

The scalar component for the $\mathbf{L}\mathbf{x}\mathbf{x}$ product is the stretching rate of $\mathbf{x}$, $\dot{\varepsilon}$. The bivector part is $\dot{\omega}$, the rotation rate of $\mathbf{x}$.

The $\dot{\omega} - \dot{\varepsilon}$ plot (Lister and Williams, 1983) in Figure E.1(a) is the Mohr circle representation of a velocity gradient. Panel (b) is a more physical representation indicating the direction of rotation of the corresponding segment angles and range of angles that are undergoing compression ($\dot{\varepsilon} < 0$, the shaded arc).

148

In Figure E.1(a) plots rotation, $\dot{\omega}$ (vertical)[2], against straining, $\dot{\varepsilon}$ (horizontal). Two defining points for the circle are: $\mathbf{Le_1 e_1} = \partial_x u - i\partial_x w$ and $\mathbf{Le_2 e_2} = \partial_z w + i\partial_z u$. The angles of the physical segments (ϕ) relative to horizontal (downstream) are measured around $f e_2 e_2$ or as double angles around the center. At the angles labeled B there is no stretching, $\dot{\varepsilon} = 0$. In this case, with plane strain, they match the rotation rate extrema ($\dot{\omega}_{max}$). The A's mark the segments that are not rotating, $\dot{\omega} = 0$.

E.2.1 Matching Rotation Rate

Waddington *et al.* (sub) suggest looking at the rotation rates of segments relative to that of the steady state isochrones. The segment that is rotating at the same rate is, in some sense, stable. Gentler segments will be flattening, while steeper ones will steepen and possibly overturn. In Chapter 1 we show that the matching rotation rate criteria is overly conservative. Because the velocity gradient changes as a segment moves along a particle path, it can actually change direction of rotation. The 'stability' angle is more of a turn–around angle.

Whatever its usefulness in predicting what disturbances will overturn and when, it is instructive to calculate what segment is momentarily stationary relative to the isochrone (or any other reference angle). This problem can be expressed as the problem of finding a unit vector $\mathbf{x_1}$ such that

$$\mathbf{Lx_1} \wedge \mathbf{x_1} = \mathbf{Lx_0} \wedge \mathbf{x_0} = \dot{\omega}_0 \qquad (E.22)$$

where $\mathbf{x_0}$ is the unit reference vector (the one aligned with the isochrone).

Given our $e_1.e_2$ basis, and the bivector part of (E.13), (E.22) can be expanded into

$$-cx_1^2 + (a-d)x_1 x_2 + bx_2^2 = \dot{\omega}_0$$

$$-c + (a-d)m + bm^2 = \dot{\omega}_0 (1 + m^2) \qquad m \equiv \frac{x_2}{x_1}$$

$$(-c - \dot{\omega}_0) + (a-d)m + (b - \dot{\omega}_0)m^2 = 0$$

This is a quadratic equation in $m = x_2/x_1 = -\tan\theta$. There are two angles that satisfy this equation, one of which is that of the isochrone itself, θ_0. The sum of the two solutions to the quadratic is simpler than either of individual solutions.

$$\tan\theta_0 + \tan\theta_1 = -m_0 - m_1 = \frac{a-d}{b - \dot{\omega}_0} \qquad (E.23)$$

---

[2] clockwise, decreasing ϕ on top, increasing θ. θ is relative to horizontal upstream.
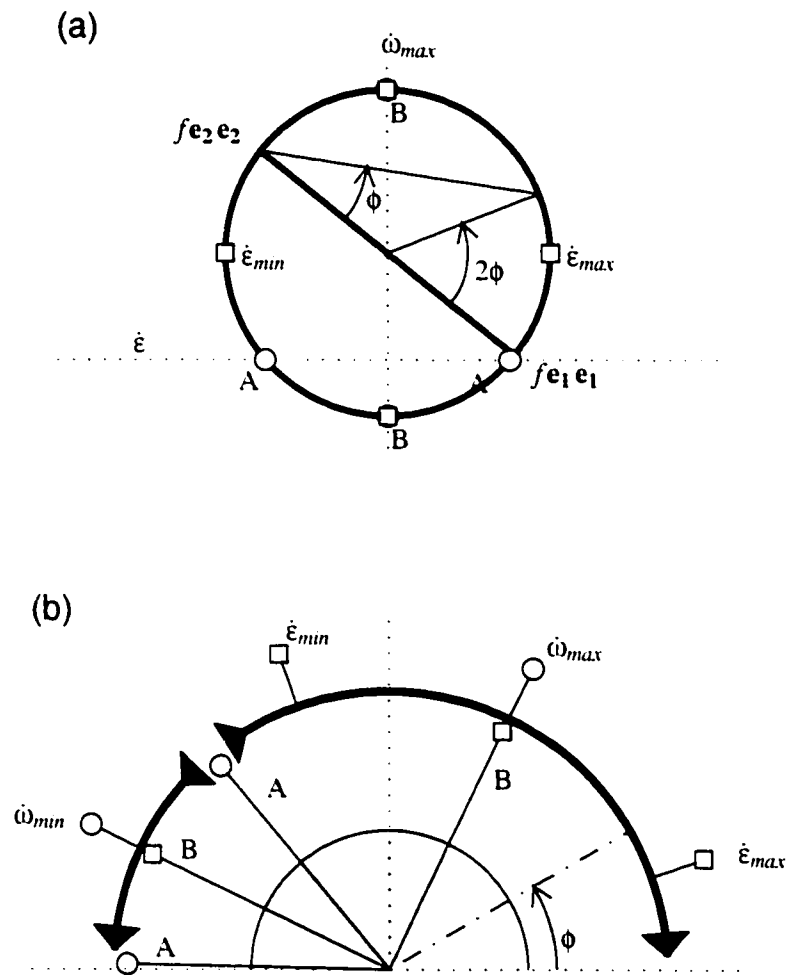
Figure E.1: (a) Mohr circle for a velocity gradient operator and the corresponding (b) physical representation. The angle convention here (ϕ) uses the supplement of the θ (relative to x upstream) used elsewhere when talking about the rotation of leading edges. Angles in the shaded area are undergoing compression ($\dot\varepsilon < 0$).
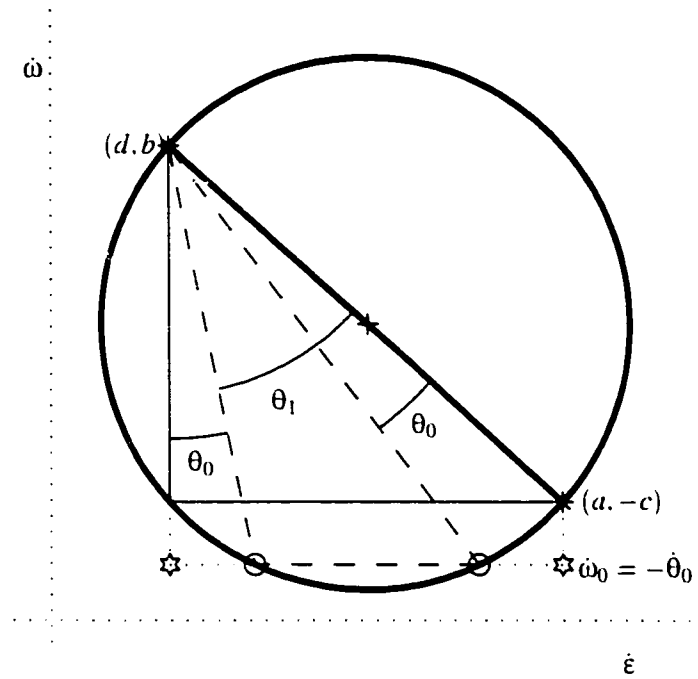
150

Figure E.2: Mohr circle for calculating the angle, θ_1, that is not rotating with respect to the surface isochrone, θ_0. $\dot\varepsilon$ and $\dot\omega$ of the θ_0 and θ_1 segments are plotted as circles near the bottom of the Mohr circle. The inscribed right triangle illustrates the equation (E.24) for $\theta_0 + \theta_1$. The hexagonal points outside the Mohr circle can be used with equation (E.23) to give $\tan\theta_0 + \tan\theta_1$.

Alternatively, using the double angle equation (E.14) for $\dot\omega$ gives a solution in terms of the sum of the two angles.

$$\frac{a-d}{2}y_{12} - \frac{b+c}{2}y_{11} = \frac{a-d}{2}y_{02} - \frac{b+c}{2}y_{01}$$

$$\frac{a-d}{b+c} = \frac{y_{11}-y_{01}}{y_{12}-y_{02}} = \frac{\cos 2\theta_1 - \cos 2\theta_0}{-\sin 2\theta_1 + \sin 2\theta_0} = \frac{2\sin(\theta_1 + \theta_0)\sin(\theta_1 - \theta_0)}{2\cos(\theta_1 + \theta_0)\sin(\theta_1 - \theta_0)} = \tan(\theta_0 + \theta_1) \qquad (E.24)$$

Figure E.2 illustrates the derivation of (E.23) and (E.24).

But in GA (and tensor algebra) we can choose any coordinate set that is convenient. In this spirit, the Mohr circle could be defined by the isochrone and the vector perpendicular to it, x_0 and $x_0 i$.

$$Lx_0 x_0 = Lx_0 \cdot x_0 + Lx_0 \wedge x_0 \qquad (E.25)$$

$$L(x_0 i)(x_0 i) = L(x_0 i) \cdot x_0 i + L(x_0 i) \wedge x_0 i \qquad (E.26)$$

From the Mohr circle in Figure E.3 it is evident that the x_1 product shares components with each defining product.

$$\mathbf{L}x_1 \, x_1 = \mathbf{L}x_1 \cdot x_1 + \mathbf{L}x_1 \wedge x_1$$

$$= \mathbf{L}(x_0\mathbf{i}) \cdot x_0\mathbf{i} + \mathbf{L}x_0 \wedge x_0 \qquad (E.27)$$

The segment that is rotating with x_0 has the same strain rate as the segment perpendicular to it. In the incompressible, plane strain case (ridge flow) this strain rate is the negative of the isochrone strain rate, $-\dot{\varepsilon}_0$.

I could also argue for (E.27) by noting that the points $\mathbf{L}x_0 x_0$, $\mathbf{L}(x_0\mathbf{i})\,(x_0\mathbf{i})$, and $\mathbf{L}x_1 \, x_1$ form an inscribed triangle, with one side being a diameter. The angle at $\mathbf{L}x_1 \, x_1$ is then a right angle. Since x_1 and x_0 have the same wedge product, one side of this triangle is horizontal (in spinor space). Consequently the x_1 to $x_0\mathbf{i}$ side must be vertical, and have the same dot product.

The relation between x_0 and x_1 is given by their geometric product, $x_0 x_1 = x_0 \cdot x_1 + x_0 \wedge x_1 = \cos\phi_{01} + \mathbf{i}\sin\phi_{01}$. The angle between these two segments, ϕ_{01}, is [3]

$$\tan\phi_{01} = \frac{\mathbf{L}x_0 \cdot x_0 - \mathbf{L}(x_0\mathbf{i}) \cdot (x_0\mathbf{i})}{-\mathbf{i}\,(\mathbf{L}x_0 \wedge x_0 - \mathbf{L}(x_0\mathbf{i}) \wedge (x_0\mathbf{i}))}$$

$$= \frac{\dot{\varepsilon}_0 - \dot{\varepsilon}_\perp}{\dot{\omega}_0 - \dot{\omega}_\perp} = \frac{\dot{\varepsilon}_0 - \dot{\varepsilon}_c}{\dot{\omega}_0 - \dot{\omega}_c} \qquad (E.28)$$

$\dot{\varepsilon}_0$ and $\dot{\omega}_0$ are the strain rate and rotation rate for x_0, and $\dot{\varepsilon}_\perp$ and $\dot{\omega}_\perp$ the values for $x_0\mathbf{i}$. $\dot{\varepsilon}_c + \mathbf{i}\dot{\omega}_c$ is the Mohr circle center point, the average of any two diameter points.

The θ_1 segment is easy to identify in the velocity gradient Mohr circle, where the rotation rates are explicitly plotted. In the more physical representations of the strain rate, such as the incremental strain ellipse, it is easier to identify straining rates. But since the θ_1 segment has the same $\dot{\varepsilon}$ as the $\theta_\perp$, the angle between those two segments and the minor and major strain rate axes ($\dot{\varepsilon}_{min}$ and $\dot{\varepsilon}_{max}$) is the same. This relation is suggested by the dashed lines in Figure E.3. It also illustrated in Figure E.4 which is the incremental strain ellipse for the symmetric strain rate tensor[4] for the $\mathbf{L}$.

---

[3] The denominator $-\mathbf{i}$ is needed to convert it to a scalar. Using $+\mathbf{i}$ would change the sign.

[4] The symmetric tensor is better than the velocity gradient in this case because the minimum and maximum $\dot{\varepsilon}$ do not rotate.
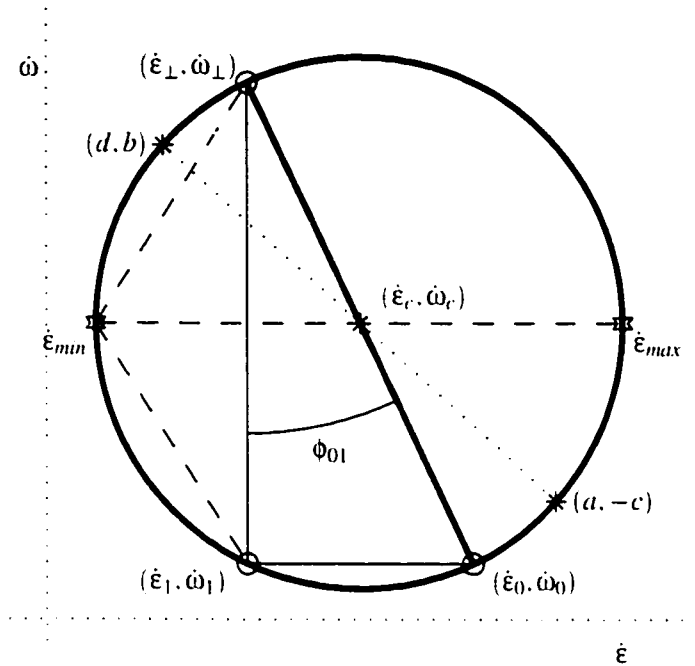
Figure E.3: Mohr circle for calculating the angle that is not rotating with respect to the surface isochrones. Segment θ_1 has the same rotation rate at isochrone segment θ_0. The inscribed right triangle illustrates the equation (E.28) for ϕ_{01}. The dashed lines show that the angle between x_1 and $\dot{\varepsilon}_{min}$ is the same as the angle between $x_\perp$ and $\dot{\varepsilon}_{min}$.

E.2.2   Vorticity Number

The L Mohr circle also illustrates the kinematic vorticity number W_k which is a measure of mix of pure and simple shear in a velocity field (Means et al., 1980; Passchier, 1988; Bobyarchick, 1986).

$$W_k = \bar{\omega}/\bar{\varepsilon} \tag{E.29}$$

where $\bar{\omega}$ is the bulk rotation rate, obtained by breaking the velocity gradient tensor into symmetric and anti-symmetric tensors, and $\bar{\varepsilon}$ is a measure of the strain rate. Several measures of this component are possible, but half the difference between the maximum and minimum strain rates $(\dot{\varepsilon}_{max} - \dot{\varepsilon}_{min})/2$ is a simple common one[5].

---

[5]For plane strain this equals the effective strain rate (the 2nd invariant of the strain-rate tensor).
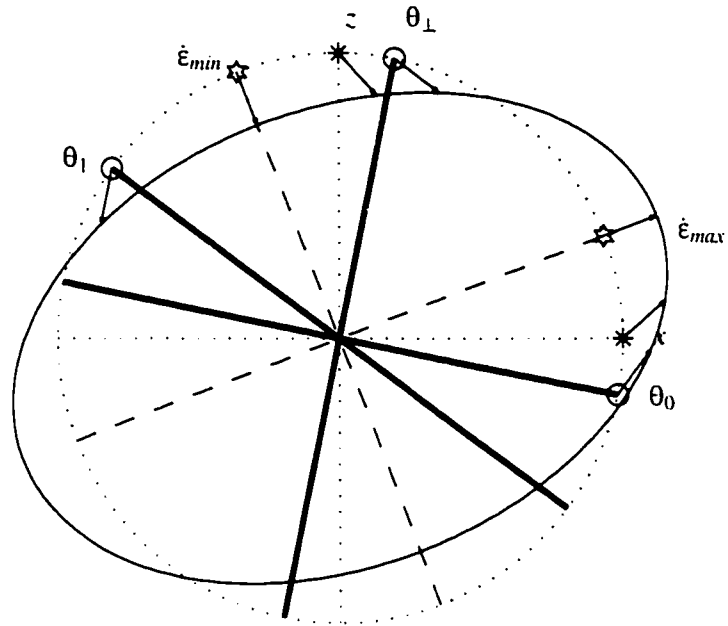
Figure E.4: Physical representation of case in Figure E.3. The ellipse is the incremental symmetric strain, corresponding to the velocity gradient in the previous figure. This does not represent the full rotation present in the gradient.

In the Mohr circle, $\bar{\omega} = \omega_c$, the height of the circle center, and $\bar{\epsilon} = \lambda_r$, its radius. The $\bar{\omega}$ is also the rotation rate of $\dot{\epsilon}_{max}$.

$$W_k = \frac{\omega_c}{\lambda_r} = \frac{b-c}{\sqrt{(a-d)^2 + (b+c)^2}}$$

(E.30)

The vorticity number could also be described as the ratio of the mean rotation rate ($\bar{\omega}$) to half the range of the rotation rates. For pure shear the mean rotation rate is 0. Half the segments rotate one way and half the other. For simple shear, the mean equals the (half) the range. All segments rotate one way, except for one that does not rotate. If $w_k > 1$ the bulk rotation is large enough that all segments, regardless of angle, are rotating. So W_k is a measure of what proportion of the segments rotate each way.
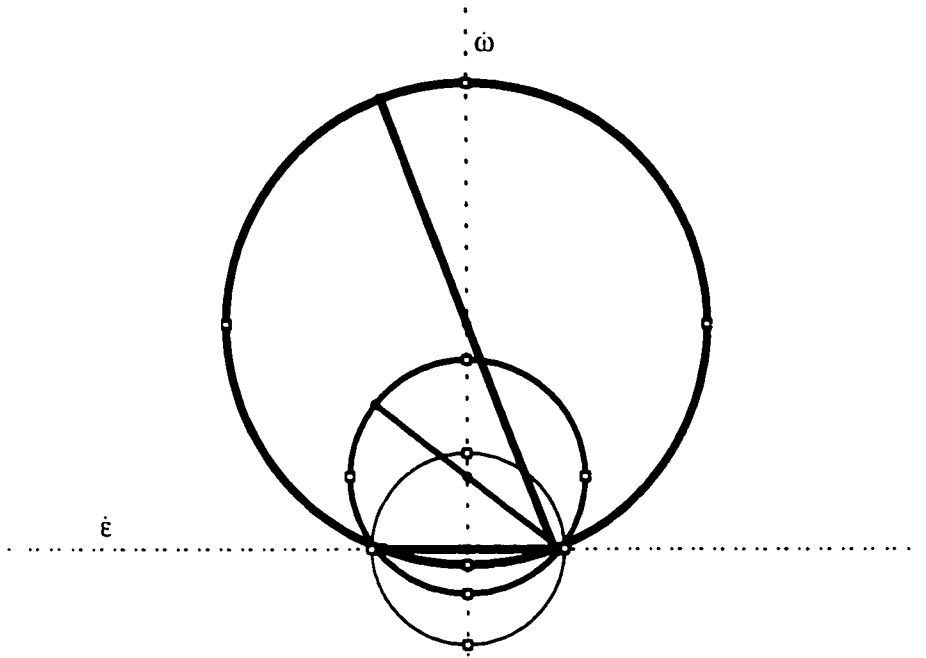
Figure E.5: Mohr circles at various points along a flowpath, showing progression from pure shear (smallest circle centered on horizontal axis) to increasing simple shear (larger circles).

E.2.3 Change in L Mohr Circles Along a Path

For a flat bed, the velocity gradient Mohr circles (Appendix E) change in a quite orderly manner along a flowpath (Figure E.5). Near the surface pure shear dominates and the circle is centered on $\omega = 0$; with depth, the shear grows, while the vertical compression remains about the same. One defining point of the circle, $(\partial_x u, -\partial_x w)$ (strain rate and rotation of a horizontal segment) remains about the same. The other point, $(\partial_z w, \partial_z u)$ moves vertically, as $\partial_z u$ increases, and $\partial_z w$ remains about the same.

E.3   Finite Strain Mohr Circle

For the deformation gradient tensor F, the linear operator expression Fx is the strained version of x. Fxx can be interpreted in terms of the parts of Fx that are parallel and perpendicular to x (E.16), but it generally is more useful to look at this product in its polar (exponential) form, $\lambda_x e^{i\phi_x}$ (E.19). λ_x is the stretch of Fx, and ϕ_x the rotation from x to Fx.

For pure shear, **F** has the tensor form, $\begin{bmatrix} \alpha & 0 \\ 0 & 1/\alpha \end{bmatrix}$. This plots as a circle with a center at $(\alpha + 1/\alpha)/2 + i0$. The point with unit stretch and no rotation, $1 + i0$, is in the interior of this circle.

When shear is added to this, $\mathbf{F} = \begin{bmatrix} \alpha & \beta \\ 0 & 1/\alpha \end{bmatrix}$. The Mohr circle is centered at $(\alpha + 1/\alpha)/2 + i\beta/2$. The radius is such that the circle does not quite touch the origin. The stretch of a horizontal segment is α with no rotation. The stretch of an initially vertical segment is β, and its rotation is almost $90°$ (to horizontal).

Figure E.6 plots the Mohr circles for the two deformations illustrated in Figure 4.3 (b) and (c). For the initial configuration, $\hat{\mathbf{F}} = \mathbf{I}$, and the Mohr circle is just the point $1 + i0$. Since this is $\hat{\mathbf{F}}$, the gradient tensor in the rotating frame aligned with the isochrones, $F_{zx} = 0$.

The circle is defined by the points $F_{xx} - iF_{zx}$ and $F_{zz} + iF_{xz}$, labeled as x_{iso} and x_h. The x_{iso} point is on the horizontal Mohr axis. The x_h point is (initially) perpendicular to the isochrone in the physical plane, and twice this in the Mohr plane.

Because the initial fold is symmetric, the angles of x_l and x_t relative to the defining diameter are the same, but in opposite directions. Since I happened to make them $90°$ apart ($45°$ and $135°$) they form a diameter themselves.

In Figure E.6(a) the three vectors have rotated in the same direction, with x_h rotating the most. The rotation for x_l and x_t is close to the same, and they are close to having the minimum ($1/2$) and maximum (2) stretch. x_l has rotated to vertical so that its initial angle and the rotation sum to $90°$, though this cannot be read directly from the Mohr circle.

A small portion of this circle is below the horizontal axis (clockwise from x_{iso}). This represents low angle leading segments that have been flattened by this strain. About half of these flattened segments have been stretched (outside the unit circle) and half compressed.

In (b) x_l has rotated more than $90°$. Its stretch is now close to one, so it has lengthened relative to its state in (a). x_l has rotated further than x_h, though it will never rotate past x_h.

The angles and lengths of these vectors are given in (D.4). With specific numerical values of $z_1 = x_1 = 2$ and $\beta = \alpha \approx \frac{4}{3}$, the vector rotation and stretch values are

$$\hat{\mathbf{F}} = \begin{bmatrix} \frac{4}{3} & \frac{4}{3} \\ 0 & \frac{3}{4} \end{bmatrix}$$

$$\hat{\mathbf{F}} \cdot x_h = \begin{bmatrix} \beta, \frac{1}{\alpha} \end{bmatrix} \quad h_1 = \begin{bmatrix} \frac{4}{3}, \frac{3}{4} \end{bmatrix}$$
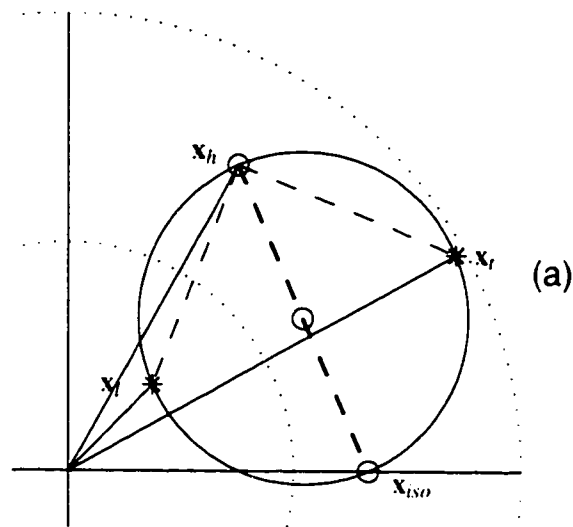
$$\hat{F} = \begin{bmatrix} 1.32 & 1.34 \\ 0.00 & 0.76 \end{bmatrix}$$

(a)
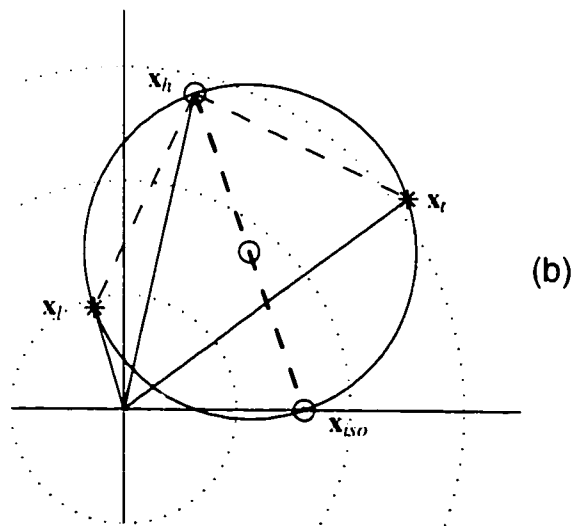
$$\hat{F} = \begin{bmatrix} 1.60 & 2.77 \\ 0.00 & 0.63 \end{bmatrix}$$

(b)

Figure E.6: Mohr circles for Figure 4.3(b) and (c). The circle is defined by the strain of the unit horizontal and vertical vectors, marked as x_{iso} and x_h. The strain of the leading and trailing edge vectors is marked as x_l and x_t. The dotted circles mark stretch of 1, 2, and 3 (polar radius).

$$\hat{\mathbf{F}} \cdot \mathbf{x}_l = \left[0. \frac{1}{\alpha}\right] z_1 = \left[0. \frac{1}{\beta}\right] x_1 = \left[0. \frac{3}{2}\right]$$

$$\hat{\mathbf{F}} \cdot \mathbf{x}_t = \left[2\alpha. \frac{1}{\beta}\right] x_1 = \left[\frac{16}{3}. \frac{3}{2}\right]$$

$$\phi_h = -\tan^{-1}\left(\frac{1}{\alpha\beta}\right) = -\tan^{-1}\left(\frac{9}{16}\right) \approx 150° \qquad \phi_h - \theta_h \approx 150° - 90° = 60°$$

$$\phi_l = 90° \qquad\qquad\qquad\qquad\qquad\qquad \phi_l - \theta_l = 45°$$

$$\phi_t = -\tan^{-1}\left(\frac{1}{2\alpha\beta}\right) = -\tan^{-1}\left(\frac{9}{32}\right) \approx 165° \qquad \phi_t - \theta_t \approx 165° - 135° = 30°$$

$$\frac{|\hat{\mathbf{F}} \cdot \mathbf{x}_h|}{|\mathbf{x}_h|} = \sqrt{\beta^2 + \frac{1}{\alpha}}^2 = \sqrt{\frac{16}{9} + \frac{9}{16}} = 1.53$$

$$\frac{|\hat{\mathbf{F}} \cdot \mathbf{x}_l|}{|\mathbf{x}_l|} = \frac{\frac{1}{\beta}}{\sqrt{1 + (\alpha/\beta)^2}} = \frac{1}{\sqrt{\beta^2 + \alpha^2}} = \frac{3}{4\sqrt{2}} = 0.53$$

$$\frac{|\hat{\mathbf{F}} \cdot \mathbf{x}_t|}{|\mathbf{x}_t|} = \frac{\sqrt{(2\alpha)^2 + (\frac{1}{\beta})^2}}{\sqrt{1 + (\alpha/\beta)^2}} = \sqrt{\frac{(2\alpha\beta)^2 + 1}{\beta^2 + \alpha^2}} = 1.96$$

These rotation and stretch values can be read off the polar coordinates in Figure E.6(a).

E.3.1 Symmetric Strain Rate and Deformation Gradient Tensors

One nice feature of the finite strain Mohr circle is that it illustrates the polar decomposition of the tensor. The nonsymmetric F can be decomposed into a rotation and a symmetric deformation, R·RS. This is the finite equivalent of splitting a velocity gradient into a rotation rate and strain rate tensor. In the rate case these combine additively. In the finite case they combine multiplicatively, and it makes a difference which order the strain and the rotation occur in. Thus there is both a right and left stretch tensor[6].

In the rate case, the symmetric strain rate tensor has the same radius as the nonsymmetric velocity gradient, but it is centered on the $\dot{\varepsilon}$ axis, with $\dot{\omega} = 0$. The rotation rate then is the height of the gradient circle above this axis.

For the finite case, the rotation transformation involves a rotation about the origin.

---

[6]The Cartesian and polar interpretations of a Mohr circle merge when the rate circle is viewed as an infinitesimal finite strain circle - that is, a very small one centered on (1,0), the point of unit finite strain. Slight horizontal motion is equivalent to a slight radial motion, and a slight vertical motion is equivalent to a slight rotational motion.

Some variants on **F** are (Malvern, 1969)

$C = F^t \cdot F$	Green deformation tensor
$RS = \sqrt{C}$	right stretch tensor
$R = F/RS$	rotation tensor
$F = R \cdot RS$	
$F = LS \cdot R$	left stretch tensor
$B^{-1} = (F^{-1})^t \cdot F^{-1}$	Cauchy deformation tensor
$LS = \sqrt{B}$	
$U = \text{eigenvectors}(C)$	principal axes
$L^2 = \text{eigenvalues}(C)$	principal values

E.3.2   3D Operators

There have been attempts to extend the Mohr circle concept to full three dimensional tensors (Treagus, 1990). While certain properties of symmetric three dimensional tensors can be depicted with a set of three Mohr circles, it has been harder to find simple geometric patterns in the operation of nonsymmetric tensors.

The $f\mathbf{x}\mathbf{x}$ product extends to R^3 quite easily. Whether this yields further insight into the problem of depicting three dimensional linear operators has yet to be determined. In R^2 the unit bivector is unique, while in R^3 the set of bivectors is spanned by three linearly independent bivectors. If $e_1 . e_2$, and e_3 are a basis for vectors, the basis for bivectors is

$$i_1 = e_2 e_3 \qquad i_2 = e_3 e_1 \qquad i_3 = e_1 e_2$$

Each can be thought of as a differently oriented face of a unit cube. In R^3, the $f\mathbf{x}\mathbf{x}$ spinor is the sum of a scalar and a bivector. As such it is a 4 dimensional object. It can also be expressed as an

exponential, where the rotation occurs in the (bivector) ϕ plane and with the angle magnitude $|\phi|$.

$$f\mathbf{x}\mathbf{x} = \lambda_0 + \lambda = \lambda e^{\phi} \tag{E.31}$$

$$\lambda = \lambda_1 \mathbf{i}_1 + \lambda_2 \mathbf{i}_2 + \lambda_3 \mathbf{i}_3$$

$$\phi = \phi_1 \mathbf{i}_1 + \phi_2 \mathbf{i}_2 + \phi_3 \mathbf{i}_3$$

$f\mathbf{x}$ and $\mathbf{x}$ both lie in the plane defined by ϕ. In general for a linear operator this plane of rotation will vary with $\mathbf{x}$, though there are some operators, such as the 2D one I have described in more detail, for which the plane has the same orientation, even if its area (bivector magnitude) differs.

160

Appendix F

BED UNDULATIONS AND SEGMENT ROTATION

Abstract

These are working notes clustered around the complications posed by bed undulations. When using a flat bed model. I have ignored the distinction between horizontal and isochrones, but when bed undulations are significant I need to distinguish between how segments rotate relative to horizontal and relative to the isochrones. Here I explore the implications of this distinction, and evaluate where the θ_r (zero rotation angle) can be extended to this case. I also seek graphical and mathematical tools for grasping the extra complexity the bed undulations introduce. The mean θ_r shows some promise as a turn–around criteria. though. in the long run. this does not replace the finite strain θ_f calculation.

F.1 F and L in the Isochrone Frame

When working with segment angles that are of the same order of magnitude as the isochrone angle. it is convenient to use a reference frame that is aligned with the isochrone. In Chapter 4 I introduced $\hat{F}$ (4.3). a variant on the deformation gradient tensor that operates in this rotating frame.

$$\hat{F} = R(\theta_{iso})^t \cdot F \cdot R(\Theta_{iso}) \tag{F.1}$$

$$R(\theta) = \begin{bmatrix} \cos\theta & \sin\theta \\ -\sin\theta & \cos\theta \end{bmatrix} \tag{F.2}$$

Θ_{iso} is the isochrone angle at the reference point. and θ_{iso} the angle at the current point.

The velocity gradient tensor L and deformation gradient tensor F are related by $\dot{F} = L \cdot F$ (1.23). Similarly the velocity gradient in the rotating frame $\hat{L}$ is related to the rotating $\hat{F}$. $\hat{L}$ can be calculated from $\hat{F}$ and its derivative.

$$\hat{L} = \dot{\hat{F}} \cdot \hat{F}^{-1} \tag{F.3}$$

Expanding the right side

$$\hat{\mathbf{L}} = \frac{\partial}{\partial t} \left(\mathbf{R}(\theta_{iso})^t \cdot \mathbf{F} \cdot \mathbf{R}(\Theta_{iso}) \right) \cdot \left(\mathbf{R}(\theta_{iso})^t \cdot \mathbf{F} \cdot \mathbf{R}(\Theta_{iso}) \right)^{-1}$$

$$= \left(\mathbf{R}(\theta_{iso})^t \cdot \dot{\mathbf{F}} \cdot \mathbf{R}(\Theta_{iso}) + \dot{\mathbf{R}}(\theta_{iso})^t \cdot \mathbf{F} \cdot \mathbf{R}(\Theta_{iso}) \right) \cdot \left(\mathbf{R}(\Theta_{iso})^t \cdot \mathbf{F}^{-1} \cdot \mathbf{R}(\theta_{iso}) \right)$$

$$= \left(\mathbf{R}(\theta_{iso})^t \cdot \mathbf{L} \cdot \mathbf{F} + \dot{\mathbf{R}}(\theta_{iso})^t \cdot \mathbf{F} \right) \cdot \left(\mathbf{F}^{-1} \cdot \mathbf{R}(\theta_{iso}) \right)$$

$$= \mathbf{R}(\theta_{iso})^t \cdot \mathbf{L} \cdot \mathbf{R}(\theta_{iso}) + \dot{\mathbf{R}}(\theta_{iso})^t \cdot \mathbf{R}(\theta_{iso}) \tag{F.4}$$

$$\dot{\mathbf{R}}(\theta)^t \cdot \mathbf{R}(\theta) = \dot{\theta} \begin{bmatrix} -\sin\theta & -\cos\theta \\ \cos\theta & -\sin\theta \end{bmatrix} \cdot \begin{bmatrix} \cos\theta & \sin\theta \\ -\sin\theta & \cos\theta \end{bmatrix} = \begin{bmatrix} 0 & -1 \\ 1 & 0 \end{bmatrix} \dot{\theta} \tag{F.5}$$

Thus $\hat{\mathbf{L}}$ can also be calculated by translating $\mathbf{L}$ into the isochrone frame and removing the rotation rate of the isochrone.

$$\hat{\mathbf{L}} = \mathbf{R}(\theta_{iso})^t \cdot \mathbf{L} \cdot \mathbf{R}(\theta_{iso}) + \begin{bmatrix} 0 & -1 \\ 1 & 0 \end{bmatrix} \dot{\omega}_{iso} \tag{F.6}$$

The xx component of $\hat{\mathbf{L}}$ is zero like the corresponding component of $\hat{\mathbf{F}}$.

The Mohr circles for $\mathbf{L}$ and $\hat{\mathbf{L}}$ are offset vertically by $\dot{\omega}_{iso}$. They also have different defining diameters, the global horizontal and vertical for $\mathbf{L}$, and the isochrone and the segment perpendicular to it for $\hat{\mathbf{L}}$. The circle radius is the same in both cases.

F.2 Sinusoidal Bed

Figure F.1 shows the variation in the $\mathbf{F}$ components when the flowband bed is sinusoidal. In reference to Figure F.1(d) and (e), varying the position of the core relative to the bed undulations makes a significant difference in the shape of the F_{xx} curve, while the other curves retain their general character, including θ_f. When B' is close to zero, F_{xx} is generally increasing as in the flat bed case. For $B' > 0$, F_{xx} is decreasing as it passes through 1, with a maximum about half way to the surface. For $B' < 0$, F_{xx} is shaped more like F_{xz} with a minimum upstream. It may even go negative. Interpreting this behavior may be tricky. F_{xx} gives the horizontal length (at points upstream) of something that is currently horizontal. A negative F_{xx} says that the horizontal segment at the core could have been a *leading edge* upstream. This is plausible if the isochrone at the core has a negative enough slope.
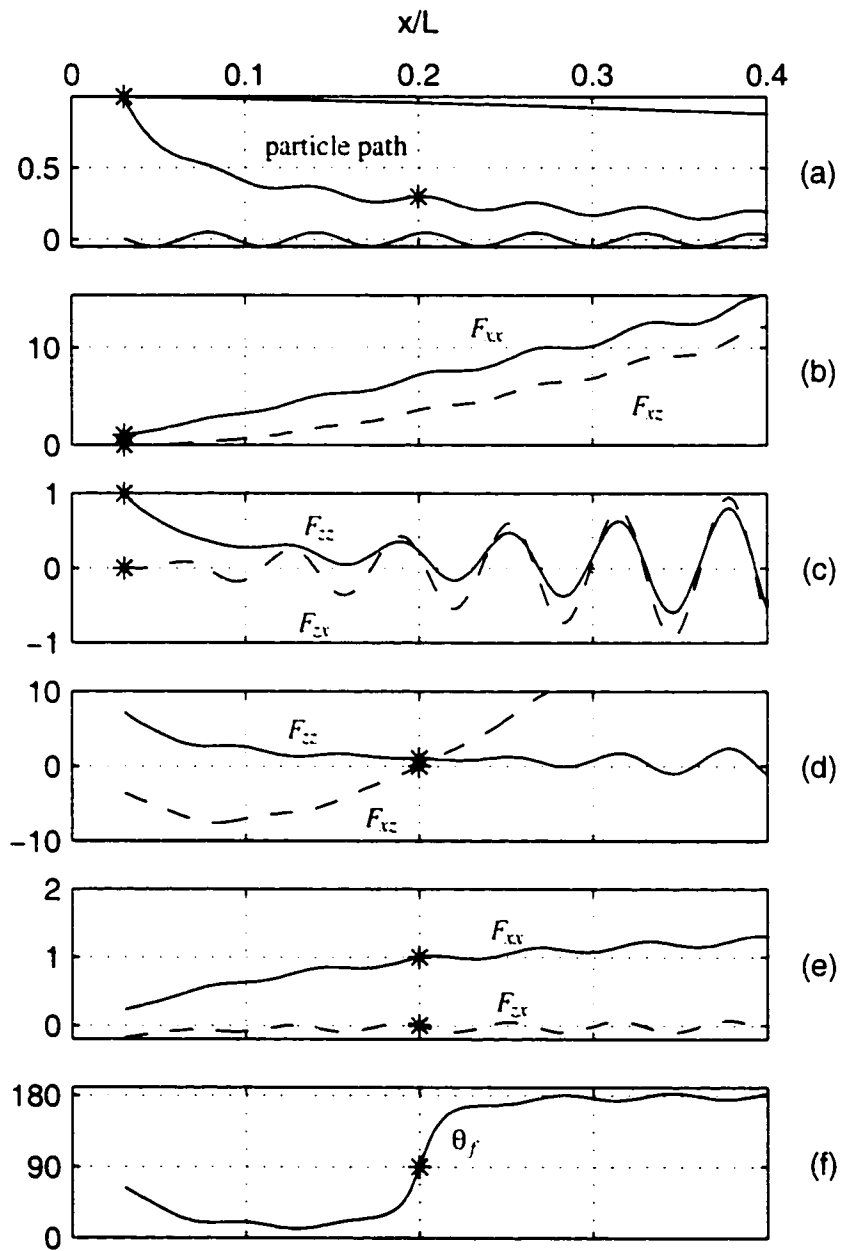
Figure F.1: **F** components along a particle path (a). In (b) and (c) the reference point (∗) is at the surface; in (d) and (e) it is at the core. $C = 0.2L$. (f) $\theta_f = \tan^{-1}(-F_{zz}/F_{xz})$.

Figure F.2 shows the same components, but for a deeper path. Perhaps the most significant difference (beyond the generally large strain values due to a longer travel time) lies in the shape of F_{xx} in panel (e).

Figure F.3 is the same path, but shows the components of $\hat{F}$. The core relative components look much more like the flat bed ones (Figure 1.12). F_{xx} has some wiggles, but no major change in shape depending on core isochrone slope. θ_f is almost devoid of local wiggles – with just slight rises over the bed dips.

One way of looking at how L and $\hat{L}$ vary along a path is to plot selected points on their respective Mohr circles at successive points along the path. Figure F.4 plots the horizontal and vertical defining points, the isochrone and its perpendicular, and the θ_1 point. I have compared such figures for both deep and shallow paths. These can also be compared to the sequence for flow over a flat bed in Figure E.5.

For a shallow path (with $d \approx 0.6$) the vorticity number oscillations are larger than for deeper ones.

The horizontal segment tends to have the same ω oscillation range as θ_0 and θ_1, but for shallow paths, its $\dot{\epsilon}$ oscillation range is smaller. For deep paths its range is significantly larger.

θ_1 oscillates (in the $\dot{\epsilon}$, ω plane) in a mirror image to θ_0. Its ω matches (by definition), but its $\dot{\epsilon}$ varies in the opposite direction. In fact, for plane strain, is just has the opposite sign. It is the $\dot{\epsilon}$ of the $\theta_0 + 90°$ segment.

For the shallow path, with the more limited ω range of the horizontal segment, the mirror image character of the θ_1 dominates, and it actually oscillates out of phase with θ_0. For a deep path, the strong oscillation of the horizontal ω dominates the oscillation of both θ_0 and θ_1, so they tend to be in phase with each other. For intermediate depths the range of the horizontal and θ_0 are about the same, resulting in a subdued angle oscillation for θ_1.

Over a sine bed, the spinor points, $\dot{\epsilon} + i\omega$, for most (if not all) angles move in loops (when plotted for successive points on the path). Those for $0°$, θ_0 and θ_1 are almost circular. That for $90°$ moves upward as it loops, reflecting the strong growth in the shear component, $\partial_z u$.

When the same spinor is calculated in the isochrone frame (using $\hat{L}$) the spinor point movement changes. For θ_0 and θ_1 the spinor moves back and forth on a line with $\omega = 0$. The spinor for $\theta_\perp$ loops upward. The spinor for for the (global) $0°$ has flattened loops, almost like squashed flower

Figure F.2: **F** components along a deeper particle path (a) starting at $x/H = 0.5$. In (b) and (c) the reference point ($*$) is at the surface; in (d) and (e) it is at the core. $C = 0.2L$. (f) $\theta_f = \tan^{-1}(-F_{zz}/F_{xz})$.
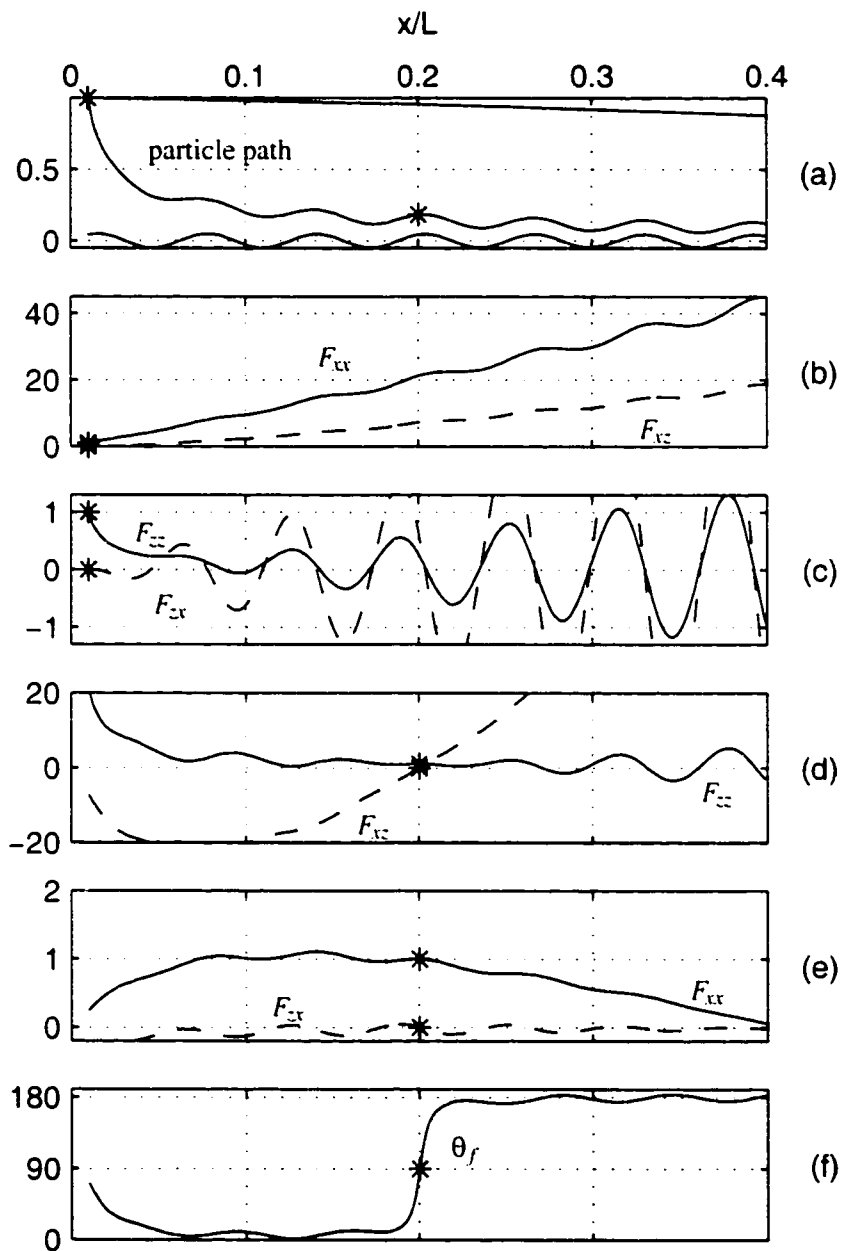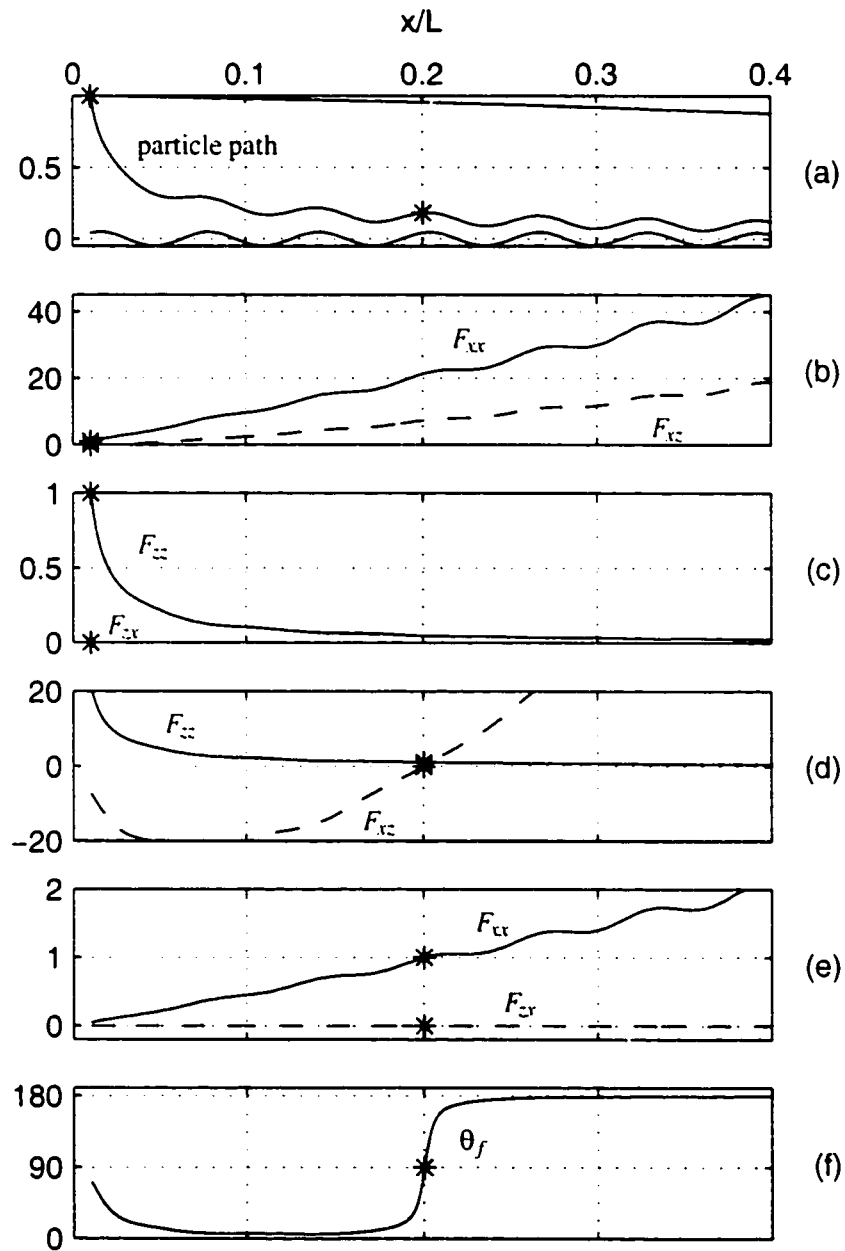
Figure F.3: $\hat{\mathbf{F}}$ components along a particle path (a) starting at $x/H = 0.5$. In (b) and (c) the reference point ($*$) is at the surface; in (d) and (e) it is at the core. $C = 0.2L$. (f) $\theta_f = \tan^{-1}(-F_{zz}/F_{xz})$.

Sine bed – Siple size [4533.29   245.923]
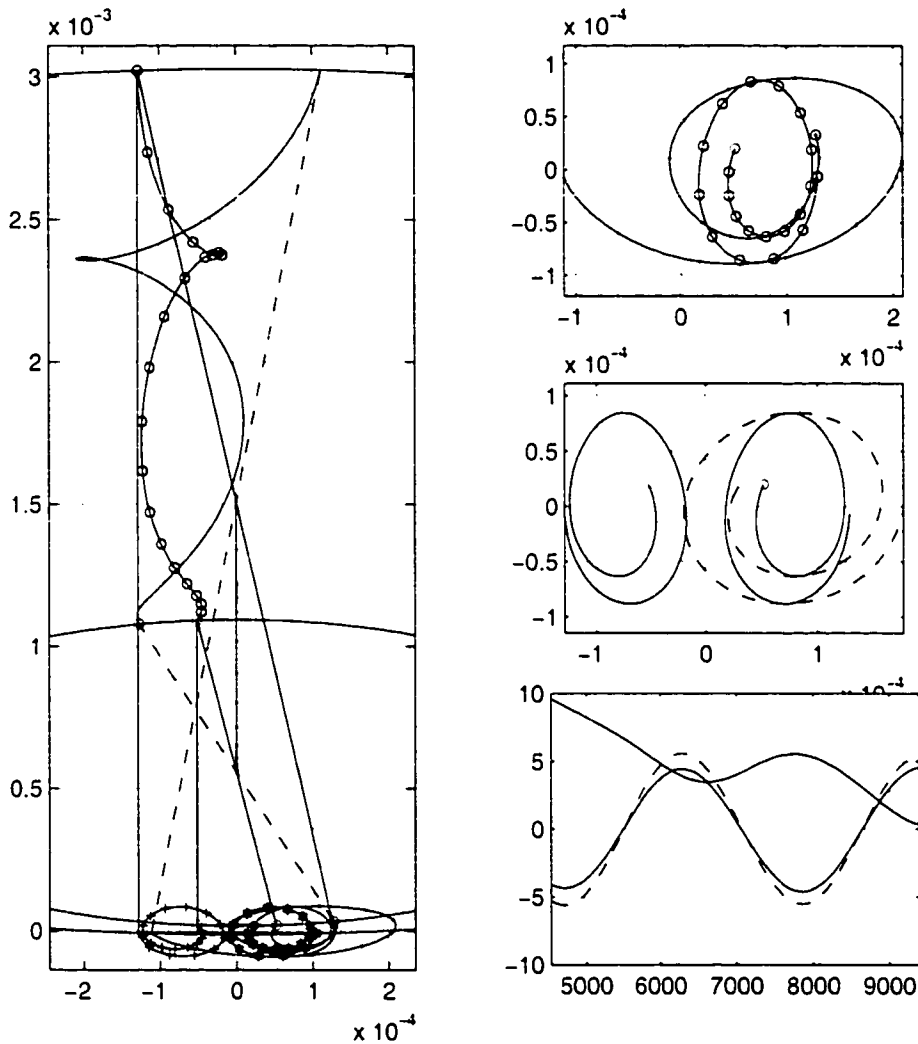
Figure F.4: Rotation and strain rates along a portion of a path (starting at $(500m. 1000m)$) over a sine bed.

(left) Two Mohr circles (zoomed). plus defining diameters (*solid*). $\theta_{iso} - \theta_\perp$ diameters (*dashed*). and points in between. Oscillating near the bottom are x_1. θ_{iso}, and θ_1. $\theta_\perp$ has a large ω like x_2.

(right 1) Zoom on $\omega = 0$ region. equal axis; x_1 (*solid*) and θ_{iso} (–o)

(right 2) Zoom on θ_1 (*left*) and θ_{iso} (*right*); bed parallel vector (*dashed*).

(right 3) θ_{iso} (*solid*). θ_1 (*solid*). bed angle (*dashed*) v. x.

petals. The resulting figure may not be a informative.

The segment rotation rate is (using (E.13) and (E.14))

$$\dot{\omega} = -c\cos^2\theta + (a-d)\cos\theta\sin\theta + b\sin^2\theta$$

$$= \frac{b-c}{2} + \frac{a-d}{2}\sin 2\theta - \frac{b+c}{2}\cos 2\theta \qquad (F.7)$$

For θ oscillating in the ± 0.4 radians range, $\sin 2\theta$ is almost linear, oscillating in step with θ. $\cos 2\theta$ is at the top of the cosine arc, so it oscillates at the double the frequency of θ.

F.2.1 The $[S'(1-\hat{d}) + B'\hat{d}]$ Isochrone Approximation

Over a flat bed, the velocity gradient Mohr circles change in an orderly manner, growing in diameter $((\dot{\epsilon}_1 - \dot{\epsilon}_3)/2)$ and moving up (W_k approaching 1) (Figure E.5). When there are bed undulations, this orderly change is modified. Most notably, the strain rates of the defining points oscillate.

Where the flowpath runs approximately parallel to the undulating bed there are a number of simplifying approximations that give some insight.

θ_0, the isochrone slope angle might be approximated by:

$$\theta_0 \approx -m_0 \approx -[S'(1-\hat{d}) + B'\hat{d}] = -h\partial_x\hat{d} \qquad (F.8)$$

This seems to hold true for quite a range of the flowpath. I have verified this numerically. It also makes sense: at the surface, isochrones should be parallel to the surface; close to bed, they should approximate the bed shape - with the big caveat, that there is no basal melting (or add on). In between, I expect some blending of the two. Linear is a good first guess.

In the following I show that the difference between θ_1 and θ_0 is approximately

$$\theta_1 - \theta_0 \approx \tan(\theta_1 - \theta_0) \approx \frac{1}{2}\left(\frac{h}{x} - h'\right)\frac{1-\hat{d}^4}{\hat{d}^3} \qquad (F.9)$$

For plane strain, $\partial_z w = -\partial_x u$. If $\partial_x w$, θ_0 and θ_1 are all small, the equation for $\theta_1 + \theta_0$ (E.24) reduces to

$$\theta_1 + \theta_0 \approx \tan(\theta_1 + \theta_0) \approx \frac{2\partial_x u}{\partial_z u}$$

With $u = \bar{u}(x)\hat{u}(\hat{d})$, $\partial_z u = -\frac{\bar{u}}{h}\partial_{\hat{d}}\hat{u}$ and $\partial_x u = \bar{u}'\hat{u} + \bar{u}\partial_{\hat{d}}\hat{u}\,\partial_x\hat{d}$

$$\theta_1 + \theta_0 = -2h\frac{\bar{u}'}{\bar{u}}\frac{\hat{u}}{\partial_{\hat{d}}\hat{u}} - 2h\partial_x\hat{d} = -2h\frac{\bar{u}'}{\bar{u}}\frac{\hat{u}}{\partial_{\hat{d}}\hat{u}} + 2\theta_0$$

Expanding on $\bar{u}'$. $\bar{u}' = \frac{Q'}{h} - \bar{u}\frac{h'}{h}$ and $h\frac{\bar{u}}{\bar{u}} = h\frac{Q'}{Q} - h'$

$$\theta_1 = -2h\frac{Q'}{Q}\frac{\hat{u}}{\partial_{d}\hat{u}} + 2h'\frac{\hat{u}}{\partial_{d}\hat{u}} + \theta_0$$

With the shallow ice laminar flow model $\hat{u} = \frac{5}{4}(1 - \hat{d}^{4})$ and $\frac{\hat{u}}{\partial_{d}\hat{u}} = -\frac{1-\hat{d}^{4}}{4\hat{d}^{3}}$

$$\begin{aligned}
\theta_1 &= h\frac{Q'}{Q}\frac{1-\hat{d}^{4}}{2\hat{d}^{3}} - h'\frac{1-\hat{d}^{4}}{2\hat{d}^{3}} + \theta_0 \\
&= h\frac{Q'}{Q}\frac{1-\hat{d}^{4}}{2\hat{d}^{3}} - (S' - B')\frac{1-\hat{d}^{4}}{2\hat{d}^{3}} - \left[S'(1-\hat{d}) + B'\hat{d}\right] \\
&= h\frac{Q'}{Q}\frac{1-\hat{d}^{4}}{2\hat{d}^{3}} - S'\left(\frac{1-\hat{d}^{4}}{2\hat{d}^{3}} + (1-\hat{d})\right) + B'\left(\frac{1-\hat{d}^{4}}{2\hat{d}^{3}} - \hat{d}\right) \\
&= h\frac{Q'}{Q}\frac{1-\hat{d}^{4}}{2\hat{d}^{3}} - S'\left(\frac{1-3\hat{d}^{4}}{2\hat{d}^{3}} + 1\right) + B'\left(\frac{1-3\hat{d}^{4}}{2\hat{d}^{3}}\right)
\end{aligned}$$

For a flowband with uniform accumulation the flux term becomes $Q = b.x$. $\frac{Q'}{Q} = \frac{1}{x}$

$$\theta_1 \approx \left(\frac{h}{x} - h'\right)\frac{1-\hat{d}^{4}}{2\hat{d}^{3}} + \theta_0 \approx B'\left(\frac{1-3\hat{d}^{4}}{2\hat{d}^{3}}\right) - S'\left(\frac{1-3\hat{d}^{4}}{2\hat{d}^{3}} + 1\right) + \frac{S-B}{x}\frac{1-\hat{d}^{4}}{2\hat{d}^{3}}$$

Focusing on B and B' terms gives

$$\begin{aligned}
\theta_1 &\approx \left(\frac{S-B}{x} - S' + B'\right)\frac{1-\hat{d}^{4}}{2\hat{d}^{3}} - S'(1-\hat{d}) - B'\hat{d} \\
&= B'\left(\frac{1-3\hat{d}^{4}}{2\hat{d}^{3}}\right) + B\left(-\frac{1-\hat{d}^{4}}{2x\hat{d}^{3}}\right) + \dots
\end{aligned} \qquad \text{(F.10)}$$

The oscillations in S and S' are subdued compared to the bed oscillations. The effect of B is also dampened by the $1/x$ term. Thus the oscillations in θ_1 are dominated by those of B'.

The coefficient of B' in (F.10) is plotted in Figure F.5. It is -1 for $\hat{d} = 1$ (bed). It is 0 for $\hat{d} = (1/3)^{1/4} \approx 0.76$, and 1 for $\hat{d} \approx 0.64$.

Close to the bed, $(1 - \hat{d}^{4})/\hat{d}^{3}$ is small, so $\theta_1 - \theta_0 \approx 0$. θ_1 varies in phase with B' and θ_0. Closer to the surface $(1 - \hat{d}^{4})/\hat{d}^{3}$ is larger, so the $x/h - h'$ and $-B'$ dominates. θ_1 then is out of phase with the bed and the isochrones. There is an intermediate depth in which the B' terms cancel, and θ_1 has rather subdued undulations. Specifically, $\frac{1}{2}(1 - \hat{d}^{4})/\hat{d}^{3} \approx \hat{d}$, that is $\hat{d} \approx 3^{-1/4} = .76$. This is specific to our $n = 3$ laminar flow approximation, and plane flow.
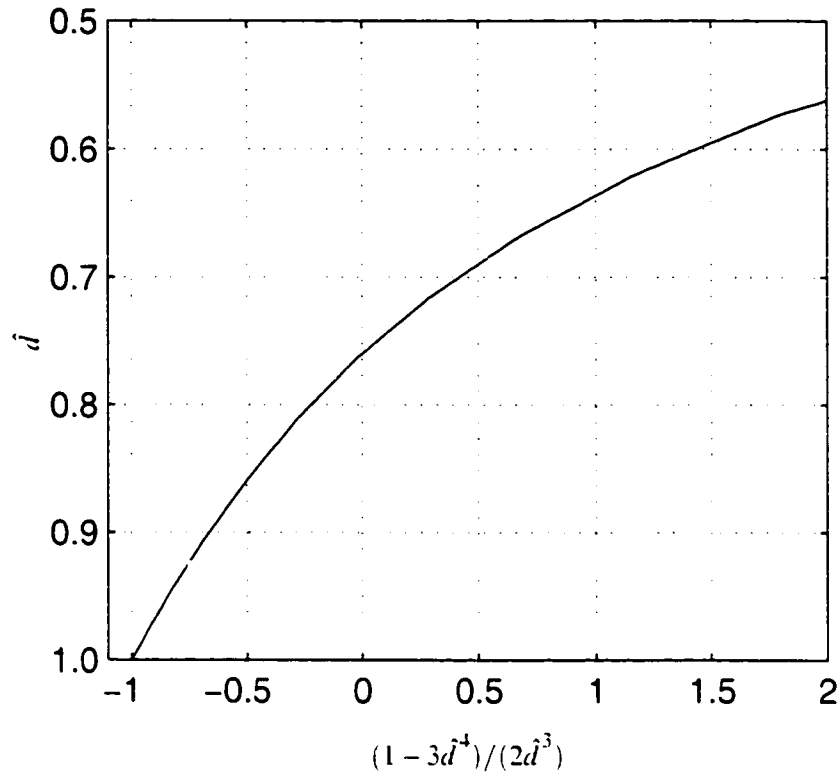
Figure F.5: The B' (F.10) coefficient versus normalized depth

I can calculate a similar expression for the particle path angle. For the uniform accumulation, shallow ice laminar flow this is:

$$u = \bar{u}\hat{u} = \frac{bx}{h}\hat{u} \qquad w = -b\hat{w} + u\left[S'(1-\hat{d}) + B'\hat{d}\right]$$

$$\frac{w}{u} = -\frac{h}{x}\frac{\hat{w}}{\hat{u}} + \left[S'(1-\hat{d}) + B'\hat{d}\right] \qquad \frac{\hat{w}}{\hat{u}} = \frac{4 - 5\hat{d} + \hat{d}^5}{5(1-\hat{d}^4)} \approx 0.8(1-\hat{d})$$

$$m_{fp} \approx -\frac{4h}{5x}(1-\hat{d}) + m_0 \tag{F.11}$$

For $\hat{d}$ close to 1 (near the bed), $\hat{w}/\hat{u} \approx 0$, so that (F.11) is dominated by the B' term. The particle path starts out (at the surface) with less stretching and greater rotation (decreasing θ). But with depth it becomes subparallel to the isochrones, which in turn are subparallel to the bed ($m_{fp} - m_0$ approaches 0_-).

The particle path slope. m_{fp} is always more negative than the isochrone slope. m_0. The path

always cuts across the isochrones in the same direction, downward, from surface side to bed side.

F.3 Conclusion

- There are several formulas for the angle that rotates along with the isochrones.
- Close to the bed, all segments tend toward being subparallel to the bed.
- Further from the bed the θ_1 angle moves out of phase.
- Over an undulating bed the θ_1 and θ_r criteria loose value in predicting overturn events
- But θ_1 based on a smoothed bed may retain some usefulness.
- The generalized Mohr circle is a valuable tool in understanding these segment rotation rate issues.

Appendix G

NOTATION

W_k kinematic vorticity number.

$\dot\omega$ rotation rate.

$\dot\varepsilon$ strain rate.

$\dot\varepsilon_{max}, \dot\varepsilon_{min}$ principal strain rates.

θ_r strain rate stability angle.

x horizontal coordinate (downstream).

z vertical coordinate.

y coordinate orthogonal to x and z.

$u(x,z)$ horizontal velocity component.

$w(x,z)$ vertical velocity component.

v $= 0$, transverse velocity component.

$\mathbf{L}$ velocity gradient tensor; $\partial_z u$ is a component.

L length of flowband, from divide to terminus.

H thickness at the divide.

$\dot b$ accumulation rate.

T $= H/\dot b$, time scale.

t time.

$S(x)$ surface profile.

S' surface slope, gradient of $S(x)$.

$B(x)$ bed profile ($B(x) = 0$).

$h(x)$ $= S - B$, thickness.

$\hat d$ $= (S - z)/h$, normalized depth.

$Q(x)$ flux through flowband cross–section at x.

$\bar u(x)$ mean horizontal velocity.

$\hat{u}(\hat{d})$ vertical profile of $u(x,z)$.

$\hat{w}(\hat{d})$ vertically integrated $\hat{u}$.

A flow parameter.

ρg ice density times gravity acceleration.

C x coordinate of a hypothetical ice core.

θ_f precore slope angle.

$\mathbf{F}$ deformation (position) gradient tensor.

$\mathbf{F}_{(\mathbf{Xx})}$ $\mathbf{F}$ with $\mathbf{X}$ reference point, $\mathbf{x}$ current point.

F_{xx} one of the components of $\mathbf{F}$.

$d\mathbf{X}, d\mathbf{x}$ reference and current segments.

Θ, θ reference and current segment angles.

θ_p angle of the particle path.

Additions for full flow model description, Appendix A

$\upsilon(x)$ flowband relative width.

$\hat{z}$ $= 1 - \hat{d}$, normalized height.

$q(x,z)$ partial flux, flux below (x,z).

$\dot{\varepsilon}, \tau$ effective strain rate and deviatoric stress.

$\dot{\varepsilon}_{xz}$ shear strain rate term.

τ_{xz} shear stress term.

n $= 3$, Glen's flow law exponent

m flowband width exponent.

$x_{div}(t)$ divide position

x_1 $= x - x_{div}$, position relative to the divide.

$\hat{u}_d, \hat{u}_f$ divide and flank $\hat{u}$.

$\hat{w}_d, \hat{w}_f$ divide and flank $\hat{w}$.

η_d, η_f divide and flank blending function.

$T_n(\xi)$ Chebyshev polynomial.

$\hat{z}_l, \hat{z}_u$ boundaries of the $\hat{z}$ range mapped onto $\xi = [-1 \ 1]$.

Added probability notation for Chapter 2

$\mathbf{x}$ position vector, $[x, z]$.

θ, t injection angle and time.

ϕ, τ observation angle and time.

$\gamma(\theta, t, \tau)$ forward angle rotation function.

$\gamma^{-1}(\phi, t, \tau)$ inverse angle rotation function.

$\theta_f(t, \tau)$ precore slope angle $= \gamma^{-1}(90°, t, \tau)$.

$P(\theta, t)$ injection probability distribution.

$p(\theta, t)$ injection probability density.

$P_{\theta}(\theta, t)$ $p(\theta, t)$ integrated over θ.

$P_t(\theta, t)$ $p(\theta, t)$ integrated over t.

$Q(\phi, \tau)$ observation probability distribution.

$Q(90°, \tau)$ overturn probability.

$Q_c(\tau)$ conditional, $Q(90°, \tau)/P(0°, \tau)$.

$q(\phi, \tau)$ observation probability density.

$g(\theta)$ Gaussian density function in angle.

$\delta(s)$ Dirac delta function.

θ_{fix} a fixed injection angle.

t_{fix} a fixed injection time.

t_u, t_d upstream and downstream boundaries of the injection region.

$t_m(\theta)$ 'minimum' injection time.

$\tau_o(\theta)$ overturn time corresponding to t_m.

R_u region between t_u and t_m.

R_d region between t_m and t_d.

Added thickness notation for Chapter 4

$z_h, w_b, \ldots$ See Table 4.1.

$\hat{\mathbf{F}}$ F tensor aligned with the rotating isochrone frame.

$\hat{\mathbf{L}}$ L tensor aligned with the rotating isochrone frame.

$\mathbf{R}(\theta)$ rotation tensor.

Added notation for Appendix E

$x_1 x_2$	geometric product of two vectors.
$x_1 \cdot x_2$	scalar dot product of two vectors.
$x_1 \wedge x_2$	bivector wedge product of two vectors.
$e_1 . e_2$	an orthonormal basis.
$i = e_1 e_2$	unit bivector in this basis.
$a + ib$	spinor, sum of a scalar and a bivector.
$e^{i\phi}$	$= \cos\phi + i\sin\phi$, unit spinor (exponential notation).
$f x$	$= f(x)$, application of linear operator f to x.
$f x_{\parallel}$	component of $f x$ parallel to x.
$f x_{\perp}$	component of $f x$ perpendicular to x.
$f x x$	spinor representation of action of f on x.
$f e_1 e_1, f e_2 e_2$	a pair of defining points for the f Mohr circle.
λ_r	$= \frac{1}{2}|f e_1 e_1 - f e_2 e_2|$ circle radius.
$\lambda_c e^{i\phi_c}$	$= \frac{1}{2}(f e_1 e_1 + f e_2 e_2)$ circle center.
x_0	vector aligned with isochrone, angle θ_0.
$x_0 i$	vector perpendicular to isochrone, angle $\theta_{\perp}$.
x_1	vector with same rotation rate as isochrone, angle θ_1.
ϕ_{01}	angle between x_0 and x_1.
$\dot{\varepsilon}_0 . \dot{\omega}_0$	strain and rotation rates for x_0.
$\dot{\varepsilon}_{\perp} . \dot{\omega}_{\perp}$	strain and rotation rates for $x_0 i$.
$\dot{\varepsilon}_c . \dot{\omega}_c$	strain and rotation rates for the circle center.

VITA

H. Paul Jacobson III

Education

- 1972. California Institute of Technology. B.S.. Engineering and Economics
- 1975. Northwestern University. M.S.. Cand.Ph.. Industrial Engineering
- 2001. University of Washington. Ph.D.. Geophysics

Employment

- 1976-1977. Loyola University. Chicago. Instructor. business statistics and management science

- 1981-1991. Chicago Research and Trading. Financial analyst and software engineer (options pricing software)

- Northwestern University and University of Washington. Research and teaching assistant

Publications

- Jacobson. H. P. and Waddington. E. W. (1996). Finite strain and folding in ice sheets. *EOS Trans. AGU. Fall Meeting Suppl.,* **77.** S.

- Nereson. N. A.. Waddington. E. D.. Raymond. C. F.. and Jacobson. H. P. (1996). Predicted age-depth scales for Siple Dome and inland WAIS ice cores in West Antarctica. *Geophysical Research Letters.* **23**(22). 3163–3166.

- Jacobson. H. P. and Raymond. C. F. (1998). Thermal effects on the location of ice stream margins. *Journal of Geophysical Research.* **103.** 12111–12122.